Virginia Commonwealth University

VCU Scholars Compass

2013

Graphene-Supported Metal Nanoparticles For Applications in Heterogeneous Catalysis

HANY ELAZAB
Virginia Commonwealth University

www.manaraa.com

Graphene-Supported Metal Nanoparticles For Applications in Heterogeneous Catalysis

A dissertation submitted in partial fulfillment of the requirements for the degree of Doctor

of Philosophy at Virginia Commonwealth University

by

Hany A. A. Elazab

M.Sc. in Chemical Engineering, Military Technical College (M.T.C)

Cairo, EGYPT

Advisors:

Prof. Dr. M. S. El – Shall   **Prof. Dr. B. Frank Gupton**

Ph. D. Professor of Physical Chemistry,   Ph.D. Research professor and chair,
Department of Chemistry   Chemical and Life Science Engineering
College of Humanities and Sciences   School of Engineering.

Virginia Commonwealth University

Department of Chemical and Life Science Engineering

Richmond, Virginia, USA

December, 2013

ACKNOWLEDGMENTS

First, I am grateful to **ALLAH** the Exalted and Mighty lord for his mercy, blessings, and gratitude. I always seek his guidance, kindness and forgiveness in this life and in the hereafter. I express my deep gratitude to my beloved country **EGYPT**; especially to the **Egyptian Armed Forces** for granting me this fully funded Ph. D. scholarship. I also thank the **National Science Foundation** (CHE-0911146 and OISE-1002970) for the support of this work. It is my pleasure to acknowledge my research advisors **Prof. Dr. M. Samy El-Shall** and **Prof. Dr. B. Frank Gupton** who kindly gave me the opportunity to continue my graduate studies and earn my Ph.D. under their kind supervision. I acknowledge them for all advice they gave me to solve my research problems. I am really so grateful for their significant contribution in advancing our research projects and communications. I truly thank both of them for their time, valuable inputs and the continuous support and help. Many thanks to my advising committee, **Prof. Dr. Kenneth J. Wynne**, **Prof. Dr. Stephen S. Fong**, and **Prof. Dr. Hani El-Kaderi**, for their encourage, guidance, and valuable feedback during the course of my study.

I want also to express my deep gratitude **Mr. Magnus Fagrell** and **Mr. Ingemar Orsen** from **Wave Craft Company** for their kind support with their new and so special microwave micro reactor that I used for synthesis of nanoparticles and using these prepared nanoparticles in an environmental application to remove carbon monoxide as discussed in chapter 4.

TABLE OF CONTENTS

LIST OF TABLES

List of Figures

ABSTRACT

Graphene-Supported Metal Nanoparticles For Applications in Heterogeneous Catalysis

By Hany Abdelmenem Abdelrahman Elazab, Ph.D.

A dissertation submitted in partial fulfillment of the requirements for the degree of Doctor of Philosophy at Virginia Commonwealth University.

Virginia Commonwealth University, 2013.

Advisors:

B. Frank Gupton, Ph.D. Research professor and chair, Chemical and Life Science Engineering, School of Engineering.

M. Samy El-Shall, Professor of Physical Chemistry, Chemistry Department, College of Humanities and Sciences.

Due to its unique properties and high surface area, Graphene has become a good candidate as an effective solid support for metal catalysts. The Nobel Prize in Physics for 2010 was awarded to Andre Geim and Konstantin Novoselov "for groundbreaking experiments regarding the two-dimensional material graphene". Microwave-assisted synthesis of various metallic nanostructured materials was investigated for CO oxidation applications. These metallic nanostructured materials were used to convert CO to CO_2 as an effective approach for carbon monoxide elimination due to its harmful effect on health and environment.

In particular, this dissertation is focusing on palladium as a transition metal that has a unique ability to activate various organic compounds to form new bonds. The prepared graphene-supported metallic nanostructured materials were successfully used to investigate Suzuki cross-coupling reaction as an important reaction in the field of pharmaceutical applications. In this research, nanostructured materials were used as solid support catalysts which showed remarkable improvements in the aspects of size, surface structure, catalytic selectivity, shape and recyclability. The nano porous structure and superparamagnetic behavior of (Fe_3O_4) nano particles that were used as an effective ingredient in graphene-supported palladium catalyst improved the catalytic activity and the catalyst recyclability simply by using an external magnetic field. This research has been divided into two main categories; the first category is to investigate other metal oxides as a solid support for palladium to be used in CO oxidation catalysis. The second category will focus on improving of solid support systems of palladium – magnetite catalyst to increase recyclability. The final stage of this investigation will study the use of these solid supported metal catalysts in continuous heterogeneous processes under flow reaction conditions. The structural, morphological and physical properties of graphene-based nanocomposites described herein were studied using standard characterization tools such as TEM, SEM, X-ray diffraction, XPS and Raman spectroscopy.

CHAPTER 1   INTRODUCTION

1.1   Overview

It is now well established that nanoparticles (1-100 nm) exhibit unique chemical and physical properties that differ from those of the corresponding bulk materials.[1-3] The dependence of the properties of nanoscale materials on the size, shape and composition of the nanocrystal is a phenomenon of both fundamental scientific interest and many practical and technological applications.[4-7] These properties are often different, and sometimes superior, to those of the corresponding bulk materials. The origins of the differences can be explained by the high surface-to-volume ratio, dispersion factors and the quantum size effects unique to a specific length scale.[8] For example, semiconductor nanoparticles in the size range of ~1 to ~20 nm in diameter (often called quantum dots) possess short-range structures that are essentially the same as the bulk semiconductors, yet have optical and/or electronic properties which are dramatically different from the bulk.[8-9] The confinement of electrons within a semiconductor nanocrystal results in the shift of the band gap to higher energy with smaller crystalline size. This effect is known as the "quantum size effect".[8-12] In the strong confinement regime, the actual size of the semiconductor particle determines the allowed energy levels and thus the optical and electronic properties of the material.

1

The characterization of the unique properties of nanocrystals can ultimately lead to identifying many potential uses and applications, ranging from catalysis, ceramics, microelectronics, sensors, pigments, and magnetic storage to drug delivery and biomedical applications.[8, 13-14] The applications of nanoparticles are thus expected to enhance many fields of advanced technology particularly in the areas of catalysis, chemical and biological sensors, optoelectronics, drug delivery, and media storage.[9, 15-24]

1.2 Dissertation Outline

This dissertation is focused on the synthesis of functional graphene-based nanocomposites of great promise for applications in energy conversion and storage, catalysis and biomedicine. The next section of chapter 1 begins with brief background and literature review on catalysis, graphene and different classes of nanostructures that is necessary for understanding subsequent sections. Then the statement of research problem is described followed by the objectives of our work. Chapter 2 presents a brief description of the instruments used in catalyst synthesis, catalytic performance evaluation, and also the physical techniques used for characterization and studying the properties of our graphene-based nanostructured materials. This dissertation is divided mainly into two main parts; the first part is concerned with CO oxidation catalysis applications as in chapters 3, 4, and 5. While the second part is concerned with cross-coupling reactions applications as in chapters 6, 7, and 8.

In chapter 3, a microwave irradiation method for decorating iron oxide, cobalt oxide, and nickel hydroxide with Pd nanocrystals of controlled size, shape, and crystalline structure was described. Research in the nanocatalysis field is focused mainly on designing superior nanostructured catalysts that are essential for many technological advances in chemical synthesis and processing, environmental detoxification and improving air quality.

2

Chapter 4 details the microwave - assisted synthesis of Pd supported on iron oxide nanocomposites prepared under flow reaction conditions and their use as heterogeneous catalysts for the low-temperature CO catalytic oxidation.

Chapter 5 presents Pd based catalysts supported on shape controlled CeO_2 and TiO_2 for low-temperature CO catalytic oxidation. This chapter is a kind of comparison between previously prepared catalysts and other catalysts with different supports and also discussing the fact that noble metal nanoparticles have received significant attention for decades because of the feasibility to tune their electronic and optical properties by changing size, shape, composition or dielectric environment.

In chapter 6, a general microwave-assisted synthesis for decorating graphene with both Pd and magnetite nanocrystals under batch reaction conditions is outlined. This catalyst was used as an efficient magnetically recyclable catalyst for Suzuki cross-coupling.

In chapter 7, the Pd – Fe_3O_4 supported on graphene catalyst that was prepared under batch reaction conditions was tested for evaluating its catalytic activity performance under flow reaction conditions.

Chapter 8 describes Laser Vaporization Controlled Condensation (LVCC) synthesis of Pd – Fe_3O_4 supported on Graphene to be used in Suzuki cross-coupling reactions. This chapter is discussing the fact that the interest in magnetic nanostructures and their composite materials, with a special emphasis on magnetite, has increased over years owing to their potential applications in electronics, optoelectronics, data storage industries, catalysis and biomedicine. This chapter was a trial to prepare the same catalysts with physical methods as a comparison.

3

1.3   CO Oxidation Catalysis in Environmental Applications

Carbon monoxide (CO) is a potentially fatal gas that is produced as a result of incomplete combustion of a hydrocarbon such as petroleum or natural gas. CO can cause severe side effects that include headache, fatigue, dizziness, sore throat…etc. Prolonged exposure can cause much more serious symptoms and in some cases, death. With oxidation catalysis, carbon monoxide removal is possible. Luckily, carbon monoxide removal is possible through the process of catalysis.[25] Hence, a large number of new catalysts for low temperature CO oxidation trials are being developed to decrease pollution for environmental concerns.[26-31] Oxidation catalysis usually requires the use of transition metals such as gold, palladium, ruthenium, platinum, iridium, or rhodium.[32-33]   All oxidation catalysts work the same way to transform carbon monoxide into carbon dioxide, thus reducing or eliminating the potential risk of CO inhalation.[34-38] Bimetallic nanoalloys for CO oxidation and nanoporous magnetic iron oxide microspheres have been successfully synthesized by the way of microwave heating.[39-42] Besides iron oxides, cobalt oxides were also investigated for environmental applications in CO catalysis. [43-47]

The Sabatier principle is a qualitative concept in chemical catalysis named after the French chemist Paul Sabatier. It states that the interactions between the catalyst and the substrate should be "just right"; that is, neither too strong nor too weak. If the interaction is too weak, the substrate will fail to bind to the catalyst and no reaction will take place. On the other hand, if the interaction is too strong, the catalyst gets blocked by substrate or product that fails to dissociate. The steps in any catalytic reaction would be generally as shown in **Figure 1-1**.

4
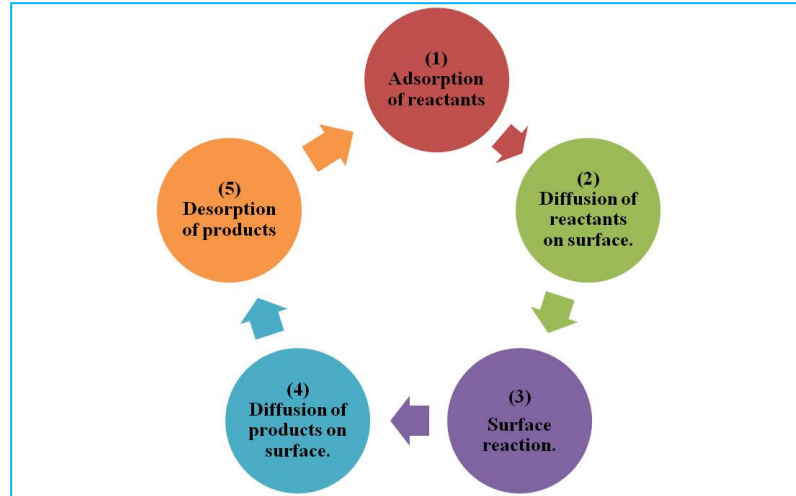
Figure 1-1 Catalytic reaction steps

So, reactants like carbon monoxide and oxygen as shown in **Figure 1-2** are adsorbed on the surface where diffusion of these reactants took place, then the reaction between oxygen adsorbed on the reduced sites of the support and CO adsorbed on Pd at the metal–oxide interface. Then, the diffusion of products on the surface would be followed by desorption of products.[48]
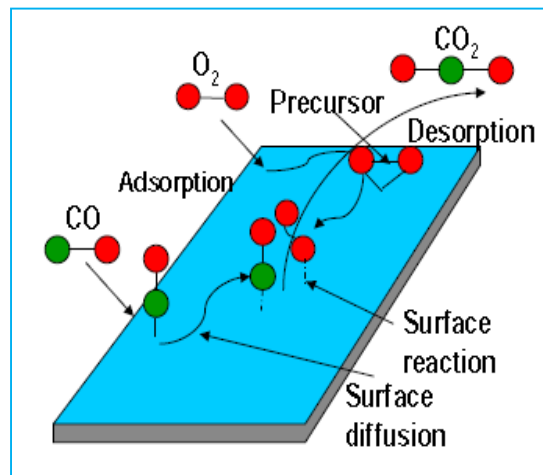
Figure 1-2 Catalytic CO Oxidation Reaction Steps*

* Nanomaterials Lectures, M. S. El-Shall

5

1.4 Metal Catalyzed Carbon-Carbon Cross-Coupling

Metal catalyzed carbon-carbon bond forming reactions have rapidly become one of the most effective tools in organic synthesis for the assembly of highly functionalized molecules. In studying the evolutionary history of organic chemistry, it is easy to conclude that no other type of reaction plays as large a role in shaping this field of science as carbon–carbon bond-forming reactions. [49-50] During the second half of the 20th century, transition metals have come to play an important role in organic chemistry which in turn led to the development of a large number of transition metal-catalyzed reactions for creating organic molecules.

Transition metals have a unique ability to activate various organic compounds and through this activation they can catalyze the formation of new bonds. One metal that was used early for catalytic organic transformations was palladium. [51-54]

In general, transition metals, and in particular palladium, have been of importance for the development of reactions for the formation of carbon-carbon bonds. The development of palladium catalyzed cross-coupling reactions represents one of the most significant advancements in contemporary organic synthesis. In 2005 the Nobel Prize in chemistry was awarded to metal-catalyzed reactions for the formation of carbon-carbon double bonds. In 2010 the Nobel Prize in chemistry is awarded to the formation of carbon-carbon single bonds through palladium-catalyzed cross-coupling reactions. Due to its outstanding physical and chemical properties; metal nanoparticles play an important role in many aspects of research ranging from catalysis and biology to material science and green chemistry. [55-61] The advanced and unique magnetic, electronic, and catalytic properties of the materials in the nanoscale attracted research centers to investigate this area of science deeply. [4, 44, 62-65]

6

In the field of catalysis, separation of catalysts is a critical step especially in medical and therapeutic applications and mainly in cross - coupling reactions. [45, 66-69] Issues associated with homogeneous catalysis remain a challenge to pharmaceutical applications of these synthetic tools due to the lack of recyclability and contamination from residual metals in the reaction product. So, heterogeneous catalysis is the key for solving these problems.

The catalytic effect of magnetic nanoparticles was an important area of research due to its huge industrial applications. [70-72] It is also remarkable that carbon materials have an increasing importance in catalytic processes when used as catalyst supports but there is also an endless effort to develop other kinds of supports like metal oxides. [47, 62, 73-80] Syntheses of nanoparticles with variable sizes have been intensively tried particularly for magnetic iron oxides with namely maghemite (α-Fe_2O_3) and magnetite (Fe_3O_4). [46, 81-88] These nanoparticles were used efficiently as magnetic recoverable catalysts for various applications. [74, 89-96]

Over the past decade, transition metal particles in nanoscale have been intensively pursued as potentially advanced catalysts due to their unique properties lying between those of single metal atoms and bulk metal. The accurate control of particle size and overall particle size distribution is one of the most important challenges to provide new chemical and physical properties. [72, 89, 97-98]

When the nanostructured materials were used as heterogeneous catalysts by comparing with traditional catalysts, the nanostructured materials showed special properties of nanoparticles and new effects caused by nanostructured combination, with remarkable improvements in the aspects of size, numbers of reaction active sites, surface structure, catalytic selectivity, and shape.

7

Thus, the nanostructured materials have great potential application in the field of heterogeneous catalysis and have become the corner stone of materials science in the area of heterogeneous catalysis especially in recent years. [56, 94, 99] Also, the nanoporous structure and superparamagnetic behavior of (Fe_3O_4) nanoparticles make them ideal for powerful application potentials in chemical, physical, biological, biomedical, and environmental engineering fields. [40, 61, 81, 84, 86, 92, 95, 100-103] Recently, the synthesis and applications of magnetic nanoparticles (MNPs) have attracted more interest in catalysis research, and MNP-derived catalysts have been used in industrially important reactions such as hydrogenation, hydroformylation, Suzuki-Miyaura and Heck cross - couplings, and olefin metathesis. [66, 82-83, 104-105]

It is well known that carbon - carbon and carbon-Heteroatom couplings are among the most relevant processes in organic synthesis. These reactions act like a bridge to a wide range of carbon-carbon and carbon-heteroatom couplings that find applications in many different areas including pharmacy, agriculture, medicine, cosmetics and natural products. Nanomaterials in general are important in many different areas, from basic research to diverse applications in electronics, biochemical sensors, catalysis and energy. The nano-sized particles increase the exposed surface area of the active component of the catalyst, hence enhancing the contact between reactants and catalyst dramatically in a way similar to that of the homogeneous catalysts. This has also led to some innovative ideas about the use of nanocatalysis for green chemistry development including the possibility of using microwave heating with nanocatalysis. [30-31, 55, 68-69, 106-107] High catalytic activity, ease of recovery using an external magnetic field and use of water as the solvent are additional eco-friendly attributes of this catalytic system. [33, 65, 87-88, 108]

Recently, researchers were focusing on the use of heterogeneous catalysis in conjunction with micro reactor technology as a strategy that can facilitate a cleaner and scalable flow methodology for organic synthesis. Specifically, transition metal catalysts such as palladium, copper, ruthenium, and nickel are used on silica, carbon based, magnetic nanoparticles and polymer supports. These catalysts have been investigated to promote a range of reactions including Heck, Sonogashira, Suzuki, Kumada, olefin metathesis, and hydrogenation reactions. [62, 91, 93, 96, 109] Mechanism of the Suzuki reaction is best viewed from the perspective of the palladium catalyst as shown in **Figure 1-3**. The first step is the oxidative addition of palladium to the halide (**2**) to form the organopalladium species (**3**). Then, reaction with base gives intermediate (**4**), which via transmetalation with the boron-ate complex (**6**) forms the organo-palladium species (**8**). Finally, reductive elimination of the desired product (**9**) restores the original palladium catalyst (**1**).[110-111]
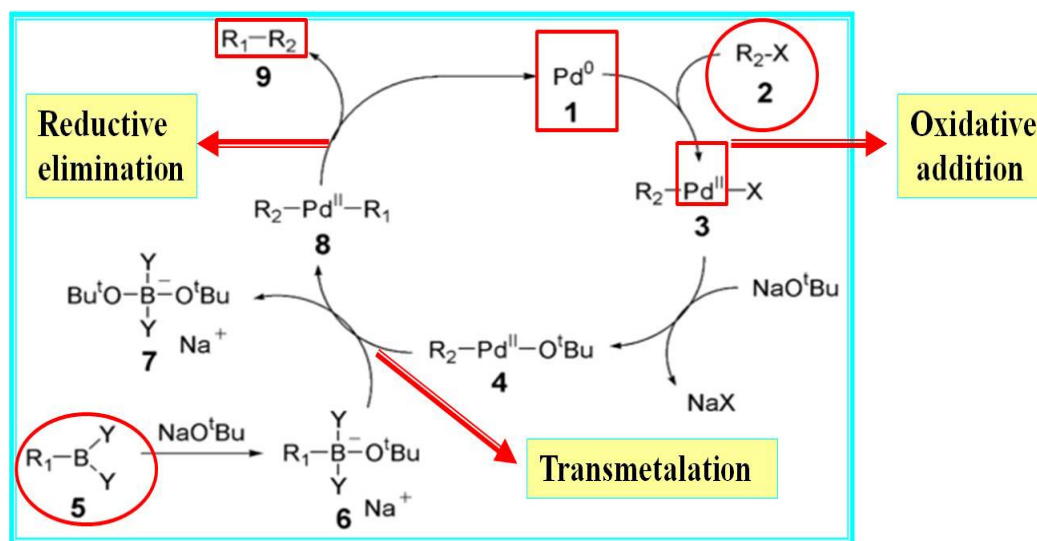
Figure 1-3 General Mechanism of Suzuki cross-coupling reaction[49]

1.5 Graphene as an Ideal Support

The carbon materials has an increasing importance in catalytic processes when used as catalyst supports but there is also an endless effort to develop other kinds of supports like metal oxides.[47, 62, 73-80]

The most exciting periods of scientific research are often associated with discoveries of novel materials that introduce opportunities to solve scientific challenges. Such a period was realized by the discovery of graphene in 2004.[112] Graphene is a two-dimensional (2D) allotrope of crystalline carbon. Its remarkable intrinsic features and electronic properties give graphene a great deal of research interest in the present and the future. Despite its short history, graphene has already revealed new physical and chemical properties to explore along with potential applications in many technological fields such as nanocomposites, nanoelectronics, sensors, batteries, supercapacitors and hydrogen storage.[113]

The recently reported properties and applications of graphene have sparked new opportunities for future systems and devices. Graphene related investigations ranging from fundamental studies to practical devices utilization have been the focus of many research communities from various disciplines. Chemists are working on developing new methods to synthesize processable graphene. Physicists are trying to understand and implement the new graphene's. Engineers are designing new systems and devices to make use of graphene's extraordinary properties and biologists are working to introduce graphene into biomedical diagnoses and treatments. The existence of such focused research and wide fruitful collaborations makes the future of graphene extremely bright.

10

1.6   Magnetic Nanoparticles Impact on Catalysis

Magnetic nanoparticles have attracted much interest in the field of medical and biological applications such as magnetic resonance imaging, drug delivery, as well as in the field of separation science.

Due to its outstanding physical and chemical properties, metal nano-particles play an important role in many aspects of research ranging from catalysis and biology to material science and green chemistry.[55-61]   The metal oxide nano catalysts is of great importance in improving the thermal-catalytic decomposition performance.[43, 103, 114] Pd nanocrystals absorbed on metal oxides and bimetallic Ni-Fe alloys have been also studied for oxidation catalysis.[6, 115-124]

The advanced and unique magnetic, electronic, and catalytic properties of the materials in the nano scale attracted research centers to investigate this area of science deeply.[4, 44, 62-65]

Syntheses of nanoparticles with variable sizes have been intensively tried particularly for magnetic iron oxides with namely maghemite (α-Fe_2O_3) and magnetite (Fe_3O_4).[46, 81-88]

In the field of catalysis, separation of catalysts is a vital step especially in medical and therapeutic applications and mainly in cross coupling reactions.[45, 66-69]   The catalytic effect of magnetic nanoparticles was an important area of research due to its huge industrial applications.[70-72]   These nano particles were used efficiently as magnetic recoverable catalysts for various applications.[74, 89-96]

1.7   Statement of the problem

This dissertation gives an overview of the two main problems discussed in this dissertation. This dissertation aims to present solutions for two main problems.

11

The first problem is related to elimination of carbon monoxide to avoid its adverse effects on environment and health. In this dissertation, different catalysts were prepared like: $Pd-Fe_3O_4$ $Pd-Co_3O_4$, $Pd-Ni(OH)_2$, these catalysts were developed by microwave-assisted synthesis under batch reaction conditions and were tested for CO oxidation. Then, $Pd-Fe_3O_4$ catalyst was developed by microwave-assisted synthesis under flow reaction conditions using a flow microreactor known as Wavecraft's One. The catalytic activity of that catalyst was evaluated against CO oxidation. Also, some trials were done to prepare the different catalysts of palladium supported on different shapes of supports like Ceria and Titania as a comparison study.

The second problem is concerned with the difficulty of catalyst separation from final product and possible routes to solve this by using heterogeneous catalysis instead of homogeneous catalysis and also by developing new magnetic catalysts which are easier to be separated. Replacement of precious metal catalysts by catalysts tailored at the nanoscale with base metals has the potential to improve chemical reactivity and reducing process costs. Issues associated with homogeneous catalysis remain a challenge to pharmaceutical applications of these synthetic tools due to the lack of recyclability and contamination from residual metals in the reaction product. One of the major problems in catalysis is in the ability to effectively conduct catalyst separations. In this dissertation, a magnetic catalyst of $Pd-Fe_3O_4/G$ was developed by microwave-assisted synthesis and was tested for Suzuki cross-coupling reactions under batch reaction conditions and also the catalytic activity of that catalyst was evaluated against Suzuki cross-coupling reaction under flow reaction conditions.

Also, some trials were done to prepare the same catalyst by physical method using Laser Vaporization Controlled Condensation (LVCC) as a kind of comparison.

12

1.8 Objectives and Technical Approach

The main objectives of this study are to explore different graphene-supported metallic nanostructured materials used as catalysts and also investigate their catalytic performance in catalysis applications to remove carbon monoxide as a critical environmental application and also in carbon-carbon cross-coupling reactions; particularly Suzuki cross-coupling reactions.

More specifically, investigating the cross-coupling catalytic activity of graphene-supported palladium-magnetite nanoparticles which were prepared using hydrazine hydrate as a reducing agent for palladium nitrate, iron nitrate, and graphene oxide under microwave heating.

The goal of this study is to synthesis the previously mentioned catalyst under batch reaction conditions, then focus more on making use of heterogeneous catalysis in conjunction with micro reactor technology applications as a strategy that can facilitate a cleaner and scalable flow methodology for organic synthesis.

13

CHAPTER 2   Characterization Techniques

2.1   Overview

Synthesis of different types of catalysts requires making use of various instruments and in this chapter, an overview of the instruments that were used in this dissertation will be presented briefly by showing the outlines, description, and theoretical background of these instruments. Characterization of nanostructured materials and composites requires studying the size, shape, morphology, composition, electronic, magnetic and optical properties, among others. To achieve this, standard techniques and characterization tools such as UV-Vis spectrophotometry, photoluminescence spectroscopy, transmission and scanning electron microscopy, X-ray diffractometry and photoelectron spectroscopy, Raman and IR spectrometry in addition to vibrating sample magnetometry are typically used. In this chapter, the experimental methods used for characterization of our graphene-based nanostructured materials are described.

2.2   Instruments used in synthesis and catalyst evaluation

2.2.1   F21100 Tube Furnace

For the CO Catalytic oxidation, tests were carried out in a continuous fixed-bed quartz-tube reactor Type F21100 Tube Furnace under ambient pressure. The sample temperature was measured by a thermocouple placed near the sample. In typical experiment, a gas mixture consisting of 3.5 wt. % CO and 20 wt. % O_2 in Helium was passed over the sample while the temperature was ramped. The gas mixture was set to flow over the sample at a rate of 100 cc/min. controlled via MKS digital flow meters.

14

The conversion of CO-CO$_2$ was monitored using an infrared gas analyzer (ACS, Automated Custom Systems Inc.). All the catalytic activities were measured (using 25 mg sample) after heat treatment of the catalyst at 110˚C in the reactant gas mixture for 15 min. in order to remove moisture and adsorbed impurities.

Figure 2-1 Schematic representation of typical set up used in CO catalytic oxidation[*]

2.2.2 CEM Focused Microwave™ Synthesis System

The CEM Focused Microwave™ Synthesis System, Discover, is designed to enhance the ability to perform chemical reactions under controlled conditions on a laboratory scale. The system facilitates either homogeneous or heterogeneous solution phase chemistry, solid phase chemistry or chemistry conducted on solid supports.

[*] Lecture on CO Catalysis, Prof. Dr. M. S. Elshall, 2011.

15

It accommodates vessels ranging in working volume from 5mL to 125mL for reactions performed under atmospheric conditions and 10mL or 35mL vessels with septa in addition to 80 mL vessels for reactions performed at elevated temperatures and pressures. Primary uses of the Discover are in the discovery and lead optimization phases of the new product development process. Microwave energy is applied to the vessel contents (reactants, catalysts, salts, solvents and/or solid supports) to accelerate the chemical reaction. The microwave absorption properties of some liquid and solid materials, due to their polar and ionic characteristics, have the capability to significantly enhance chemical reactions relative to traditional energy application (heating) techniques. The microwave interaction properties with the reactants, intermediates, catalysts, solid supports and salts provide unique opportunities for the synthetic chemists and chemical engineers.
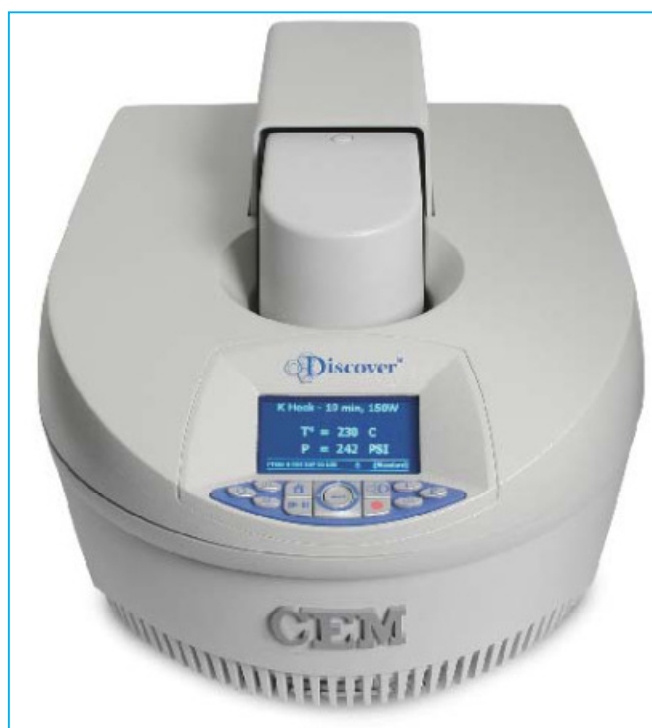
Figure 2-2 Discover System - Front View[*]

* Discover - S Class, CEM Corporation, 2006.

2.2.3 Wave Craft CF-MAOS System

Continuous Flow Microwave-Assisted Organic Synthesis (CF-MAOS) is in many ways performed like conventional (convective heating) continuous flow synthesis. The main difference in this case is the speed of reaction, the simplicity in operating the system and the fact that there is no thermal wall effect due to the lack of physical contact between the reactor and the surroundings. Microwaves heat by a different mechanism than conventionally heated organic reactions. Microwaves heat by perturbing ionic, dielectric and polar molecules. These molecules will be subjected to a strong push and pull effect from the electric component of the microwave electromagnetic field which changes direction with the frequency of the microwaves. The energy in this motion is dissipated as heat to the surrounding molecules. The heating is often termed "volumetric" as it happens everywhere in the heated volume at the same time. The Wave Craft CF-MAOS system works with a broad range of solvents and reagents. It is simple to set up, so experimenting with your own chemistry and optimizing conditions using simple design of experiment models is likely to be the best way to discover how CF-MAOS works with your reaction. Solvents propensity to absorb microwaves depend on ionic or dipolar properties. When selecting a solvent for a specific reaction it is important to take into consideration the bulk chemical properties of the whole reaction mixture flowing through the reactor. It is often tempting to avoid polar solvents as they are poor microwave absorbers. However, in Wave Craft's experience it is feasible to perform reactions in polar solvents. They may heat slower, but may reach temperatures far beyond their boiling points.

17
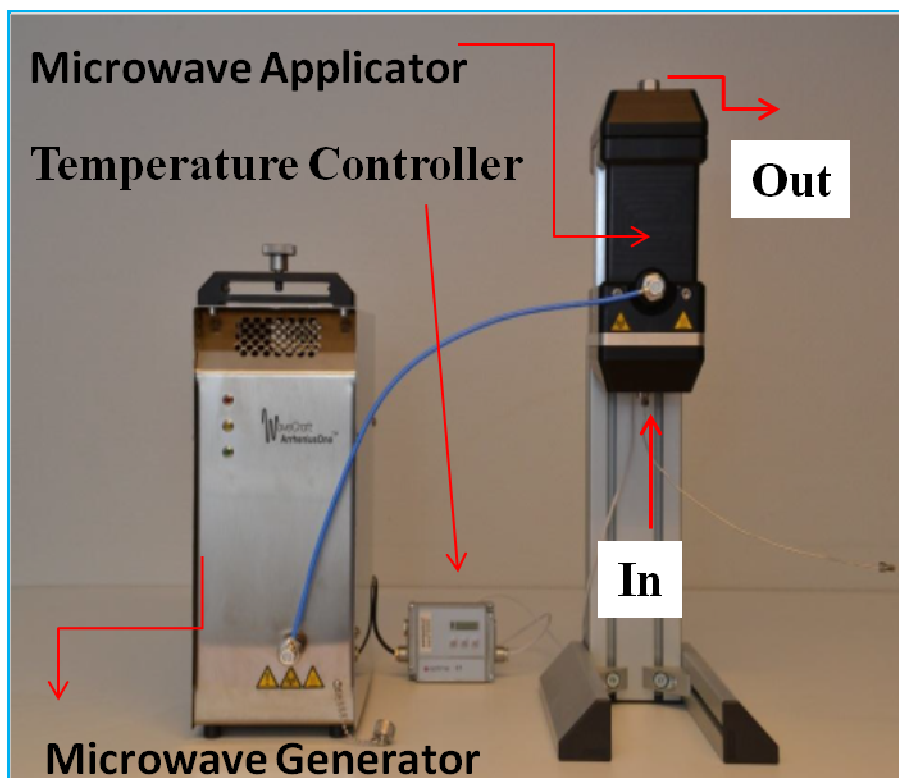
Figure 2-3 Continuous Flow Microwave-Assisted Organic Synthesis (CF-MAOS)[*]

Residence time is defined as the time when the reaction mixture is in the reaction zone exposed to microwaves. The residence time can be calculated using the following equation:

$$RT = \frac{L*(R^2*\pi)}{F} \qquad 2\text{-}1$$

Where: RT is residence time in minutes, L is the length of the reactor in millimeter, R is the radius of the reactor in millimeter, F is the flow rate in micro liter per minute and π is 3.14.

* Wave Craft AB Company.

The CF-MAOS system consists of a microwave generator, an applicator to transfer the microwave energy to the reaction mixture, and a tubular borosilicate reactor in which the reaction mixture passes through the applicator (**Figure 2-3**). The microwave generator consists of a transistor-based two-stage microwave amplifier, powered by a 32 V, 20 A power supply, and a controller unit that is connected to a computer and the IR temperature sensors in the applicator. The generator contains an active cooling module using liquid coolant (tap water or circulated coolant) and temperature sensors to prevent the amplifier from overheating. The first stage of the amplifier generates the microwave power output and microwave frequency set in the software. The second stage amplifies the signal to the determined level. The system is able to generate from 0−150 W of output in a frequency range from 2.4 to 2.5 GHz, which is within the allowed range for public use in microwave instruments. The microwaves are applied to the reaction mixture in the tubular reactor by means of a helical antenna made of an Al−Cu material.

The axial-field microwave applicator is based on a novel design using a nonresonant structure that suppresses mode patterns (standing waves) in the applicator, thus avoiding hot and cold spots. As opposed to single and multimode applicators, the axial field applicator is not based on the cavity resonator principle. In the axial field applicator the microwave field is generated in a coil surrounding the flow reactor, allowing the microwave field to be concentrated axially inside the coil. The coil is automatically tuned to maximize the heating in the reactor tube by changing the frequency. Reactors of different sizes can be used by changing the length and diameter of the coil in the applicator, allowing the optimization of reaction conditions such as residence time and flow capacity. The physical shape of the antenna determines the homogeneity of the microwave field. The reactor consists of a straight tube, made of microwave-transparent borosilicate glass.

2.2.4 X-Cube continuous flow reactor

The X-Cube™ is a continuous flow reactor, capable of performing chemical reaction under inert conditions, temperatures up to 200°C and pressures up to 150 bar. It has been reported that carbon-carbon forming reactions are far more efficient on the X-Cube™ in comparison to batch mode. In the typical standard protocol of the X-Cube™, the reaction conditions, pressure, temperature and flow rate were set using the touch screen of the X-Cube™. The reaction solvent was allowed to flow through the X-Cube™ system for 10 minutes to equilibrate the filled CatCart with heterogeneous or immobilized-homogeneous reagent/catalyst. A sample of the starting materials in the reaction solvent was pumped through the X-Cube™, the total amount of product mixture was collected to sample vial and the column was washed with the eluent to remove any material still absorbed to the CatCart, then the product mixture was analyzed by GC-MS, HPLC-MS and NMR.
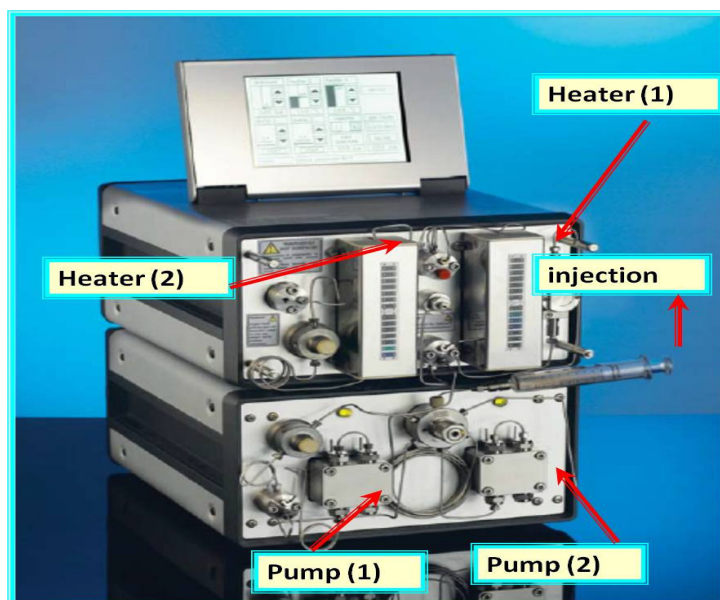
Figure 2-4 X-Cube continuous flow reactor (Thales Nano Inc.)*

20

It was demonstrated through various reactions that the X-Cube™ can be used to perform carbon - carbon coupling reactions with high conversion rates, purity and yields. Furthermore, the reaction times were dramatically reduced in comparison to the commercial batch mode.

2.3   Characterization techniques

2.3.1   UV-Vis absorption and photoluminescence spectroscopy

UV-Vis absorption spectroscopy involves the measurement of the attenuation of wavelengths from 200-900 nm of light beam after it passes through an absorbing medium. The measurement of absorption spectra of semiconductor and metallic nanostructures can provide valuable information about size and shape of the nanocrystals. Photoluminescence spectroscopy is a powerful technique for studying the electronic properties of semiconductor nanocrystals. It provides information about quality, defects, impurity concentrations and bandgaps. When semiconductor nanocrystals are excited with light photons of energy greater than that of the band gap, an electron is elevated to conduction band leaving behind a hole in the valence band.
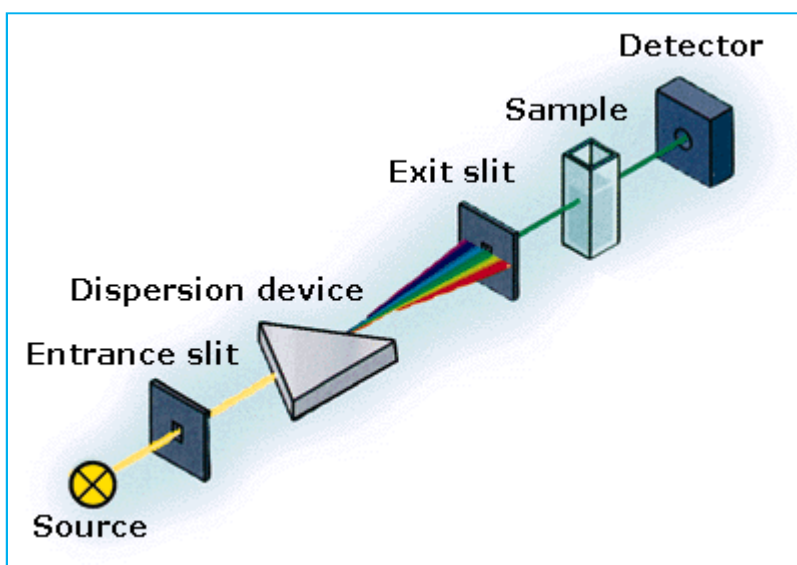
Figure 2-5 Schematic of a wavelength-selectable, single-beam UV-Vis spectrophotometer[*]

21

Upon electron-hole recombination, a photon of an energy characteristic to the band gap is emitted. Other useful information about the charge or energy transfer between semiconductor nanocrystals and graphene, for example, can be also obtained from photoluminescence studies.

In this work, UV-Vis absorbance spectra were recorded using HP-8453 spectrophotometer. Diluted suspensions of test samples were placed in 1 cm UV-quartz cuvette and absorption spectra were recorded within the appropriate scan range and using the pure respective solvent as a reference. Photoluminescence spectra of diluted suspension were measured using Varian (CARY) spectrofluorometer equipped with xenon lamp as an exciting source. Both excitation and emission slits were set at 5 nm and the excitation wavelength was chosen according to the absorption characteristics.

2.3.2   Transmission and scanning electron microscopy

Electron microscopes utilize electrons which have short wavelengths and thus allow observation of matters with atomic resolution. The two microscopy techniques adopted here are the transmission electron microscopy (TEM) and the scanning electron microscopy (SEM).

Both techniques provide valuable means to acquire morphological, crystallographic and surface topographic information. In this work, TEM studies were conducted on Joel JEM-1230 electron microscope operated at 120 kV equipped with Gatan UltraScan 4000SP 4K × 4K CCD camera. Samples for TEM were prepared by placing a droplet of colloid suspension in respective solvent on a Formvar carbon-coated, 300-mesh copper grid (Ted Pella) and allowing them to evaporate in air at ambient conditions.
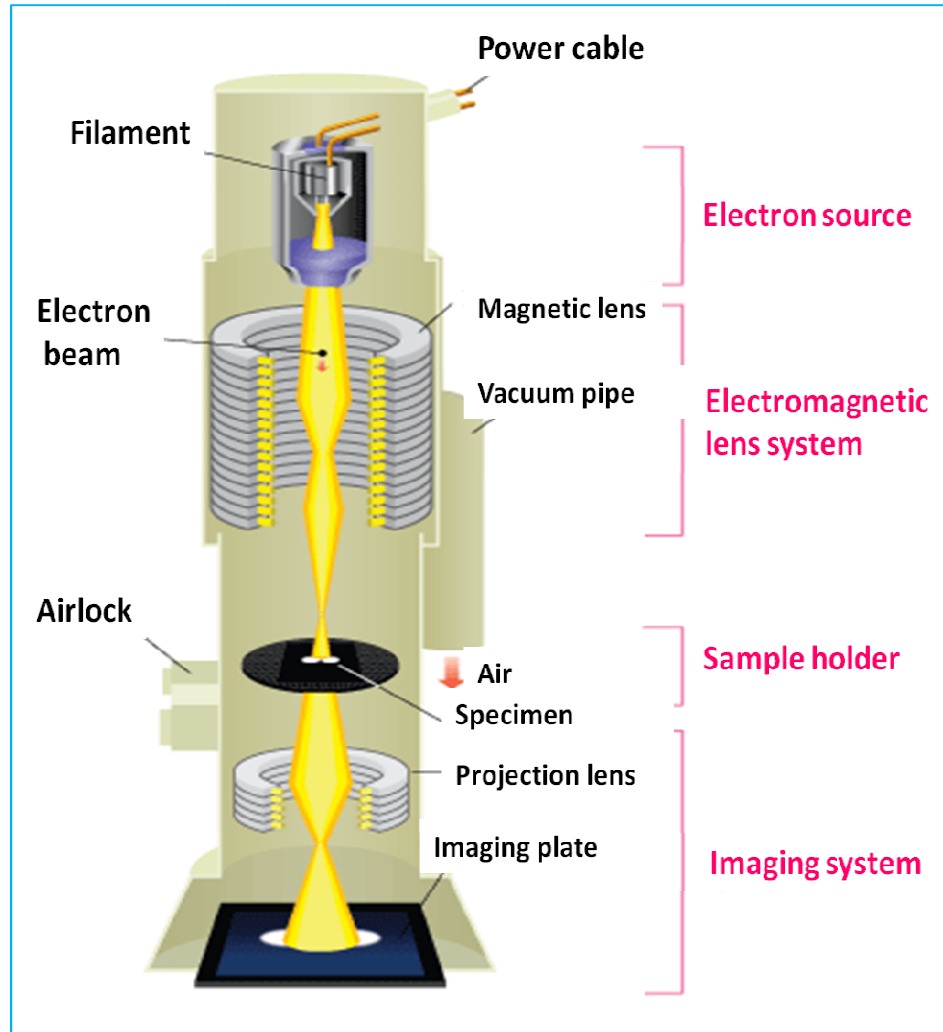
Figure 2-6 The schematic outline of a TEM. [*]

Size distribution and average size were determined using image J analysis software package. SEM, STEM and EDAX measurements were carried out using a Quantum DS-130S dual stage electron microscope.

2.3.3 Powder X-ray diffraction (XRD)

X-ray diffractometry (XRD) is the most essential tool to study and evaluate the crystal structure of a material.

---

[*] Basic principles of TEM, Nitj Shiksha.

المنارة للاستشارات

www.manaraa.com

The powder XRD measurements are based on the well-known Bragg's law ($\lambda = 2d \sin \theta$). It is generally accepted that XRD reflection peaks of nancorystalline solids are broader than those of bulk counterpart solids. In our work, the X-ray diffraction (XRD) patterns of the powder samples were measured at room temperature with a standard X'Pert Philips Materials Research diffractometer with Cu $K_{\alpha 1}$ radiation. The database used for the identification of crystal structures of materials investigated in this work is the Joint Committee on Powder Diffraction Standards-International Center for Diffraction Data (JCPDS-ICCDD) system.
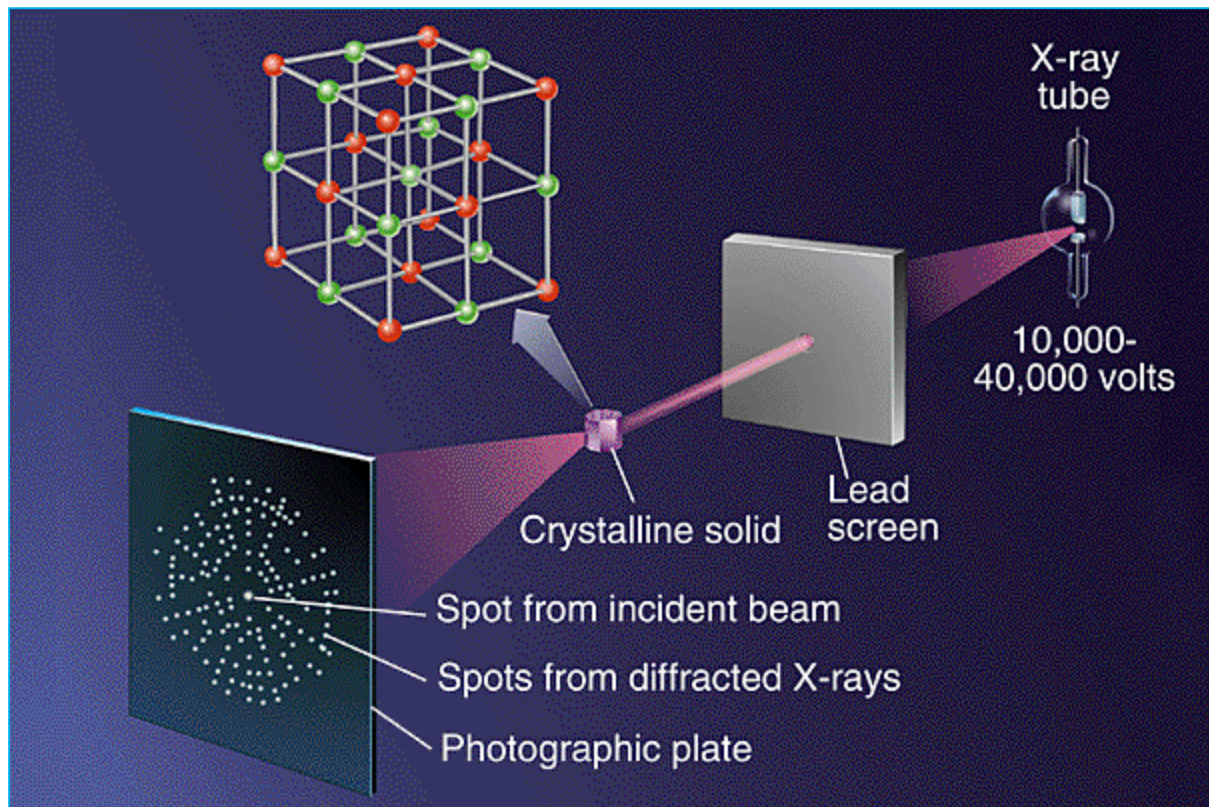
Figure 2-7 X-Ray Diffraction Technique.[*]

24

2.3.4   X-ray photoelectron spectroscopy (XPS)

Among the experimental spectroscopic techniques that provide electronic information about atoms, molecules, ions, compounds and solid surfaces by measuring the kinetic energy of electrons ejected from investigated materials are surface analytical tools such as X-ray photoelectron spectroscopy (XPS, formerly known as electron spectroscopy for chemical analysis, ESCA), UV photoelectron spectroscopy (UPS) and Auger electron spectroscopy (AUS).
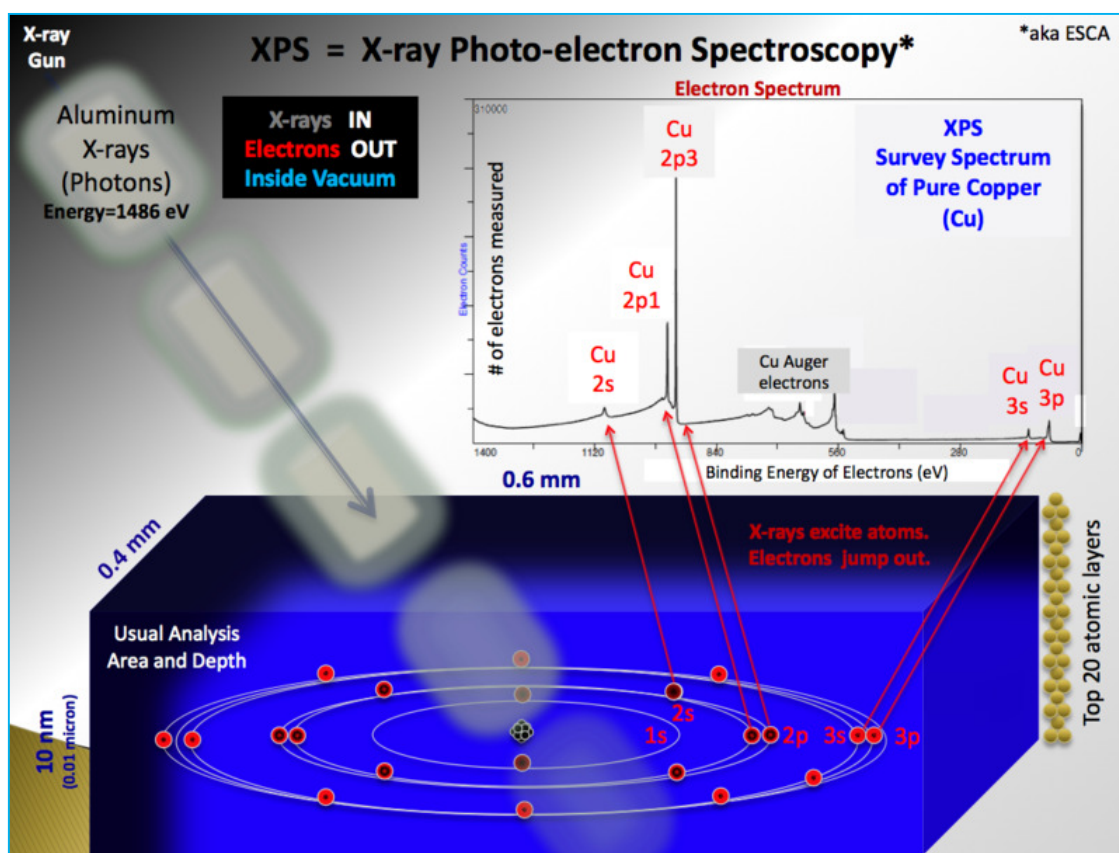
Figure 2-8 X-ray photoelectron spectroscopy (XPS)[*]
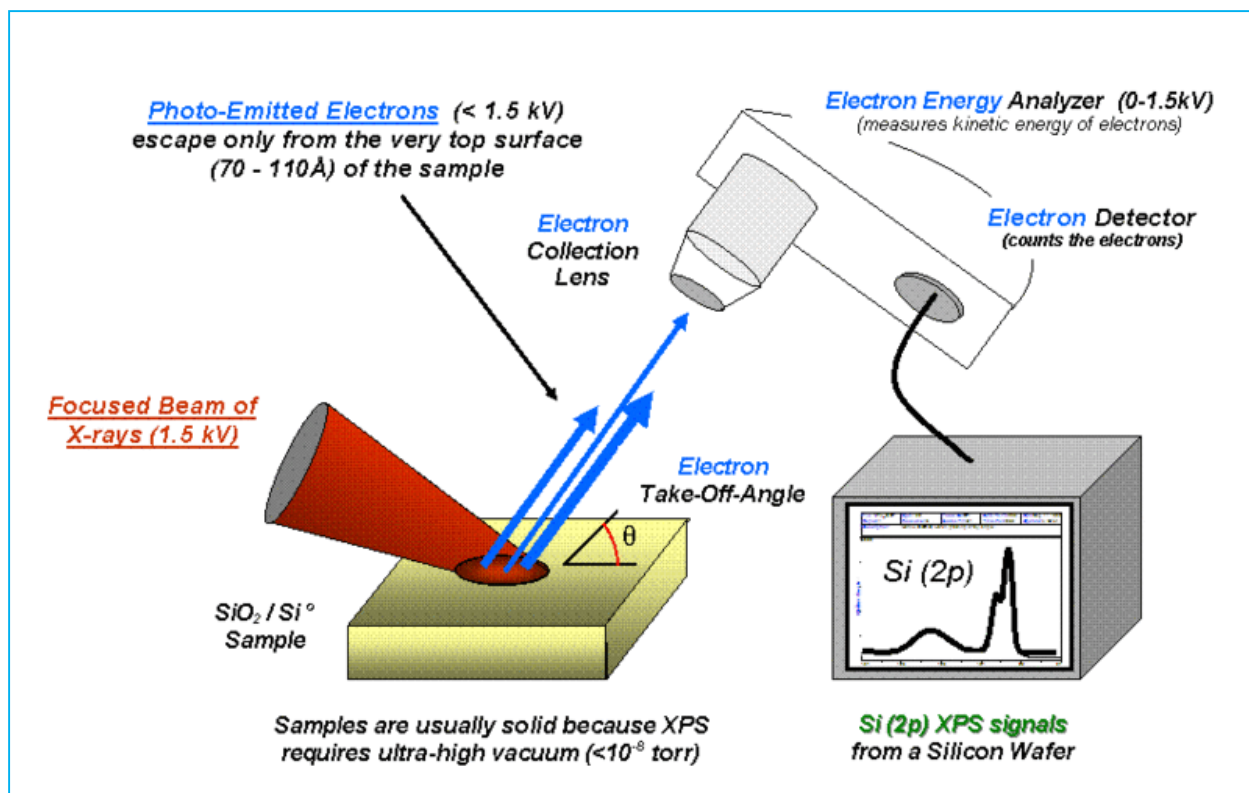
Figure 2-9 X-ray photoelectron spectroscopy (XPS) Technique[*]

XPS in particular is an extremely powerful analytical tool that identifies elemental composition, chemical state, empirical formula and electronic states of the elements within the outer 1-10 nm region of any solid surface, down to 0.1 atomic %.[125] Spectra are obtained by bombarding a given sample with a beam of Al or Mg X-rays and simultaneously measuring the kinetic energy and the number of electrons that escape from the top surface (1-10 nm) of the sample. The technique allows revealing the speciation or the chemical environment with minimal sample preparation, easy analysis, surface specificity (<10 nm) and high sensitivity (>0.05 atomic %).[125] For the work described herein, XPS measurements were performed on a Thermo Fisher Scientific ESCALAB 250 using a monochromatic Al Kα X-ray of ~ 1.4 keV.

[*] B. Vincent Crist, PhD

2.3.5 Vibrating Sample Magnetometry (VSM)

Characterization of magnetic properties of nanostructures is generally carried out by measuring the magnetization curves using a vibrating sample magnetometer (VSM). In transverse-coil configuration VSM, the vibration (z) axis is perpendicular to the field applied by the electromagnet, and the pickup coils are arranged to sense the moment along the field direction. When a material is placed within a uniform magnetic field and made to undergo sinusoidal motion (i.e. mechanically vibrated), there is some magnetic flux change. This induces a voltage in the pick-up coils (Hall sensor), which is proportional to the magnetic moment of the sample.
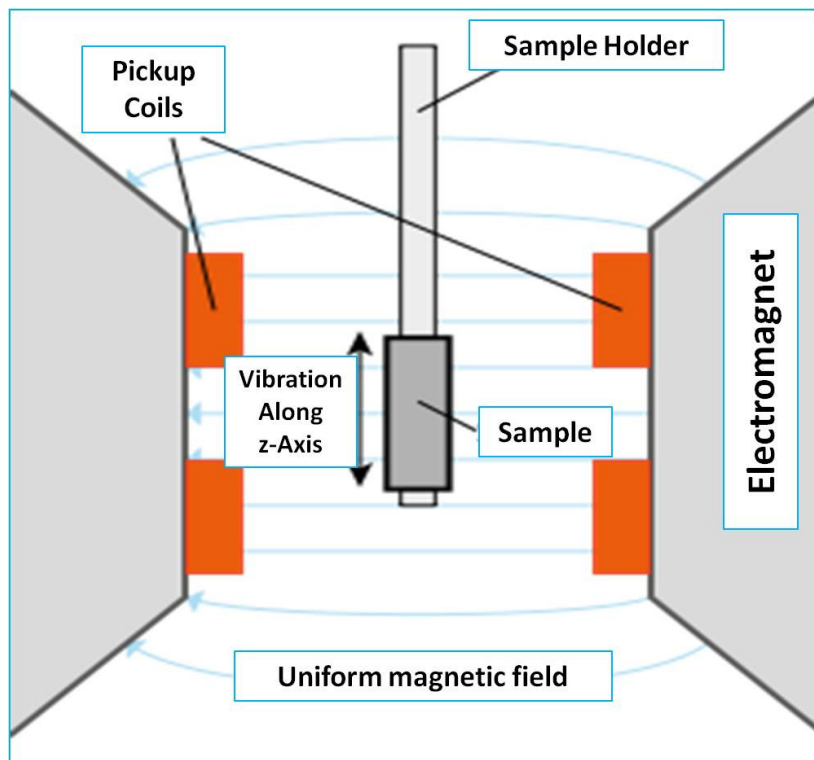
Figure 2-10 Vibrating Sample Magnetometer (VSM)*

* Foner, S. "Versatile and Sensitive Vibrating-Sample Magnetometer". Rev. Sci. Instrum **30** (7): 548–557.

With VSM one can obtain magnetization versus field or versus temperature data, and from these curves information about size and magnetic behavior can be drawn. In studying ferromagnetic materials, for example, one observes a decrease in transition temperature with a decrease in particle size and when the particle size is very small (<10–15 nm), the particles become superparamagnetic. Magnetization curves reported herein were acquired using cryogen-free cryocooler-based 3-tesla VSM – VersaLab that has a temperature range of 50 to 400 K.

2.3.6 Fourier-Transform IR spectrometry

When an IR radiation is passed through a sample, some of the radiation is absorbed by the sample and some passes through. The resulting spectrum represents the molecular absorption and transmission, creating a molecular fingerprint of the sample with absorption peaks that correspond to the frequencies of vibration between the bonds of the atoms making up the material.

A beam of IR energy radiated from the source (usually a glowing black-body) is passed through an aperture which controls the amount of energy delivered to the sample/detector. When the beam enters the interferometer, spectral encoding takes place and the resulting interferogram leaves the interferometer as a signal. In the sample compartment, certain IR frequencies which are unique to the test sample are absorbed. Finally the transmitted beam passes to the detector where a unique interferogram signal is measured. The signal measured is digitized and sent to the computer. After the Fourier transformation process, a final IR frequency spectrum is generated. The model of the FTIR spectrometer utilized in this work is Nicolet 6700 FTIR.

CHAPTER 3   Microwave – assisted Synthesis of an Efficient Catalyst of Palladium Nanoparticles Supported on Fe_3O_4, Co_3O_4, Ni $(OH)_2$ for Applications in CO Oxidation

3.1   Overview

This chapter summarizes microwave irradiation methods for the preparation of metal oxide nanoparticles and their catalytic properties and applications. Microwave irradiation provides rapid decomposition of metal precursors and can be extended for synthesis of a wide range of metal oxide nanoparticles with various compositions, sizes and shapes.[20] This chapter introduces the microwave method and describes the nucleation and growth process for the formation nanocrystals. A broad overview is offered here for metal oxide nanostructures synthesized by microwave irradiation including: Fe_3O_4, Co_3O_4, and Ni $(OH)_2$, transitional metal oxides and metal oxides nanostructures supported on graphene. Finally, there is a description of the application of metal oxides in the removal of carbon monoxide. The metal oxide nano catalysts are of great importance in improving the thermal-catalytic decomposition performance.[43, 103, 114] The advanced and unique magnetic, electronic, and catalytic properties of the materials in the nano scale attracted research centers to investigate this area of science deeply.[4, 44, 62-65]   In the field of catalysis; separation of catalysts is a vital step especially in medical and therapeutic applications and mainly in cross coupling reactions.[45, 66-69]

29

The catalytic effect of magnetic nanoparticles was an important area of research due to its huge industrial applications.[70-72] Gold nanocrystals deposited on metal oxides and bimetallic Ni-Fe alloys have been also studied for oxidation catalysis.[6, 115-124] The carbon materials have an increasing importance in catalytic processes when used as catalyst supports but there is also an endless efforts to develop other kinds of supports like metal oxides.[47, 62, 73-80]

Cobalt, iron and nickel are mainly used as Fischer-Tropsch catalysts while their magnetic characterization provides valuable information about catalyst reduction, sizes of ferromagnetic nanoparticles, chemisorption on ferromagnetic.[5, 98, 126-133] Syntheses of nanoparticles with variable sizes have been intensively tried particularly for magnetic iron oxides with namely maghemite (α-Fe$_2$O$_3$) and magnetite (Fe$_3$O$_4$).[46, 81-88] These nano particles were used efficiently as magnetic recoverable catalysts for various applications.[74, 89-96]

Over the past decade, transition metal particles in nano scale have been intensively pursued as potentially advanced catalysts due to their unique properties lie between those of single metal atoms and bulk metal. The accurate control of particle size and overall particle size distribution is one of the most important challenges to provide new chemical and physical properties.[72, 89, 97-98] When the nanostructured materials were used as heterogeneous catalysts by comparing with traditional powder catalysts, the nanostructured materials showed special properties of nanoparticles and new effects caused by nanostructured combination, with remarkable improvements in the aspects of size, numbers of reaction active sites, surface structure, catalytic selectivity, shape and so on.[2] Hence, the nanostructured materials have great potential application in the field of heterogeneous catalysis and have become the corner stone of materials science in the area of heterogeneous catalysis especially in the past few recent years.[56, 94, 99]

30

The nano porous structure and superparamagnetic behavior of (Fe_3O_4) nano particles make them ideal for powerful application potentials in chemical, physical, biological, biomedical, and environmental engineering fields like catalyst or drug carrier, absorption, separation.[40, 61, 81, 84, 86, 92, 95, 100-103] Nano-alloys are also used as catalysts for hydrogen generation. Moreover, these catalysts can be easily magnetically separated for recycle purpose.[58, 71] Such alloy catalysts are expected to be useful for various applications as metal-air batteries, fuel cells, and electrochemical sensors.[29, 67, 90, 130, 134-135] Besides iron oxides, cobalt oxides were also investigated for environmental applications in CO catalysis.[43-47] Some recent developments had been achieved in the application of magnetic methods for investigation of Fischer-Tropsch catalysts involving cobalt, iron and nickel.[5, 41-42, 126-128, 131-133, 136-140] Recently, the synthesis and applications of magnetic nanoparticles (MNPs) have attracted more interest in catalysis research, and MNP-derived catalysts have been used in such industrially important reactions as hydrogenation, hydroformylation, Suzuki-Miyaura and Heck cross - couplings.[66, 82-83, 104-105]

3.2   Introduction

The synthesis and characterization of nanocrystals with controlled size and shape have attracted rapidly growing interest both for fundamental scientific interest and many practical and technological applications.[2, 141] Shape control and assembly of nanostructures into organized patterns provide valuable routes to the design of functional materials and to a variety of applications.[20, 141] Several methods based on physical and chemical approaches have been developed for the synthesis of controlled size and shape nanostructures.

31

Examples of these approaches include sonochemical reactions, kinetic growth control, solvothermal methods, template-assisted, and thermolysis of single-source precursor in ligating solvents.[4, 40, 43-44, 142]

Microwave Irradiation (MWI) methods provide simple and fast routes to the synthesis of nanomaterials since no high temperature or high pressure is needed. Furthermore, MWI is particularly useful for a controlled large-scale synthesis that minimizes the thermal gradient effects.[20, 40, 143-145] The heating of a substance by microwave irradiation depends on the ability of the material (solvent or reagent) to absorb microwave radiation and convert it into heat. This is based on two principal mechanisms: dipole rotation and ionic conduction, that is, by reversal of solvent dipoles and the resulting replacement of charged ions of a solute. [1, 39, 145]

Polar reactants with a high microwave extinction coefficient can be excited by direct absorption of microwaves. Due to the difference in the solvent and reactant dielectric constants, selective dielectric heating can provide significant enhancement in reaction rates. By using metal precursors that have large microwave absorption cross-sections relative to the solvent, very high effective reaction temperatures can be achieved. The rapid transfer of energy directly to the reactants (faster than they are able to relax), causes an instantaneous internal temperature rise.[19-20, 39, 146] Thus, the activation energy is essentially decreased as compared with conductive heating and the reaction rate increases accordingly. As a consequence, reactions might be performed at lower temperatures and hotspots or other temperature inhomogeneities can be prevented. Furthermore, reaction parameters such as temperature, time, and pressure can be controlled easily. This also allows the rapid decomposition of the precursors thus creating highly supersaturated solutions where nucleation and growth can take place to produce the desired nanocrystalline products.[7, 20, 147-148]

32

These conditions lead to the formation of very small nanocrystals since the higher the supersaturation the smaller the critical size required for nucleation. Thus, in the synthesis of nanocrystals using MWI, the reaction can be controlled very conveniently, and the resulting nanocrystals show very good monodispersity and crystallinity.[20, 149-150]

MWI methods have been demonstrated for the synthesis of a variety of high quality metal and metal oxide nanoparticles as well as one-dimensional nanostructures.[20, 22, 144, 149-151]

In this chapter, we describe several examples of the application of MWI for the synthesis of a variety of metal oxide nanostructures of controlled size and shape. A key objective of nanocatalysis research is to produce catalysts with 100% selectivity, extremely high activity, low energy consumption, and long lifetime. In order to provide a basic understanding of nanoparticle's formation, a brief overview of the classical nucleation theory (CNT) will be presented since nucleation and growth greatly influence the control of the size and shape of nanoparticles which consequently determine the unique properties that may characterize nanoparticles. This can be achieved only by precisely and efficiently controlling the size, shape, spatial distribution, surface composition and electronic structure, thermal and chemical stability of the individual nanocomponents.[18, 20, 150]

3.2.1   Brief Overview of Nucleation and Growth from the Vapor Phase

Nucleation of liquid droplets from the vapor or nanocrystals from the solution phase can occur homogeneously or heterogeneously. Homogeneous nucleation occurs in the absence of any foreign particles or surfaces when the vapor molecules themselves cluster to nuclei within the supersaturated vapor or solution. According to the Classical Nucleation Theory (CNT) for vapor phase nucleation, embryonic clusters of the new phase can be described as spherical liquid droplets with the bulk liquid density inside and the vapor density outside.[20, 150, 152]

33

The free energy of theses clusters relative to the vapor is the sum of two terms: a positive contribution from the surface free energy and a negative contribution from the bulk free energy difference between the supersaturated vapor and the liquid. The surface free energy results from the reversible work in forming the interface between the liquid droplet and the vapor. For a cluster containing n atoms or molecules, the interface energy is given by:

$$\sigma A(n) = 4\Pi\sigma(3v/4\Pi)^{2/3}n^{2/3} \qquad 3-1$$

Where r is the interfacial tension or surface energy per unit area, A(n) is the surface area of the clusters, and v is the volume per molecule in the bulk liquid. Since n molecules are transferred from the vapor to the cluster, the bulk contribution to the free energy is n ($\mu_L - \mu_v$) where μ_L and μ_v are the chemical potentials per molecule in the bulk liquid and vapor, respectively. Assuming ideal vapor, it can be shown that:

$$(\mu_1 - \mu_V) = -n\,k_B\,T\,\ln S \qquad 3-2$$

Where k_b is the Boltzmann constant, T is the temperature, and S is vapor supersaturation ration defined as S = P/P$_e$, where P is the pressure of the vapor and P_e is the equilibrium or ''saturation'' vapor pressure at the temperature of the vapor (T).

The sum of the contributions in Eqs. (3.1) and (3.2) is the reversible work (free energy) W(n), done in forming a cluster containing n atoms or molecules. This free energy is given by:

$$W(n^*) = -n\,k_B\,T\,\ln S + 4\Pi\sigma(3v/4\Pi)^{2/3}n^{2/3} \qquad 3-3$$

Because of the positive contribution of the surface free energy, there is a free energy barrier which impedes nucleation.

34

The smallest cluster n* which can grow with a decrease in free energy is determined to be:

$$n^* = [32\pi \sigma^3 \upsilon^2] / 3[K_B T \ln S]^3 \qquad\qquad 3\text{-}4$$

Substituting n* into Eq. 3.3 yields the barrier height W (n*), given by:

$$W(n^*) = 16\pi \sigma^3 \upsilon^2 / 3(K_B T \ln S)^2 \qquad\qquad 3\text{-}5$$

It is clear from Eq. (3-5) that increasing the supersaturation (S) reduces the barrier height and the critical cluster size (n*) and hence, fluctuations can allow some clusters to grow large enough to overcome the barrier and grow into stable droplets.[20, 150, 153-156]

3.2.2 Nucleation and Growth from Supersaturated Solutions

The formation of nanocrystals in supersaturated solutions follows the basic principles of crystallization: a nucleation event precedes the growth of nanocrystals and eventually bulk crystals. The most widely accepted mechanism is known as La Mer-mechanism.[157] According to this mechanism, the reaction can be divided into three phases: first, the concentration of reactant increases gradually and eventually exceeds solubility. Second, the concentration of reactants reaches the critical limit of supersaturation and rapid nucleation occurs. This nucleation burst results in a sudden decrease of reactant concentration. Finally, nuclei grow slowly as the reaction solution depletes in reactants.[13, 16, 150, 152]

Since growth is usually thermodynamically favored over nucleation, nanoparticles can be grown monodispersely when the second phase can be limited to a short period of time by suitable choice of reactant concentration and temperature. The overall nanocrystals' formation can be described in terms of three stages: (1) nucleation, (2) growth and (3) competitive growth which is commonly referred to as Ostwald ripening.[150, 156-157]

35

For the formation of monodisperse nanocrystals, single rather than multiple nucleation events are necessary in order to prevent additional nucleation during the subsequent growth process.[157-161] Therefore, the key point to achieve good control over the size and size distribution of nanoparticles is to decouple the nucleation and growth processes. In the nucleation stage, the number and size of the small nuclei formed are controlled by the degree of the solution supersaturation.[20, 162] As shown by the CNT above, the larger the supersaturation, the smaller the critical size of the nucleus and the smaller the nanocrystals that can grow. At the second stage, nanocrystals exhibit a monotonic growth due to the addition of atoms from the solution into the nuclei which results in decreasing the degree of supersaturation with time and increasing the total volume of the nanocrystals. Finally, when the nanocrystals are large enough and the degree of supersaturation is negligible, since all atoms are already incorporated in the nanocrystals, Ostwald ripening starts to operate where competitive growth or diffusion-limited aggregation takes place.[20, 157, 162-163] This process results in an increase in the mean size of the nanocrystals due to the mass transfer from smaller to larger particles. The net result is that larger particles grow and smaller particles shrink in size. Another result is that the number of particles in a system is drastically reduced, as smaller particles vanish completely in order to donate their atoms for the continued growth of the larger particles.[157, 162]

Therefore, not only does the surface-to-volume ratio of the larger particles decrease, making them more stable, but the less stable (smaller) particles become fewer, and the total surface energy of the system decreases. The growth of the newly formed nanocrystals can be effectively inhibited by the adsorption of ligating organic surfactants that bind strongly to the nanocrystals, thus stabilizing and passivating the surface.[20]

The ability to cap the nanocrystal's surface provides a way not only to control the surface states, but also to prevent rapid agglomeration of the particles due to Ostwald ripening. MWI in organic solutions allows the production of high degrees of supersaturation due to the rapid heating of the nanocrystals' precursors. [20, 39, 154-155]The size of the nanocrystals is tuned by varying the concentration of the precursors and the MWI times, while the shape is controlled by varying the concentration and composition of the ligating solvents which stabilize the nanocrystals by passivating the surfaces.[20] Following MWI for the desired time in an organic phase, the synthesized nanocrystals can be separated by size-selective precipitation through the gradual addition of a hydrophilic solvent such as ethanol to the toluene or hexane dispersion containing nanoparticles with various particles sizes. The large nanoparticles tend to precipitate first because of their strong van der Waals attraction.

3.3   Experimental

3.3.1   Chemicals and reagents

A JEOL JEM-1230 electron microscope operated at 120 kV has been used to obtain TEM images. The electron microscope is equipped with a Gatan UltraScan 4000SP 4K X 4K CCD camera. TEM samples were prepared by placing a droplet of the prepared catalyst dissolved in ethanol on a 300-mesh copper grid and then left to evaporate in air at room temperature. The X-ray photoelectron spectroscopy (XPS) analysis was executed on a Thermo Fisher Scientific ESCALAB 250 using a monochromatic Al KR X-ray.

The samples were perfectly fastened on an indium foil that was previously fixed on the carbon tape which in turn was completely attached to the sample holder by a double face. The X-ray diffraction patterns were measured at room temperature using X'Pert PRO PANanalytical X-ray diffraction unit.

37

For all the syntheses described here, a conventional microwave oven (2.45 GHz) operating at 600–1,000 W was used. For the CO Catalytic oxidation; tests were carried out in a continuous fixed-bed quartz-tube reactor Type F21100 Tube Furnace under ambient pressure. The sample temperature was measured by a thermocouple placed near the sample. In typical experiment, a gas mixture consisting of 3.5 wt. % CO and 20 wt. % O_2 in Helium was passed over the sample while the temperature was ramped. The gas mixture was set to flow over the sample at a rate of 100 cc/min. controlled via MKS digital flow meters. The conversion of CO-CO_2 was monitored using an infrared gas analyzer (ACS, Automated Custom Systems Inc.). All the catalytic activities were measured (using 25 mg sample) after heat treatment of the catalyst at 110˚ C in the reactant gas mixture for 15 min. in order to remove moisture and adsorbed impurities. Catalytic tests were carried out in a continuous fixed-bed quartz-tube reactor Type F21100 Tube Furnace under ambient pressure. The typical procedure includes removing the reactor from the tubular furnace and cleaning it with Tissue and compressed air till it becomes clean. The gas inlet source is attached to the reactor and the O ring is placed by the right way to avoid any leakage. Small piece of Glass wool is put inside the reactor around the thermocouple which is used in direct contact with the catalyst to monitor the temperature of the reactor. Then 20 mg of catalyst is added inside the reactor slowly and then another small piece of Glass wool is added. So, now the catalyst is between two pieces of glass wool. Finally, small amount of Glass balls are added inside the reactor and then another small pieces of glass wool. Attach the gas outlet to the reactor and also be careful about the 'O' ring and be sure it is in the correct place to avoid any kind of CO leakage. A test run is performed till the concentrations of both CO and CO_2 at room temperature are constant.

After that, the test is stopped and the first run of the catalyst is started inside the tubular furnace which is the activation run. After the first run is finished the run is stopped and run test is performed again and also we have to stop the furnace and switch the flow gas to Ar gas instead of $CO/O_2/He$ gas mixture. Before the second run starts, there should be a wait time till temperature reaches the room temperature in the flow of Ar gas. Then, we switch the flow gas to $CO/O_2/He$ gas mixture and wait till the concentrations of both CO and CO_2 at room temperature are constant (all this during the test run) then we stop the test run and start the second run which is our actual run.

3.3.2 Microwave Synthesis of Palladium Nanoparticles Supported on Fe_3O_4, Co_3O_4, and $Ni (OH)_2$

All chemicals used in our experiments were purchased and used as received without further purifications. Palladium nitrate (10 wt. % in 10 wt. % HNO_3, 99.999%) and hydrazine hydrate (80%, Hydrazine 51%) were obtained from Sigma Aldrich. Aryl bromide and potassium carbonate, aryl substituted boronic acid were also purchased from Aldrich and used as received. A mixture of ethanol/deionized water was used for the Suzuki cross-coupling reactions.

In the typical synthesis of Pd/Fe_3O_4, different ratios has been prepared (5, 20, 40, 50 wt %) Palladium Nitrate $Pd (NO_3)_2$ supported on iron as will be shown respectively. Weigh (687.2, 578.7, 434.1, 361.7) mg of iron (iii) nitrate nonahydrate $Fe(NO_3)_3.9H_2O$, and then add 20 ml Deionized water in 150 ml beaker and sonicate the solution for 1 hr. Then, add (97, 388, 776, 970) µl of palladium nitrate to the sonicated solution;   then, stirr for 1 hr. After stirring; add (600) µl Hydrazine Hydrate at room temperature. The mixture turned to reddish brown and hence; the precursor suspension was heated by microwave for (60) s (intervals) and the black product was obtained. So, finally washing was done using hot deionized water 2-3 times, and then ethanol 2-3 times, dries in oven at 80˚C.

39

While, in the typical synthesis of Pd/Co_3O_4, different ratios has been prepared 10, 20, 30, 40, 50 wt % Palladium Nitrate Pd $(NO_3)_2$ supported on cobalt as will be shown respectively. Weigh 443.9, 394.6, 345.2, 295.9, 246.6 mg of cobalt (II) nitrate hexahydrate $Co(NO_3)_2.6H_2O$, and then add 20 ml deionized water in 150 ml beaker and sonicate the solution for 1 hr. Then, add 194, 388, 582, 776, 970 µl of palladium nitrate to the sonicated solution;   then, stirr for 1 hr. After stirring, add 600 µl Hydrazine Hydrate and microwave for 60 s (intervals), wash with hot deionized water 2-3 times, then ethanol 2-3 times, dry in oven at 80˚C.

Also, in the synthesis of Pd/Ni $(OH)_2$, different ratios has been prepared 30, 50, 70 wt % Palladium Nitrate Pd $(NO_3)_2$ supported on nickel as will be shown respectively. Weigh 346.7, 247.6, 148.6 mg of Nickel (II) nitrate hexahydrate $Ni(NO_3)_2.6H_2O$, and then add 20 ml deionized water in 150 ml beaker and sonicate the solution for 1 hr. Then, add   582, 970, 1358 µl of palladium nitrate to the sonicated solution,   then, stirr for 1 hr. After stirring, add 600 µl Hydrazine Hydrate and microwave for 60 s (intervals), wash with hot deionized water 2-3 times, then ethanol 2-3 times, dry in oven at 80˚C. But, to prepare 100 wt % Pd, 1940 µl of palladium nitrate were added to 20 ml deionized water. sonicate for 1 hr. Then, stirr for 1 hr. After stirring is finished, add 600 µl Hydrazine Hydrate. Then; microwave for 60 s (intervals), wash with hot deionized water 2-3 times, then ethanol 2-3 times, dry in oven at 80˚C.

Also, in case of preparing 100 wt % Fe_3O_4 nanoparticles, 723.42 mg of iron (III) nitrate nonahydrate Fe $(NO_3)_3.9H_2O$ were added to 20 ml deionized water. sonicate for 1 hr. Then, stirr for 1 hr. After stirring is finished, add 600 µl Hydrazine Hydrate. Then, microwave for 60 s (intervals), wash with hot deionized water 2-3 times, then ethanol 2-3 times, dry in oven at 80˚C.

Similarly, in case of 100 wt % Co_3O_4 nanoplates, 493.27 mg of Cobalt (ii) nitrate hexahydrate Co $(NO_3)_2.6H_2O$ were added to 20 ml deionized water. sonicate for 1 hr. Then, stirr for 1 hr. After stirring is finished, add few drops of 10 M solution of sodium hydroxide and finally add 600 µl Hydrazine Hydrate. Then, microwave for 60 s (intervals), wash with hot deionized water 2-3 times, then ethanol 2-3 times, dry in oven at 80˚C.

Also, in case of 100 wt % $Ni(OH)_2$, 495.298 mg of Nickel (II) nitrate hexahydrate Ni $(NO_3)_2.6H_2O$ were added to 20 ml deionized water. sonicate for 1 hr. Then, stirr for 1 hr. After stirring is finished, add few drops of 10 M solution of sodium hydroxide and finally add 600 µl Hydrazine Hydrate. Then, microwave for 60 s (intervals), wash with hot deionized water 2-3 times, then ethanol 2-3 times, dry in oven at 80˚C.

Some trials were done to Synthesis 30 wt % Pd – 70 wt % (Fe_3O_4 – Co_3O_4) oxide mixture magnetic catalyst so, in case of synthesis of (Fe_3O_4 – Co_3O_4) - (1:3), 126.6 mg of iron (III) nitrate nonahydrate Fe $(NO_3)_3.9H_2O$, 258.966 mg of cobalt (II) nitrate hexahydrate Co $(NO_3)_2.6H_2O$ were added to 20 ml deionized water. sonicate for 1 hr. Then, add 582 µl of palladium nitrate to the iron and cobalt nitrate solution, then, stir for 1 hr. After stirring is finished; add 600 µl Hydrazine Hydrate. Then; microwave for 60 s (intervals), wash with hot deionized water 2-3 times, then ethanol 2-3 times, dry in oven at 80˚C.

Also, in case of synthesis of (Fe_3O_4 – Co_3O_4) oxide - (1:1), 253.2 mg of iron (III) nitrate nonahydrate Fe $(NO_3)_3.9H_2O$, 172.644 mg of cobalt (II) nitrate hexahydrate Co $(NO_3)_2.6H_2O$ were added to 20 ml deionized water. Sonicate for 1 hr. Then, add 582 µl of palladium nitrate to the iron nitrate and cobalt solution, then, stirr for 1 hr. After stirring is finished, add 600 µl Hydrazine Hydrate. Then, microwave for 60 s (intervals), wash with hot deionized water 2-3 times, then ethanol 2-3 times, dry in oven at 80˚C.

41

Similarly, in case of synthesis of ($Fe_3O_4 - Co_3O_4$) oxide - (3:1), 379.8 mg of iron (III) nitrate nonahydrate $Fe(NO_3)_3.9H_2O$, 86.322 mg of cobalt (II) nitrate hexahydrate $Co(NO_3)_2.6H_2O$ were added to 20 ml deionized water. sonicate for 1 hr. Then, add 582 μl of palladium nitrate to the iron nitrate and cobalt solution, then, stirr for 1 hr. After stirring is finished, add 600 μl Hydrazine Hydrate. Then, microwave for 60 s (intervals), wash with hot deionized water 2-3 times, then ethanol 2-3 times, dry in oven at 80˚C.

While in case of synthesis of ($Pd:Fe_3O_4:Co_3O_4$) - (15:15:70), 108.51 mg of iron (III) nitrate nonahydrate $Fe(NO_3)_3.9H_2O$, 345.289 mg of cobalt (II) nitrate hexahydrate $Co(NO_3)_2.6H_2O$ were added to 50 ml deionized water. sonicate for 1 hr. Then, add 291 μl of palladium nitrate to the iron and cobalt nitrate solution, then, stirr for 1 hr. After stirring is finished, add 600 μl Hydrazine Hydrate. Then, microwave for 60 s (intervals), wash with hot deionized water 2-3 times, then ethanol 2-3 times, dry in oven at 80˚C.

In typical synthesis of ($Pd:Fe_3O_4:Co_3O_4$) - (40:40:20), 289.37 mg of iron (III) nitrate nonahydrate $Fe(NO_3)_3.9H_2O$, 98.654 mg of cobalt (II) nitrate hexahydrate $Co(NO_3)_2.6H_2O$ were added to 50 ml deionized water. sonicate for 1 hr. Then, add 776 μl of palladium nitrate to the iron nitrate and cobalt solution, then, stirr for 1 hr. After stirring is finished, add 600 μl Hydrazine Hydrate. Then, microwave for 60 s (intervals), wash with hot deionized water 2-3 times, then ethanol 2-3 times, dry in oven at 80˚C.

Similarly, synthesis of ($Pd:Fe_3O_4:Co_3O_4$) - (45:45:10) was made by adding 325.54 mg of iron (III) nitrate nonahydrate $Fe(NO_3)_3.9H_2O$, 49.327 mg of cobalt (II) nitrate hexahydrate $Co(NO_3)_2.6H_2O$ to 50 ml deionized water.

Sonicate for 1 hr. Then, add 873 μl of palladium nitrate to the iron nitrate and cobalt solution, then, stirr for 1 hr. After stirring is finished, add 600 μl Hydrazine Hydrate. Then, microwave for 60 s (intervals), wash with hot deionized water 2-3 times, then ethanol 2-3 times, dry in oven at 80˚C.

Annealing for selected samples has been made for our best results 30 wt %Pd – 70 wt % Co_3O_4 and 50 wt % Pd – 50 wt % Fe_3O_4. Annealing was done by using a tube furnace for heating at 350˚C for 3 hours with a continuous flow of hydrogen gas to get rid of remaining hydrazine. While, Synthesis of Pd – Fe_3O_4 and Pd – Co_3O_4 supported on GO was done by using Graphite oxide that was prepared from graphite powder by Hummers and Offeman method.[164] So, the pre-prepared catalysts 50 wt % Pd – 50 wt % Fe_3O_4 and 30 wt % Pd – 70 wt % Co_3O_4 were used by dissolving 40 mg of each catalyst separately in 50 ml deionized water and sonicate for 2 hrs. Then, at the same time prepare two solutions of 160 mg of graphite oxide dispersed in 100 ml and also sonicated for 2 hrs. then add the 40 mg catalyst to the 160 mg Go solution and stir for 2 hrs then centrifuge, wash with hot deionized water 2-3 times, then ethanol 2-3 times, dry in oven at 80˚C.

3.3.3   Synthesis of Graphene Oxide (GO)

In the typical synthesis, Graphene oxide was prepared according to Hummers and Offeman method[164] in which oxidation of high-purity graphite powder (99.9999%, 200 mesh) was done using a mixture of H_2SO_4/$KMnO_4$. Briefly, 4-5 g of graphite and 2.5 g of $NaNO_3$ were mixed in a conical flask. Then the mixture was kept in an ice bath and 115 mL of conc. H_2SO_4 was poured into it with constant stirring. Subsequently, after a period of 20 min., 15 g of $KMnO_4$ was slowly added over about 2 - 2.5 h with constant stirring. Stirring was again continued for 3 h in ice bath.

43

After that the mixture was continuously stirred for 3 h at room temperature, 230 mL of deionized water H_2O was slowly added to the above mixture. Then, after 20 min., 700 ml deionized water H_2O were added when temperature was around 80˚C. Then, after 20 min., 20 ml (10%) H_2O_2 were added drop by drop. Solid product was separated from the reaction mixture using centrifuge to remove water soluble oxidant and other inorganic salts. Collected yellowish-brown cake of solid was washed 3 - 5 times with 1M HCl followed by washing 10 – 15 times with hot deionized water . After each time of washing solid was suspended by ultra sonication and again collected by centrifugation. Then the solid sample (graphite oxide) was dried in a vacuum oven at 40˚C. Resultant graphite oxide could be readily exfoliated to completely water dispersed graphene oxide (GO) by ultra-sonication.

3.3.4 Synthesis of Pd-Fe₃O₄ supported on Graphene

Sixty milligrams of the above solid was dispersed in 50 mL of water for 1 h in a sonication bath to produce aqueous dispersion of graphene oxide. Then; 50 mL of deionized water in which 388 µl of Palladium Nitrate Pd $(NO_3)_2$ and 144.68 mg of iron (III) nitrate nonahydrate $Fe(NO_3)_3.9H_2O$ were added and sonicated for 1 h; the 50 ml solution was added to the aqueous dispersion of graphene oxide and stirred for 1 h. After stirring, add 1 ml Hydrazine Hydrate at room temperature. The mixture turned to reddish brown and hence, the precursor suspension was heated by microwave for (60) s (intervals) and the black product was obtained. So, finally washing was done using hot deionized water 2-3 times, and then ethanol 2-3 times, dries in oven at 80˚C.

3.3.5 Synthesis of Pd-Co₃O₄ supported on Graphene

Sixty milligrams of the above solid was dispersed in 50 mL of water for 1 h in a sonication bath to produce aqueous dispersion of graphene oxide. Then; 50 mL of deionized water in which 388 μl of Palladium Nitrate Pd (NO₃)₂ and 98.654 mg of cobalt (II) nitrate hexahydrate Co(NO₃)₂.6H₂O were added and sonicated for 1 h, the 50 ml solution was added to the aqueous dispersion of graphene oxide and stirred for 1 h. After stirring, add 1 ml Hydrazine Hydrate at room temperature. The mixture turned to reddish brown and hence; the precursor suspension was heated by microwave for (60) s (intervals) and the black product was obtained. So, finally washing was done using hot deionized water 2-3 times, and then ethanol 2-3 times, dries in oven at 80˚C.

3.3.6 Synthesis of Pd- Ni(OH)₂ supported on Graphene

Sixty milligrams of the above solid was dispersed in 50 mL of water for 1 h in a sonication bath to produce aqueous dispersion of graphene oxide. Then, 50 mL of deionized water in which 388 μl of Palladium Nitrate Pd (NO₃)₂ and 99.0596 mg of nickel (II) nitrate hexahydrate Ni(NO₃)₂.6H₂O were added and sonicated for 1 h, the 50 ml solution was added to the aqueous dispersion of graphene oxide and stirred for 1 h. After stirring, add 1 ml Hydrazine Hydrate at room temperature. The mixture turned to reddish brown and hence, the precursor suspension was heated by microwave for (60) s (intervals) and the black product was obtained. So, finally washing was done using hot deionized water 2-3 times, and then ethanol 2-3 times, dries in oven at 80˚C.

3.3.7 Synthesis of Fe_3O_4 Hexagonal Nanoplates

Graphene has received a great attention in recent years because of its extraordinary structural, optical, thermal, mechanical and electrical properties.[165-167] Such intriguing and unique features make graphene promising in wide array of potential applications such as nanocomposites, supercapacitors, transparent conducting films, batteries, paper-like materials and others.[168] Anchoring superparamagnetic iron oxide nanostructures on chemically synthesized graphene will impart the desirable superparamagnetic features into graphene, making such graphene-based composite material promising for a wide range of fields such as magnetic energy storage, magnetic fluids, catalysis, electromagnetic materials and coatings, environmental remediation, aligned substrates for nanodevices, magnetic separation and biological imaging.[169-178] The control of the morphology, size and magnetic features of magnetic nanoparticles has gained considerable attention in the past few years due to the significance in fundamental understanding and wide technological applications in catalysis, high density magnetic and energy storage media, drug delivery, color imaging and biological separations.[179-181] The size and morphological changes in magnetite nanostructures, in particular, have been shown to significantly affect the magnetic features.[182-185] In addition, Fe_3O_4 have been brought into sharp focus due to their superior magnetic properties, low toxicity and biocompatibility. To control the size and shape of magnetic nanocrystals, various synthetic methods adopting hydro- or solvothermal treatment, wet chemical etching, reverse-micelles or polyol molecules have been introduced to prepare a variety of structures such as magnetite nanospheres,[186] nanopyarmids,[181] 1D nanowires,[187-188] nanocubes,[184, 189] nanooctahedra,[180, 190] and nanorods.[191] Chemical synthetic routes offer large scale production of graphene-based composite materials with potentially low cost. Recently, composite structures of graphene or graphene oxide and magnetic nanostructures prepared by the wet chemical methods have been synthesized and applied to arsenic removal,

46

catalysis, magnetic-controlled switches, magnetic resonance imaging (MRI), electrochemical sensing, and targeted drug carriers.[169-176, 192-197] As a simple and fast route, microwave irradiation (MWI) has been used extensively for the large scale synthesis of high crystalline nanostructures that minimizes the thermal gradient effects.[39, 198] Heating of a substance by microwave irradiation is based on dipole rotation and ionic conduction, that is, by reversal of solvent dipoles and the resulting replacement of charged ions of a solute.[39, 198] Due to the difference in the solvent and reactant dielectric constants, selective dielectric heating can provide significant enhancement in reaction rates. The rapid transfer of energy directly to the reactants causes an instantaneous internal temperature rise. Thus, the activation energy is essentially decreased as compared with conventional heating methods and the reaction rate increases accordingly. This also allows the rapid decomposition of the precursors thus creating highly supersaturated solutions where nucleation and growth can take place to produce the desired nanocrystals.

Herein, a simple strategy to control the shape of magnetite nanocrystals, both free standing and those attached to graphene sheets is described, integrating in such way the superparamagnetic properties of magnetite nanoparticles of different morphologies and the superior conductivity of graphene in a single compartment composite structure. We performed two different microwave-assisted syntheses using same metal precursors and reducing agent. The two syntheses included the preparation of Fe_3O_4 hexagonal nanoplates both free-standing and supported on co-synthesized graphene sheets. In a such synthesis of Fe_3O_4 hexagonal nanoplates, 3.9×10^{-1} mmol of $Fe(NO_3)_3.9H_2O$ was dissolved in 100 ml DI water followed by stirring and addition of 2 ml hydrazine hydrate (78-82% assay) at room temperature. The reaction mixture was then transferred to a microwave oven and was irradiated for 2 min. Upon microwave irradiation, the color of the solution turned black indicating the formation of Fe_3O_4 nanocrystals.

47

Particles were then separated by centrifuge, washed twice with hot DI water and once with ethanol and finally dried in an oven at 80˚C overnight. For the preparation of Fe_3O_4 nanoplates supported on graphene, 60 mg of graphene oxide was dispersed in 50 ml using sonication. Then 3.9×10^{-1} mmol of Fe $(NO_3)_3.9H_2O$ was added followed by addition of 2 ml hydrazine while stirring. The whole mixture was then microwaved for 2 min and composite particles were separated and washed as described before.

3.4   Results and Discussion

3.4.1   Characterization of Pd-Fe₃O₄

From analysis of data obtained using Type F21100 Tube Furnace under ambient pressure; it was found that increasing the weight ratio of palladium nitrate with respect to iron nitrate enhanced the catalytic activity of our catalyst as shown in **Figure 3-1**. So, the complete conversion was accomplished at lower temperatures until our best temperature at which complete conversion happened was 127 ˚C as shown in **Table 3-1** in case of 50 wt % Pd – 50 wt % Fe $_3O_4$ catalyst. While higher temperatures were noticed when using palladium nitrate and iron nitrate alone. This may be due to a kind of agglomeration as there is no support used in these two cases.

Figure 3-2a displays the XRD pattern of palladium supported on iron oxide (Fe_3O_4) or magnetite for different ratios of palladium to iron that was prepared by microwave method. The palladium shows the typical sharp diffraction peak at $2\theta = 40˚$. The XRD patterns indicate that the products were all (Fe_3O_4) magnetite with reference code (ICCD-00-003-0863) in case of (50 wt % Pd – 50 wt % Fe_3O_4) and (20 wt % Pd - 80 wt % Fe_3O_4), while reference code was (ICCD-00-0021035) in case of 100 % Fe.

48

It is also easily to notice that the sharp diffraction peak at $2\theta = 40°$ which is characteristic to palladium is larger in case of (50 wt % Pd - 50 wt % Fe_3O_4) if it is compared with the (20 wt % Pd - 80 wt % Fe_3O_4) and also the characteristic peaks of Fe_3O_4 is shown as a sharp diffraction peak at $2\theta = 35°$.

The XPS technique is more sensitive for the analysis of surface oxides than XRD. All the samples had a C1s binding energy around 284.5 eV derived from the carbon contamination in the analysis.

In **Figure 3-2b, 3-2c, and 3-2d**, Samples showed that the binding energy of Fe $2P^{3/2}$ was 710.5 eV, indicating that the Fe was present as Fe_3O_4 and also the binding energy of Fe $2P^{1/2}$ was 723.7 eV indicating that Fe was present as Fe_3O_4. Also, the binding energy of Pd $3d^{5/2}$ was 334.8 eV, and Pd $3d^{3/2}$ was 340.1 eV indicating that the Pd was present as Pd^0.

Similarly, the binding energy of Pd $3d^{3/2}$ was 341.38 eV, and Pd $3d^{5/2}$ was 336.23 eV indicating that the Pd was present as PdO (Pd^{2+}).

Table 3-1 "CO oxidation as a function of temperature for the reactant gas mixture containing 4.0 wt% CO and 20.0 wt% O_2 for different catalysts of Pd supported on Fe_3O_4"

wt % Pd in Fe_3O_4	$T_{100\%}$ (°C)
5	204
10	180
20	157
40	130
50	127
80	168
100 (pure Pd nanoparticles)	179
0 (pure Fe_3O_4 nanoparticles)	273
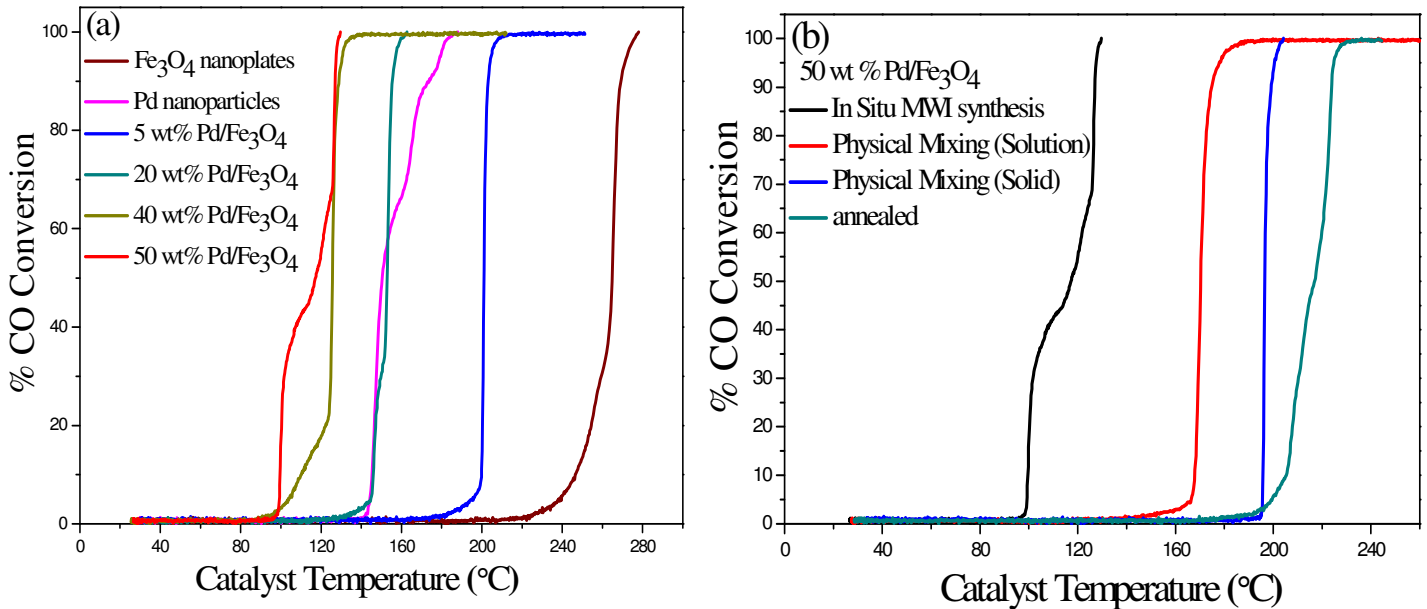
Figure 3-1 CO – Catalytic conversion of Palladium supported on magnetite (Fe₃O₄) – (a) Different Ratios, (b) Different mixing methods, and annealing.

To confirm the stronger interaction between the Pd and Fe_3O_4 nanoparticles prepared simultaneously using the MWI method as compared to the physical mixing of individual Pd and Fe_3O_4 nanoparticles, we measured the catalytic activity of a 50 wt% physical mixture of Pd and Fe_3O_4 nanoparticles prepared separately under identical conditions to the preparation of the supported 50 wt% Pd/Fe_3O_4 catalyst.

As shown in **Figure 3-1b**, the physical mixture exhibits a significantly lower activity than the supported catalyst prepared simultaneously using the MWI. This provides evidence for stronger interaction between the Pd and Fe_3O_4 nanoparticles which is reflected in the enhanced catalytic activity.

50

The catalytic activity of the 50 wt% Pd/Fe_3O_4 catalyst prepared here using the simple one-step MWI-assisted chemical reduction is comparable to that of the Pd/Fe_2O_3 hybrid nanocatalysts prepared by a seed-mediated process for the synthesis of Pd core nanoparticles followed by deposition of Fe_3O_4 surface layers in solution and then thermal annealing at 300° C.[21] The 100% conversion of CO into CO_2 was measured for the Pd/Fe_3O_4 hybrid catalyst at 125° C as compared to 128°C for the 50 wt% Pd/Fe_3O_4 catalyst prepared in this work. While other methods like physical mixing either solution or solid and also annealing in hydrogen at 400°C for three hours didn't make improvement to the catalytic activity.

To characterize the surface composition of the supported nanocatalysts, XPS measurements were carried out as shown in **Figure 3-2** for the 50 wt% Pd/Fe_3O_4 catalyst. The data reveals the presence of Fe(III) as indicated by the observed peaks at 724.2 eV and 710.5 eV corresponding to the binding energies of the $2p^{1/2}$ and $2p^{3/2}$ electrons, respectively. The broad Fe(III) $2p^{3/2}$ peak centered at 710.5 eV most likely contain contributions from the Fe(II) $2p^{3/2}$ which normally occurs at ~ 708 eV. For Pd, the observed binding energies of 334.8 eV and 340.1 eV indicate the presence of 82% Pd^0 and 18% Pd^{2+} (due to the presence of PdO). However, these values are slightly lower than the binding energies of Pd 3d electrons in pure Pd nanoparticles where the values of 335 eV and 341.1 eV have been reported for Pd^0 and Pd^{2+}, respectively.[21] The decrease in the binding energy of the Pd 3d electron in the Pd/Fe_3O_4 supported catalyst indicates that the Pd in the supported catalyst is more electron rich than in pure Pd nanoparticles. This could be due to electron transfer from Fe_2O_3 to Pd consistent with similar results obtained for the Pd/Fe_2O_3 hybrid nanocatalysts prepared by a seed-mediated process,[21] and also for Pd nanoparticles grown by vapor phase deposition on ordered crystalline Fe_3O_4 films.[43]

51
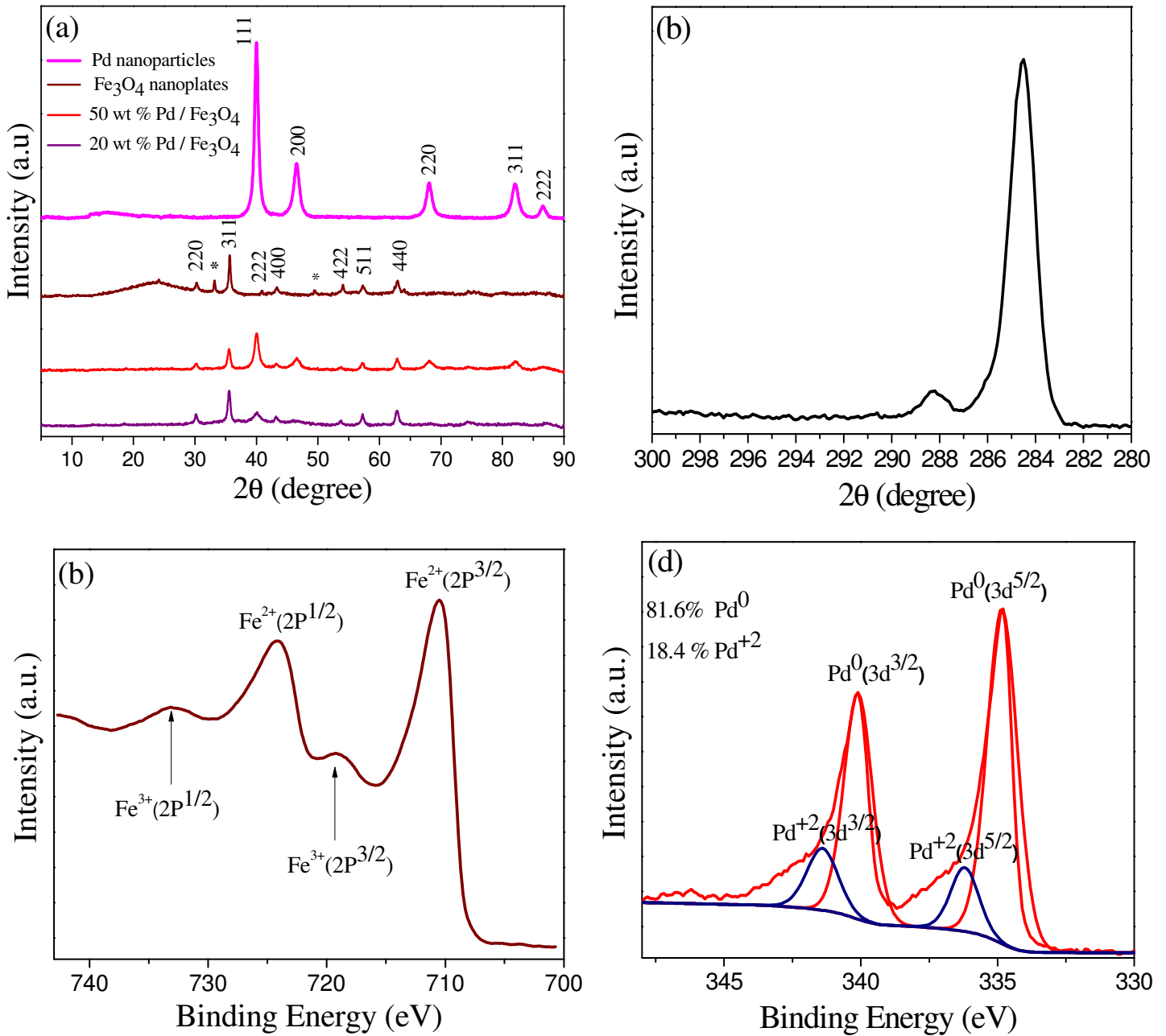
Figure 3-2 **(a)** **XRD Pattern, (b) XPS (C1s), (c) XPS (Fe2p) and (d) XPS (Pd3d) of Palladium supported on Fe₃O₄**

52
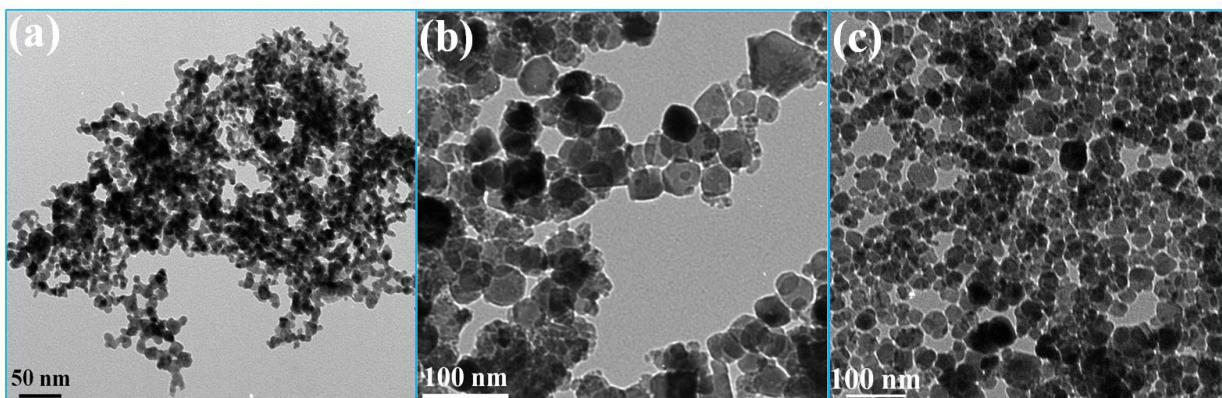
Figure 3-3 TEM images of nanoparticles prepared by HH reduction under MWI of (a) Pd, (b) Fe₃O₄, and (c) 50 wt% Pd/Fe₃O₄

It is clear that both the individual Fe_3O_4 and Pd nanoparticles show poor activities with 100% conversion temperatures of 273 ^oC and 179 ^oC, respectively. In the case of pure Pd, this is mostly due to the aggregation of the Pd nanoparticles and the complete coverage by CO molecules on the catalyst surface so there are not many open sites available for the adsorption of the O_2 molecules. The data also shows that the 5 wt% Pd/Fe₃O₄ catalyst has lower activity than the pure Pd nanoparticle catalyst indicating that not enough Pd nanoparticles are interacting with the Fe_3O_4 nanoparticles to create a sufficient number of active interfaces for the CO oxidation. Increasing the Pd wt% up to 50% increases the activity as shown before. However, catalysts containing more than 50 wt% Pd show similar behavior to the pure Pd nanoparticle catalyst confirming the importance of the support in dispersing the catalyst nanoparticles and decreasing their tendency for aggregation and sintering. Therefore, it appears that the 50 wt% Pd/Fe₃O₄ catalyst provides reasonable optimization between the adsorption of the CO and O_2 molecules on the Pd-Fe₃O₄ interfaces to allow efficient oxidation of CO.

3.4.2 Characterization of Pd-Co$_3$O$_4$

Figure 3-4a displays the XRD pattern of palladium supported on cobalt for different ratios of palladium to cobalt that was prepared by microwave method. The 100% Co$_3$O$_4$ nanoparticles show the characteristic peaks for the spinal Co$_3$O$_4$ phase (ICCD-00-030-044300). For the 20 wt%, 30 wt% and 50 wt% Pd/Co$_3$O$_4$ nanoparticles, peaks due to Pd and Co$_3$O$_4$ are present and with no indication of the presence of other phases.

The palladium shows the typical sharp diffraction peak at $2\theta = 40°$. The XRD patterns indicate that the catalysts were all Co$_3$O$_4$ with reference code (ICCD-00-030-0443) in case of (20 wt % Pd - 80 wt % Co$_3$O$_4$), (30 wt % Pd - 70 wt % Co$_3$O$_4$) and (100 wt % Co$_3$O$_4$), while reference code was (ICCD-00-045-0031) in case of (50 wt % Pd - 50 wt % Co$_3$O$_4$). It is also easily to notice that the sharp diffraction peak at $2\theta = 40°$ which is characteristic to palladium is larger in case of (50 wt % Pd - 50 wt % Co$_3$O$_4$) if it is compared with the (30 wt % Pd - 70 wt % Co$_3$O$_4$) or (20 wt % Pd - 80 wt % Co$_3$O$_4$) and also the characteristic peaks of Co$_3$O$_4$ are shown. In **Figure 3-4b, 3-4c, and 3-4d**; Samples showed that the binding energy of Co 2p was 796.99 and 780.77 eV indicating that most of the Co was present as Co$_3$O$_4$ as shown. Also; the binding energy of Pd 3d$^{5/2}$ was 335.4 eV, and Pd 3d$^{3/2}$ was 340.68 eV indicating that the Pd was present as Pd^0. Similarly, the binding energy of Pd 3d$^{3/2}$ was 342.47 eV, and Pd 3d$^{5/2}$ was 337.174 eV indicating that the Pd was present as PdO (Pd^{2+}). The Co and Pd XPS data for the 50 wt% Pd/Co$_3$O$_4$ catalyst are shown in Figure 4(b) and 4(c) for the Co-2p and Pd-3d electron binding energies, respectively. The data reveals the presence of Co(II) and Co(III) as indicated by the observed peaks at 796.8 eV and 780.7 eV corresponding to the Co(II) 2p$^{1/2}$ and 2p$^{3/2}$ binding energies, respectively, and at 802.6 eV and 786.2 eV corresponding to the Co(III) 2p$^{1/2}$ and 2p$^{3/2}$ binding energies, respectively.

For Pd, the observed binding energies of 340.7 eV and 335.4 eV indicate the presence of 86% Pd^0 ($3d^{5/2}$) and 342.5 eV and 337.2 eV indicate the presence of 14% Pd^{2+} (due to the presence of PdO).
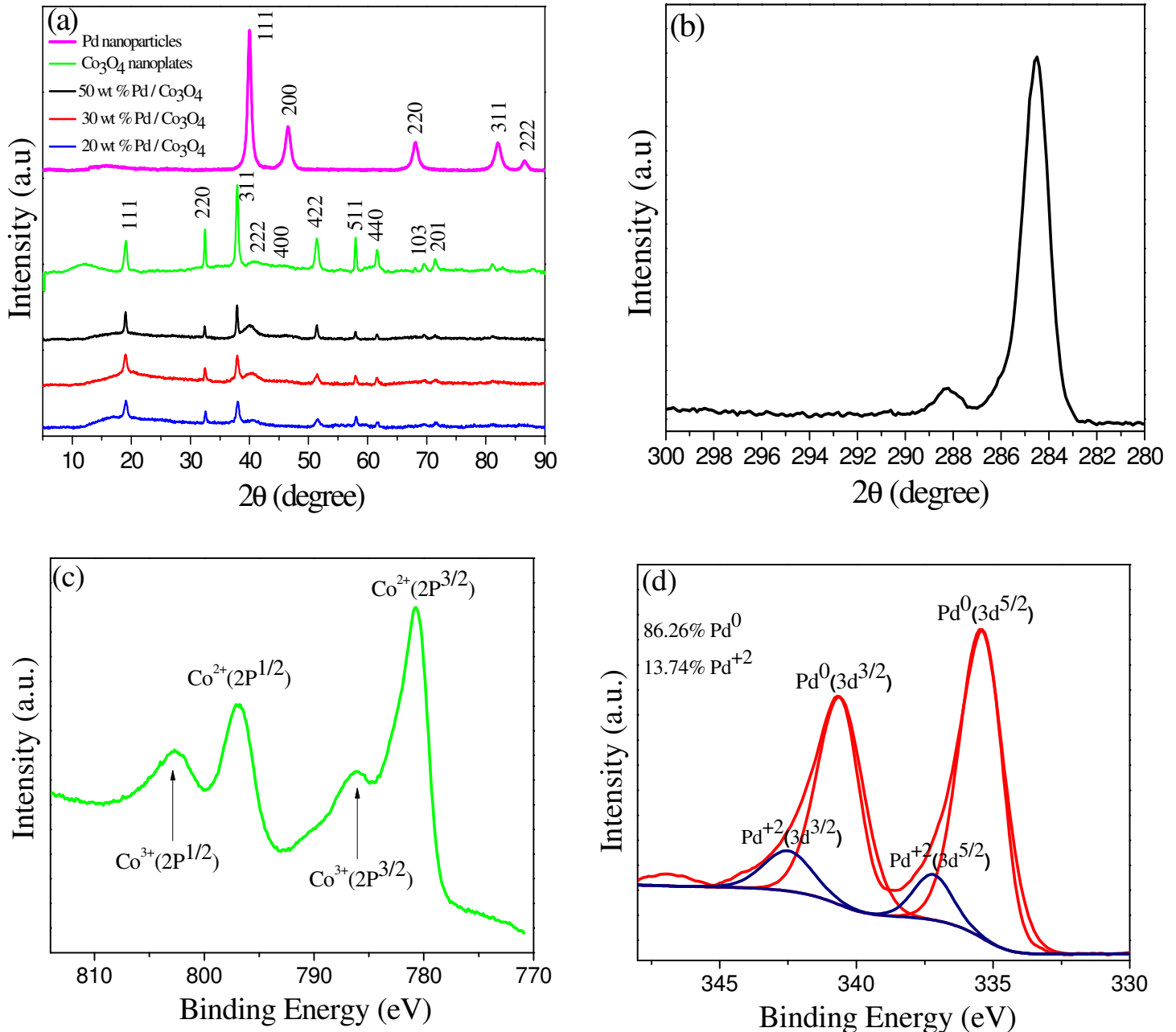
Figure 3-4 (a) XRD Pattern, (b) XPS (C1s), (c) XPS (Fe2p)and (d) XPS (Pd3d) of Palladium supported on Co_3O_4

55

Similarly, it was found that increasing the weight ratio of palladium nitrate with respect to cobalt nitrate enhanced the catalytic activity of our catalyst as shown in **Figure 3-5a**.

So, the complete conversion was accomplished at lower temperatures until our best temperature at which complete conversion happened was 127 ˚C as shown in **Table 3-2** in case of 30 wt % Pd – 70 wt % Co_3O_4 catalyst.

While higher temperatures were noticed when using palladium nitrate in higher weight ratio. This may be due to a kind of agglomeration.

Also, a kind of room temperature catalytic activity was noticed when using 10 wt % and 20 wt % Pd supported on cobalt oxide but reaction after that was slower to be comparable to the other ratios.

Table 3-2 "CO oxidation as a function of temperature for the reactant gas mixture containing 4.0 wt% CO and 20.0 wt% O_2 for different catalysts of Pd supported on Co_3O_4"

wt % Pd in Co_3O_4	$T_{100\%}$ (˚C)
5	172
10	164
20	151
30	**127**
40	135
50	165
100 (pure Pd nanoparticles)	179
0 (pure Co_3O_4 nanoparticles)	140
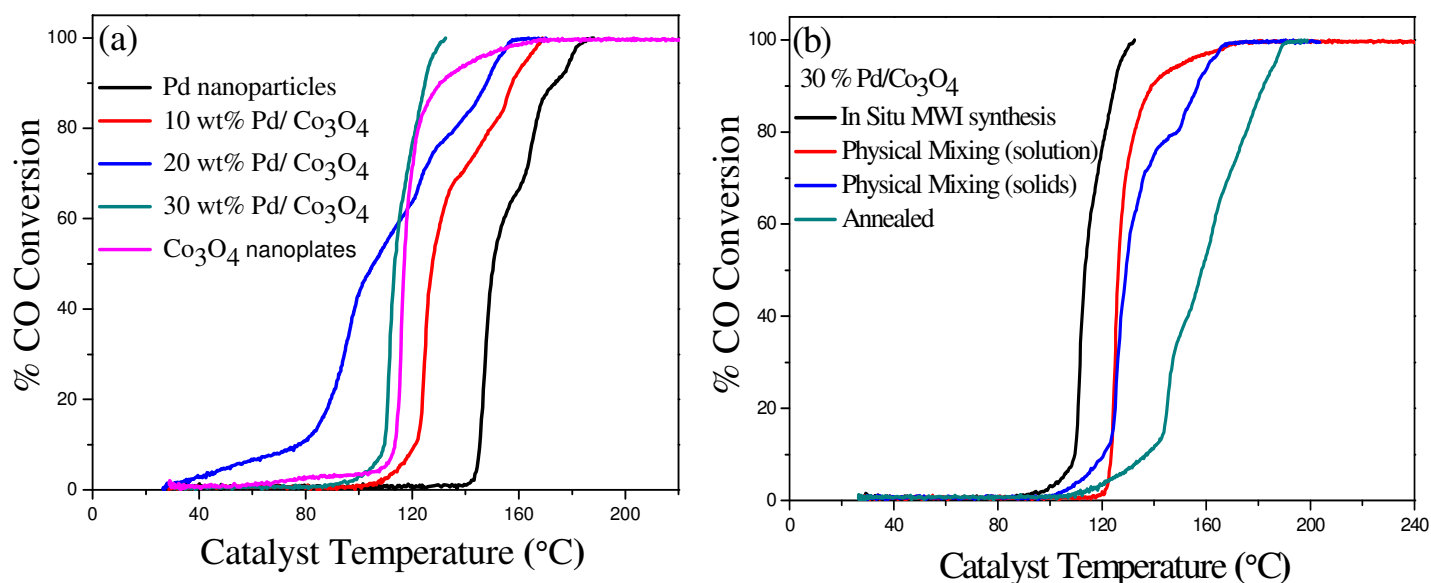
Figure 3-5 CO – Catalytic conversion of Palladium supported on magnetite (Co$_3$O$_4$) – (a) Different Ratios, (b) Different mixing methods, and With annealing

Figure 3-5 compares the catalytic oxidation of CO over Co$_3$O$_4$ and Pd nanoparticles as well as 10 wt%, 20 wt% and 30 wt% Pd nanoparticles supported on Co$_3$O$_4$. Unlike the pure Fe$_3$O$_4$ nanoparticles, the Co$_3$O$_4$ nanoparticles exhibit a significant activity for CO oxidation with T_{50} (the temperature at which CO conversion reaches 50%) and T_{100} occurring at 115˚C and 140˚C, respectively. The same trend of increasing catalytic activity with increasing the Pd wt% in the catalyst is also observed in the Pd/Co$_3$O$_4$ system as in the Pd/Fe$_3$O$_4$ system. However, significant activity is observed for the 20 wt% Pd/Co$_3$O$_4$ catalyst especially at lower temperatures. For example, **Figure 3-5 a** shows a 10 % conversion of CO into CO$_2$ at 70˚C and a T_{50} of about 110˚C for the 20 wt% Pd/Co$_3$O$_4$ catalyst. It appears that Co$_3$O$_4$ is responsible for the low temperature oxidation of CO since this behavior is also weakly observed in pure Co$_3$O$_4$ nanoparticles as shown in Figure 5(a). The lowest T_{100} is obtained at 128 °C for the 30 wt% Pd/Co$_3$O$_4$ catalyst, similar to the 50 wt% Pd/Fe$_3$O$_4$ catalysts.

57

This indicates that Co_3O_4 nanoparticles provide a more active support for the Pd nanocatalyst than Fe_3O_4 nanoparticles, and hence a lower amount of the Pd nanoparticles can be used to achieve the same T_{100}. Also, similar to the result obtained for the 50 wt% Pd/Fe_3O_4 catalyst, the physical mixture of Pd and Co_3O_4 nanoparticles results in lower activity than that of the supported 50 wt% Pd/Co_3O_4 catalyst, as shown in **Figure 3-5 b**, indicating that the simultaneous reduction of Pd and Co nitrates under MWI produces supported Pd nanoparticles on the Co_3O_4 nanoplates and not simply a mixture of Pd and Co_3O_4 nanoparticles.

It is also obvious that the best catalytic activity was reached when preparing the catalyst in situ as conversion of carbon monoxide to carbon dioxide started at $100\ ^\circ$C and complete conversion was at $127\ ^\circ$C for the catalyst 30 wt % Pd – 70 wt % Co_3O_4. While other methods like physical mixing either solution or solid and also annealing in hydrogen at $400\ ^\circ$C for three hours did not improve the catalytic activity.
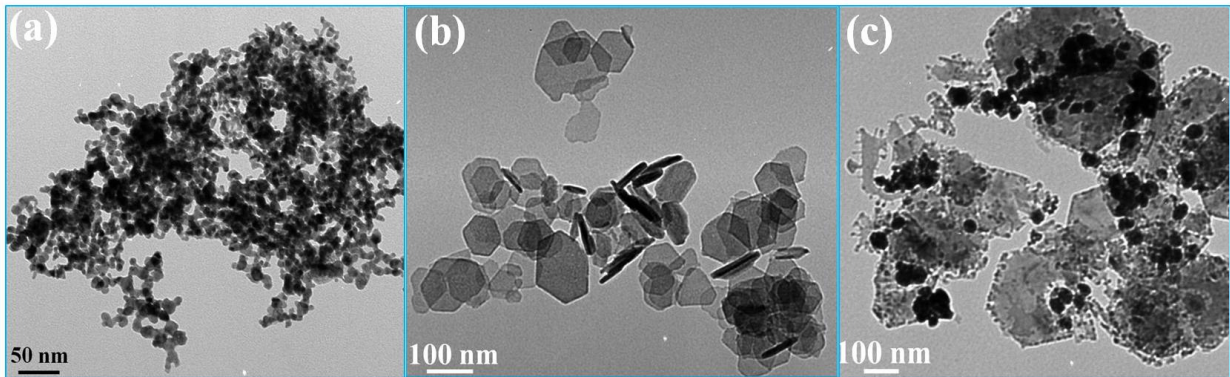
Figure 3-6 TEM – images of nanoparticles prepared by HH reduction under MWI of (a) Pd, (b) Co_3O_4, and (c) 30 wt% Pd/Co_3O_4

58

3.4.3 Characterization of Pd – Ni (OH)$_2$

Figure 3-7a displays the XRD patterns of the Pd, Ni(OH)$_2$, 30 wt% Pd/ Ni(OH)$_2$, 50 wt% Pd/Ni(OH)$_2$ and 70 wt% Pd/Ni(OH)$_2$ nanoparticles prepared by the HH reduction under MWI. The palladium shows the typical sharp diffraction peak at $2\theta = 40°$. The 100% Ni(OH)$_2$ nanoparticles show the characteristic peaks for the hexagonal phase (ICCD-00-001-1047). Small diffraction peaks due to Ni(OH)$_2$ can be observed in the XRD pattern of the 30 wt% Pd/ Ni(OH)$_2$ sample as shown. However, for samples containing more than 30 wt% Pd, the XRD patterns are dominated by the Pd diffraction peaks. It is obvious that using nickel as a support for palladium didn't make any enhancement for the catalytic activity for the catalyst. While the ratio of (50 wt % Pd: 50 wt % Ni (OH)$_2$) was better than the ratios of 100 wt % Pd, (30 wt % Pd: 70 wt % Ni (OH)$_2$), and (70 wt % Pd: 30 wt % Ni (OH)$_2$) respectively but it still less active than the catalyst (30 wt % Pd – 70 wt % Fe$_3$O$_4$) and the catalyst (30 % Pd – 70 % Co$_3$O$_4$) which still our best conditions as shown in **Table 3-3**.

Table 3-3 "CO oxidation as a function of temperature for the reactant gas mixture containing 4.0 wt% CO and 20.0 wt% O$_2$ for different catalysts of Pd supported on Ni(OH)$_2$"

wt % Pd in Ni(OH)$_2$	T$_{100\%}$ (˚C)
5	240
10	206
20	195
30	188
50	**168**
70	184
100 (pure Pd nanoparticles)	179
0 (pure Ni(OH)$_2$ nanoparticles)	244

59
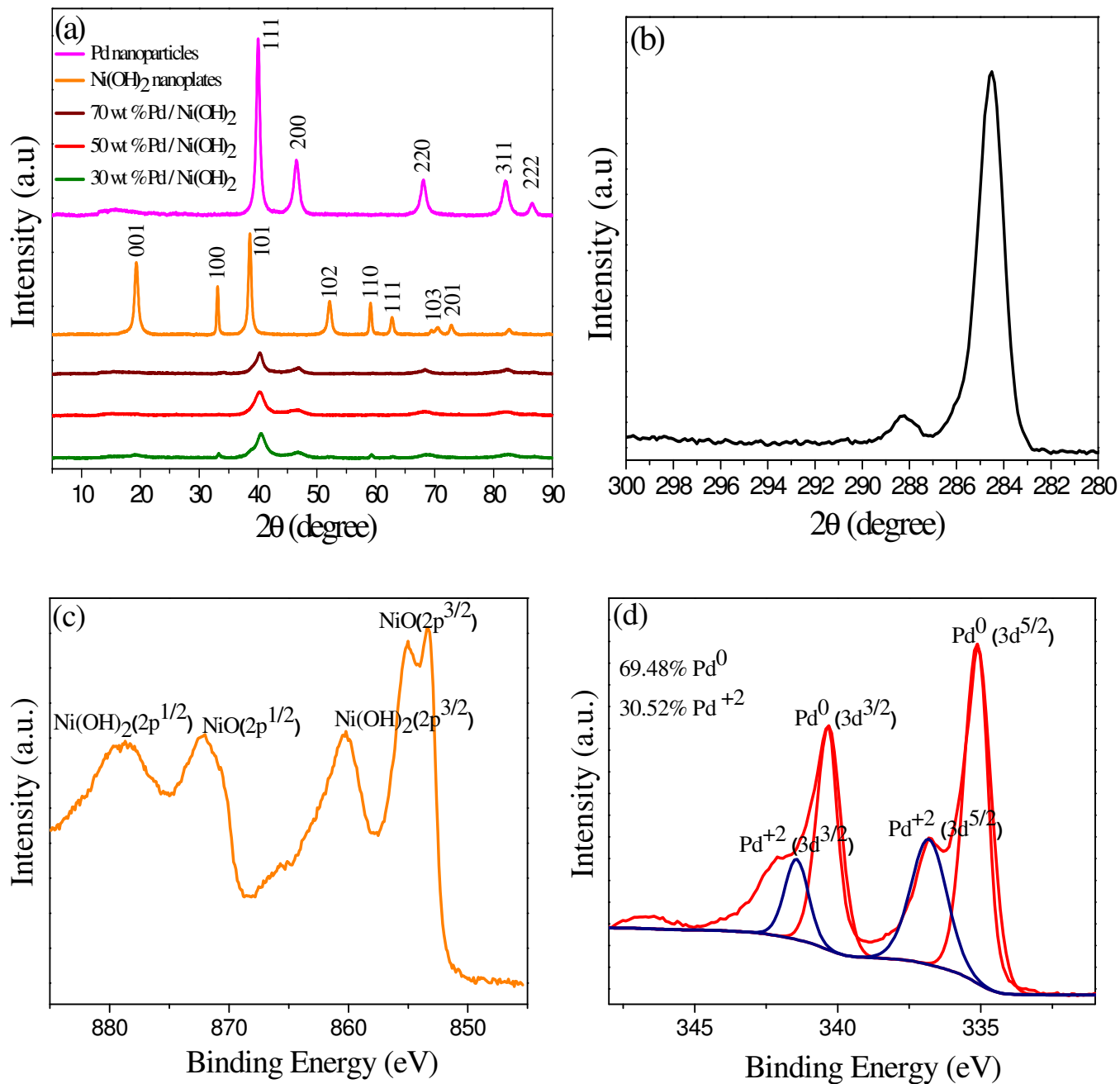
Figure 3-7 **(a) XRD Pattern, (b) XPS (C1s), (c) XPS (Ni2P) and (d) XPS (Pd3d) of Palladium supported on Ni (OH) 2**

Also, as shown later in **Figure 3-8a**, it is obvious that using nickel hydroxide as a support for palladium didn't make any enhancement for the catalytic activity for the catalyst. While the ratio of (50 wt % Pd:50 wt % Ni $(OH)_2$) was better than the ratios of 100 wt % Pd, (30 wt % Pd:70 wt % Ni $(OH)_2$), and (70% Pd:30 % Ni $(OH)_2$) respectively but it still less active than the catalyst (30 wt % Pd – 70 wt % Fe_3O_4) and the catalyst (30 wt % Pd – 70 wt % Co_3O_4) which still our best conditions. In previous **Figures 3-7b, 3-7c, and 3-7d**, Samples showed that the binding energy of Ni $2p^{1/2}$, $2p^{3/2}$ was 873.7 and 855.75 eV indicating that most of the Ni was present as Ni $(OH)_2$ and Samples showed also that the binding energy of Ni $2p^{1/2}$, $2p^{3/2}$, and $2p^{3/2}$ was 872.07, 853.33 and 855.2 eV indicating that some Ni was present as NiO as shown. Also, the binding energy of Pd $3d^{5/2}$ was 335.1 eV, and Pd $3d^{3/2}$ was 340.35 eV indicating that the Pd was present as Pd^0. Similarly; the binding energy of Pd $3d^{3/2}$ was 341.4 eV, and Pd $3d^{5/2}$ was 336.7 eV indicating that the Pd was present as PdO. The ICP-OES was done for our best samples in catalytic activity including palladium supported on iron oxide, cobalt oxide and nickel hydroxide. The obtained data as shown in **Table 3-4**, showed that the weight ratio was confirmed to be consistent with mixing ratios.

Table 3-4 "CO oxidation as a function of temperature for the reactant gas mixture containing 4.0 wt% CO and 20.0 wt% O_2 for prepared catalysts in comparison with literature"

Catalyst	Wt% Pd nanoparticles	Wt% Fe_3O_4 nanoplated	Wt% Co_3O_4 nanoplates	Wt% Ni(OH)₂ nanoplates	$T_{50\%}$ (°C)	$T_{100\%}$ (°C)	Literature
Pd –Fe_3O_4	50	50	--	--	105	127	
Pd –Co_3O_4	30	--	70	--	110	127	
Pd –Ni $(OH)_2$	50	--	--	50	160	168	
Pd –Fe_3O_4	By using different methods for preparation				112	125	[199]
Pd –Al_2O_3					150	154	[200]
Pt –Al_2O_3					169	176	[200]

61
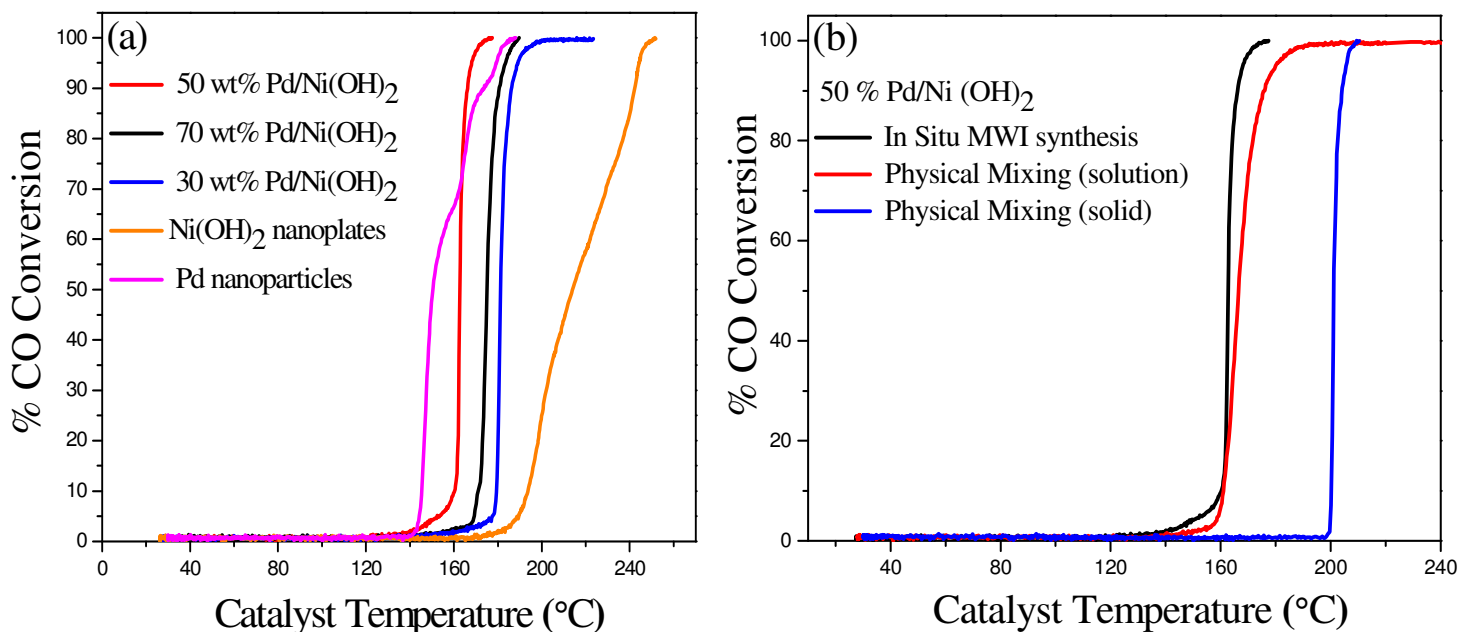
Figure 3-8 CO – Catalytic conversion of Palladium supported on Ni(OH)₂ – (a) Different Ratios, (b) Different mixing methods.

Figure 3-8a compares the catalytic oxidation of CO over Ni(OH)$_2$ and Pd nanoparticles as well as 30 wt%, 50 wt% and 70 wt% Pd nanoparticles supported on Ni(OH)$_2$. The pure Ni(OH)$_2$ nanoparticles show low activity for CO oxidation with T_{50} and T_{100} occurring at 213°C and 244°C, respectively. This is very different from the activity of the Co$_3$O$_4$ nanoplates which exhibit higher activities for CO oxidation with T_{50} and T_{100} occurring at 117°C and 140°C, respectively. The activity of Pd/Ni(OH)$_2$ nanoparticles does not show much improvement over that of the unsupported Pd nanoparticles. For example, the best Pd/(NiO)$_2$ catalyst (50 wt% Pd) has T_{50} and T_{100} occurring at 162°C and 168°C, respectively which are not significantly different from the T_{50} and T_{100} of unsupported Pd nanoparticles (150°C and 179°C, respectively).

This indicates a lack of favorable interactions between the Pd nanoparticles and the Ni(OH)$_2$ support. This is consistent with the similar activity shown for the 50 wt% Pd/Ni(OH)$_2$

62

catalyst and the physical mixture of Pd and Ni(OH)$_2$ nanoparticles as shown in **Figure 3-8b**, indicating that the simultaneous reduction of Pd and Ni nitrates under MWI produces weakly interacting Pd nanoparticles and Ni(OH)$_2$ nanoplates without strong catalyst-support interactions. This is also consistent with the stronger interactions between the Pd nanoparticles and the iron or cobalt oxide nanoparticles which can directly enhance the activity of the supported Pd/Fe$_3$O$_4$ and Pd/Co$_3$O$_4$ catalysts for the catalytic oxidation of CO. While other methods like physical mixing either solution or solid and also annealing in hydrogen at 400˚C for three hours didn't make improvement to the catalytic activity. Generally, it is obvious that the annealing treatment of our best samples did not improve the catalytic performance of the catalysts towards CO oxidation but unfortunately makes it worse than the catalyst without annealing. Also, a comparison had been made between three different methods of preparation of palladium supported on iron oxide, cobalt oxide and nickel hydroxide. The obtained data as shown in **Figures 3-1b, 3-5b, and 3-8b**, showed that mixing iron, cobalt and nickel nitrate with palladium nitrate in situ and then applying reduction in microwave by the hydrazine hydrate as a strong reducing agent gave the best results for complete carbon monoxide conversion into carbon dioxide. While; reducing each of them separately and then adding the reduced solutions together gave worse results than the previous case. But the worst case at all was when pre-prepared solids were added together as shown in **Table 3-5**.

Table 3-5 "CO oxidation as a function of temperature for the reactant gas mixture containing 4.0 wt% CO and 20.0 wt% O$_2$ for different prepared catalysts"

Catalyst	In Situ	Physical Mixing (Solution)	Physical Mixing (Solid)
50 wt % Pd/Fe$_3$O$_4$	127	176	200
30 wt % Pd/Co$_3$O$_4$	127	147	160
50 wt % Pd/Ni (OH)$_2$	168	178	205
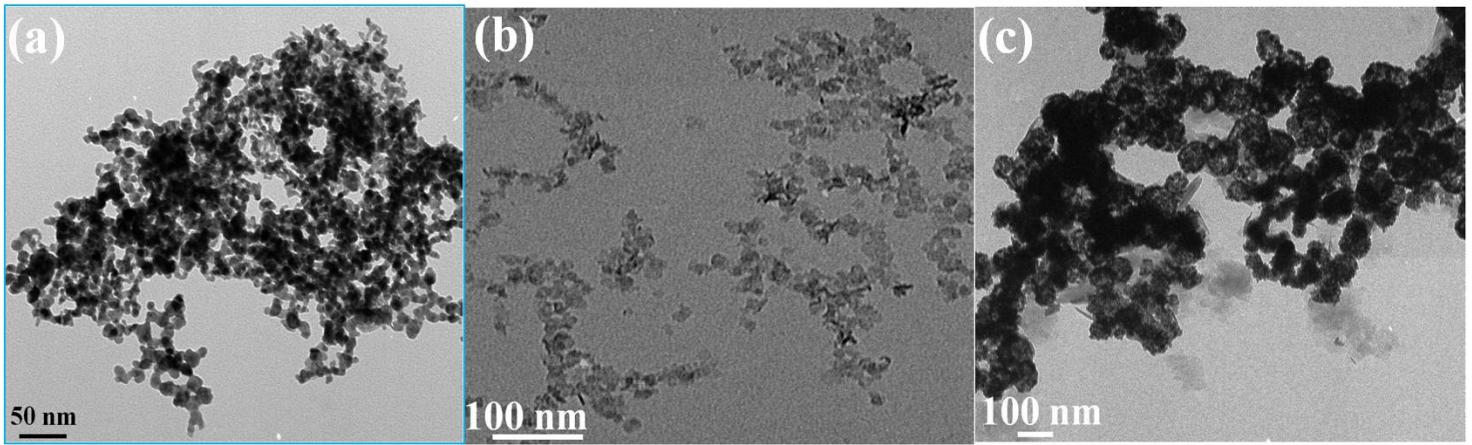
Figure 3-9 TEM – images of nanoparticles prepared by HH reduction under MWI of (a) Pd, (b) Ni (OH) $_2$, and (c) 50 wt% Pd/Ni (OH) $_2$

Table 3-6 summarizes the catalytic activities of the Pd nanoparticle catalysts supported on Fe$_3$O$_4$, Co$_3$O$_4$ and Ni(OH)$_2$. Both the Pd/Fe$_3$O$_4$ and Pd/Co$_3$O$_4$ catalysts show high activity mainly due to stronger interactions between Pd nanoparticles and the Fe$_3$O$_4$ and Co$_3$O$_4$ nanoplates. The Pd/Co$_3$O$_4$ catalyst shows improved activity over the Pd/Fe$_3$O$_4$ catalyst as indicated by achieving the same T_{100} of 127˚C for the 50 wt% Pd/ Fe$_3$O$_4$ catalyst but with only 30 wt% Pd in the 30 wt% Pd/ Co$_3$O$_4$ catalyst.

Table 3-6 Temperatures at which CO conversion reaches 50% (T_{50}) and 100% (T_{100}) for Pd, Fe$_3$O$_4$, Co$_3$O$_4$ and Ni(OH)$_2$ nanoparticles as well as the supported catalysts Pd/Fe$_3$O$_4$, Pd/Co$_3$O$_4$ Pd/Ni(OH)$_2$.

Wt % Pd/Fe$_3$O$_4$	$T_{50\%}$ (℃)	$T_{100\%}$ (℃)
5	200	204
20	153	157
40	125	130
50	116	127
Wt % Pd/Co$_3$O$_4$	**$T_{50\%}$ (℃)**	**$T_{100\%}$ (℃)**
10	127	164
20	105	151
30	113	127
Wt % Pd /Ni(OH)$_2$	**$T_{50\%}$ (℃)**	**$T_{100\%}$ (℃)**
30	181	188
50	162	168
70	174	184
Pd nanoparticles	150	179
Fe$_3$O$_4$ nanoparticles	264	273
Co$_3$O$_4$ nanoparticles	117	140
Ni(OH)$_2$ nanoparticles	213	244

Also, it is obvious from **Figures 3-10a and 3-10b** that palladium supported on cobalt oxide is more efficient as a catalyst in CO oxidation catalytic activity than palladium supported on iron oxide as it reduced the ratio of palladium to 30 wt % with cobalt instead of 50 wt % with iron with nearly the same catalytic performance. While as shown in **Figures 3-10c and 3-10d**, it is obvious that using a mixture of iron and cobalt oxides as a support for palladium didn't make any enhancement for the catalytic activity for the catalyst. While the ratio of (1:1) of iron to cobalt was better than the ratios of (1:3) and (3:1) respectively but it still less active than or nearly the same like (30 wt % Pd/Fe$_3$O$_4$). But the catalyst (30 wt % Pd/Co$_3$O$_4$) still our best conditions as shown in figure 10b. While the ratio of (15:70) of iron to cobalt was better than the ratios of (40:20) and (45:10) respectively but it still less active than (30 wt % Pd/Fe$_3$O$_4$). But the catalyst (30 wt % Pd/Co$_3$O$_4$) still our best conditions as shown in **Table 3-6**.

65
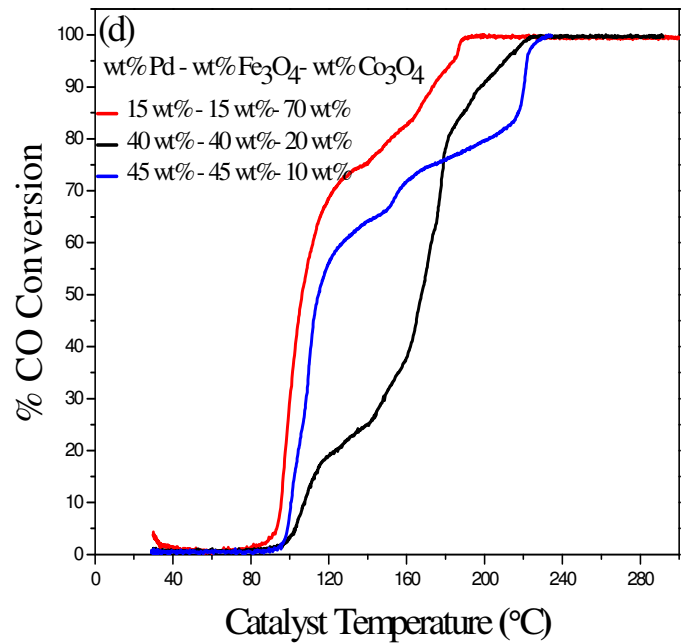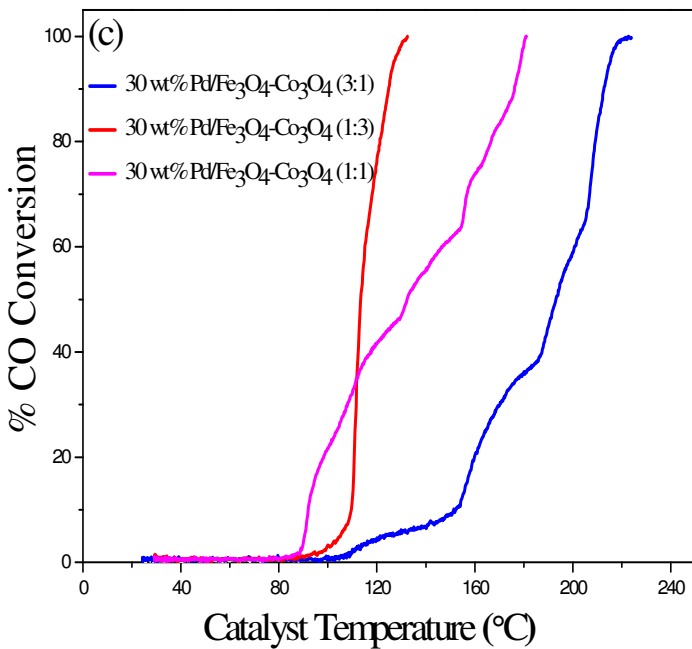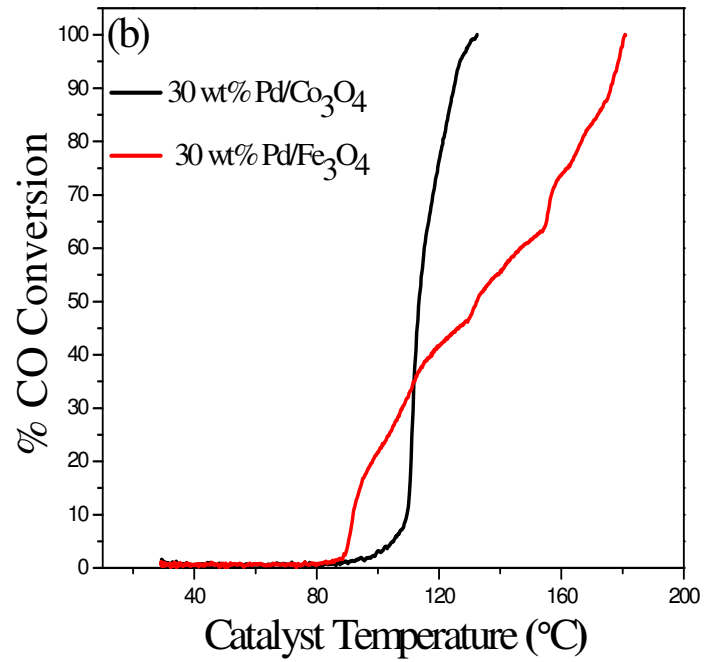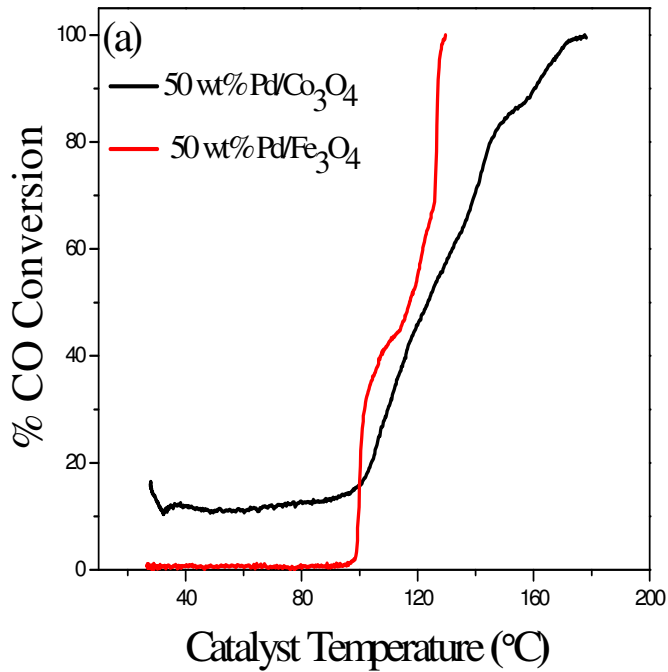
Figure 3-10 CO – catalytic conversion of (a) 50 wt % Palladium supported on Iron and Cobalt oxide, (b) 30 wt % Palladium supported on Iron and Cobalt oxide, (c), and (d) Palladium supported on different ratios of Iron and Cobalt oxide.

66

Table 3-7 Temperature at which complete conversion of CO is recorded"

Catalyst	$T_{100\%}$ ($^\circ$C)
30 wt % Pd/Fe₃O₄	179
30 wt % Pd/Co₃O₄	**127**
(Pd:Fe₃O₄:Co₃O₄) - (15:15:70)	182
(Pd:Fe₃O₄:Co₃O₄) - (40:40:20)	209
(Pd:Fe₃O₄:Co₃O₄) - (45:45:10)	221
30 wt % Pd – Fe₃O₄: Co₃O₄ (3:1)	215
30 wt % Pd – Fe₃O₄: Co₃O₄ (1:3)	187
30 wt % Pd – Fe₃O₄: Co₃O₄ (1:1)	180

From **Table 3-7**, it is obvious that annealing attempts in H_2 at 400 $^\circ$C for 3 hrs, which was done to enhance the catalytic activity didn't make any improvements in the catalyst.

Table 3-8 Temperature at which complete conversion of CO is recorded"

Catalyst	$T_{100\%}$ ($^\circ$C)
30 wt % Pd/Co₃O₄	127 $^\circ$C
30 wt % Pd/Co₃O₄ (annealed)	186 $^\circ$C
50 wt % Pd/Fe₃O₄	127 $^\circ$C
50 wt % Pd/Fe₃O₄ (annealed)	224 $^\circ$C

It is also obvious from **Figure 3-11** that adding graphite oxide as a support to both palladium-iron and palladium – cobalt systems not only didn't enhance the catalytic performance but also made it worse than the case when catalyst was used without using graphite oxide. The complete conversion of carbon monoxide to carbon dioxide happens at 235 $^\circ$C compared to 127 $^\circ$C and 281 $^\circ$C compared to 127 $^\circ$C in case of (50 wt % Pd/Fe₃O₄) and (30 wt % Pd/Co₃O₄) respectively as shown in **Table 3-8**.

67

Table 3-9 Temperature at which complete conversion of CO is recorded"

Catalyst	$T_{100\%}$ ($^\circ$C)
50 wt % Pd/Fe$_3$O$_4$	127
30 wt % Pd/Co$_3$O$_4$	127
20 wt % (50 wt %Pd/Fe$_3$O$_4$)/GO	235
20 wt % (30 wt %Pd/Co$_3$O$_4$)/GO	281
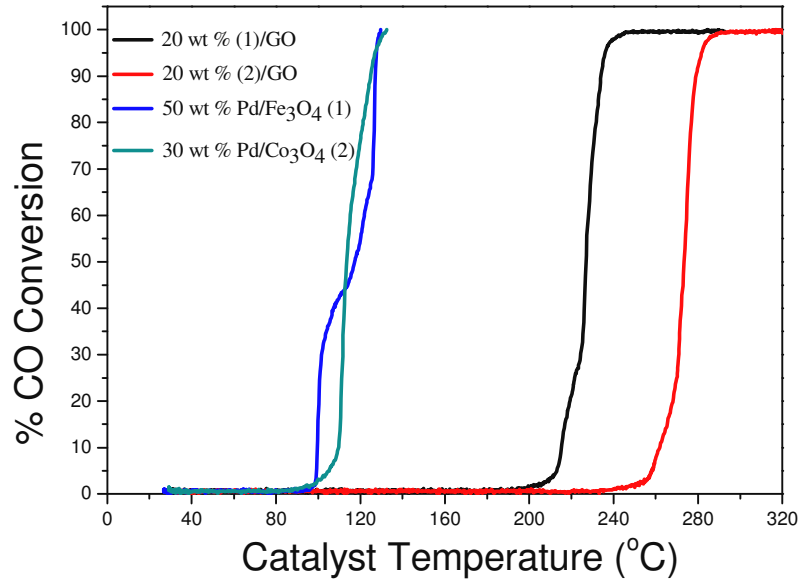
Figure 3-11 Catalytic Oxidation of Carbon monoxide of Palladium-Iron and Palladium - Cobalt supported on GO

Hence, it is obvious that palladium supported on cobalt is more efficient as a catalyst in CO oxidation catalytic activity than palladium supported on iron as it reduced the ratio of palladium to 30 wt % with cobalt instead of 50 wt % with iron with nearly the same catalytic performance.

3.4.4 Characterization of Fe₃O₄ Hexagonal Nanoplates

TEM micrographs images of magnetite hexagonal nanoplates both free-standing and supported on graphene sheets are shown in **Figure 3-13** shows the Fe2p XPS spectrum corresponding to as-synthesized magnetite nanoplates prepared by HH reduction of iron nitrate by MWI. The spectrum is featured with two peaks at binding energies of 710 and 724.5 eV corresponding to Fe2p$^{(3/2)}$ and Fe2p$^{(1/2)}$, By adjusting the MWI time we produced Fe₃O₄ nanocrystals with nanoplate morphology with and without graphene and using different precursors. A similar trend was also observed when Pd was introduced to the mixture.

Figure 3-12 shows TEM image of Pd/Fe₃O₄ free-standing (**Figs. 3-12 a, 3-12b**) and supported on graphene (**Figs. 3-12c**). **Figure 3-15** shows the XRD patterns of as-synthesized magnetite nanoplates in different compositions with Pd and graphene. The XRD reflections can be indexed to the inverse cubic spinel structure of Fe₃O₄.
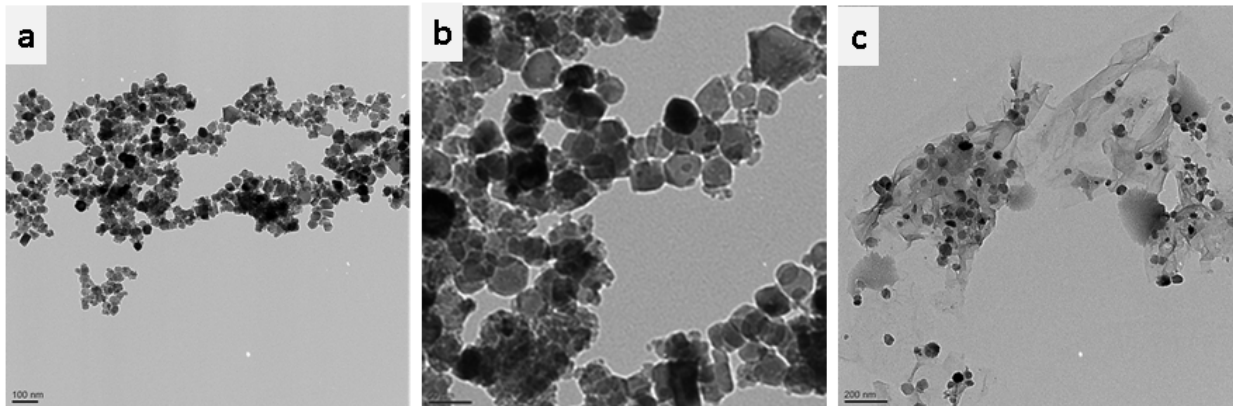
Figure 3-12. TEM image of Fe₃O₄ hexagonal nanoplates free-standing (a,b) and supported on graphene sheets (c) prepared from iron nitrate by hydrazine hydrate reduction and MWI.
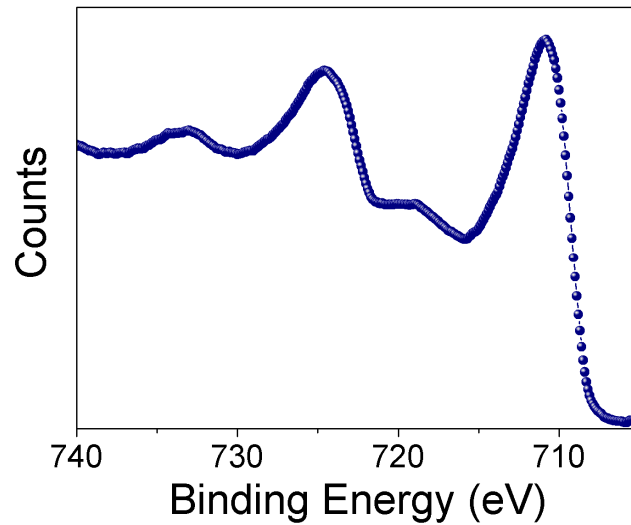
Figure 3-13 High-resolution Fe$_{2p}$ XPS spectrum of Fe$_3$O$_4$ prepared by MWI using hydrazine hydrate showing peaks due to Fe III at 710 and 724.5 eV and the other two peaks at 719 and 733.5 eV.
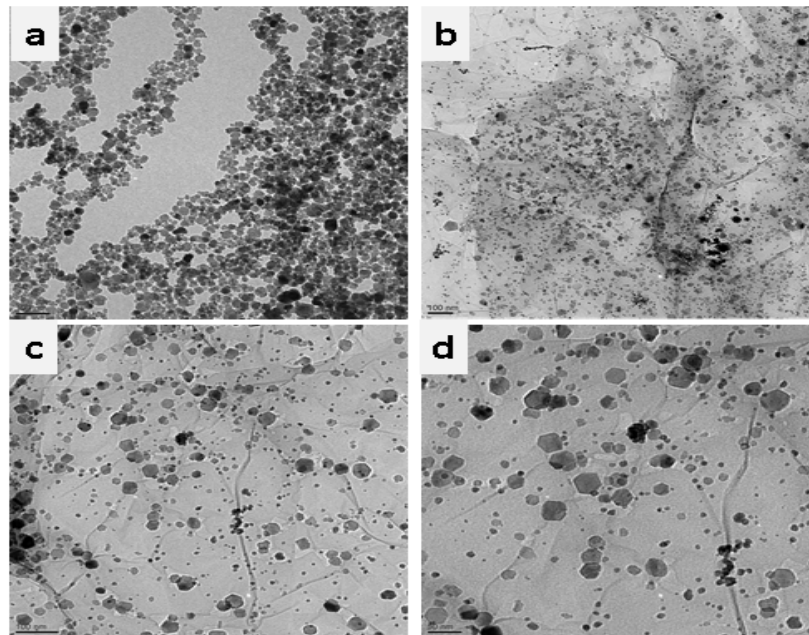
Figure 3-14. TEM image of Pd/Fe$_3$O$_4$ hexagonal nanoplates both free-standing (a) and supported on graphene sheets (b-d) prepared by hydrazine hydrate reduction and MWI.
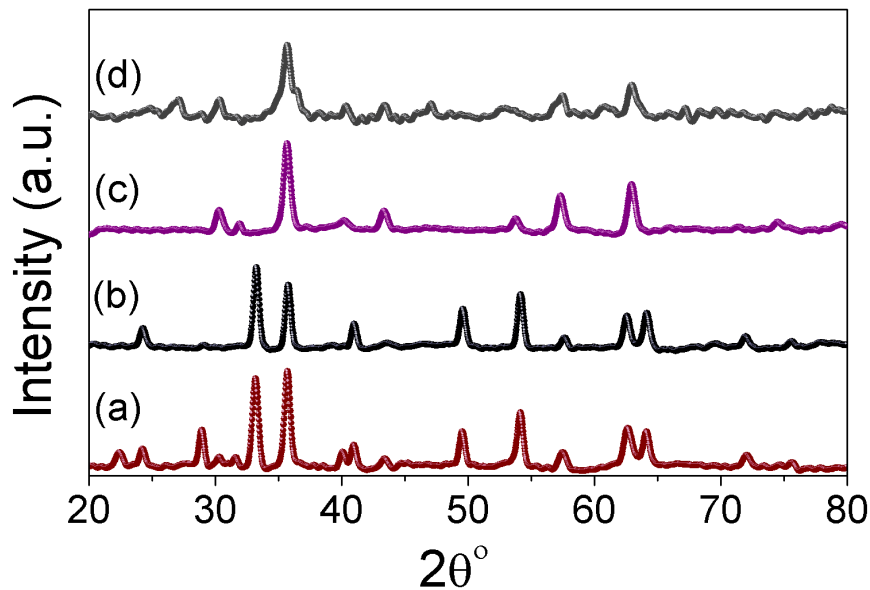
Figure 3-15. XRD patterns of (a) Fe$_3$O$_4$, (b) Fe$_3$O$_4$/graphene (c) Pd/Fe$_3$O$_4$, and (d) Pd/Fe$_3$O$_4$/graphene prepared from iron nitrate by hydrazine hydrate reduction and MWI.

As can be seen from TEM, XPS and XRD studies, by MWI of iron nitrate in presence of hydrazine hydrate, Fe$_3$O$_4$ forms hexagonal nanoplates similar to that formed by MWI of iron acetylacetonate in presence of oleic acid/oleylamine mixture as described in the PhD dissertation prepared by A. Zedan. However, magnetite hexagons prepared from nitrate source are smaller in size compared to those prepared from acetylacetonate by MWI for 20 min as described in the dissertation which could be due to the short microwave irradiation time. These results along with results from similar work from our group confirm that morphology of growing magnetite nanocrystals can be tailored by adjusting the reaction temperature or MWI time and precursors molar ratios. The method can be also extended to synthesize a wide range of functional oxide nanostructures of controlled size and shape. To further demonstrate the chemical structure and provide an indirect evidence of the magnetite phase of the formed hexagonal nanoplates, some results described in the dissertation prepared by A. Zedan (VCU, 2013) are reproduced for the purpose of supporting our work.

71

In their work, Zedan et al. prepared various shaped- and sized- Fe_3O_4 nanocrystals individually and anchored to graphene by MWI of Fe (acac)$_3$ precursors in benzyl ether and a mixture of oleylamine and oleic acid, as summarized in **Table 3-9**. The MWI delivers a great amount of heat that accelerate the decomposition of Fe (acac)$_3$ precursors leading to the burst of nucleation and further growth. When supersaturation is reached in reaction medium, the Fe-O species start to cluster in the reaction medium of benzyl ether to give numerous nuclei. The aggregation of these numerous nuclei above the saturation threshold leads to sintering resulting in formation of primary Fe_3O_4 nanocrystals. The primary formed Fe_3O_4 nanocrystals are then further grown by diffusion and stacking the respective atomic species derived from the partial reduction and decomposition of Fe (oleate)$_3$ in presence of oleylamine-oleic acid mixture onto the primary nanocrystals.

Table 3-10. Summary of different Fe_3O_4 morphologies with corresponding experimental parameters

Fe_3O_4 Shape	OAm (mmol)	OAc (mmol)
Tiny spheres	3.2	0
Tiny spheres	0	4.2
Spheres (small)	4.2	5.6
Spheres (large)	4.2	11.2
Cubes	4.2	2.8
Triangles	2.1	2.8
Spheres/RGO	4.2	5.6
Spheres/RGO	4.2	5.6
Cubes/RGO	4.2	2.8
Triangles/RGO	2.1	2.8
Hexgonal Plates	4.2	5.6
Hexagons/Graphene	4.2	5.6

As shown in **Fig. 3-16**, Fe_3O_4 nanoparticles prepared by MWI of Fe(acac)$_3$ in benzylether and using 3.2 mmol or 4.2 mmol of oleylamine or oleic acid, respectively, are spherical in shape.
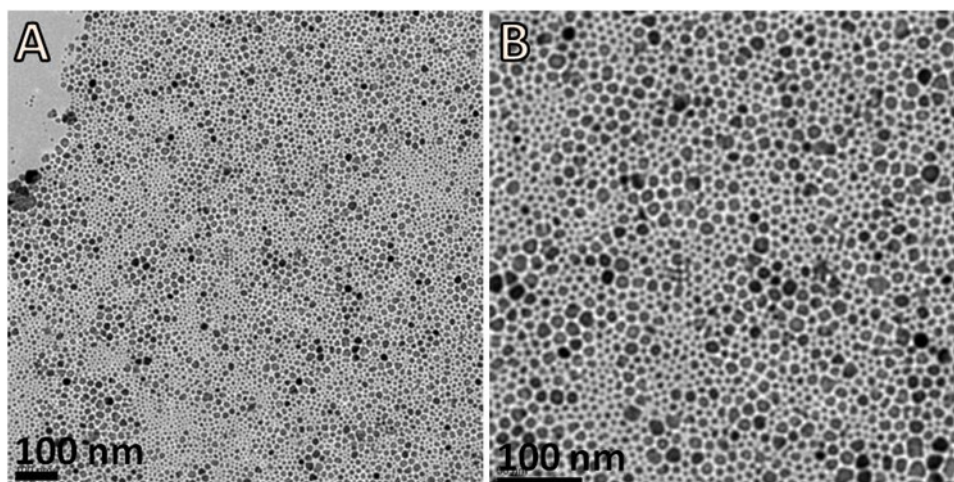
Figure 3-16 TEM images of spherical Fe₃O₄ nanocrystals prepared by MWI of Fe(acac)3 in benzyl ether for 20 min.
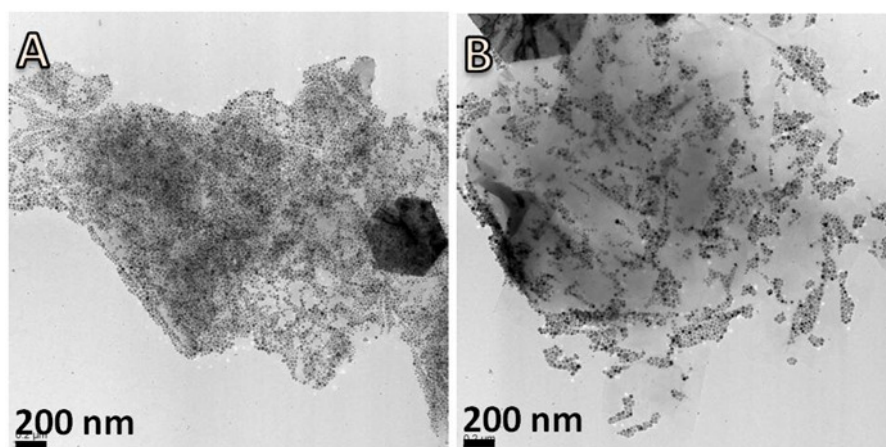
Figure 3-17 TEM images of spherical Fe₃O₄/RGO nanocomposite structures prepared by MWI of Fe(acac)₃ in benzyl ether for 20 min using 4.2 mmol OAm and 5.6 mmol OAc and in presence of GO/DMSO.

When the growth conditions of growing spherical Fe₃O₄ (4.2 mmol OAm/5.6 mmol OAc) were altered by introducing GO suspension in DMSO, large single crystal of Fe₃O₄ hexagonal nanoplates were successfully prepared. Some of these hexagonal nanoplates formed along with the spherical Fe₃O₄ in presence of RGO are shown in TEM images displayed in **Fig. 3-17**. Low-resolution SEM images of Fe₃O₄ hexagonal nanoplates are shown in **Fig. 3-18.**
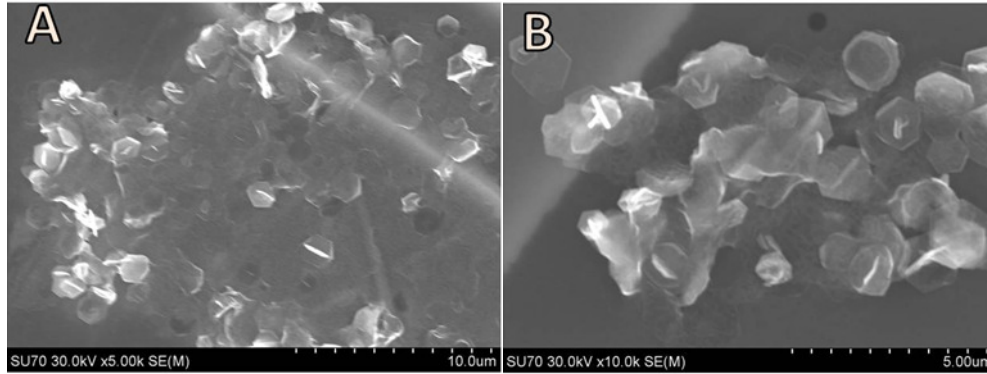
Figure 3-18 Low-resolution SEM images of Fe₃O₄ hexagonal nanoplates wrapped in RGO sheets and prepared from acetylacetonate.

It can be hypothesized that the prolonged microwave irradiation of reaction mixture leads first to thermal decomposition of iron precursors in benzyl ether that serve as a high-boiling point solvent.

When the supersatuartion is reached this triggers the formation of Fe₃O₄ nuclei followed by the subsequent growth of these nuclei to primary nanoparticles. On the basis of the TEM results combined with the experimental conditions, thermodynamic and kinetic factors could lead to shape evolution at different stages of the microwave irradiation process.

The adsorption of surfactants to different extents under different conditions combined with altering the molar ratio between the two surfactants could play a crucial role in selective passivation of different crystal planes and hence different growth rates at those faces.[201]

This could stabilize the [14] facets of growing Fe₃O₄ nanocrystals and thus led to termination or slower relative growth rate.

74

3.5 Conclusions

In conclusion, a simple, versatile, and rapid method has been developed for the synthesis of Pd nanoparticle catalysts supported on Fe_3O_4, Co_3O_4 and $Ni(OH)_2$ nanoplates via microwave irradiation. The important advantage of microwave dielectric heating over convective heating is that the reactants can be added at room temperature (or slightly higher temperatures) without the need for high-temperature injection. Furthermore, the same method can be used to synthesize bimetallic nanoalloys supported on metal oxide nanoparticles as nanocatalysts for CO oxidation. The current results reveal that the $Pd/Co3O4$ catalyst has particularly high activity for CO oxidation as a result of the strong interaction between the Pd nanoparticles and the $Co3O4$ nanoplates. Optimizations of the size, composition, and shape of these catalysts could provide a new family of efficient nanocatalysts for the low temperature oxidation of CO. We are currently exploring the effects of MW frequency, duration, and solvent polarity on the morphology, particle size, and shape of the supported metal nanoparticle catalysts.

CHAPTER 4   Microwave-Assisted Synthesis of Pd-Fe$_3$O$_4$ Nanoparticles under flow reaction conditions; an Efficient Highly Magnetic Catalyst for CO Oxidation Catalysis

4.1   Overview

We have developed a facile microwave assisted reduction technique to prepare highly active Pd/Fe$_3$O$_4$ nanoparticles (Pd/Fe$_3$O$_4$) for CO oxidation catalysis. The method involves simultaneous reduction of the corresponding Pd(NO$_3$)$_2$ and Fe(NO$_3$)$_3$.9H$_2$O under the microwave irradiation conditions using Wave Craft's microwave flow reactor called ArrheniusOne. Hydrazine hydrate was used as the reducing agent under flow reaction conditions. The Pd/Fe$_3$O$_4$ nanoparticles have shown to exhibit extremely high catalytic activity for CO oxidation catalysis. The remarkable catalytic activity of these materials can be attributed to the high degree of dispersion and concentration ratio of the Pd nanoparticles deposited on the surface of magnetite (Fe$_3$O$_4$) with a small particle size in all prepared catalysts ranging from 5-10 nm due to the effective microwave assisted reduction method. These nanoparticles are further characterized by variety of spectroscopic techniques including X-ray photoelectron spectroscopy (XPS), X-ray diffraction (XRD), and transmission electron microscopy (TEM). The catalysis data revealed that palladium supported on iron oxide catalysts showed remarkable high catalytic activity towards CO-oxidation.

4.2 Introduction

The metal oxide nano catalysts are of great importance in improving the thermal-catalytic decomposition performance.[43, 103, 114] The advanced and unique magnetic, electronic, and catalytic properties of the materials in the nano scale attracted research centers to investigate this area of science deeply.[4, 44, 62-65] The catalytic effect of magnetic nanoparticles was an important area of research due to its huge industrial applications.[70-72]

Compared to conventional methods used in synthesis of metal nanoparticles, MW-assisted synthesis represents a unique approach that could be used for the synthesis of a variety of nanomaterials including metals, semiconductors, bimetallic alloys, and metal oxides with controlled shape and size without using high temperature or high pressure reaction conditions. In case of using MW, the heating process is performed by the interaction of the permanent dipole moment of the molecule with the high frequency electromagnetic radiation. Oxidation catalysis usually requires the use of transition metals such as gold, palladium, ruthenium, platinum, iridium, and rhodium.[32-33] All oxidation catalysts work the same way to transform carbon monoxide into carbon dioxide, thus reducing or eliminating the potential risk of CO inhalation.[34-38] Bimetallic nanoalloys for CO oxidation and Nanoporous magnetic iron oxide microspheres have been successfully synthesized by the way of microwave heating.[39-42] Microreactor technology has the capacity to transform current batch nanoproduction practices into continuous processes with rapid, uniform mixing and precise temperature control.[202] Furthermore, nanoparticles with smaller mean particle size and narrow particle size distribution had been developed with continuous flow micro reactors compared to bulk batch reactors.[203]

Continous flow microreactors has many advantages, such as easy control, high temperature adaptability, high yield, and simple operation. But it has also some disadvantages like wide size distribution as a result of poor mixing, contamination due to contact with channel walls, and clogging.

4.3   Experimental

4.3.1   Chemicals and reagents

All chemicals used in our experiments were purchased and used as received without further purifications. Palladium nitrate (10 wt. % in 10 wt. % HNO_3, 99.999%) and hydrazine hydrate (80%, Hydrazine 51%) were obtained from Sigma Aldrich. Deionized water (D.I. H_2O, ~ 18 MΩ) was used for all experiments. High-purity graphite powder (99.9999%, 200 mesh) was purchased from Alfa Aesar.

A JEOL JEM-1230 electron microscope operated at 120 kV has been used to obtain TEM images. The electron microscope is equipped with a Gatan UltraScan 4000SP 4K X 4K CCD camera. TEM samples were prepared by placing a droplet of the prepared catalyst dissolved in ethanol on a 300-mesh copper grid (Ted Pella) and then left to evaporate in air at room temperature. The X-ray photoelectron spectroscopy (XPS) analysis was executed on a Thermo Fisher Scientific ESCALAB 250 using a monochromatic Al KR X-ray. The samples were perfectly fastened on an indium foil that was previously fixed on the carbon tape which in turn was completely attached to the sample holder by a double face.

The X-ray diffraction patterns were measured at room temperature using X'Pert PRO PANanalytical X-ray diffraction unit, with CuKα. For the CO Catalytic oxidation; tests were carried out in a continuous fixed-bed quartz-tube reactor Type F21100 Tube Furnace under ambient pressure.

78

4.3.2 Synthesis of Pd-Fe$_3$O$_4$ under Batch Reaction Conditions

Fe (NO$_3$)$_3$.9H$_2$O (90 mg, 0.223 mmol) was dissolved in deionized water (50 ml) and sonicated for 1 h. then, Palladium nitrate (10 wt. % in 10 wt. % HNO$_3$, 99.999%, 200 µl) was added to the iron nitrate solution. Then, the whole mixture was stirred for 3 h followed by the addition of the reducing agent hydrazine hydrate (1 ml) at room temperature and once the solution was heated by microwave for (90) s under batch reaction conditions, the color changed to dark black color, indicating the completion of the chemical reduction. Then, the final product washed using hot deionized water 2-3 times, ethanol 2-3 times, and then dries in oven at 80˚C.

4.3.3 Synthesis of Pd-Fe$_3$O$_4$ under Flow Reaction Conditions

Different catalysts were prepared but using different method from the one used under batch reaction conditions.

In this method, the catalysts were prepared under flow reaction conditions using Wave Craft's microwave flow reactor called ArrheniusOne as shown in **Figure 4-1**. This technique was used to prepare the Pd/Fe$_3$O$_4$ catalyst in large amounts compared with small amounts that was prepared under batch reaction conditions and also to produce a catalyst with the same specifications each time of preparation to avoid problems of inconsistent performance and specifications of catalysts that were prepared under batch reaction conditions.

The ArrheniusOneTM unit is controlled and operated by the WaveCraft Control Application (WCA) software program.

79
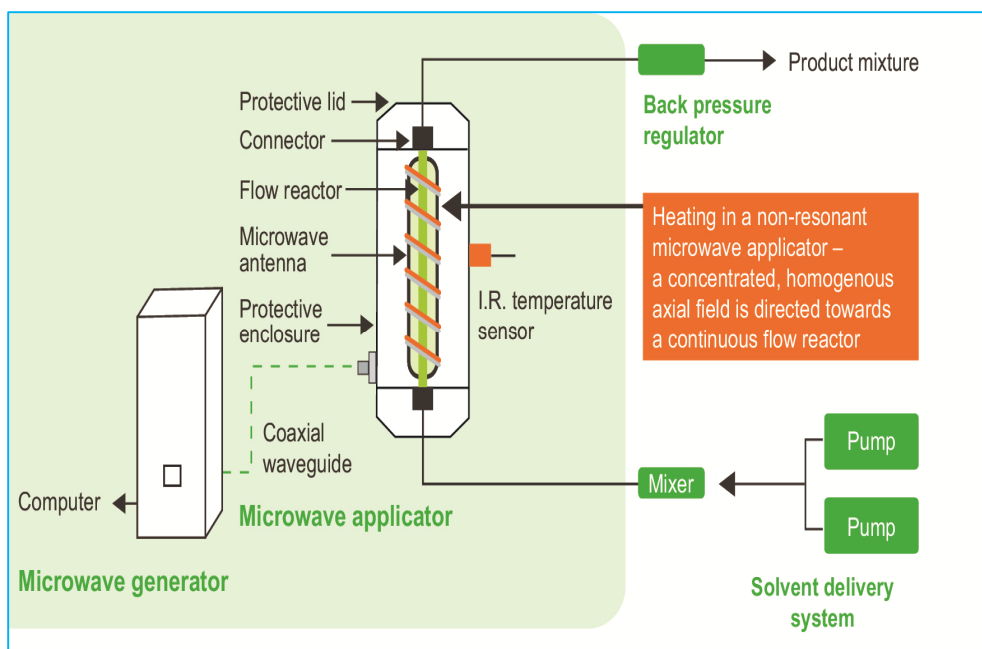
Figure 4-1 WaveCraft's ArrheniusOne Microwave Flow Reactor

The apparatus consists of a microwave generator and a microwave applicator that transfers the generated energy to the reaction mixture. A consumable tubular borosilicate reactor vessel, available in different dimensions from 160 µL to 6 mL, is housed inside the applicator through which the reaction mixture passes. The generator output of 0-150 W is linked with IR sensor positioned along the reactor vessel while the microwave frequency is automatically adjusted at 2.4-2.5 GHz. Five different catalysts were prepared under different reaction conditions to investigate the optimum preparation method as in **Tables 4-1, 4-2, and 4-3**.

Table 4-1 Different Catalysts of Pd-Fe$_3$O$_4$ prepared at 80 ˚C under flow reaction conditions

Catalyst	1	2	3	4
Temperature (˚C)	80	80	80	80
Flow Rate of (Pd Nitrate - Fe Nitrate) (ml/min.)	0.5	1	0.5	1
Flow Rate of Hydrazine Hydrate (ml/min.)	0.5	0.5	1	1
(Pd Nitrate - Fe Nitrate) : Hydrazine Hydrate	0.5 : 0.5	1 : 0.5	0.5 : 1	1 : 1
T$_{100\%}$ (˚C)	254	200	190	168

80

Table 4-2 Different Catalysts of Pd-Fe₃O₄ prepared at 150 ˚C under flow reaction conditions

Catalyst	6	7	8	9
Temperature (˚C)	150	150	150	150
Flow Rate of (Pd Nitrate - Fe Nitrate) (ml/min.)	0.5	1	0.5	1
Flow Rate of Hydrazine Hydrate (ml/min.)	0.5	0.5	1	1
(Pd Nitrate - Fe Nitrate) : Hydrazine Hydrate	0.5 : 0.5	1 : 0.5	0.5 : 1	1 : 1
$T_{100\%}$ (˚C)	210	177	160	137

Table 4-3 Different Selected Catalysts of Pd-Fe₃O₄ prepared under batch and flow reaction conditions

Catalyst	4	5	9	10
Temperature (˚C)	80	120	150	100
Flow Rate of (Pd Nitrate - Fe Nitrate) (ml/min.)	1	1	1	Batch Reaction Conditions
Flow Rate of Hydrazine Hydrate (ml/min.)	1	1	1	
(Pd Nitrate - Fe Nitrate) : Hydrazine Hydrate	1 : 1	1 : 1	1 : 1	--
Pd (0) %	61	69	72	81.6
Pd (II) %	39	31	28	18.4
$T_{100\%}$ (˚C)	168	150	137	128

In the axial field applicator the microwave field is generated in a coil surrounding the flow reactor as shown in Figure 4-2a, 4-2b, allowing the microwave field to be concentrated axially inside the coil. The coil is automatically tuned to maximize the heating in the reactor tube by changing the frequency. Figure 4-2c shows that reactors of different sizes can be used by changing the length and diameter of the coil in the applicator, allowing the optimization of reaction conditions such as residence time and flow capacity. The physical shape of the antenna determines the homogeneity of the microwave field. The reactor consists of a straight tube, made of microwave-transparent borosilicate glass.

As shown in Figure 4-2d, after running a synthesis the reactor will have residual pressure due to the back pressure regulator. It is necessary to vent this pressure before disassembling the reactor. To vent the over-pressure carefully remove the tubing at the inlet of the back pressure regulator using suitable tools.
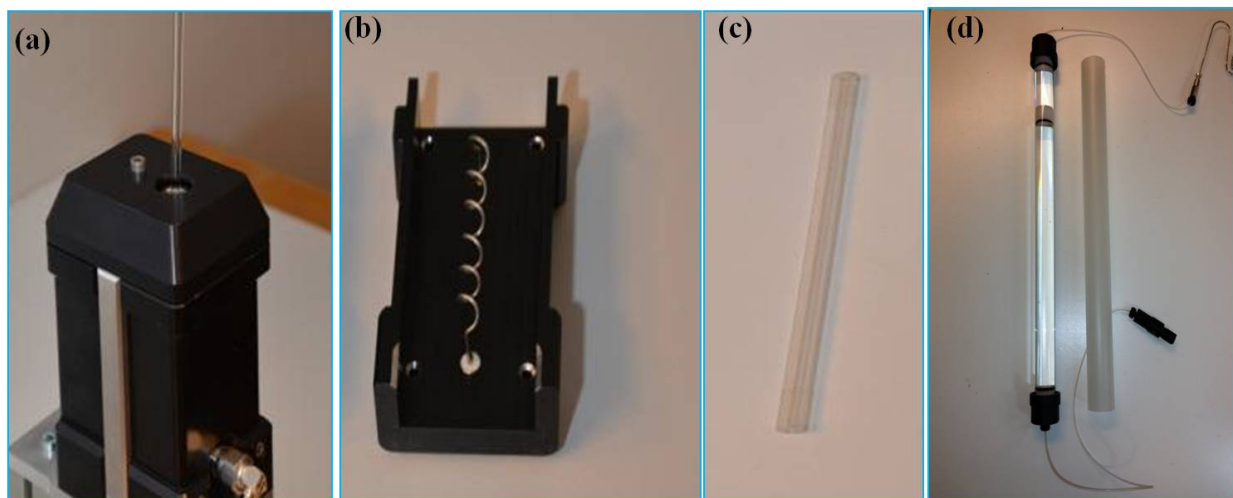
Figure 4-2 (a) Microwave Applicator, (b) Antenna Casing, (c) 3 mm borosilicate glass reactor (d) Tube used for collecting the catalyst connected to a back pressure regulator

In all catalysts prepared, a solution of Fe $(NO_3)_3.9H_2O$ (90 mg, 0.223 mmol) was dissolved in deionized water (50 ml) and sonicated for 1 h. Palladium nitrate (10 wt. % in 10 wt. % HNO_3, 99.999%, 200 µl) was added to the iron nitrate solution.

Then, the whole mixture was stirred for 3 h. Similarly, another solution of Hydrazine Hydrate was mixed with deionized water to be used as a reducing solution for palladium nitrate – iron nitrate solution. Different ratios of (Hydrazine Hydrate - deionized water) were prepared to investigate the effect of reducing agent concentration. Ratios used were (1:0.5, 0.5:1, and 1:1), and reaction was performed under 80 ˚C, 120 ˚C and 150 ˚C.

82

The catalysts were prepared by injecting both (Hydrazine Hydrate - deionized water) solution and (palladium nitrate – iron nitrate) solution through using pumps to T-Mixer where they were mixed together before being introduced to the microwave applicator where the reaction takes place inside 3 mm reactor equipped from both sides with end sleeves made of Teflon material, for correct sealing of the fluidic system. It is remarkable to notice that the color changed to dark black color, indicating the completion of the chemical reduction. Then, the final product washed using hot deionized water 2-3 times, ethanol 2-3 times, and then dries in oven at 80˚C. Experiments for the CO catalytic oxidation were performed using a fixed bed-programmable flow tube furnace reactor (Thermolyne 2100) [39]. In a typical experiment, 20 mg of the test catalyst was dispersed in glass wool and placed inside a Pyrex glass tube.

The sample and furnace temperatures were measured by a thermocouple placed in contact with the catalyst bed and in the middle of the tube furnace, respectively. Signals from thermocouples were processed using an SC-2345 data acquisition board. To plot temperatures and other measurement parameters, a data acquisition software using Labview was utilized. A gas mixture consisting of 4 wt % CO and 20 wt % O_2 in balance helium was passed over the sample at a flow rate of 100 cm^3/min while the temperature was ramped. The flow rate was controlled by a set of MKS digital mass flow meters. The conversion of CO to CO_2 was monitored using an online infrared gas analyzer (ACS, Automated Custom Systems Inc.) to detect the exit gas, which is then vented to outlet. All the catalytic activities were measured after heat treatment of the catalyst at 110˚C in the reactant gas mixture for 15 min. in order to remove moisture and adsorbed impurities.

83

4.4 Results and Discussion
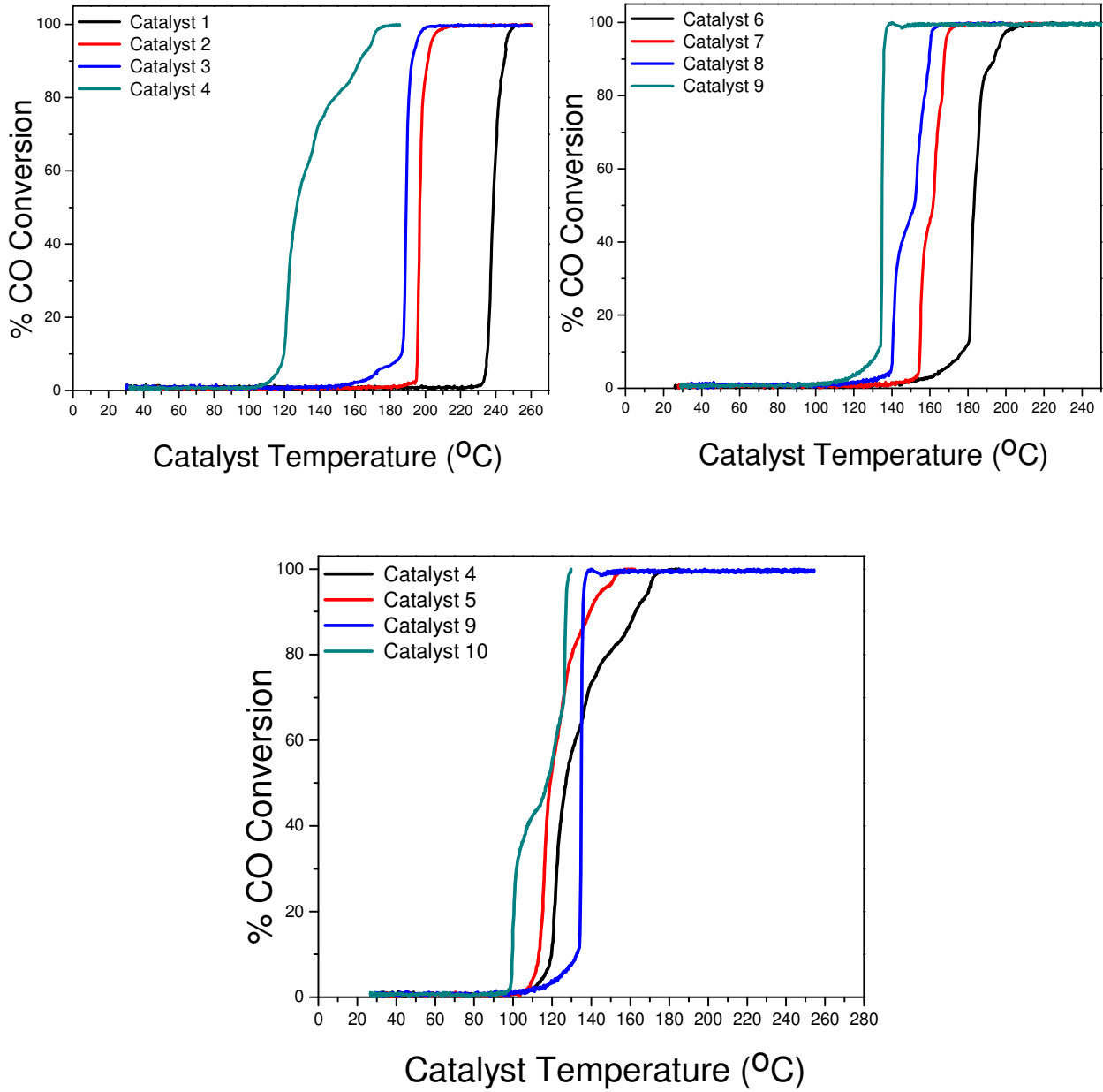
Figure 4-3 CO – Catalytic conversion of Palladium supported on magnetite (Fe₃O₄)

84
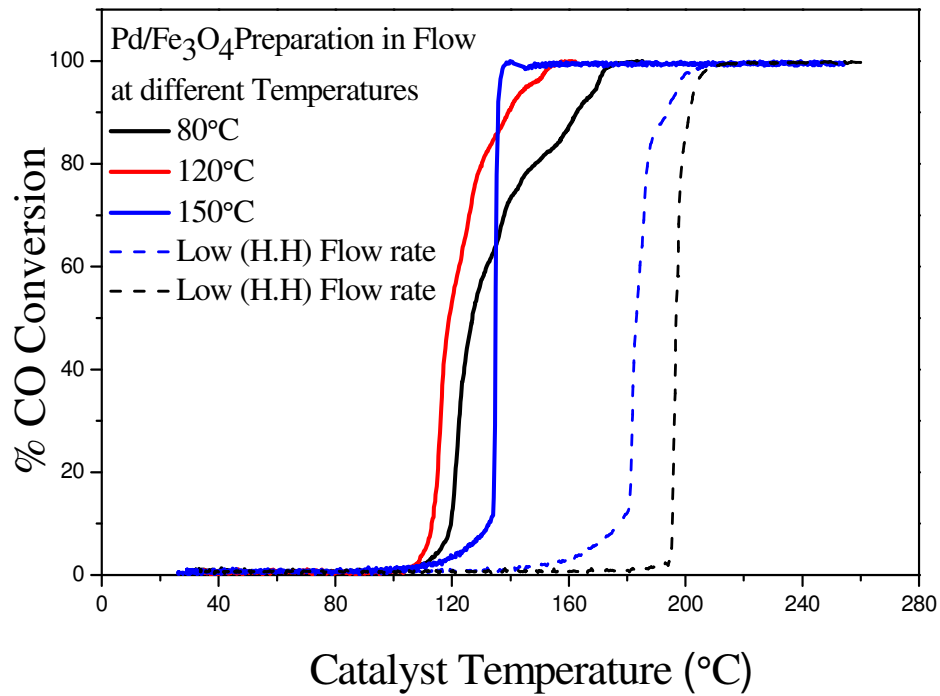
Figure 4-4 CO – Catalytic conversion of different catalysts of Pd/Fe$_3$O$_4$ catalysts 4, 5, 9 at 80, 120, 150℃ respectively

As shown in **Figure 4-3** and **Figure 4-4**, the catalytic activity of different prepared catalyst was evaluated towards CO oxidation catalysis. It was found that catalysts 4, 5, and 9 that were prepared under the same reaction conditions except temperature that was varied as 80, 120, and 150˚C respectively. Catalyst 9 was found to be the best catalyst for catalytic performance as the temperature at which CO was completely converted to CO$_2$ was 137˚C compared to 168˚C and 150˚C in case of catalyst 4 and 5 respectively. This high catalytic activity of catalyst 9 that was prepared under flow reaction conditions was very close to catalyst 10 that was prepared under batch reaction conditions. Characterization of the Pd supported on Fe$_3$O$_4$ samples prepared by MWI, method was examined in detail using XRD, XPS, and TEM analyses.

85
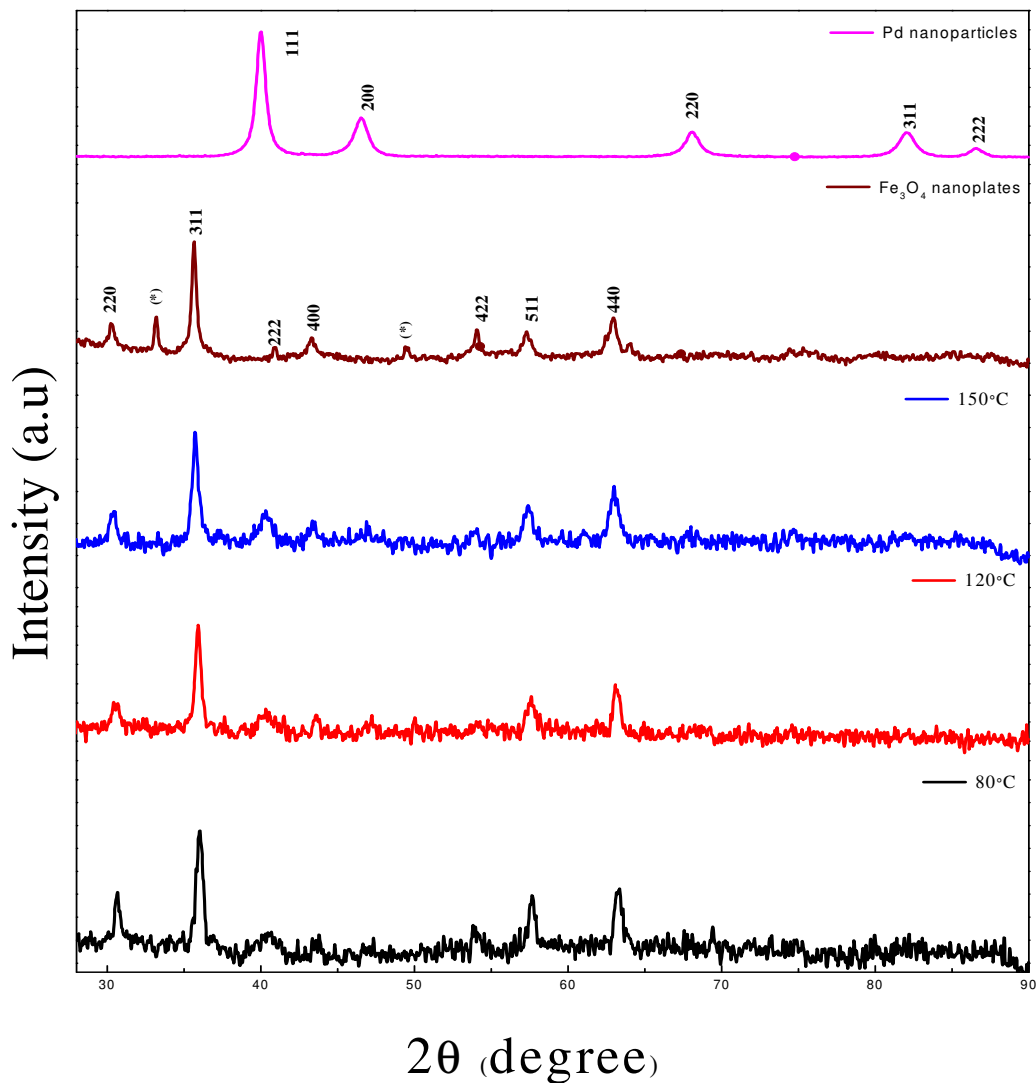
Figure 4-5 (a) XRD Pattern of Palladium-Fe$_3$O$_4$ Catalysts

Generally as shown in **Figure 4-5**, the XRD pattern clearly indicates that the product is enriched with Fe$_3$O$_4$ and Pd (0). The palladium shows the typical sharp diffraction peak at $2\theta = 40°$. The XRD patterns indicate that the products were all (Fe$_3$O$_4$) magnetite with reference code (ICCD-00-003-0863). It is also easily to notice that the sharp diffraction peak at $2\theta = 40°$ which is characteristic to palladium and also the characteristic peaks of Fe$_3$O$_4$ is shown as a sharp diffraction peak at $2\theta = 35°$.

86

The diffraction peaks (2θ) of Pd- Fe_3O_4 at 40, 46.8, and 68.2 are ascribed to the (111), (200), and (220) planed of Pd NPs which are similar to pure palladium and also to the peaks of Pd- Fe_3O_4 as shown. **Figure 4-6** and **Figure 4-7** display representative TEM images of the Pd-Fe_3O_4 catalysts that were prepared and tested for CO oxidation catalysis. The TEM images show the presence of uniform well-dispersed Pd nanoparticles on Fe_3O_4. However, the Pd nanoparticles supported on magnetite prepared under flow reaction conditions as in catalysts 1, 4, 5, 6, and 9 that were shown in (**Figure 4-6 a, b, c, d, e**) respectively appear to be smaller than those prepared under batch reaction conditions as in catalyst 10 (**Figure 4-6f**). From these TEM images, it was found that Catalyst 1, the particle size of Pd was (4-6 nm) while it was (10-12 nm) for magnetite as in **Figure 4-6a**. Catalyst 4, the particle size of Pd was (4-6 nm) while it was (11-13 nm) for magnetite as in **Figure 4-6b**. Catalyst 5, the particle size of Pd was (5-7 nm) while it was (12-14 nm) for magnetite as in **Figure 4-6c**.
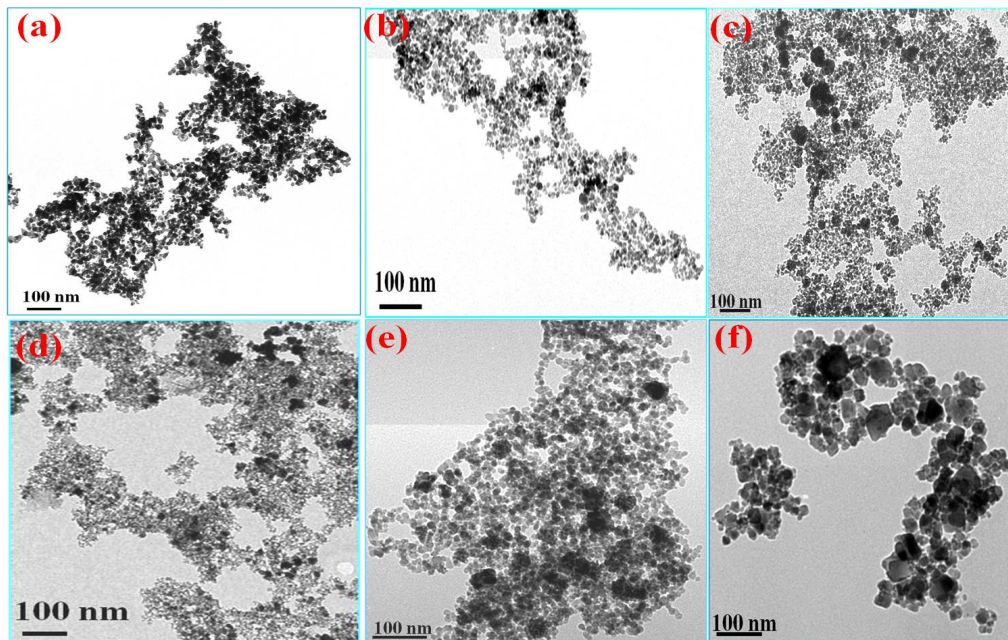
Figure 4-6 TEM – images of Different Selected Catalysts

Catalyst 6, the particle size of Pd was (6-8 nm) while it was (14-16 nm) for magnetite as in **Figure 4-6d**. Catalyst 9, the particle size of Pd was (7-9 nm) while it was (16-18 nm) for magnetite as in **Figure 4-6e**. Catalyst 10, the particle size of Pd was (12-14 nm) while it was (28-30 nm) for magnetite as in **Figure 4-6f**. Also, a mapping was done for one of these TEM images to confirm that Pd is supported on magnetite as it is obvious in **Figure 4-6a, b**.
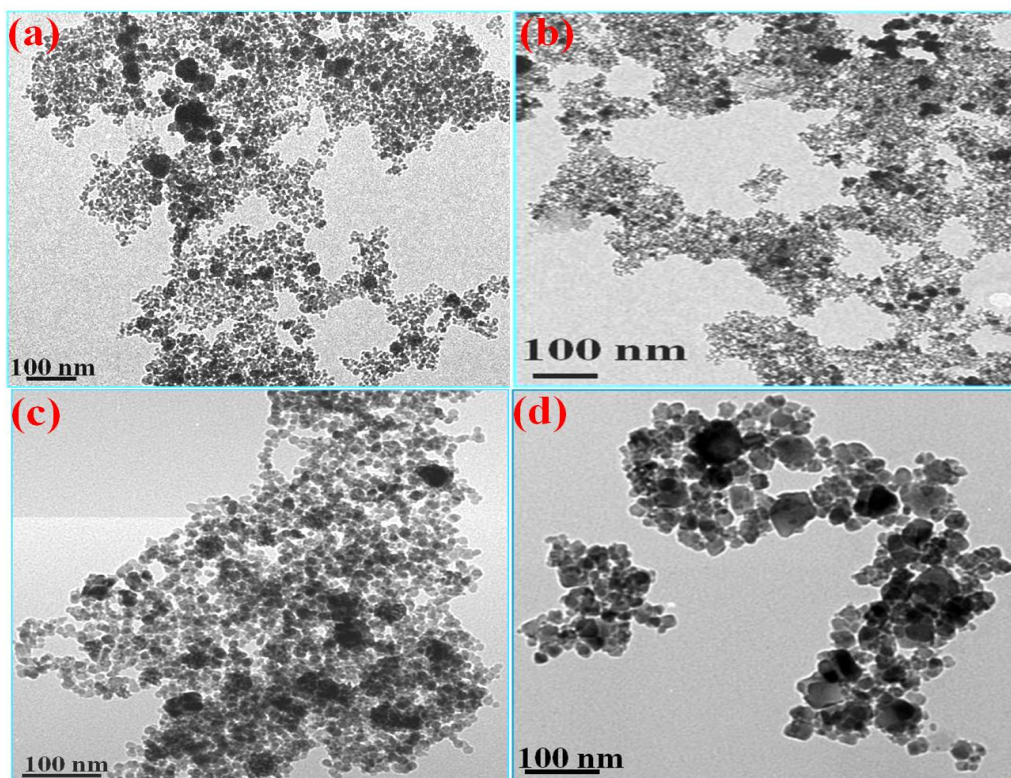
Figure 4-7 TEM – images of Different Catalysts, (a) Catalyst 4, (b) Catalyst 5, (c) Catalyst 9, (d) Catalyst10

Generally it is obvious that catalyst 9 is the best one in dispersion of Pd nanoparticles on the magnetite surface and also it has smaller particle size with respect to the catalyst that was prepared under batch reaction conditions (Catalyst 10) which is a very important and decisive factor in catalysis. This is very consistent with the catalytic activity data obtained from experimental testing of these catalysts as previously mentioned in **Table 4-3**.
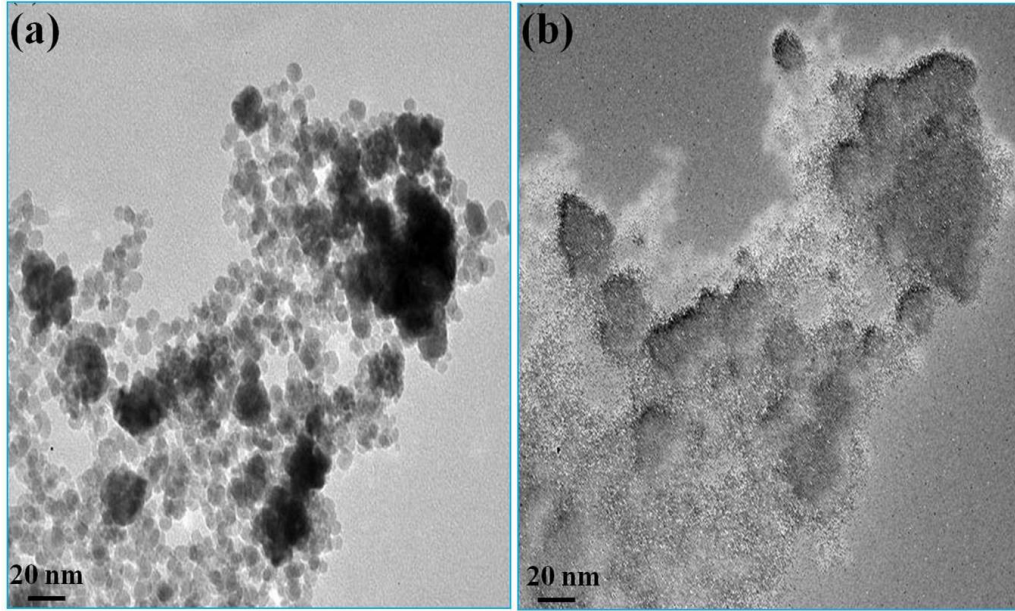
Figure 4-8 TEM – images of Iron Mapping (a) Original Image, (b) Iron Only "white sections"

Samples showed that the binding energy (the energy difference between the initial and final states of the photoemission process) of Fe 2P 3/2 was 710.5 eV, indicating that the Fe was present as Fe_3O_4 and also the binding energy of Fe 2P 1/2 was 723.7 eV indicating that Fe was present in the oxidation state of Fe_3O_4 as shown in **Figure 4-9a**. It is so important to note that in case of all catalysts as shown in **Figure 4-9b**, some of Pd is in form of PdO or (Pd^{+2}) but some of Pd is in the form of Pd^0. Also; the binding energy of Pd 3d5/2 was 334.8, 335.14 eV, and Pd 3d3/2 was 340.1, 340.57 eV corresponding to Pd^0. Similarly; the binding energy of Pd 3d3/2 was 341.38, 343.2 eV, and Pd 3d5/2 was 336.23, 337.85 eV corresponding to Pd (II).
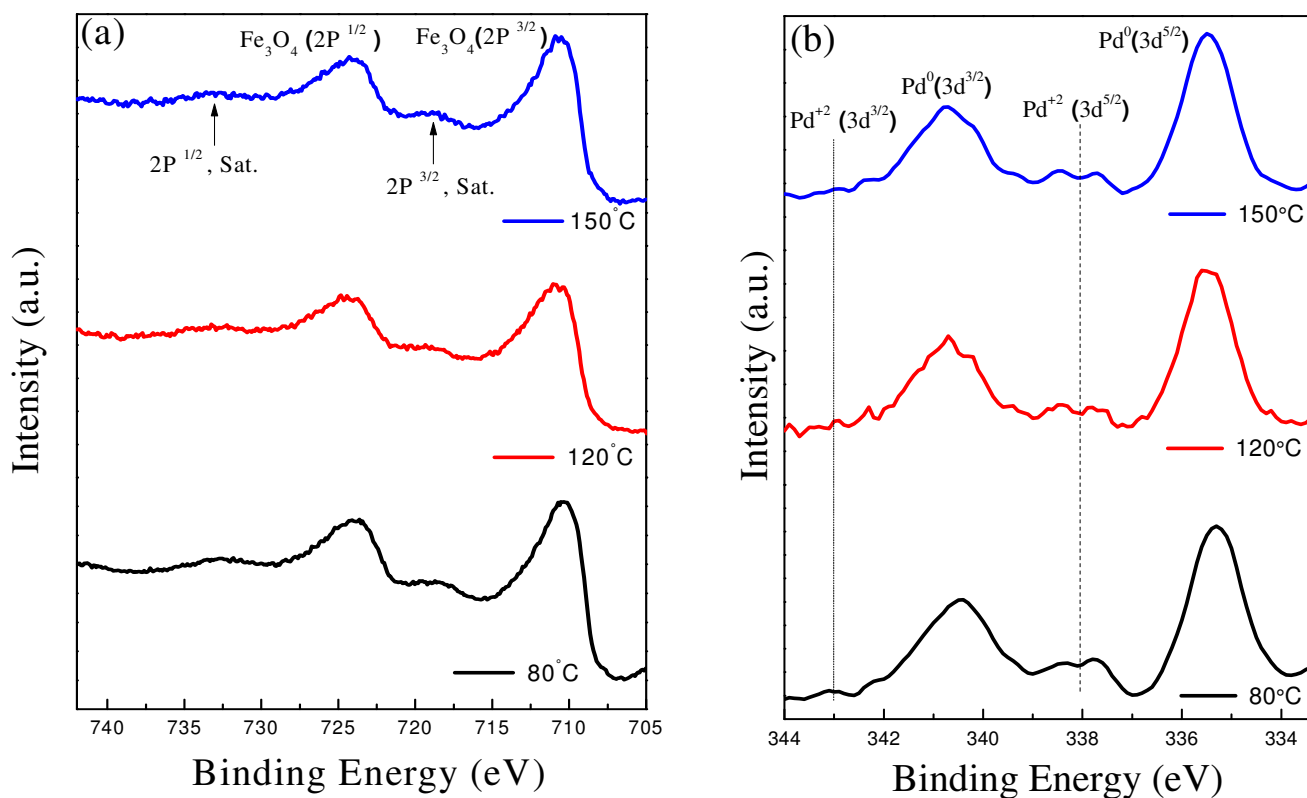
Figure 4-9 **(a) XPS-Fe2p, (b) XPS-Pd3d for different Pd supported on Fe$_3$O$_4$ catalysts. Dashed lines show the locations of the 3d electron binding energies of Pd^{2+}.**

It is also interesting to notice the easy separation process of the catalyst during the process of purification by washing with deionized water and ethanol via applying an external magnetic field using a strong magnet due to the high magnetic properties of the palladium supported on magnetite catalyst as shown in **Figure 4-10** and **Figure 4-13**.

The magnetic properties of prepared catalysts were carried out by using Vibrating Sample Magnetometer (VSM) analysis. **Figure 4-11** presents the magnetic hysteresis loop of Pd - Fe$_3$O$_4$ and reveals the magnetic response of this catalyst to the varying magnetic field. This figure simply shows the hysteresis curves obtained for Pd - Fe$_3$O$_4$ with an applied field sweeping from - 40 to 40 kOe.

90
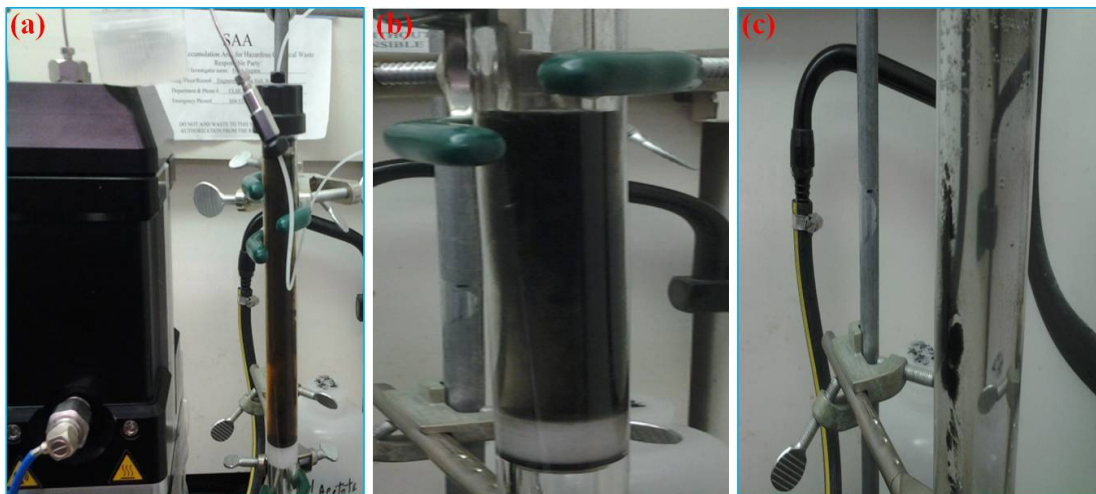
Figure 4-10   (a,b) Catalyst after preparation. (c) Separating the catalyst using a strong magnet.
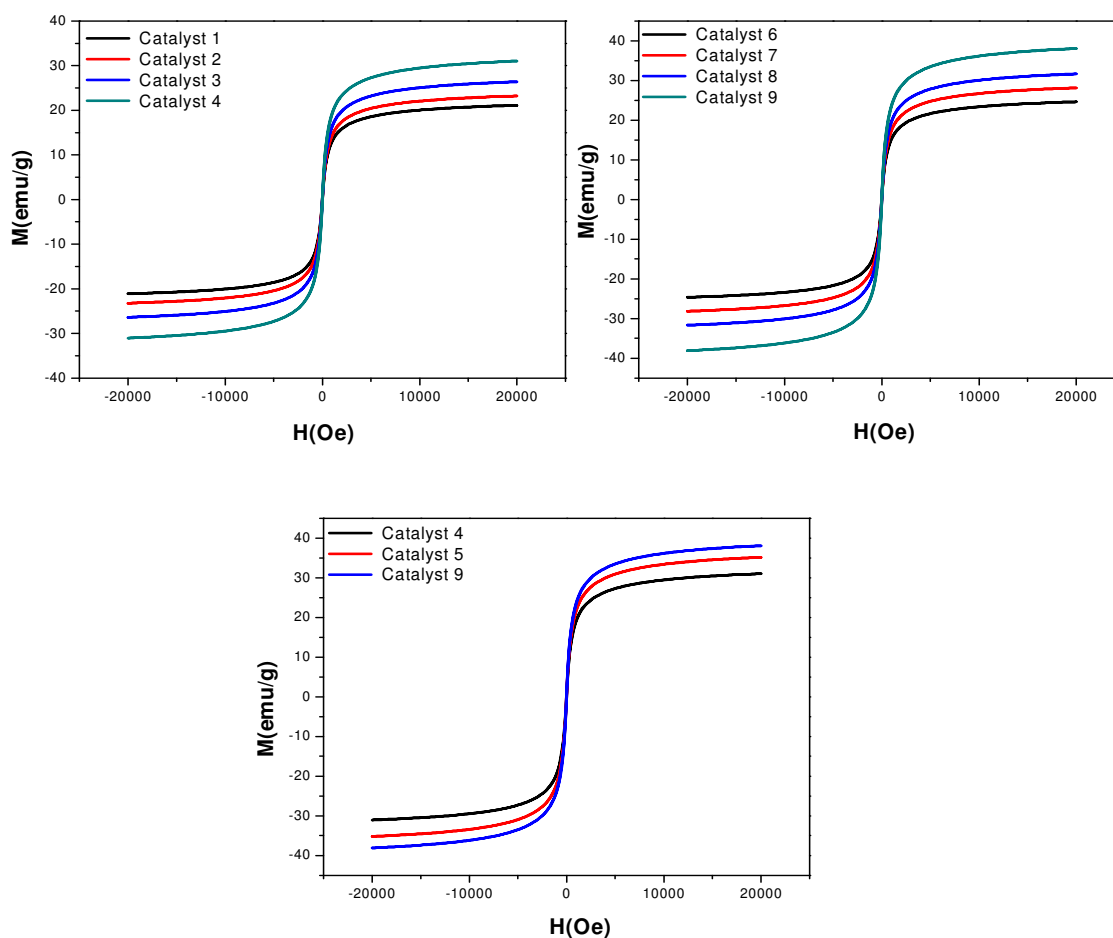
Figure 4-11 Magnetic hysteresis loops of Pd/Fe$_3$O$_4$ at room temperature after MWI

91
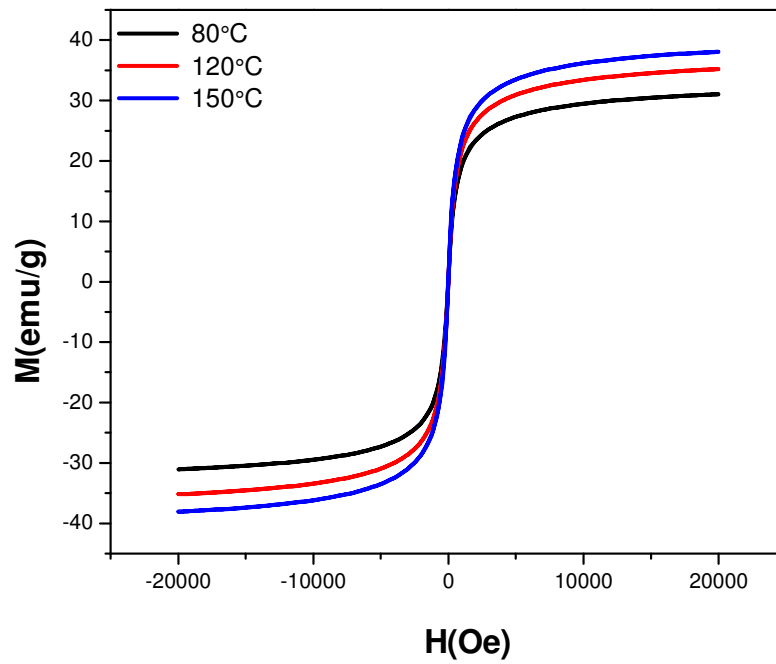
Figure 4-12 Magnetic hysteresis loops of Pd/Fe$_3$O$_4$ at room temperature after MWI

As mentioned before, TEM images show that as temperature increases, the particle size increases as well. So, it is obvious that catalyst prepared at 80 ˚C (catalyst 4) has a smaller particle size than catalyst prepared at 120 ˚C (catalyst 5) which has also a smaller particle size than catalyst prepared at 150 ˚C (catalyst 9). As a result, it can be observed that the saturation magnetization decreased as the size decreased. This agrees with the known fact that the magnetization of small particles decreases as the particle size decreases.[204] In **Figure 4-12**, the hysteresis loop of the prepared sample reveals superparamagnetic behavior at room temperature with nearly zero coercivity and extremely low remnant magnetization values. The lack of remaining magnetization when the external magnetic field is removed is in agreement with a superparamagnetic behavior observed in magnetite nanosheets Fe$_3$O$_4$ decorated with Pd nanoparticles.

92
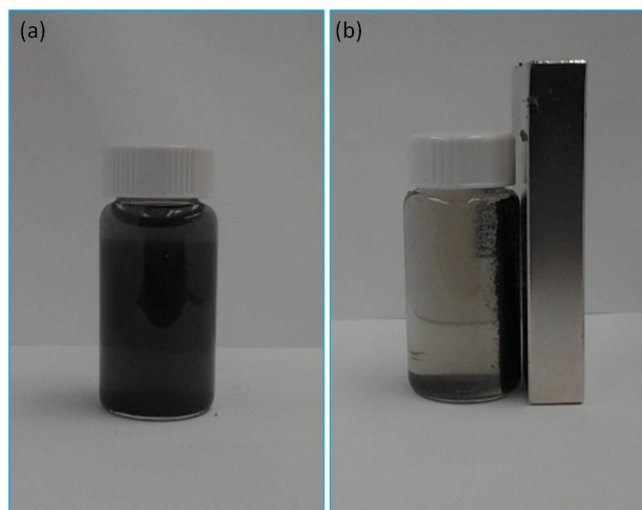
Figure 4-13 (a) Catalyst after preparation. (b) Separating the catalyst after washing by a strong magnet.

4.5 Conclusions

In conclusion, an application for a novel nonresonance microwave applicator was presented as the heating source in a continuous-flow synthesis system. The applicator was designed for continuous-flow chemistry, to provide uniform heat over 3 mm section of a tubular borosilicate reactor. Due to the possibility of varying the MW frequency between 2.4 and 2.5 GHz, efficient heating could easily be achieved up to $150\,^{\circ}$C.

Due to the excellent heating capacity, small-scale microwave batch experiments were easily adapted to nonresonance MW assisted continuous-flow processing. The heating performance with a range of different flow rates of reactants was investigated and demonstrated the usefulness of the system in CO oxidation catalysis. The fast heating, small reactor volume, and rapid change in reaction temperature in real time are unique features of this instrument.

93

It is believed that the nonresonant CF-MAOS system presented here is an unprecedented laboratory tool for safe and fast optimization of reaction conditions and scale-out synthesis. An efficient magnetic catalyst has been developed and successfully synthesized using a reliable, reproducible fast and simple method using microwave irradiation (MWI) approach.

This is a facile approach used for the synthesis of a well dispersed magnetically separable palladium supported on magnetite, which can act as a unique catalyst against CO oxidation catalysis due to the well dispersion of palladium nano particles throughout the magnetite surface.

The prepared catalysts are magnetic which is an advantage in the separation process of catalyst from the reaction medium. The separation process is achieved via applying of strong external magnetic field which makes separation process easy, reliable and environmentally friendly. The catalytic activity performance of different prepared catalyst was evaluated towards CO oxidation catalysis.

It was found that catalysts 4, 5, and 9 that were prepared under the same reaction conditions except temperature that was varied as 80, 120, and 150˚C respectively. Catalyst 9 was found to be the best catalyst for catalytic performance as the temperature at which CO was completely converted to CO_2 was 137˚C compared to 168˚C and 150˚C in case of catalyst 4 and 5 respectively. This high catalytic activity of catalyst 9 that was prepared under flow reaction conditions was very close to catalyst 10 that was prepared under batch reaction conditions.

The typical synthesis was conducted under continuous flow reaction conditions by using hydrazine hydrate (H.H) as a strong reducing agent for the reaction mixture under microwave irradiation synthesis (MWI). The palladium played a crucial role in the catalytic CO oxidation at low temperatures (100–137˚C).

94

Such a catalytic activity is supposed to be connected with the reaction between oxygen adsorbed on the reduced sites of the support and CO adsorbed on Pd at the metal–oxide interface. The results would be useful for preparation of metal–oxide catalysts under continuous flow reaction conditions with high performance at low temperatures.

By applying this method, the catalyst was prepared in larger amounts and in the same time without any differences in catalytic activity from batch to batch. This technique was used to prepare the Pd/Fe_3O_4 catalyst in large amounts compared with small amounts that was prepared under batch reaction conditions and also to produce a catalyst with the same specifications each time of preparation to avoid problems of inconsistent specifications of catalysts that is prepared under batch reaction conditions.

CHAPTER 5   Pd-based Catalysts Supported on Shape-Controlled CeO$_2$ and TiO$_2$ for CO Oxidation

5.1   Overview

Research in nanocatalysis taregts the design of nanostructured catalysts for many technological advances in chemical synthesis and processing, environmental detoxification and improving air quality. Such catalysts should possess improved catalytic features such as low temperature operation, stability, durability, selectivity and resistance to degradation and poisoning [39]. One of the environmental issues that has been studied extensively is the catalytic oxidation of carbon monoxide, mainly due the fact that CO is an odorless and invisible gas and could be lethal even at the very low exposure levels [39]. There is a need for an inexpensive catalyst meeting the requirement for ideal one to operate under ambient conditions for many applications. Ceria constitutes one of the most important classes of the rare earth oxide nanostructures.[122, 205-206] Because of its unique redox properties, the high refractive index (1.6 – 2.5 at 633 nm), the strong absorption in the UV range, the high oxygen storage capacity, the optical transparency in the visible range and the interesting catalytic and free radical scavenging properties, cerium oxides structures have received a significant attention from the research institutes.[207-215] They have been extensively studied for application in fast ion conduction in solid oxide fuel cells, as environmental heterogeneous catalysts support, oxygen pumps, in oxidation-resistance coatings, three-way catalysts and diesel fuel, as UV absorbers in UV-blocking, gas sensing, fine chemical synthesis, mechanical polishing, and recently in toxicity and biomedical applications.[37-38, 123, 216-221]

5.2 Introduction

Research exploration in nanocatalysis can be roughly divided into four stages: catalyst design and synthesis, characterization, implementation and exploring reaction kinetics and mechanism. Obviously, the most important of these stages is the stage of designing and synthesizing a particular proper catalyst that meets criteria required by a particular application. Nevertheless, the understanding of the mechanisms of the catalytic reaction can help finding better ways of catalyzing a particular reaction. With the fact that different catalyst supports possess different activation energies, reducible metal oxides such as CeO_2, TiO_2, Fe_3O_4 and Fe_2O_3 were found to be superior in catalyzing CO oxidation among others compared to irreducible metal oxides such as Al_2O_3, SiO_2 and ZrO_2.

The metal oxide support involved in the reaction can directly catalyze activation of the molecular oxygen [222], favor electronic interaction with transition metal catalyst [223] or impose strains on metal clusters [224]. It is known also that metal support structures of nanocrystalline size are more active than that with larger size. The two reducible metal oxides, CeO_2 and TiO2 have gained particular interest and accordingly are widely used in catalytic industry and as active and thermally stable supports for noble and transition metal-based catalysts, such as Pd, Au and Cu. A particular attention has been focused on the effect of the shape and preparation conditions on the activity of the test catalyst. Over years numerous catalysts have been used for the CO catalytic oxidation including Au and Pd-based catalysts. In particular catalysts that can catalyze the oxidation reaction at low temperature have gained a special focus, mainly due to the potential in industrial and environmental applications such as in pollution control devices and others. In this work, the CO catalytic oxidation over Pd-supported on TiO_2 and CeO_2 of different shapes is studied.

97

For TiO$_2$ catalysts, Pd activity is tested over TiO$_2$ nanotubes and nanospheres and for CeO$_2$ catalysts, Pd activity is tested over CeO$_2$ cubes and spheres. The effects of preparation conditions and post-synthesis treatment are as well as the ratio of Pd loading upon the CO oxidation activity were investigated.

5.3 Experimental

5.3.1 Chemicals and reagents

In this work, two different types of spherical CeO$_2$ nanoparticles were used as precursor to prepare ceria cubes. A one type is a commercial (Aldrich) ceria spheres and the second sample is prepared in our laboratory. The second spherical sample was prepared as follows, a solution of 1.0 mmol of Ce(NO$_3$)$_3$.6H$_2$0 in 50 ml ethylenediamine (EDA) was aged under vigorous stirring for 24 h. After complete washing and drying, a portion of the as-prepared powder was calcinated by heat treatment in a muffle furnace under air. The furnace temperature was ramped to 450 $^\circ$C at a rate of 25 $^\circ$C /min. and then held at 450 for 3 hours. The calcinated powder was then cooled to ambient temperature and grinded.

For TiO$_2$, commercial spherical TiO$_2$ nanoparticles were purchased from Sigma and used as precursors for the synthesis of TiO$_2$ tubes.

An alkaline treatment of spherical nanoparticles precursor at temperature of 200 ^{o}C for 16 h was followed for the synthesis of CeO$_2$ nanocubes and TiO$_2$ nanotubes and shape transformation of spherical samples. After preparation and drying, all samples were calcinated at 450°C for 3 hours. The colloidal deposition of Pd nanospheres on the metal support (CeO$_2$ spheres and cubes and TiO$_2$ spheres and tubes) was achieved as follows: 100 mg of the solid support was suspended in 100 ml deionized (DI) water and sonicated at room temperature for 15 min.

98

A predetermined volume of NaOH aqueous solution was added to the obtained suspension to adjust the pH and hence maximize Pd loadings. An appropriate amount of Pd $(NO_3)_2$ 10 wt. % dissolved in 10 wt. % nitric acid was added to the reaction mixture while stirring. The mixture was then aged while stirring. After reaction is complete, the mixture was centrifuged and the precipitate was washed three times in boiling DI water to remove unreacted species and residual anions and finally was dried in oven at 80 ˚C overnight. Upon drying and grinding, part of the catalyst was calcinated for 2 h at 450˚C and a comparison of CO catalytic activity was studied for catalysts with and without calcination.

5.3.2   Characterization

Samples were characterized by XRD, TEM and XPS. The X-ray diffraction (XRD) patterns of the powder samples were measured at room temperature with an X'Pert Philips Materials Research diffractometer with Cu $K_{\alpha1}$ radiation. Transmission electron microscopy studies (TEM) were conducted using a Joel JEM-1230 electron microscope operated at 120 kV equipped with a Gatan UltraScan 4000SP 4K × 4K CCD camera. Samples for TEM were prepared by placing a droplet of colloid suspension in respective solvent on a Formvar carbon-coated, 300-mesh copper grid (Ted Pella) and allowing them to evaporate in air at ambient conditions. The X-ray photoelectron spectroscopy (XPS) analysis was performed on a Thermo Fisher Scientific ESCALAB 250 using a monochromatic Al Kα X-ray.

Experiments for the CO catalytic oxidation were performed using a fixed bed-programmable flow tube furnace reactor (Thermolyne 2100) [39]. In a typical experiment, 20 mg of the test catalyst was dispersed in glasswool and placed inside a pyrex glass tube. The sample and furnace temperatures were measured by a thermocouple placed in contact with the catalyst bed and in the middle of the tube furnace, respectively.

99

Signals from thermocouples were processed using an SC-2345 data acquisition board. To plot temperatures and other measurement parameters, data acquisition software using Lab view was utilized. A gas mixture consisting of 4 wt % CO and 20 wt % O_2 in balance helium was passed over the sample at a flow rate of 100 cm^3/min while the temperature was ramped. The flow rate was controlled by a set of MKS digital mass flow meters. The conversion of CO to CO_2 was monitored using an online infrared gas analyzer (ACS, Automated Custom Systems Inc.) to detect the exit gas, which is then vented to outlet.

5.4 Results and Discussion

Ceria (CeO_2) has been studied as a useful oxide additive for ceramics, glass polishers, oxygen sensors, solid electrolytes and catalytic supports. CeO_2 has the fluorite structure which is stable even at high temperature. **Figure 5-1** shows the XRD pattern of CeO_2 spheres powder precursor before the alkaline treatment. The XRD pattern after alkaline treatment, drying and calcination for CeO_2 cubes is shown in **Figure 5-2.**
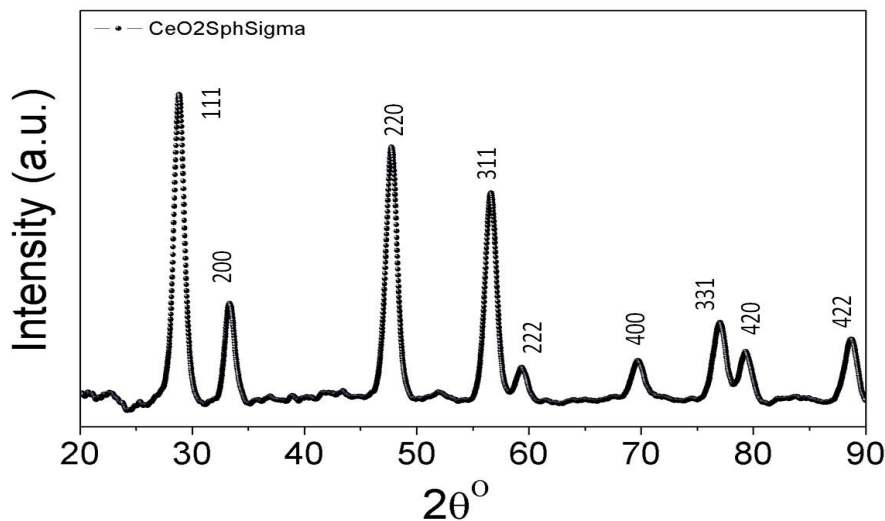
Figure 5-1 XRD pattern of commercial spherical CeO₂ nanoparticles.
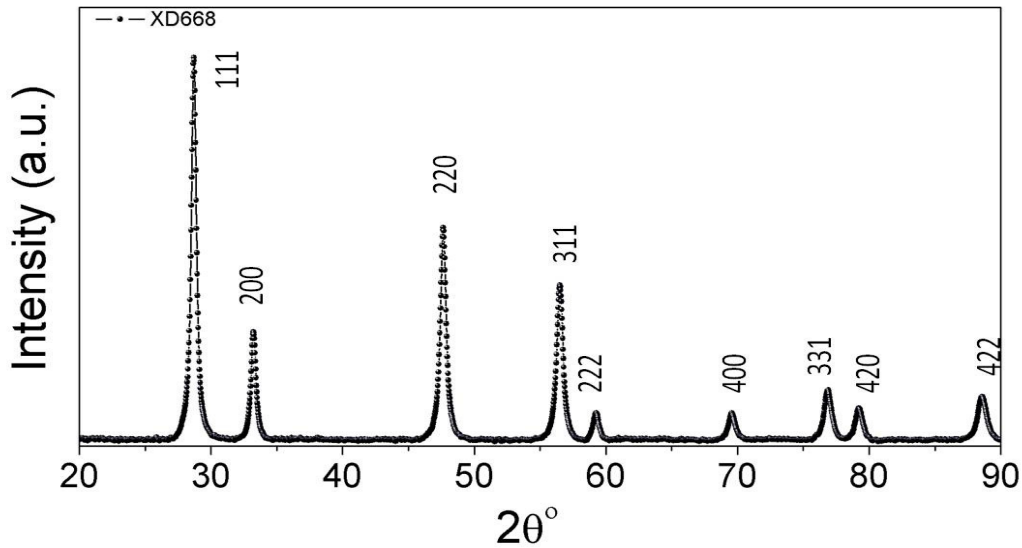
Figure 5-2 XRD pattern of CeO$_2$ cubes prepared by alkaline treatment of commercial spherical CeO$_2$ nanoparticles.

The XRD patterns of CeO$_2$ spheres prepared by EDA prior to alkaline treatment and shape transformation **(Figure 5-3)** and after shape transformation into cubes **(Figure 5-4)**. All samples before and after the alkaline treatment exhibit XRD reflections that are assigned to the typical fcc fluorite crystal structure, in an agreement with literature [225].
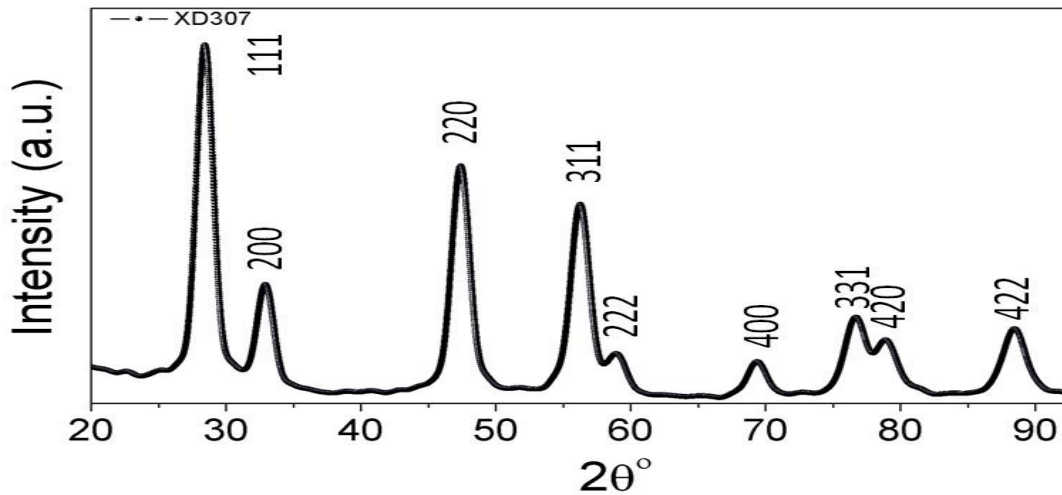
Figure 5-3 XRD pattern of calcinated CeO$_2$ spheres prepared by EDA at 110° C as precursors for cubic CeO$_2$ nanoparticles.

101
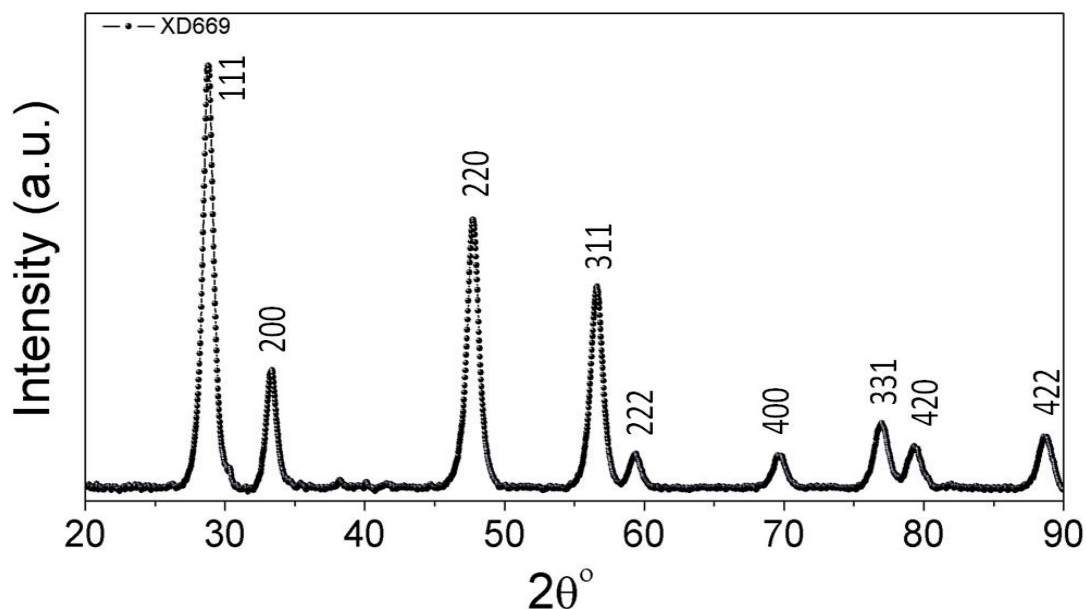
Figure 5-4 XRD pattern of CeO₂ cubes prepared by hydrothermal alkaline treatment of spherical CeO₂ nanoparticles prepared previously by EDA

However, the XRD reflections of the two CeO_2 cubes samples prepared by alkaline treatment of CeO_2 spheres are relatively narrower and sharper indicating that these CeO_2 cubes samples have higher crystallinity and probably larger in size. **Figure 5-5, Figure 5-6** show TEM images of CeO_2 cubes prepared by hydrothermal alkaline treatment method (**Figures 5-5b and 5-6,d-i**) of both commercial CeO_2 spheres (**Figure 5-5,a**) and CeO_2 spheres previously prepared by EDA-assisted solvothermal treatment (**Figure 5-6,a-c**).

As shown in the figures both commercial and EDA-prepared particles are spherical in shape and are approximately 4-5 nm in size. Upon the alkaline treatment the shape transformation of into cubic nanoparticles is clear in the TEM images. The formation of cubic nanoparticles from nanospheres could result from the presence of cerium hydroxide species that self-assemble via orientated attachments and grow into cubic shaped nanoparticles.

102
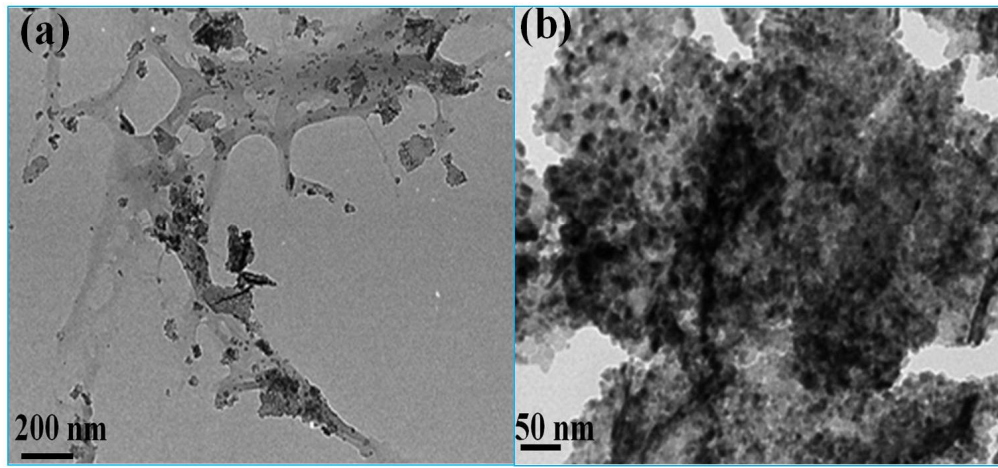
Figure 5-5 TEM images of CeO$_2$ cubes (a) prepared by alkaline treatment of commercial spherical CeO$_2$ nanoparticles (b).
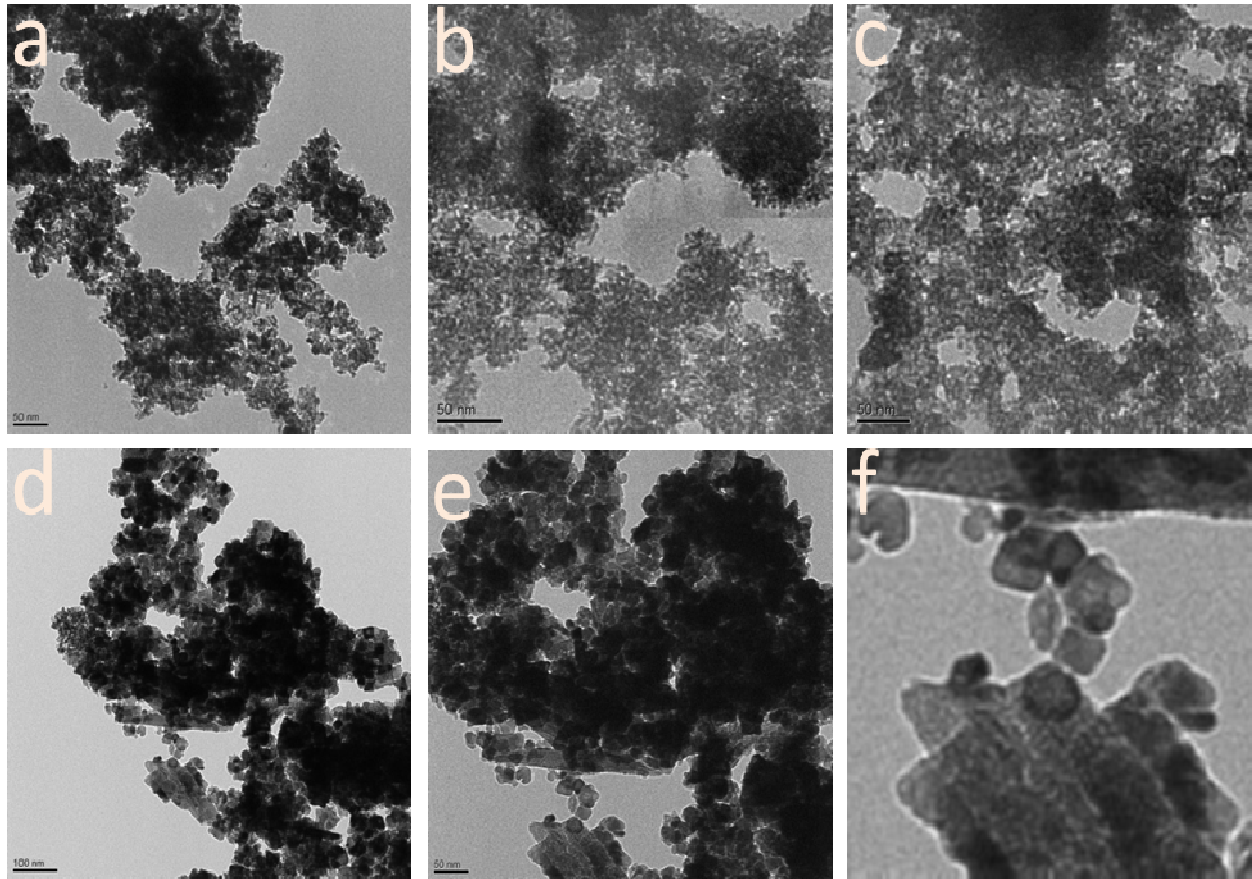
Figure 5-6   TEM images of CeO$_2$ cubes prepared by alkaline treatment of CeO$_2$ nanoparticles which was previously prepared by EDA.

Titania (TiO$_2$), a semiconducting oxide, shows unique optical, electronic and electrical properties and thus has been studied in many applications such as in photonics, solar cells, water splitting, chemical sensing and heterogeneous catalysis [226]. TiO$_2$ nanotubes in particular have gained an increased attention due to the enhanced performance over spherical particles especially in catalysis and photo degradation applications. Alkaline hydrothermal treatment has been shown to provide an easy method to fabricate TiO$_2$ nanotubes using TiO$_2$ spherical particles as precursors. [227] **Figure 5-7** shows the XRD pattern of TiO$_2$ spherical particles used as precursors for growing titania nanotubes. The XRD of TiO$_2$ nanotubes prepared by the hydrothermal treatment of TiO$_2$ spherical nanoparticles in NaOH is shown in **Figure 5-8**. The XRD reflections can be indexed to the anatase phase as described in the literature [228].
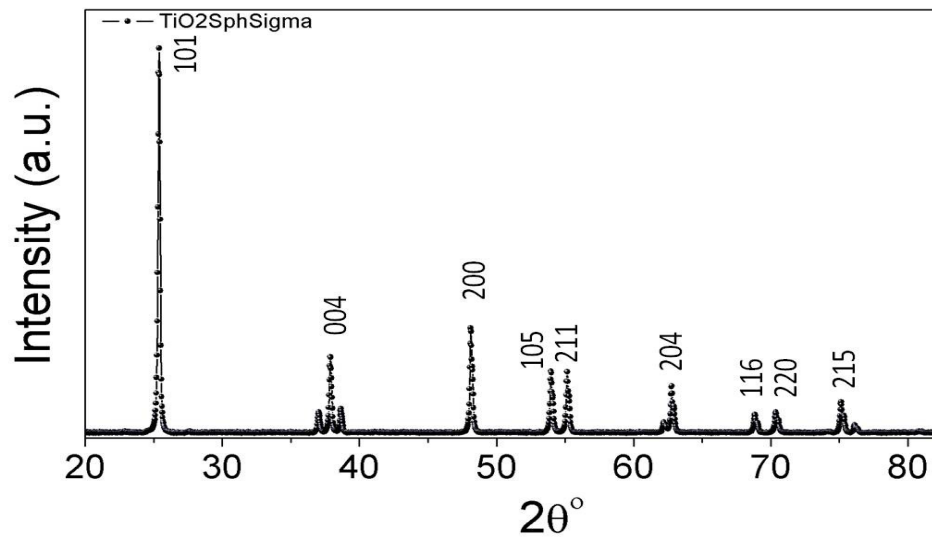
Figure 5-7 XRD pattern of commercial spherical TiO$_2$ nanoparticles (Sigma)
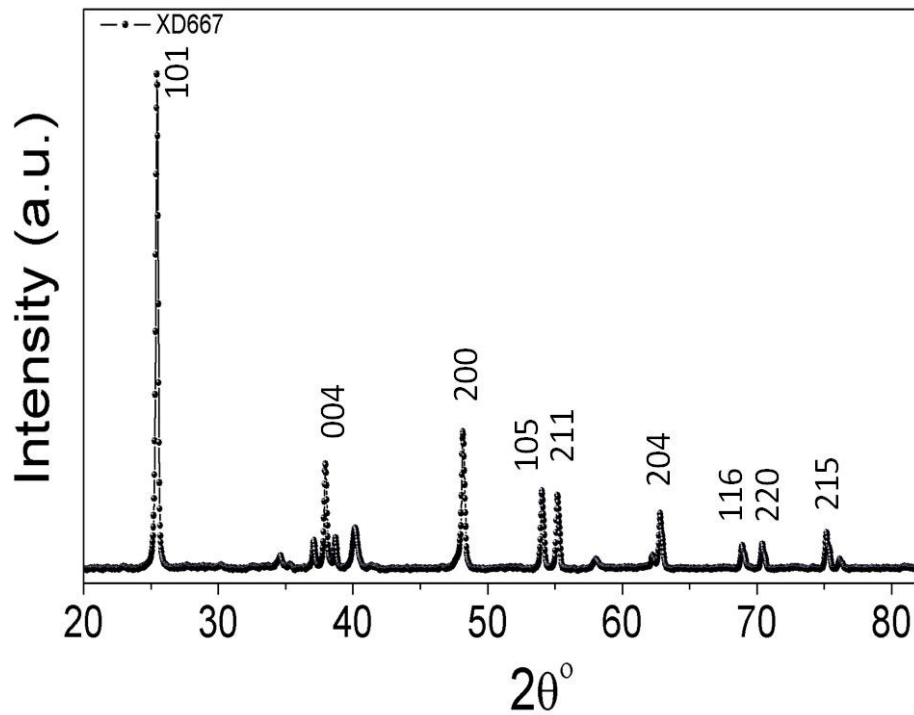
Figure 5-8 XRD pattern of TiO$_2$ nanotubes prepared by hydrothermal alkaline treatment of commercial spherical TiO$_2$ and calcinated at 450 $^\circ$C for 3 h

The treatment of spherical TiO$_2$ particles with NaOH resulted in the rupture of Ti-O-Ti bonds and formation of lamellar sheets which are converted into nanotubes at high pH [227] as can be seen clearly in TEM images of TiO$_2$ before (**Figure 5-9,a-c**) and after hydrothermal treatment in NaOH (**Figure 5-9,d-i**).

105
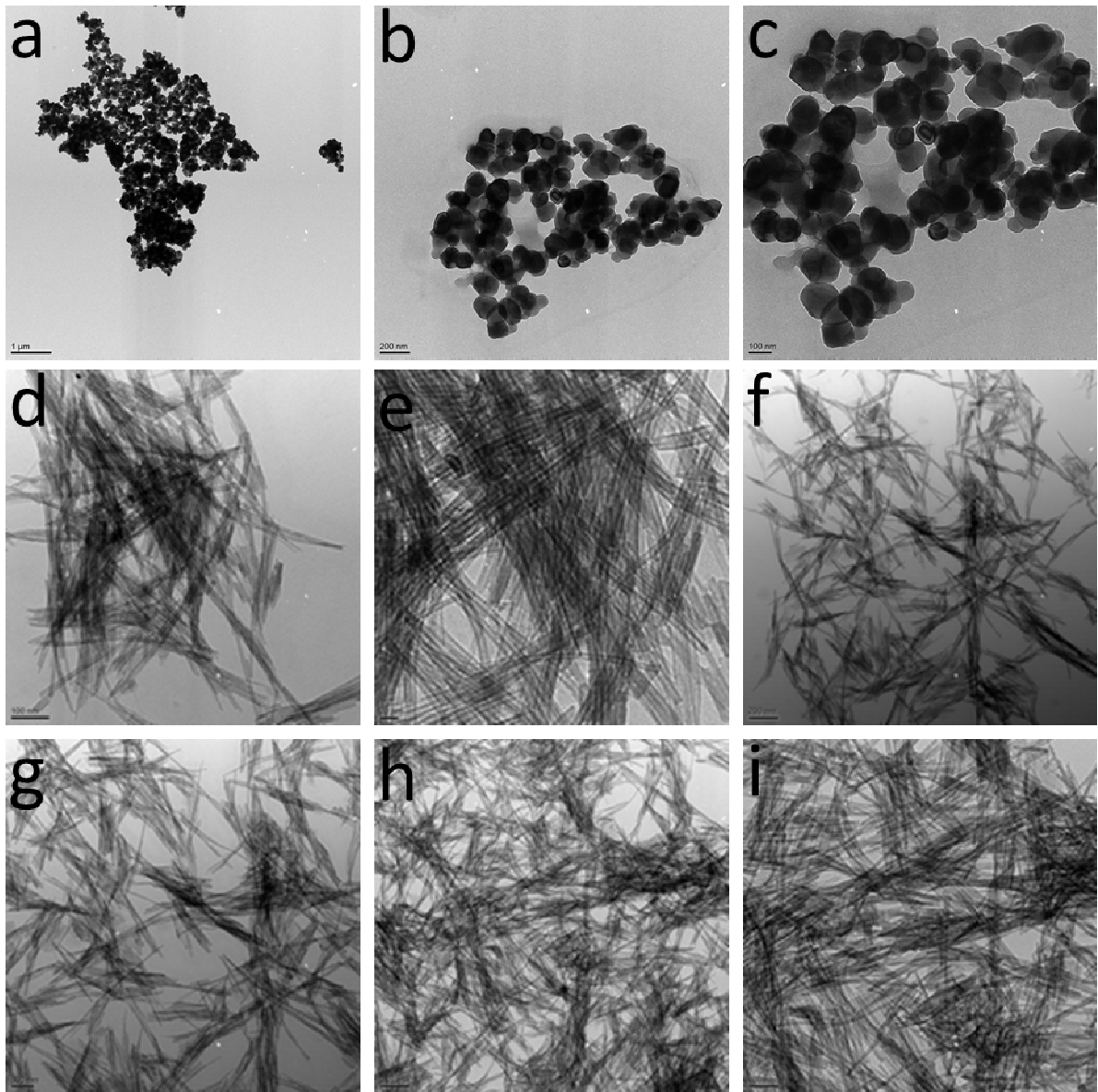
Figure 5-9 TEM images of TiO₂ nanotubes (d-i) prepared by hydrothermal alkaline treatment of spherical TiO₂ nanoaprticles (a-c).

Heterogeneous catalytic oxidation of carbon monoxide (CO) to carbon dioxide (CO_2) using metal-based catalysts has been studied extensively as a model reaction [229-240].

106

The popularity of CO oxidation as a model system stems from reaction simplicity where only diatomic molecules are involved and product formation takes place over few steps.

It is also an important practical modality for CO removal in many environmental and industrial applications such as air purification, closed-cycle CO_2 lasers, polymer electrolyte membrane (PEM) fuel cells, [241-242] purification of H_2 from CO traces in H_2 fuel cells, removing toxic CO in effluents and car exhaust. [243] Oxidation of CO can be catalyzed with highly dispersed noble transition metals, particularly Au, Pd and Ru, on various reducible oxides as supports at low temperature. [244-246] Moreover, the sensitivity of CO molecules to the structure of the surface can be used to probe active sites on metal surfaces, which can help understanding the nature and mechanism of active coordination sites. [247] Adsorption of CO on the surfaces can be simply traced by IR spectroscopy, among others. Nevertheless, a critical point in CO catalytic oxidation is to develop simple strategies for preparing catalysts with higher reactivity and stability by increasing the metal-support interaction. [248]

Pd-based heterogonous catalysts integrated with Rh and Pt structures are widely used for CO oxidation I catalytic converters since they show better durability in automotive exhaust systems. Recently, heterogeneous catalysts that contain only Pd have been suggested as an alternative for 3-way catalysts industry. Most Pd-based catalysts studied for CO oxidation are supported on metal oxides such as TiO_2, Al_2O_3, SiO_2 and CeO_2. The effects of different metal oxides on the low-temperature CO oxidation and on Pd activity has been attributed to the varying surface defects densities which determines the extent the CO and O_2 are stabilized. [249]

Catalysts investigated in this work were prepared by colloidal deposition of Pd on TiO_2 and CeO_2 nanostructures.

107

The effect of the preparation conditions, loading percentages, post-synthesis treatment and shape of the support on the catalytic activity of CO oxidation is investigated.

It is reported that the catalytic activity strongly depends on the nature of the catalyst particles and dispersion which in turn is very sensitive to the procedure of preparation and pre-or post-treatments. [250-256] Plots of CO conversion percentages versus temperature for different Pd catalysts are shown in **Figures 5-10**, it can be seen that increasing the reaction temperature inside the tube furnace leads to a gradual ramp in percentages of CO conversion.
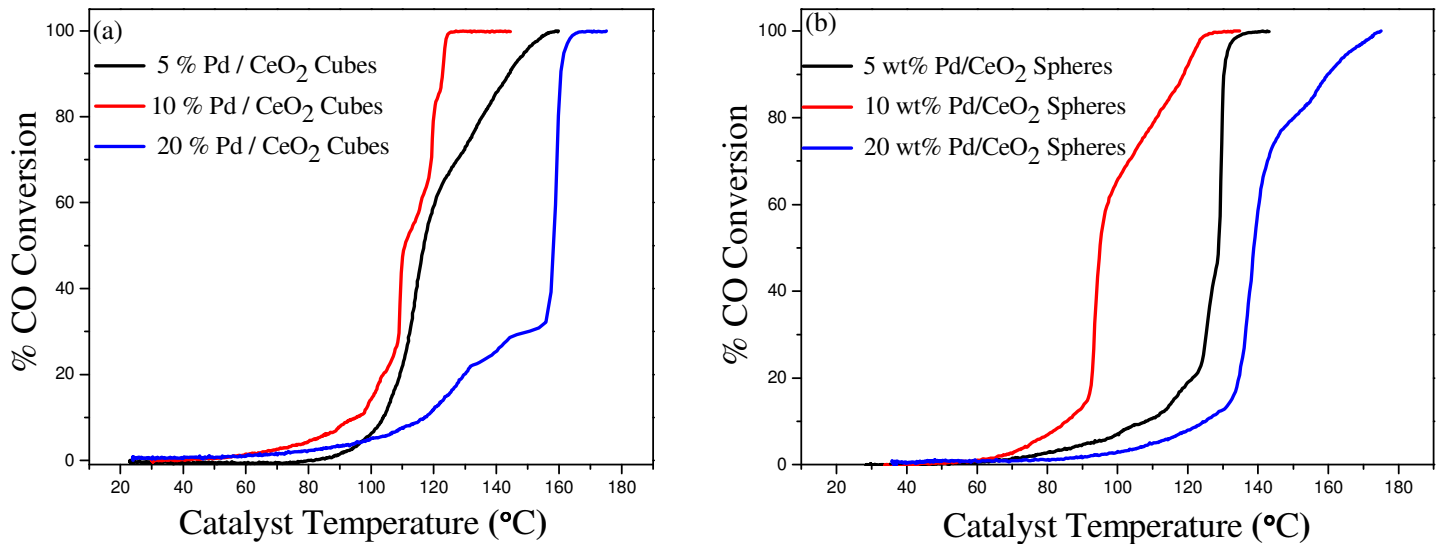
Figure 5-10 CO – Catalytic conversion of Palladium supported on (a) cubic CeO₂ nanoaprticles, (b) spherical CeO₂ nanoaprticles.

Generally, as using 5 wt% Pd (weight percent) the catalytic conversion was completely reached at 158˚C and 135˚C in case of cubic and spherical nanoparticles respectively. While, using 10 wt% Pd (weight percent) the catalytic conversion was completely reached at 125˚C in both cases of cubic and spherical nanoparticles.

108

But, when using 20 wt% Pd (weight percent) the catalytic conversion was completely reached at 165 °C and 173 °C in case of cubic and spherical nanoparticles respectively which may be due to high percentage of palladium that may cause agglomeration.
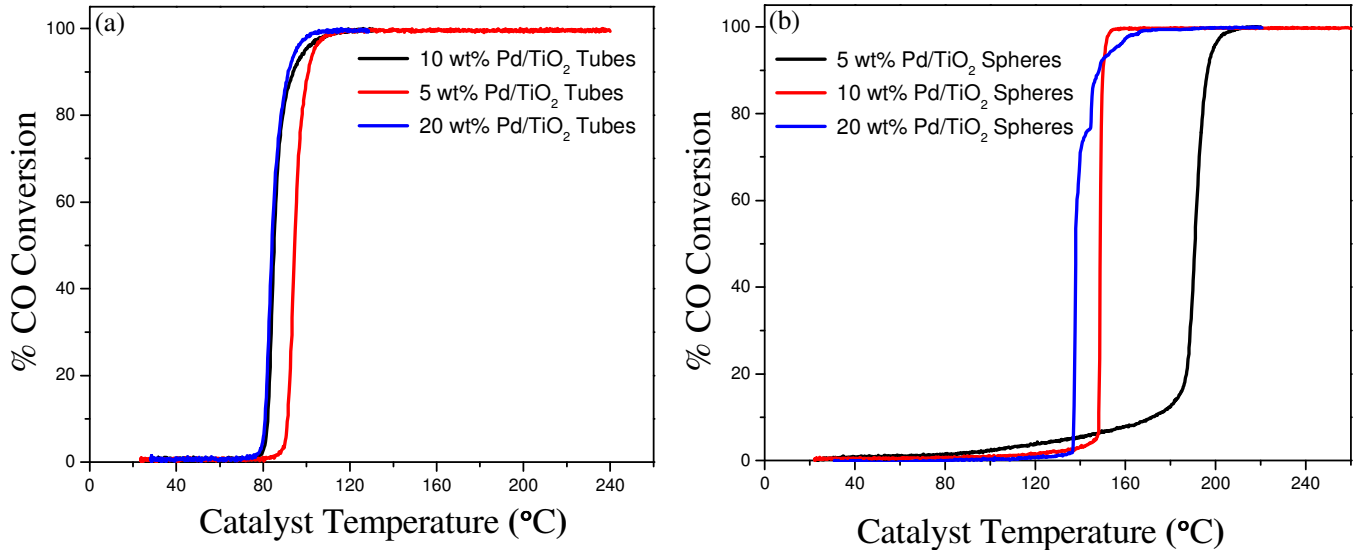
Figure 5-11 CO – Catalytic conversion of Palladium supported on (a) tubes of TiO$_2$ nanoaprticles, (b) spherical TiO$_2$ nanoaprticles.

Generally, as using 5 wt% Pd (weight percent) the catalytic conversion was completely reached at 130 °C and 208 °C in case of tubes and spherical nanoparticles respectively. While, using 10 wt% Pd (weight percent) the catalytic conversion was completely reached at 110 °C and 153 °C in case of tubes and spherical nanoparticles respectively. But, when using 20 wt% Pd (weight percent) the catalytic conversion was completely reached at 104 °C and 168 °C in case of tubes and spherical nanoparticles respectively.

So, it is obvious from **Figure 5-11** that the shape of tubes of TiO$_2$ shows higher catalytic activity than spherical nanoparticles of TiO$_2$.

109

5.5 Conclusions

In conclusion, we report here a facile approach used for the synthesis of a well dispersed palladium supported on different shapes of, which can act as a unique catalyst against CO oxidation catalysis due to the well dispersion of palladium nanoparticles throughout the support surface. We show here the fact that different catalyst supports possess different activation energies, reducible metal oxides such as CeO_2, TiO_2 were found to be superior in catalyzing CO oxidation among others compared to irreducible metal oxides such as Al_2O_3, SiO_2 and ZrO_2 as mentioned in literature. The two reducible metal oxides, CeO_2 and TiO2 have gained particular interest and accordingly are widely used in catalytic industry and as active and thermally stable supports for noble and transition metal-based catalysts, such as Pd, Au and Cu.

In this work, the CO catalytic oxidation over Pd-supported on TiO_2 and CeO_2 of different shapes is studied. For TiO_2 catalysts, Pd activity is tested over TiO_2 nanotubes and nanospheres and for CeO_2 catalysts, Pd activity is tested over CeO_2 cubes and spheres. The effects of preparation conditions and post-synthesis treatment are as well as the ratio of Pd loading upon the CO oxidation activity were investigated. It was possible to prepare different catalysts with different catalytic activity and the optimum conditions of preparing these catalysts were achieved when 10 % Pd was supported on cubes and spheres of CeO_2 as the complete conversion of carbon monoxide to carbon dioxide could be achieved around 125˚C. Also, it was possible to prepare different catalysts with different catalytic activity and the optimum conditions of preparing these catalysts were achieved when 20 %, 10 % Pd were supported on tubes and spheres of CeO_2 as the complete conversion of carbon monoxide to carbon dioxide could be achieved around 104˚C, 153˚C in case of tubes and spherical nanoparticles respectively.

CHAPTER 6　Microwave-Assisted Synthesis of Pd/Fe$_3$O$_4$ Nanoparticles Supported on Graphene, an Efficient and Magnetically Recyclable Catalyst for Suzuki Cross-Coupling Reactions under Batch Reaction Conditions

6.1　Overview

Since its discovery in 2004, graphene has been one of the most widely studied materials in all of science.　Its unique structural and electronic properties have motivated the development of new composite materials for nanoelectronics and related devices. However, it's high thermal, chemical and mechanical stability as well as its large surface area represents desirable attributes as support layers for metallic nanoparticles in catalysis. One of the catalytic applications for which graphene support systems have been shown to demonstrate significant advantages is in the area of cross-coupling chemistry.

Palladium-catalyzed cross-coupling reactions have been of strategic importance in organic synthesis since their discovery in the 1970s. These reactions have been widely used for the assembly of complex organic molecules in a broad range of applications in the chemical and pharmaceutical industries.　They remain the method of choice for carbon-carbon bond formation. Cross-coupling reactions have been most frequently practiced under homogeneous conditions employing a ligand to enhance the catalytic activity and selectivity for specific reactions.

However, the issues associated with homogeneous catalysis remain a challenge to pharmaceutical applications due to the lack of recyclability and potential contamination from residual metals in the reaction product. Product contamination is of particular importance in pharmaceutical applications where this chemistry is practiced extensively. Ligand-free heterogeneous palladium catalysis presents a promising option to address this problem as evidenced by the significant increase in research efforts in this area. Therefore, the development of highly active heterogeneous Pd nanocatalysts that can be easily separated from the reaction medium and recycled is an important goal of nanomaterials research that is likely to have considerable impact on cross-coupling applications in the future.

Recently, we reported the remarkable cross-coupling catalytic activity of palladium nanoparticles deposited onto a graphene substrate. The catalyst was prepared from palladium nitrate and graphene oxide using hydrazine hydrate as a reducing agent with microwave heating. This procedure yielded highly uniform palladium nanoparticles which were evenly distributed across the graphene surface. These catalysts demonstrated extremely high turnover frequencies ($108,000\ h^{-1}$) for Suzuki cross-coupling reactions and could be recycled multiple times without loss of catalytic activity. However, the isolation of these catalysts from the reaction mixture was found to be quite difficult and time consuming. In order to address this issue, we hypothesized that we could employ the same procedure to prepare bimetallic palladium, iron nanoparticles supported on graphene sheets, which would provide a means to magnetically separate these materials from the reaction mixture. Herein, we report on the preparation and characterization of graphene supported $Pd-Fe_3O_4$ which exhibits excellent Suzuki cross-coupling catalytic activity and can be magnetically separated from the reaction mixture and recycled multiple times without loss of catalytic activity.

112

In 2010 the Nobel Prize in chemistry was awarded to the formation of carbon-carbon through palladium-catalyzed cross-coupling reactions. Metal-catalyzed carbon-carbon bond forming reactions have rapidly become one of the most effective tools in organic synthesis for the assembly of highly functionalized molecule.[49] Palladium-catalyzed coupling reactions provide outstanding widely applied tools in the field of organic synthesis.[49, 54, 152] These reactions have typically been carried out under homogeneous reaction conditions, which require the use of ligands to solubilize the catalyst and broaden its window of reactivity.[49, 144]

However, the use of these catalysts under homogeneous conditions has limited their commercial viability because of product contamination as a direct result of inability to effectively separate the catalyst from the reaction product. The issue of product contamination is of particular importance in pharmaceutical applications where this chemistry is practiced extensively. Ligand-free heterogeneous palladium catalysis presents a promising option to address this problem as evidenced by the significant increase in research activity in this area.[49, 144] Most of research groups in both academia and industry focus now on using palladium not only for the high stability of organopalladium compounds to water and air in most cases except in some phosphane complexes but also in achieving mild reaction conditions that definitely will minimize the formation of undesirable side products and, hence it becomes possible to achieve high selectivity.[75, 257-259] It is well known that using nano-sized particles increase the exposed surface area of the active component of the catalyst, hence enhancing the contact between reactants and catalyst dramatically in a way similar to that of the homogeneous catalysts.[62, 80, 94-96, 109, 260-263] Syntheses of nanoparticles with variable sizes have been intensively tried particularly for magnetic iron oxides or magnetite (Fe_3O_4).[6, 58, 82, 264]

113

These nanoparticles were used efficiently as magnetic recoverable catalysts for various applications.[265] Also, it is remarkable that iron amount added to some kinds of Pd-containing catalysts may also have an influence on catalytic performance.[266] In lab-scale experiments, the magnetic catalyst can be collected by applying an external strong magnetic field via using a strong magnet to be hold to the glass wall of the reaction flask and decanting the product solution. After washing steps, the magnet was removed and the catalyst was dispersed in the appropriate solvent to be used in the following experiment.[71, 75-76, 129, 267] High catalytic activity, ease of recovery using an external magnetic field and use of water as the solvent are additional attributes of this catalytic system. Specifically, transition metal catalysts such as palladium, copper, ruthenium, and nickel are used on silica, carbon based, magnetic nanoparticles and polymer supports.[93, 98, 140, 268-274]

Recently, although the synthesis and applications of magnetic nanoparticles (MNPs) of noble metal nanoparticles supported on graphene still a new area of research but it has attracted more interest in catalysis research and have been used in some industrially important reactions.[264, 275-277]

6.2 Introduction

Although the main disadvantage of using palladium in different reactions is due to high price and toxicity of the metal residue which is critical especially in pharmaceutical industry but these disadvantages could be minimized by using very small amounts of palladium catalysts especially in medical and therapeutic applications and mainly in cross coupling reactions. Issues associated with homogeneous catalysis remain a challenge to pharmaceutical applications of these synthetic tools due to the lack of recyclability and contamination from residual metals in the reaction products.[34, 78, 267, 278-280]

114

As a result, enormous efforts had been exerted to perform complete and simple separation of expensive noble metal catalysts from the desired products not only due to economic point of view but also due to considerations related to product quality as in pharmaceutical applications.[263, 278, 281-282]   So, the use of magnetic nanoparticles in catalysis is the magic key for solving these problems due to its huge industrial applications. The advanced and unique magnetic, electronic, and catalytic properties of the materials in the nanoscale attracted research centers to investigate this area of science deeply.[29, 32, 45, 63, 66-67, 71, 100, 126, 128]

It is also remarkable that carbon materials has an increasing importance in catalytic processes when used as catalyst supports but there is also an endless efforts to develop other kinds of supports like metal oxides.[6, 43, 59, 84, 271] Only recently both graphene (G) and graphite oxide (GO) have been considered as potential support systems for palladium-catalyzed C–C coupling applications. Due to the higher specific surface area (1500 m2/g, theoretical value 2600 m^2/g) and thermal stability of graphene when compared to graphite oxide (surface area 200–400 m^2/g).[1, 22, 144-145, 194, 197]

The aim of this study is to deposit metal nanoparticles on the surface of graphene sheets. In order to prepare this magnetic catalysts; Palladium nitrate and iron nitrate are mixed with the graphene oxide nanosheet surface, followed by microwave-assisted reduction in presence of hydrazine hydrate. Chemical reduction methods using microwave heating have been employed for the production of metal/metal-oxide nanoparticles supported on the defect sites of reduced graphene oxide (GO) nanosheets. MWI has been demonstrated for the synthesis of a variety of nanomaterials including metals, metal oxides, bimetallic alloys, and semiconductors with controlled size and shape without the need for high temperature or high pressure.[144-145]

115

The main advantage of MWI over other conventional heating methods is that the reaction mixture is heated uniformly and rapidly. This has been demonstrated for the acceleration of homogeneous catalysis in organic synthesis. [1, 144] In the present work, the Pd-Fe$_3$O$_4$/G nanocatalysts were prepared using microwave irradiation (MWI) method. Due to the difference in the solvent and reactant dielectric constants, selective dielectric heating can provide significant enhancement in the transfer of energy directly to the reactants, which causes an instantaneous internal temperature rise.[20, 145, 149, 283] This temperature rise in the presence of hydrazine hydrate as a reducing agent has provided a facile and efficient method by which palladium ions and GO can be effectively reduced into a dispersion of metallic nanoparticles supported on the large surface area of the graphene sheets. The reduction of GO by hydrazine hydrate under MWI proceeds by rapid deoxygenation of GO to create C–C and C = C bonds.[1, 20] Unlike conventional thermal heating, MWI allows better control of the extent of GO reduction by hydrazine hydrates as both the MWI power and time can be adjusted to yield a nearly complete concurrent reduction of GO, iron nitrate and the palladium salt. Supporting the metal nanoparticles on the graphene sheets could prevent the formation of stacked graphitic structures because the metal nanoparticles can act as spacers to increase the distance between the sheets. This could lead to an increase in the surface area of the nanoparticle – graphene composites.[1, 20] Good dispersion of the metal nanocrystals on the graphene sheets can be achieved by the simultaneous reduction of the metal salts and GO during the MWI irradiation process.[20, 144]

This work is a kind of extension of our group previously work[284] in preparing palladium nanoparticles supported on graphene (Pd /G) as the separation and recycling process could be done much easier by using magnetic nanoparticles and the same catalytic activity and recyclability was also achieved.

116

6.3 Experimental

6.3.1 Chemicals and reagents

All chemicals used in our experiments were purchased and used as received without further purifications. Palladium nitrate (10 wt. % in 10 wt. % HNO_3, 99.999%) and hydrazine hydrate (80%, Hydrazine 51%) were obtained from Sigma Aldrich. Deionized water (D.I. H_2O, ~ 18 MΩ) was used for all experiments. High-purity graphite powder (99.9999%, 200 mesh) was purchased from Alfa Aesar. Aryl bromide, bromobenzene and potassium carbonate were also purchased from Aldrich and used as received. A mixture of ethanol-deionized water was used for the Suzuki cross-coupling reactions.

A JEOL JEM-1230 electron microscope operated at 120 kV has been used to obtain TEM images. The electron microscope is equipped with a Gatan UltraScan 4000SP 4K X 4K CCD camera. TEM samples were prepared by placing a droplet of the prepared catalyst dissolved in ethanol on a 300-mesh copper grid (Ted Pella) and then left to evaporate in air at room temperature. The X-ray photoelectron spectroscopy (XPS) analysis was executed on a Thermo Fisher Scientific ESCALAB 250 using a monochromatic Al KR X-ray. The X-ray diffraction patterns were measured at room temperature using X'Pert PRO PANanalytical X-ray diffraction unit. GC–MS analyses were performed on Agilent 6890 gas chromatograph equipped with an Agilent 5973 mass selective detector. A CEM Discover microwave instrument was used for cross-coupling reactions. The reactions were performed at operator selectable power output of 250 W.

117

6.3.2 Microwave Synthesis of an Efficient Catalyst of Palladium Nanoparticles Supported on Fe₃O₄, Co₃O₄, Ni (OH)₂ for Suzuki Cross – Coupling

An efficient magnetic catalyst has been successfully synthesized using a reliable, reproducible fast and simple method using microwave irradiation conditions. The prepared catalysts are magnetic which is an advantage in the separation process of catalyst from the reaction medium via applying a strong external magnetic field. What is reported here is a facile approach used for the synthesis of palladium supported on iron oxides, cobalt, and nickel hydroxide. Nanoparticles of magnetite (Fe_3O_4) and cobalt oxide Co_3O_4, and Nickel hydroxide $Ni(OH)_2$ have been prepared by a simple microwave heating method using Hydrazine hydrate as a strong reducing agent for mixtures of palladium nitrate in combination with Fe $(NO_3)_3.9H_2O$ and Co $(NO_3)_2.6H_2O$ that were successfully used as a source of iron and cobalt. Our catalyst showed high catalytic activity towards Suzuki cross – coupling reaction with 100% conversion for the catalyst first run.

6.3.3 Microwave Synthesis of an Efficient Catalyst of Palladium Nanoparticles with Fe₃O₄, Co₃O₄, and Ni (OH)₂ Supported on Graphene for Suzuki Cross – Coupling

Graphene oxide was prepared according to Hummers and Offeman method in which oxidation of high-purity graphite powder (99.9999%, 200 mesh) was done using a mixture of H_2SO_4/$KMnO_4$. Graphite (4.5 g, 0.375 mol) and $NaNO_3$ (2.5 g, 0.0294 mol) were mixed in a conical flask. The mixture was kept in an ice bath under continuous stirring while adding conc. H_2SO_4 (115 ml, 2.157 mol) followed by $KMnO_4$ (15 g, 0.095 mol) which was slowly added over 2.5 h. Then, deionized water (230 ml) was slowly added to the above mixture and once the mixture temperature became stable it was kept around 80˚C. Then, after 20 min.; deionized water (700 ml) were added followed by dropwise addition of (10%) H_2O_2 (20 ml, 0.667 mol).

118

The resulting yellowish-brown cake of solid was washed several times with 1M HCl followed by washing with hot deionized water. Then the poweder (graphite oxide) was dried under vacuum overnight. Resultant graphite oxide could be readily exfoliated to completely water dispersed graphene oxide (GO) by ultra-sonication. Four different catalysts were prepared under the same reaction conditions as in **Table 6-1**.

Table 6-1 Different Catalysts of Pd-Fe3O4/G

Catalyst	1	2	3	4
Pd (%)	50	20	6	10
Fe $(NO_3)_3.9H_2O$ (%)	50	20	34	30
Graphite Oxide (%)	-	60	60	60
(Pd - wt %) using ICP-OES	48	13	4.8	6

Catalyst 1 was prepared without using GO support, to prepare catalyst 1, Fe $(NO_3)_3.9H_2O$ (317.5 mg, 0.785 mmol) was dissolved in deionized water (50 ml) and sonicated for 1 h. then, Palladium nitrate (10 wt. % in 10 wt. % HNO_3, 99.999%, 1000 µl) was added to the iron nitrate solution. Then, the whole mixture was stirred for 3 h followed by the addition of the reducing agent hydrazine hydrate (1 ml) at room temperature and once the solution was heated by microwave for (120) s , the color changed to dark black color, indicating the completion of the chemical reduction. Then, the final product washed using hot deionized water 2-3 times, ethanol 2-3 times, and then dries in oven at 80˚C.

Catalyst 2 was prepared using GO support; to prepare catalyst 2, GO (60 mg) was dispersed in 50 mL of water for 1 h in a sonication bath to produce aqueous dispersion of graphene oxide. Then, deionized water (50 mL) in which appropriate amount of Palladium nitrate (10 wt. % in 10 wt. % HNO_3, 99.999%, 400 µl) and $Fe(NO_3)_3.9H_2O$ (127 mg, 0.314 mmol) were added and sonicated for 1 h, the solution was added to the aqueous dispersion of graphene oxide (GO) and stirred for 3 h.

119

After stirring the whole mixture for 3 h, the reducing agent hydrazine hydrate (2 ml) was added at room temperature and once the solution was heated by microwave for (120) s and the color changed to dark black color, indicating the completion of the chemical reduction. Then, the final product washed using hot deionized water 2-3 times, ethanol 2-3 times, and then dries in oven at 80°C.

Catalyst 3 was prepared using GO support; to prepare catalyst 3, GO (60 mg) was dispersed in 50 mL of water for 1 h in a sonication bath to produce aqueous dispersion of graphene oxide. Then, deionized water (50 mL) in which appropriate amount of Palladium nitrate (10 wt. % in 10 wt. % HNO_3, 99.999%, 120 µl) and $Fe(NO_3)_3.9H_2O$ (216 mg, 0.534 mmol) were added and sonicated for 1 h, the solution was added to the aqueous dispersion of graphene oxide (GO) and stirred for 3 h. after stirring the whole mixture for 3 h, the reducing agent hydrazine hydrate (2 ml) was added at room temperature and once the solution was heated by microwave for (120) s and the color changed to dark black color, indicating the completion of the chemical reduction. Then, the final product washed using hot deionized water 2-3 times, ethanol 2-3 times, and then dries in oven at 80°C.

Catalyst 4 was prepared using GO support; to prepare catalyst 4, GO (60 mg) was dispersed in 50 mL of water for 1 h in a sonication bath to produce aqueous dispersion of graphene oxide. Then, deionized water (50 mL) in which appropriate amount of Palladium nitrate (10 wt. % in 10 wt. % HNO_3, 99.999%, 200 µl) and $Fe(NO_3)_3.9H_2O$ (190.5 mg, 0.471 mmol) were added and sonicated for 1 h, the solution was added to the aqueous dispersion of graphene oxide (GO) and stirred for 3 h. After stirring the whole mixture for 3 h, the reducing agent hydrazine hydrate (2 ml) was added at room temperature and once the solution was heated by microwave for (120) s and the color changed to dark black color, indicating the completion of

120

the chemical reduction. Then, the final product washed using hot deionized water 2-3 times, ethanol 2-3 times, and then dries in oven at 80˚C.

6.3.4 General Procedure for Suzuki Cross-Coupling

The general procedure of different catalyst systems for Suzuki reactions was done by applying the following procedure in which Aryl bromide (0.51 mmol, 1 eq.) was dissolved in a mixture of 4mL H_2O:EtOH (1:1) and placed in a 10-mL microwave tube. To this were added the aryl boronic acid (0.61 mmol, 1.2 eq.) and Potassium carbonate (1.53 mmol, 3 eq.) and finally the palladium catalyst were then added with the previously mentioned prepared ratios. Afterwards, the tube was sealed with cap and heated under microwave irradiation (250W, 2.45 MHz) at the assigned temperature and time. After completing the reaction duration, the reaction mixture was poured into beaker. The progress of the reaction was monitored using GC-MS analysis.

6.3.5 General Procedure for Catalyst recycling

Aryl bromide (0.51 mmol, 1 eq.) was dissolved in a mixture of 4mL H_2O: EtOH (1:1) and placed in a 10-mL microwave tube. To this were added the aryl boronic acid (0.61 mmol, 1.2 eq.) and Potassium carbonate (1.53 mmol, 3 eq.) and finally the palladium-magnetite on graphene nanoparticles (Pd-Fe3O$_4$/G) (3.5 mg, 2.55 µmol, 0.5 mol %) were then added. Then, the tube was sealed with cap and heated under microwave irradiation (250W, 2.45 MHz) at the assigned temperature and time. After the reaction completed, the progress of the reaction was monitored using GC-MS analysis to an aliquot of the reaction mixture. After the reaction was completed; the mixture was diluted with ethanol and shaken. Then, the solvent above the catalyst was completely magnetically decanted and the catalyst was completely removed using external strong magnet.

121

Ethanol washing for the catalyst was repeated for 5 times to make sure that all products were removed from catalyst surface. The catalyst was then transferred directly to another microwave tube and fresh reagents were added for next run. This procedure of recycling the catalyst was repeated for every run, the GC-MS was used to determine the percent conversion of the product.

6.4 Results and Discussion

6.4.1 Palladium nanoparticles supported on Fe_3O_4, Co_3O_4, $Ni(OH)_2$ supports for Suzuki Cross – Coupling

The Suzuki cross coupling reaction of bromobenzene and phenyl boronic acid in a mixture of H_2O: EtOH (1:1) at different temperatures was investigated. As shown below in table 9; it illustrates the conversion of reaction for different loadings of the Pd/Fe_3O_4 catalysts. While most ratios of the catalyst demonstrated different kind of activity toward Suzuki coupling. All Pd supported on iron oxide catalysts show complete conversion (100%) of aryl bromide to the biphenyl product within 5-10 min, at 120 ^{o}C. While there was no conversion at all when testing 100% Pd, Fe, Co catalyst for cross coupling and this may be due to the absence of any kind of supports if this was compared to the palladium supported on iron oxide case. Similarly; the Suzuki cross coupling reaction of bromobenzene and phenyl boronic acid in a mixture of H_2O: EtOH (1:1) at different temperatures was investigated. As it shown in **Table 6-2** below, it illustrates the conversion of reaction for different loadings of the Pd/Co catalysts. While most ratios of the catalyst demonstrated different kind of activity toward Suzuki coupling. All Pd supported on cobalt oxide catalysts show weak conversion (10%) of aryl bromide to the biphenyl product within 5-10 min, at 80 ^{o}C. while there was no conversion at all when testing 100% Pd, Fe, Co catalyst for cross coupling and this may be due to the absence of any kind of supports if this was compared to the palladium supported on cobalt oxide case.

122

It was noticed that the conversion was increased as the amount of palladium loading increased until 85 % conversion was obtained within 10 min, at 120 ^{o}C in case of 30% Pd – 70% Co. But increasing the palladium content didn't enhance the conversion as in case of 50% Pd – 50% Co which was around 48% conversion. But in case of Pd supported on nickel hydroxide the conversion was around 25 % as shown in **Tables 6-2 and 6-3**.

Table 6-2 Conversion percentage for different ratios of Pd-Fe$_3$O$_4$

Catalysts	mol%	Temp (^{o}C)	Time (min.)	Conversion%
40 wt% Pd/Fe$_3$O$_4$	1	80 ^{o}C, μw	5	41
	1	80 ^{o}C, μw	10	44
	1	120 ^{o}C, μw	10	100
20 wt% Pd/Fe$_3$O$_4$	1	80 ^{o}C, μw	5	41
	1	80 ^{o}C, μw	10	72
	1	120 ^{o}C, μw	10	100
	1	120 ^{o}C, μw	5	100
50 wt% Pd/Fe$_3$O$_4$	1	80 ^{o}C, μw	5	66
	1	80 ^{o}C, μw	10	100
	1	120 ^{o}C, μw	10	100
	1	120 ^{o}C, μw	5	100
100 % Fe$_3$O$_4$, Pd, Co$_3$O$_4$, Ni (OH)$_2$	1	120 ^{o}C, μw	10	Conversion ‹ 40

123

Table 6-3 Conversion percentage for different ratios of Pd – Co₃O₄

Catalysts	mol%	Temp (°C)	Time (min.)	Conversion%	Base
10 wt% Pd/Co₃O₄	1	80 °C, μw	10	10	
20 wt% Pd/Co₃O₄	1	120 °C, μw	5	23	K₂CO₃
30 wt% Pd/Co₃O₄	1	120 °C, μw	10	85	
50 wt% Pd/Co₃O₄	1	120 °C, μw	10	48	

Magnetic Recycling
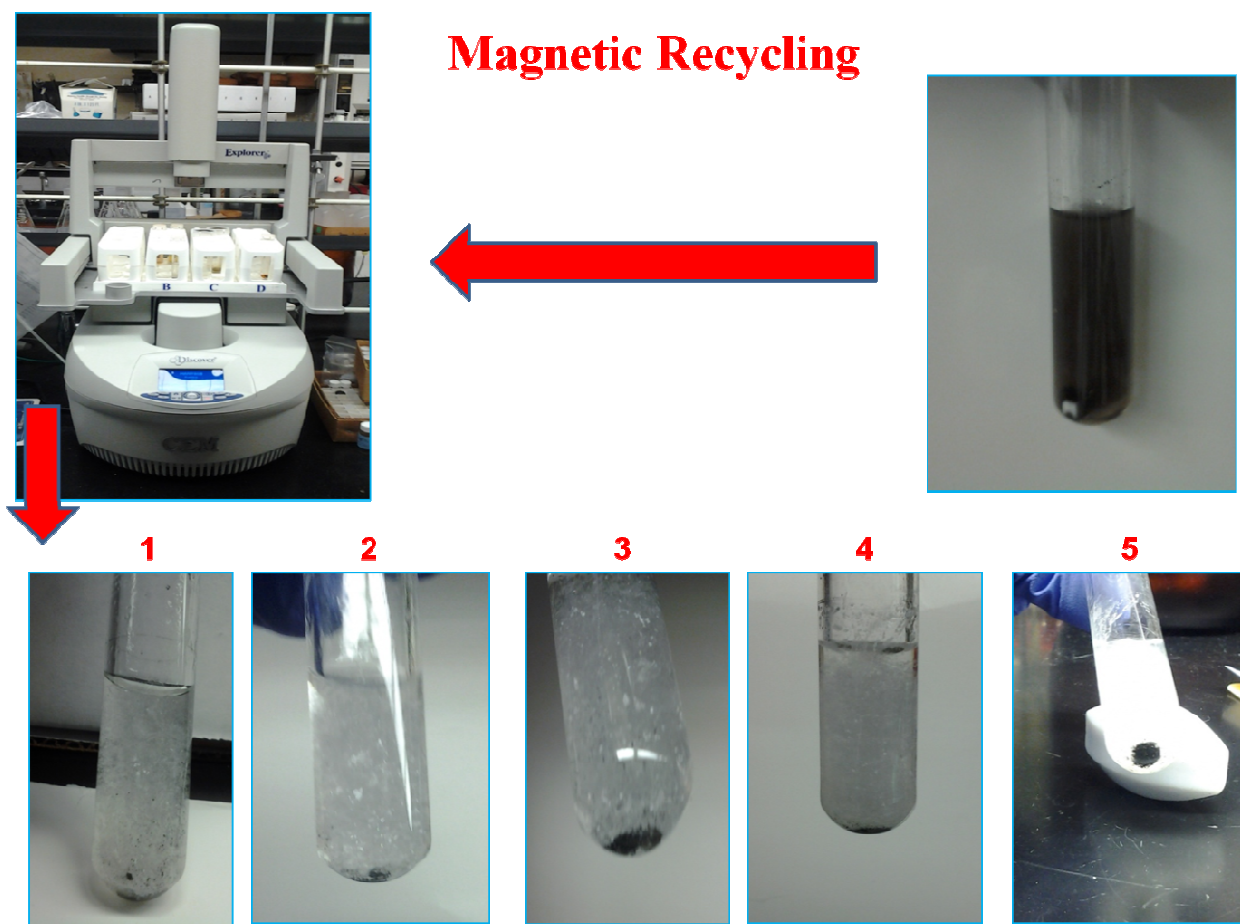
Figure 6-1 General Recycling Process of magnetic catalysts

6.4.2 Palladium – Fe$_3$O$_4$, Co$_3$O$_4$, Ni (OH) $_2$ supported on Graphene for Suzuki Cross – Coupling

The Suzuki cross coupling reaction of bromobenzene and phenyl boronic acid in a mixture of H$_2$O: EtOH (1:1) at different temperatures was investigated. As shown below in table 11; it illustrates the conversion of reaction for different types of the catalysts. While most ratios of the catalyst demonstrated different kind of activity toward Suzuki coupling. All Pd- Fe$_3$O$_4$ and Pd- Co$_3$O$_4$ catalysts show complete conversion (100%) of aryl bromide to the biphenyl product within 5 min, at 80 $^{\circ}$C. while there was less catalytic activity in case of Pd- Ni (OH)$_2$.
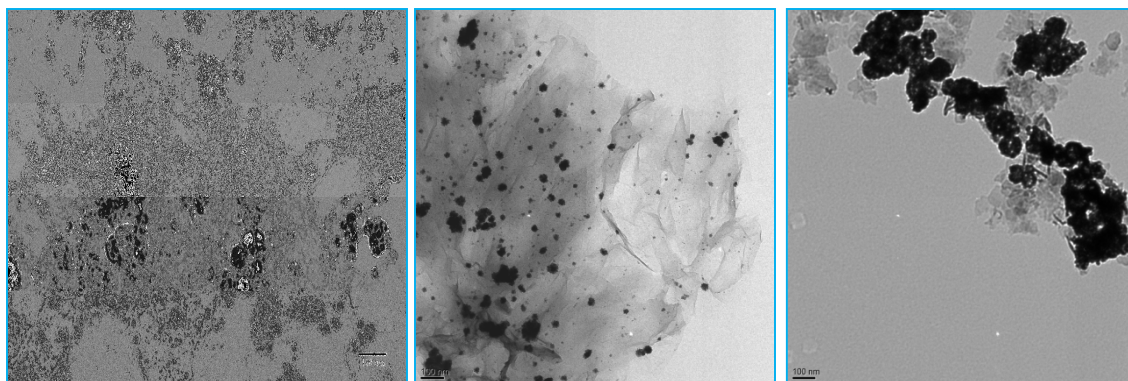
Figure 6-2 TEM – images of (a) Pd-Fe$_3$O$_4$/G , (b) Pd- Co$_3$O$_4$/G, and (c) Pd-Ni(OH)$_2$/G

From the TEM images in **Figure 6-2**, it is easy to remark the well dispersed palladium nanoparticles of size (35 ± 2 nm) and (25 ± 2 nm) as in figures 6-2a and 6-2b respectively while for the same figures the size of Fe$_3$O$_4$ and Co$_3$O$_4$ was (52 ± 2 nm) and (45 ± 2 nm) respectively. The TEM images here is consistent with the experimental results that showed a high catalytic activity in case of Pd/Fe$_3$O$_4$ and Pd/Co$_3$O$_4$ supported on graphene when compared with and Pd/Ni (OH)$_2$ supported on graphene which is probably due to the severe agglomeration in the later case compared with the former case.

125

Table 6-4 Conversion percentage for different ratios of Fe₃O₄, Co₃O₄, Ni (OH)₂ supported on Graphene

Catalysts	Mol%	Temperature ($^{\circ}$C)	Time (min.)	Conversion%
Pd-Fe$_3$O$_4$/G	1	$^{\circ}$C, μw	5	100
Pd-Co$_3$O$_4$/G	1	$^{\circ}$C, μw	5	100
Pd-Ni (OH)$_2$/G	1	$^{\circ}$C, μw	5	Conversion ‹ 60

Characterization of the graphene supported Pd-Fe₃O₄ samples prepared by the HH-MWI, method was examined in detail using XRD, XPS, and TEM analyses. Here, we focus on the characterization and catalytic activity of the Pd-Fe₃O₄ /G nanocatalysts. The palladium content in Pd/Fe₃O₄ and three different Pd/Fe₃O₄/G catalysts was determined by means of inductively coupled plasma (ICP-OES) and amounted to 48, 13, 4.8, and 6 wt %, respectively as shown in **Table 6-1**.

Figure 6-3a displays the XRD patterns of the initial graphite powder, the prepared GO, and Pd-Fe₃O₄/G prepared by the HH-MWI method. The initial graphite powder shows the typical sharp diffraction peak at $2\theta = 26.7^{\circ}$ with the corresponding d-spacing of 3.34 ˚A. The exfoliated GO sample shows no diffraction peaks from the parental graphite material and only a new broad peak at $2\theta = 10.9^{\circ}$ with a d-spacing of 8.14 ˚A observed. This indicates that the distance between the carbon sheets has increased due to the insertion of interplaner oxygen functional groups.

After MWI of the GO in the presence of HH as the reducing agent, the XRD of the resulting graphene shows the disappearance of the 10.9˚ peak confirming the complete reduction of the GO sheets. A similar XRD spectrum is observed for the Pd-Fe₃O₄/G sample prepared by the simultaneous reduction of GO and palladium nitrate – iron nitrate mixture using HH under MWI.

The very small broad peak around $2\theta = 26.7°$ in the Pd-Fe_3O_4/G sample could suggest the presence of a minor component of multilayer graphene. The presence of Pd nanoparticles could enhance the interaction among a few graphene layers.

Figure 6-3 (a) XRD Pattern of Graphite and Graphite Oxide (b) XRD Pattern of Fe_3O_4 , Palladium, Palladium-Fe_3O_4 , and catalysts 2, 3, and 4 (Palladium-Fe_3O_4 / Graphene)

However, the very weak intensity of the $2\theta = 26.7°$ peak indicates that the extent of multilayer graphene in the Pd-Fe_3O_4/G sample is insignificant. Generally, the XRD pattern in **Figure 6-3b** clearly indicates that the product is enriched with Fe_3O_4 and metal Pd (0). The palladium shows the typical sharp diffraction peak at $2\theta = 40°$. The XRD patterns indicate that the products were all (Fe_3O_4) magnetite with reference code (ICCD-00-003-0863). It is also easily to notice that the sharp diffraction peak at $2\theta = 40°$ which is characteristic to palladium and also the characteristic peaks of Fe_3O_4 is shown as a sharp diffraction peak at $2\theta = 35°$.

127

The very small broad peak around $2\theta = 26°$ in Pd- Fe_3O_4 /G sample could suggest the presence of a minor component of multilayer graphene. The diffraction peaks (2θ) of Pd- Fe_3O_4 /G at 40, 46.8, and 68.2 are ascribed to the (111), (200), and (220) planed of Pd NPs which are similar to pure palladium and also to the peaks of Pd- Fe_3O_4 as shown. **Figures 6-4a, b, c, and d** display representative TEM images of the Pd-Fe_3O_4 and Pd-Fe_3O_4/G catalysts. The TEM images show the presence of uniform well-dispersed Pd-Fe_3O_4 nanoparticles on Graphene.
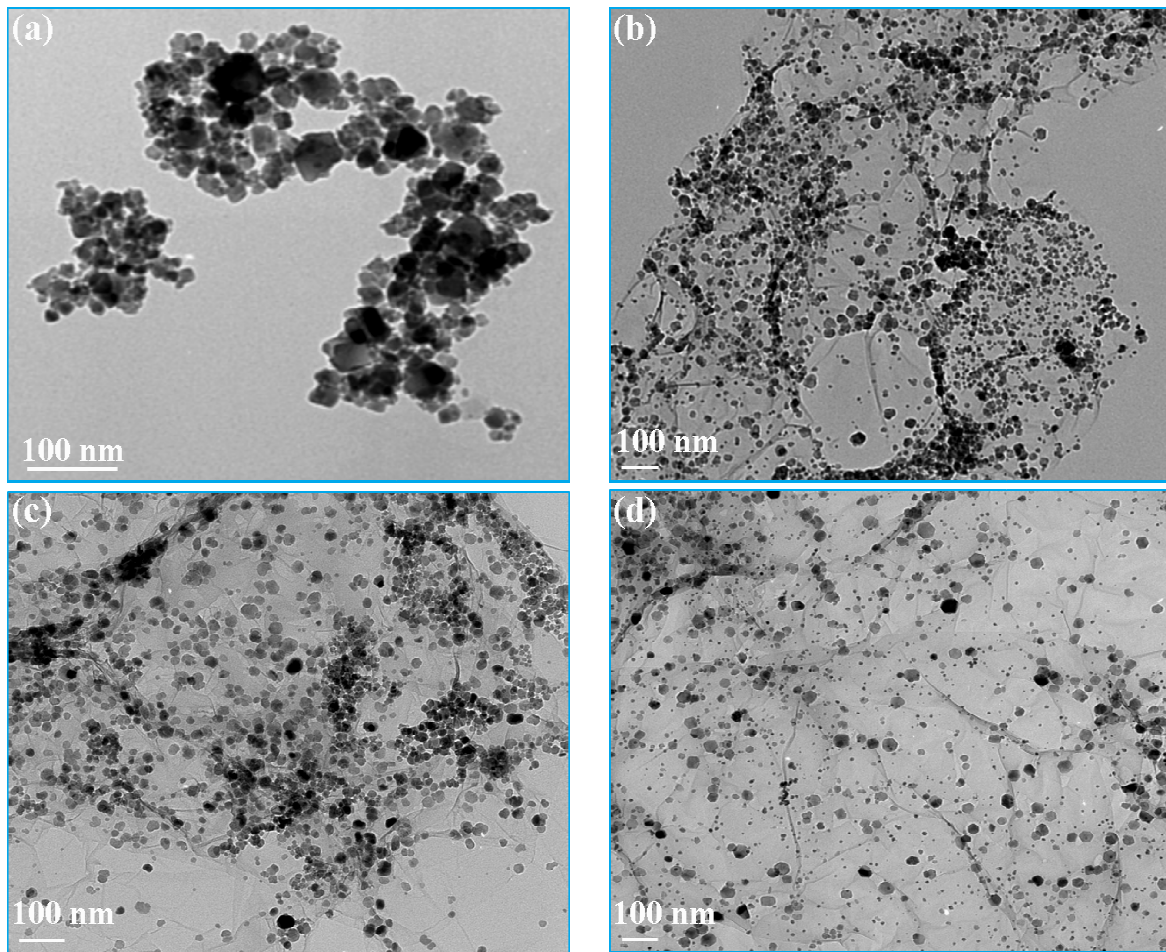
Figure 6-4 TEM – images of Different Catalysts Catalyst 1, (b) Catalyst 2, (c) Catalyst 3, (d) Catalyst 4

From these TEM images, it was found that for catalyst 1, the particle size of Pd was (26-28 nm) while it was (48-50 nm) for magnetite as in **Figure 6-4a**. For catalyst 2, the particle size of Pd was (14-16 nm) while it was (28-30 nm) for magnetite as in **Figure 6-4b**. For catalyst 3, the particle size of Pd was (10-12 nm) while it was (22-24 nm) for magnetite as in **Figure 6-4c**. For catalyst 4, the particle size of Pd was (4-6 nm) while it was (18-20 nm) for magnetite as in **Figure 6-4d**. So, generally it is obvious that catalyst 4 is the best one in dispersion of Pd – Fe_3O_4 on the graphene surface and also it has smaller particle size which is a very important and decisive factor in catalysis. This is very consistent with the catalytic activity data obtained from experimental testing of these catalysts.
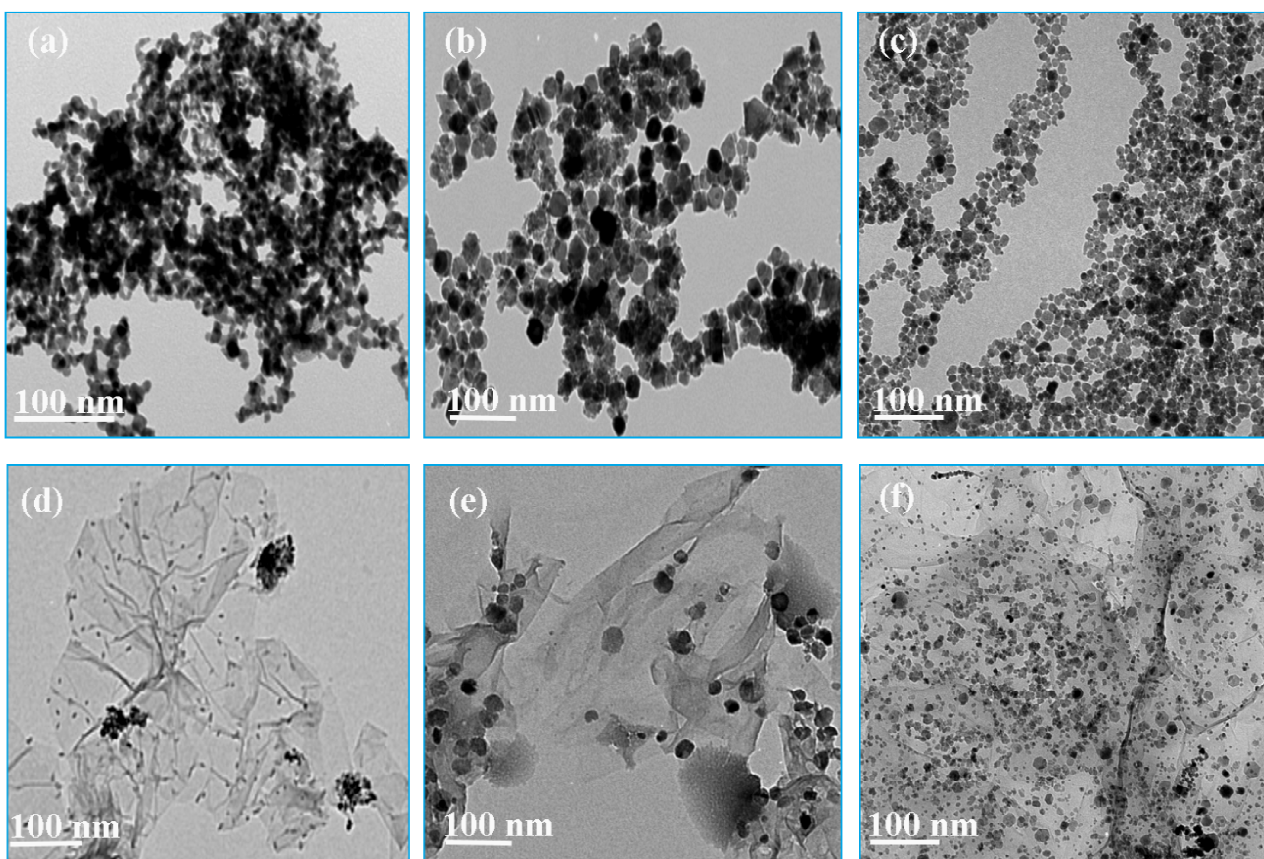
Figure 6-5 TEM – images of (a) Pd, (b) Fe_3O_4, (c) Pd-Fe_3O_4, (d) Pd-G, (e) Fe_3O_4 – G,   (f) Pd-Fe_3O_4/G

It is very interesting to note the role of Pd^{+2} in assisting the formation of magnetite nanoparticles onto the surface of the nanosheets of graphene. Generally, it is clear from **Figure 6-5** that palladium presence is a decisive factor in avoiding the agglomeration of products after microwave-assisted reduction of graphene oxide with Fe^{+2} alone using hydrazine hydrate. To differentiate between Pd, Fe_3O_4, and Graphene, TEM images were used to differentiate between different shapes. As shown in **Figure 6-5**, all these catalysts were prepared under the same conditions of preparation to make use of its TEM images as a reference for each catalyst in case of using a combination of Pd, Fe_3O_4, and Graphene. From these TEM images, it was found that the particle size of Pd was (15-17 nm) as in **Figure 6-5a**, Fe_3O_4 was (36-38 nm) as in **Figure 6-5b**, Pd - Fe_3O_4 was (15-17 nm) and (36-38 nm) as in **Figure 6-5c**, Pd - G was (8-10 nm) as in **Figure 6-5d**, Fe_3O_4 - G was (30-32 nm) as in **Figure 6-5e**, Pd-Fe_3O_4-G was (4-6 nm) and (16-18 nm) as in **Figure 6-5f**. So, generally it was determined that the smaller particles are palladium while the larger ones were for magnetite.

The XPS technique is more sensitive for the analysis of surface oxides than XRD. All the samples had a C1s binding energy around 284.5 eV derived from the carbon contamination in the analysis as shown in **Figure 6-6a**.

Samples showed that the binding energy (the energy difference between the initial and final states of the photoemission process) of Fe 2P 3/2 was 710.5 eV, indicating that the Fe was present as Fe_3O_4 and also the binding energy of Fe 2P 1/2 was 723.7 eV indicating that Fe was present in the oxidation state of Fe_3O_4 as shown in **Figure 6-6b**.
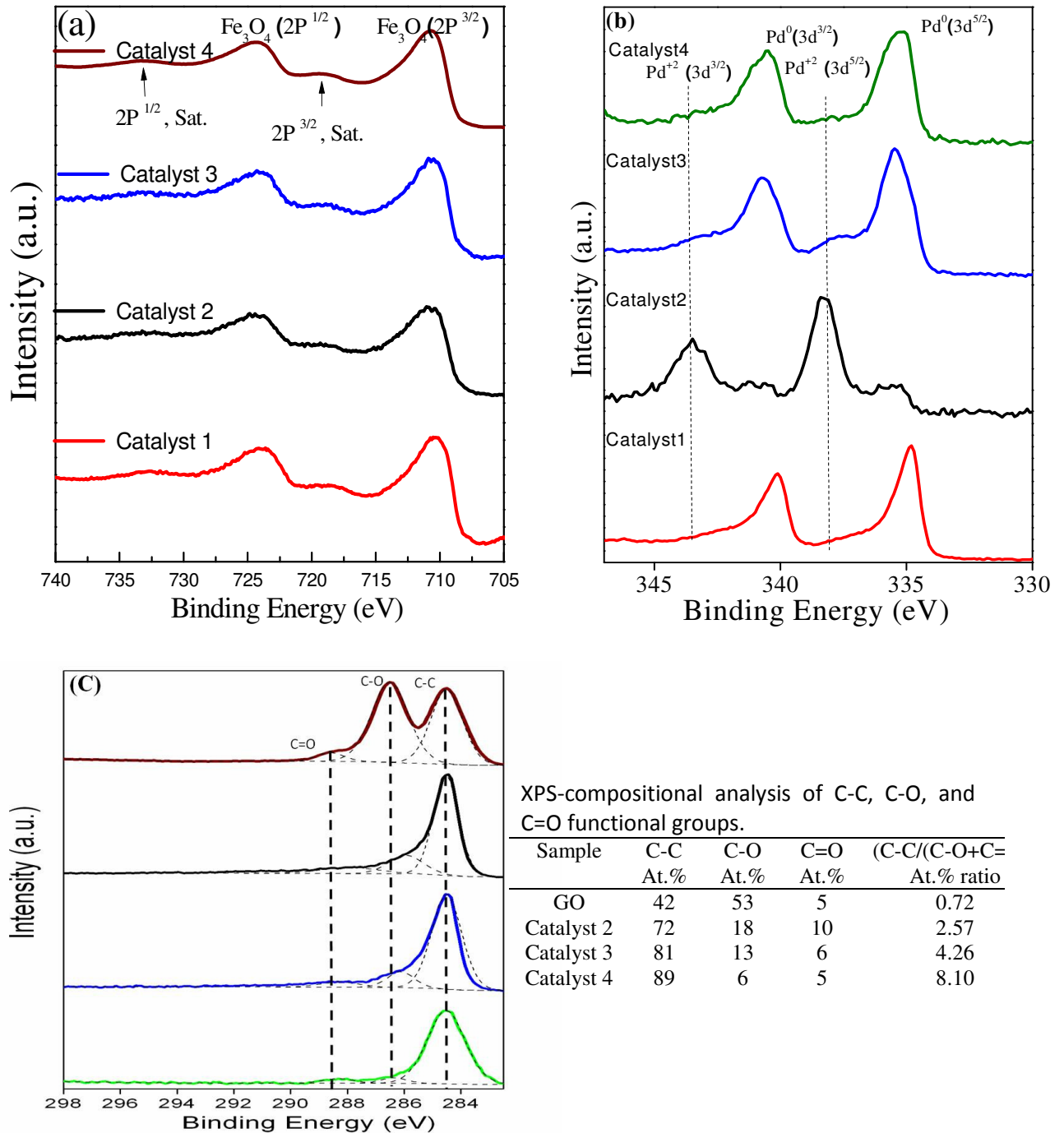
Figure 6-6 **(a) XPS spectra of Fe 2p $^{3/2}$ and Fe 2p $^{1/2}$ electrons binding energies, (b) XPS spectra of Pd 3d $^{5/2}$ and Pd 3d $^{3/2}$ electrons binding energies for Palladium - Fe$_3$O$_4$ " cat. 1", Palladium - Fe$_3$O$_4$ supported on graphene "cat. 2, 3, and 4", (c)) XPS spectra of C 1s electrons binding energies for GO, Palladium-Fe$_3$O$_4$ supported on graphene "cat. 2, 3, and 4".**

131

It is so important to note that in case of catalyst 2 as shown in **Figure 6-6a**, some of Pd is in form of PdO or (Pd^{+2}) but some of Pd is in the form of Pd^0 . While, **Figure 6-6b** shows that in case of catalyst 3, nearly all of Pd is in form of Pd (0) - which is consistent with the better catalytic activity of catalyst 3 compared to catalyst 2. While, **Figure 6-6a** shows that in case of catalyst 4 –also most of Pd is in the form of Pd^0 which besides excellent dispersion of palladium on graphene surface as shown previously in TEM images is consistent with experimental data that reveals the excellent catalytic activity of this catalyst among all catalysts that were investigated for Suzuki cross coupling reactions.

Also, the binding energies of Pd 3d5/2 was 334.8, 335.14 eV, and Pd 3d3/2 was 340.1, 340.57 eV corresponding to Pd^0. Similarly, the binding energies of Pd 3d3/2 was 341.38, 343.2 eV, and Pd 3d5/2 was 336.23, 337.85 eV corresponding to Pd (II).

6.4.3   Recycling of Palladium – Fe_3O_4 / Graphene Catalysts

The Suzuki cross coupling reaction of bromobenzene and phenyl boronic acid in a mixture of H_2O: EtOH (1:1) at different temperatures was investigated for different types of the catalysts. While most ratios of the catalysts demonstrated different kind of activity toward Suzuki coupling. All Pd- Fe_3O_4 / G catalysts in general showed complete conversion (100%) of aryl bromide to the biphenyl product within 5 min, at 80 °C.

Table 6-5 display different catalysts that were tested. The palladium content in catalysts was determined by means of inductively coupled plasma (ICP-OES) and amounted to be 4.8 wt. % and 6 wt. % for catalysts 3 and 4 respectively. **Table 6-5** shows also recycling experiments with Pd/Fe_3O_4 and Pd- Fe_3O_4 /G catalysts using a concentration of 0.7 mol%.
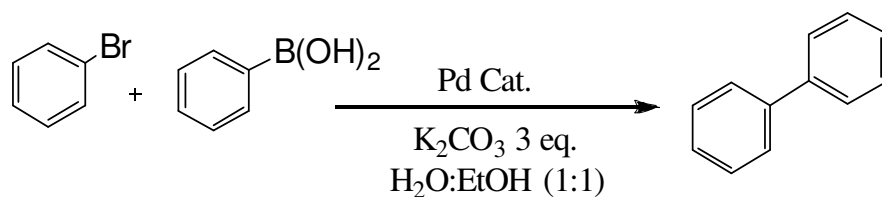
Scheme 6-1 Suzuki cross-coupling reaction with Pd-Fe$_3$O$_4$/G

Table 6-5 Recycling experiments for different ratios of Pd-Fe$_3$O$_4$/G catalyst using a concentration of 0.5, 1 mol %.[a]

Run	Conversion (%)[b] Cat. 3 (0.5 mol %)	Conversion (%)[b] Cat. 3 (1 mol %)	Conversion (%)[b] Cat. 4 (0.5 mol %)	Conversion (%)[b] Cat. 4 (1 mol %)
1	100	100	100	100
2	100	96	100	100
3	100	94	93	93
4	90	93	91	93
5	81	92	90	92
6	67	82	79	92
7	62	79	71	92
8	60	-	65	89
9	46	-	-	81
10	-	-	-	80

[a] Bromobenzene (50 mg, 0.32 mmol), boronic acid (47 mg, 0.382 mmol, 1.2 eq.), potassium carbonate (133 mg, 0.96 mmol, 3 eq.), and Pd-Fe$_3$O$_4$/G (2.17 mg, 1.16 µmol, 0.5 mol%) or (4.34 mg, 2.32 µmol, 1 mol%) in 4 mL (H2O:EtOH) (1:1) were heated at 80˚C (MWI) for 10 min.

[b] Conversions were determined by GC–MS.

It was also found as in table 2 that catalyst 4 shows more catalytic activity than catalyst 3. As in case of using catalyst 3 with 0.5 mol % it could be recycled up to three times with 100 % conversion; while using catalyst 4 with the same mole percentage could be recycled up to four times with 100 % conversion. Also; by increasing the mole percentage to 1 mol %, catalyst 3 could be recycled up to five times with 100 % conversion; while using catalyst 4 could be recycled up to seven times with 100 % conversion.

133

The general procedure of catalyst recycling as discussed in details before is shown in **Figure 6-7**. It is interesting to notice the easy separation process of the catalyst by applying an external magnetic field using a strong magnet.
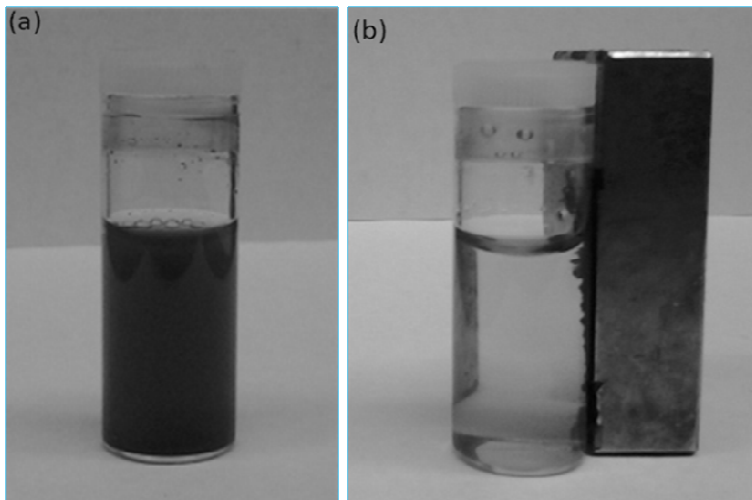
Figure 6-7   (a) The mixture after reaction. (b) Separating the catalyst 4 from reaction mixture by a strong magnet
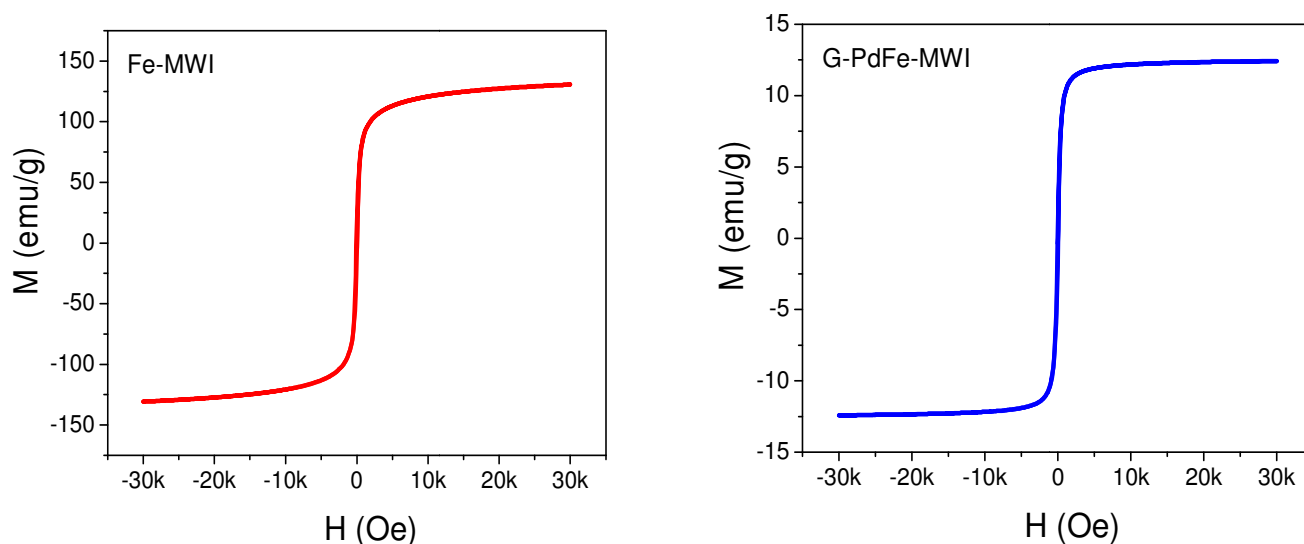
Figure 6-8   Magnetic hysteresis loops of Fe₃O₄ and Pd - Fe₃O₄ / G at room temperature after MWI

The magnetic properties of selected catalysts were carried out by using Vibrating Sample Magnetometer (VSM) analysis. **Figure 6-8** presents the magnetic hysteresis loop of Fe_3O_4 and $Pd - Fe_3O_4 / G$ and reveals the magnetic response of both of them to the varying magnetic field.

134

Figure 6-8 simply shows the hysteresis curves obtained for Fe_3O_4 and Pd - Fe_3O_4 / G with an applied field sweeping from -30 to 30 kOe.

The hysteresis loops of prepared samples reveal superparamagnetic behavior at room temperature with nearly zero coercivity and extremely low remnant magnetization values. The lack of remaining magnetization when the external magnetic field is removed is in agreement with a superparamagnetic behavior observed in graphene nanosheets decorated with Pd-Fe_3O_4 nanoparticles.
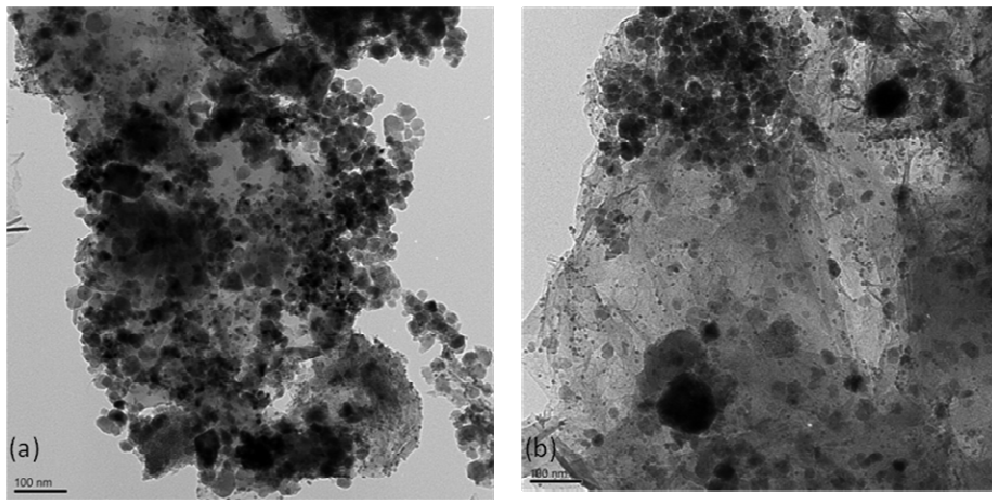
Figure 6-9 TEM images of Pd-Fe$_3$O$_4$/G after the 6th run for (a) catalyst 3 and (b) catalyst 4.

It also remarkable that using the catalyst for more recycles still give a remarkable catalytic activity of 80 % for run 10. The activity of catalyst 3 dropped in run 8 and 9, showing only 60 % and 46 % conversions, respectively. But in case of catalyst 4; the activity dropped in run 8 and 10, showing 89 % and 80 % conversions, respectively. TEM images of Pd-Fe_3O_4/G can be an evidence for deactivation that happens to catalysts after 8th run, which clearly demonstrates the agglomeration and accumulation of both Pd and Fe_3O_4 nanoparticles on the surface of graphene as shown in **Figure 6-9**.

135

These results indicate that the mechanism of deactivation of the catalyst is likely to involve the formation of aggregated Pd and Fe_3O_4 nanoparticles which result in decreasing the surface area and the saturation of coordination sites. The leaching of Pd from the Pd/Fe_3O_4/G catalyst was also investigated; the Pd concentration in the product solution after first run followed by magnetic separation using a strong magnet was monitoredusing ICP-MS that showed that the Pd concentration was 25 ppb. This value is lower than any other value that had been reported before.[277]

6.5 Conclusions

Graphene is a unique high surface area support for metallic and bimetallic nanoparticle catalysts for a variety of important chemical transformations. In addition to the large surface area, the high thermal, chemical, and mechanical stability make graphene an excellent catalyst support. Furthermore, structural defects in the graphene lattice can be useful in anchoring the metal nanoparticles to the graphene surface thus achieving new surface functionalities with tunable metal-support interaction. Several studies have demonstrated unusual catalytic activity for metallic and bimetallic nanoparticles supported on the defect sites of the graphene nanosheets. An efficient magnetic catalyst has been successfully synthesized using a reliable, reproducible fast and simple method using microwave irradiation (MWI) approach. Microwave irradiation (MWI) method is considered a facile approach used for the synthesis of a well dispersed magnetically separable palladium-magnetite supported on graphene, which can act as a unique catalyst against carbon-carbon cross-coupling due to the well dispersion of palladium nano particles throughout the magnetite-graphene surface.

136

Nanoparticles of Pd with magnetite (Fe_3O_4) and Cobalt oxide Co_3O_4 and supported on graphene have been prepared by a simple microwave heating method using Hydrazine hydrate as a strong reducing agent for mixtures of palladium nitrate in combination with Fe $(NO_3)_3.9H_2O$ and Co $(NO_3)_2.6H_2O$ that were successfully used as a source of iron and cobalt.

The prepared catalyst showed a remarkable catalytic activity towards Suzuki cross – coupling reaction with 100% conversion for the catalyst first run. Furthermore, the prepared catalyst could be easily recovered and recycled up to eight times with high catalytic activity near 100% in case of palladium – iron oxide supported on graphene under batch reaction conditions, thus providing high economic viability. In summary, we have developed an efficient method to generate highly active Pd-Fe_3O_4 nanoparticles supported on graphene by microwave assisted chemical reduction of the corresponding aqueous mixture of a palladium nitrate, ferric nitrate and dispersed graphite oxide sheets. The bimetallic material offers a number of advantages including high reactivity, mild reaction conditions and short reaction times in an environmentally benign solvent system. Furthermore, the magnetic properties imparted by the iron oxide component of the catalyst enables the material to be easily isolated and recycled, thus greatly simplifying the ability to purify the reaction product and recycle the catalyst. This catalyst also provided excellent yields over a broad range of highly functionalized substrates.

137

CHAPTER 7 Microwave-Assisted Synthesis of Pd/Fe$_3$O$_4$ Nanoparticles Supported on Graphene; an Efficient and Magnetically Recyclable Catalyst used for Suzuki Cross-Coupling Reactions in a High Temperature / Pressure Capillary Flow Reactor

7.1 Overview

A facile microwave assisted reduction technique has been developed to prepare a well dispersed highly active Pd/Fe$_3$O$_4$ nanoparticles supported on graphene sheets (Pd-Fe/G), which can act as a unique catalyst against Suzuki cross coupling reactions due to the uniform decoration of palladium nanoparticles throughout the surface of magnetite - graphene. The method involves simultaneous reduction of the corresponding Pd (NO$_3$)$_2$ and Fe (NO$_3$)$_3$.9H$_2$O in the presence of graphene oxide (GO) sheets under the microwave irradiation conditions using hydrazine hydrate as the reducing agent. The Pd-Fe$_3$O$_4$/G nanoparticles have shown to exhibit extremely high catalytic activity for Suzuki cross coupling reactions under batch reaction conditions. The remarkable catalytic activity and recyclability of these materials can be attributed to the high degree of dispersion and concentration ratio of the Pd/Fe nanoparticles deposited on the surface of graphene with a small particle size of 3-6 nm due to the effective microwave assisted reduction method. These nanoparticles are further characterized by variety of spectroscopic techniques including X-ray photoelectron spectroscopy (XPS), X-ray diffraction (XRD), and transmission electron microscopy (TEM). High-temperature/pressure organic synthesis can be performed under continuous flow conditions in a stainless steel microtubular flow reactor capable of achieving temperatures of 350 °C and 200 bar (X-Cube ™). Reaction optimization was performed by changing the temperatures, pressures and flow rates "on-the-fly".

138

In general, the chemistry optimized under high-temperature microwave batch conditions could be successfully translated to a scalable flow regime.

7.2 Introduction

In the present work, the Pd-Fe$_3$O$_4$/G nanocatalyst was prepared using microwave irradiation (MWI) method. MWI has been demonstrated for the synthesis of a variety of nanomaterials with controlled size and shape without the need for high temperature or high pressure. The main advantage of MWI over other conventional heating methods is that the reaction mixture is heated uniformly and rapidly as mentioned before.

The use of a microfluidics-based flow reactor (X-CubeTM) offers an elegant solution for the problems that appear under batch reaction conditions. It is easy to be used as catalysts are placed in CatCartTM cartridges. Moreover, it enables the synthesis of chemical libraries of a great number of products in a short time and optimization of reaction conditions in minutes. Here, the catalytic activity of the catalyst was evaluated on the cross-coupling reactions of bromobenzaldehyde in the presence of phenyl boronic acid carried out in the flow reactor X-CubeTM using PdFe$_3$O$_4$ / G catalyst as in **Figure 7-1**. A detailed investigation of the effects of the changes in the reaction conditions (temperature, flow rate) has been carried out.

7.3 Experimental

7.3.1 Chemicals and reagents

All chemicals used in our experiments were purchased and used as received without further purifications. Palladium nitrate (10 wt. % in 10 wt. % HNO$_3$, 99.999%) and hydrazine hydrate (80%, Hydrazine 51%) were obtained from Sigma Aldrich. Deionized water (D.I. H$_2$O, ~ 18 MΩ) was used for all experiments.

139

High-purity graphite powder (99.9999%, 200 mesh) was purchased from Alfa Aesar. Aryl bromide, bromobenzene and potassium carbonate were also purchased from Aldrich and used as received. A mixture of ethanol-deionized water was used for the Suzuki cross-coupling reactions. A JEOL JEM-1230 electron microscope operated at 120 kV has been used to obtain TEM images. The electron microscope is equipped with a Gatan UltraScan 4000SP 4K X 4K CCD camera. TEM samples were prepared by placing a droplet of the prepared catalyst dissolved in ethanol on a 300-mesh copper grid (Ted Pella) and then left to evaporate in air at room temperature. The X-ray photoelectron spectroscopy (XPS) analysis was executed on a Thermo Fisher Scientific ESCALAB 250 using a monochromatic Al KR X-ray. The X-ray diffraction patterns were measured at room temperature using X'Pert PRO PANanalytical X-ray diffraction unit. GC–MS analyses were performed on Agilent 6890 gas chromatograph equipped with an Agilent 5973 mass selective detector.

The X-Cube™ is a continuous flow reactor, capable of performing chemical reaction under inert conditions, temperatures up to 200°C and pressures up to 150 bar. It has been reported that carbon-carbon forming reactions are far more efficient on the X-Cube™ in comparison to batch mode. The reaction solvent was allowed to flow through the X-Cube™ system for 10 minutes to equilibrate the filled CatCart as shown in **Figure 7-1a** , where the catalyst were loaded using manual piston as shown in **Figure 7-1b**. A sample of the starting materials in the reaction solvent was pumped through the X-Cube™, the total amount of product mixture was collected to sample vial and the column was washed with the eluent to remove any material still absorbed to the CatCart; the product mixture was analyzed by GC-MS, HPLC-MS and NMR.

140
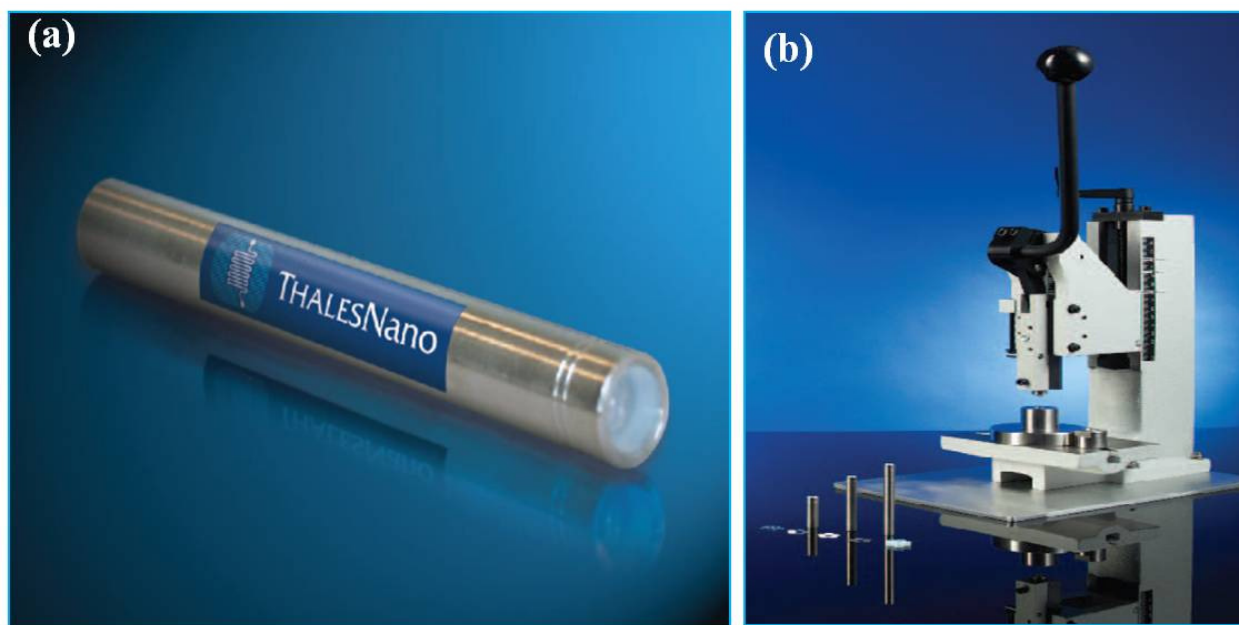
Figure 7-1 (a) CatCart cartridge filled with catalyst. (b) Manual piston used for loading the catalyst inside CatCart cartridge.

The microreactor system used for the studies is a high temperature, high pressure microtubular flow unit that can be used for processing homogeneous reaction mixtures (X-Cube Flash™), as in **Figure 7-2**. The reactor uses stainless steel coils of variable length that can be directly heated across their full length by electric resistance heating to temperatures up to 350 °C. The reaction mixture is introduced to the reactor block containing the steel coils and a heat exchanger via one (or more) standard HPLC pumps.[285]
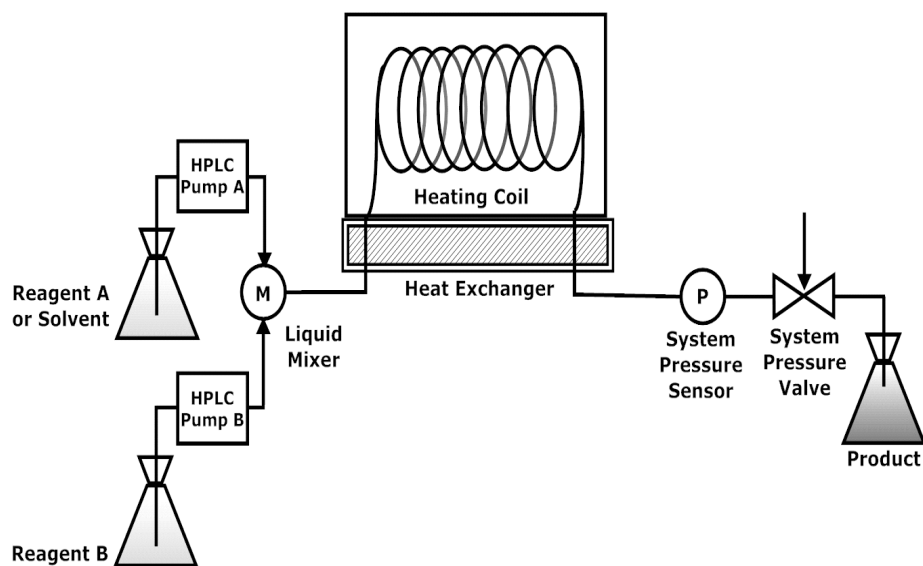
Figure 7-2 High-temperature/pressure capillary flow reactor (schematic).[285]

Conceptually similar continuous flow equipment has already been described in the late 1970s by Köll and Metzger. In these setups a stainless steel coil was combined with standard HPLC equipment, i.e., pumps, pressure valves, etc., and a GC oven as a heat source to reach high temperatures (340 °C) and pressures (250 bar) under continuous flow conditions.[285]

The instrument having the heating block, pressure sensors and back pressure regulator, all controlled by the integrated controlling unit, can either work on its own with independent HPLC pumps or with a dedicated pump unit when connected to an Ultra mobile PC

(UMPC) with touch screen controls. The exchangeable heating block contains stainless steel coils (steel type SX 316L, i.d. 1000 lm) of variable length. These coils are directly heated across their full length by electric resistance, which heats to temperatures of up to 350 °C. The temperature of the coils is measured by thermocouples attached to the outer surface of the stainless steel tubing at two different points along the length of the coil.

142

This will approximately reflect the temperature of the reaction mixture contained inside the coils. Since the readout from the thermocouples is used to control the generator power heating the coils, a genuine temperature feedback mechanism exists that can prevent unwanted temperature rises inside the coils, e.g., as a result of exotherms or thermal runaways. The front aluminum plate when fixed to the stainless steel housing serves as a heat sink or heat exchanger. This heat exchange is efficient enough to cool the reaction mixture from high temperatures (> 300 °C) to room temperature within seconds and continuously for many hours. Naturally, the stainless steel (SX 316L) components of the flow reactor are prone to corrosion if concentrated acids, e.g., aqua regia, HCl, H_2SO_4, bromine, chlorine, etc., are used. However, dilute acids can be used with caution and weak organic acids such as acetic acid can be employed at all temperatures without fear of corrosion, even as neat solvents.[285] The instrument can be operated at flow rates from 0.1–9.99 mL/min (a maximum flow rate of 19.98 mL/min is attained by employing both available HPLC pumps simultaneously), giving a wide range of residence times utilizing the 4, 8 and 16 mL heating coils. In general, transformations requiring only short residence times (< 30 min) can be performed in a single pass, but for longer reaction/residence times, the option of multiple passes and closed-loop circulation for several hours can be exploited. The pressure in the reactor is automatically maintained at the set value by the control unit with the help of a backpressure valve.[286]

The pressure can be set between 50 and 200 bar either before the start of the reaction, or can be increased to any higher value during the run. The stability of the instrument at the set values of temperature and pressure can depend on the stability of the backpressure regulator, which in turn may depend on many factors, in particular the state of the solvent at a particular temperature/pressure regime.

143

If the mixture in the reactor is not totally in the liquid state and/or a gas is being produced for any reason, then to release the extra pressure, the valve has to open and close rhythmically to maintain the set pressure value, and hence, avoid development of over pressure. As an extra safety measure, the instrument stops heating until the set pressure is restored, and as a consequence, the temperature also fluctuates. Since it is possible to both increase and decrease the temperature and to increase the pressure and flow rate during a run "on-the-fly", reaction optimization studies can be performed with relative ease utilizing different temperatures keeping the pressure and flow rate constant. Alternatively, the effects of changes in pressure and flow rate can be studied by adding increments to the set values during a run and allowing the system to become stable after attaining the new values.[287] It is possible to use two pumps, one for the reaction mixture and the second pump for the solvent, if a single batch is processed in an automated fashion. However, for temperature effect studies or studies on the effect of pressure and flow rate, where one or more of these parameters must be changed, or a range of different samples differing in composition are processed, it is usually easier to work with one pump, by unchecking the dialogue box for switching the pumps. In this mode the inlet tube must be switched manually between the solvent flask and vials containing the reaction mixtures. Care must be taken to avoid air locking of the pump while switching, especially if working at flow rates higher than 2.5 mL/min.[288]

The performance of synthetic transformations in the X-Cube Flash™ reactor allows the use of extreme reaction temperatures (350 °C). In many instances, the stability of a particular solvent in these reaction environments is unknown and needs to be carefully scrutinized before attempting a chemical reaction.

144

At higher temperature/pressures, many common organic solvents may decompose, leading to degradation products that may influence the flow processes or producing precipitation of solid particles in the flow system, ultimately leading to a blocking of the reactor. The same is true for reagents, which may also have limited stability at high reaction temperatures.

As far as the stability of solvents is concerned, only limited data sets are available on the stability of common organic solvents, in particular in the temperature range of 250–350 °C[285].

For this reason, the stability of a number of solvents has been examined under high temperature processing conditions by passing the pure solvent through the X-Cube Flash reactor using elevated temperature and pressure regimes, and monitoring any apparent decomposition processes by HPLC and GC-MS analysis.

Similar screening experiments were performed for a variety of pure organic solvents in order to obtain information about the maximum recommended temperature range for operation in the X-Cube Flash reactor.

7.3.2 Synthesis of graphene oxide

Graphene oxide was prepared according to Hummers and Offeman method in which oxidation of high-purity graphite powder (99.9999%, 200 mesh) was done using a mixture of H_2SO_4/$KMnO_4$. Graphite (4.5 g, 0.375 mol) and $NaNO_3$ (2.5 g, 0.0294 mol) were mixed in a conical flask. The mixture was kept in an ice bath under continuous stirring while adding conc. H_2SO_4 (115 ml, 2.157 mol) followed by $KMnO_4$ (15 g, 0.095 mol) which was slowly added over 2.5 h. Then deionized water (230 ml) was slowly added to the above mixture and once the mixture temperature became stable it was kept around 80 °C.

145

Then, after 20 min., deionized water (700 ml) were added followed by dropwise addition of (10%) H_2O_2 (20 ml, 0.667 mol). The resulting yellowish-brown cake of solid was washed several times with 1M HCl followed by washing with hot deionized water. Then the poweder (graphite oxide) was dried under vacuum overnight. Resultant graphite oxide could be readily exfoliated to completely water dispersed graphene oxide (GO) by ultra-sonication.

7.3.3   Synthesis of Pd-Fe$_3$O$_4$ supported on Graphene

Catalyst was prepared using GO support; to prepare catalyst, GO (60 mg) was dispersed in 50 mL of water for 1 h in a sonication bath to produce aqueous dispersion of graphene oxide. Then, deionized water (50 mL) in which appropriate amount of Palladium nitrate (10 wt. % in 10 wt. % HNO_3, 99.999%, 200 µl) and $Fe(NO_3)_3.9H_2O$ (190.5 mg, 0.471 mmol) were added and sonicated for 1 h, the solution was added to the aqueous dispersion of graphene oxide (GO) and stirred for 3 h. After stirring the whole mixture for 3 h, the reducing agent hydrazine hydrate (2 ml) was added at room temperature and once the solution was heated by microwave for (120) s and the color changed to dark black color, indicating the completion of the chemical reduction. Then, the final product washed using hot deionized water 2-3 times, ethanol 2-3 times, and then dries in oven at 80˚C.

7.3.4   General Procedure for Suzuki Cross-Coupling

Aryl bromide (0.51 mmol, 1 eq.) was dissolved in a mixture of 4mL H_2O: EtOH (1:1) and placed in a 10-mL microwave tube. To this were added the aryl boronic acid (0.61 mmol, 1.2 eq.) and Potassium carbonate (1.53 mmol, 3 eq.) and finally the reactants mixture is introduced to flow continuously over the palladium-magnetite on graphene nanoparticles (Pd-Fe$_3$O$_4$/G) (10, 25, 35, 50, 100 mg) that were previously loaded into CatCart cartridge, and heated at the

146

assigned temperature and time. After the reaction completed, the progress of the reaction was monitored using GC-MS analysis to an aliquot of the reaction mixture.

7.4   Results and Discussion

Characterization of the graphene supported Pd-Fe$_3$O$_4$ samples prepared by the HH-MWI, method was examined in detail using XRD, XPS, and TEM analyses. Here, we focus on the characterization and catalytic activity of the Pd-Fe$_3$O$_4$ /G nanocatalysts. The palladium content in Pd/Fe$_3$O$_4$ and three different Pd/Fe$_3$O$_4$/G catalysts was determined by means of inductively coupled plasma (ICP-OES) and amounted to 6 wt %.

Figure 7-3 displays the XRD patterns of the initial graphite powder, the prepared GO, and Pd-Fe$_3$O$_4$/G prepared by the HH-MWI method. The initial graphite powder shows the typical sharp diffraction peak at $2\theta = 26.7°$ with the corresponding d-spacing of $3.34°$A. The exfoliated GO sample shows no diffraction peaks from the parental graphite material and only a new broad peak at $2\theta = 10.9°$ with a d-spacing of $8.14°$A observed. This indicates that the distance between the carbon sheets has increased due to the insertion of interplaner oxygen functional groups.

After MWI of the GO in the presence of HH as the reducing agent, the XRD of the resulting graphene shows the disappearance of the $10.9°$ peak confirming the complete reduction of the GO sheets. A similar XRD spectrum is observed for the Pd-Fe$_3$O$_4$/G sample prepared by the simultaneous reduction of GO and palladium nitrate – iron nitrate mixture using HH under MWI. The very small broad peak around $2\theta = 26.7°$ in the Pd-Fe$_3$O$_4$/G sample could suggest the presence of a minor component of multilayer graphene. The presence of Pd nanoparticles could enhance the interaction among a few graphene layers.

Figure 7-3 (a) XRD Pattern of Graphite and Graphite Oxide (b) XRD Pattern of Fe_3O_4 , Palladium, and (Palladium-Fe_3O_4 / Graphene) catalyst.

However, the very weak intensity of the $2\theta = 26.7°$ peak indicates that the extent of multilayer graphene in the Pd-Fe_3O_4/G sample is insignificant.

Generally, the XRD pattern clearly indicates that the product is enriched with Fe_3O_4 and metal Pd (0). The palladium shows the typical sharp diffraction peak at $2\theta = 40°$. The XRD patterns indicate that the products were all (Fe_3O_4) magnetite with reference code (ICCD-00-003-0863). It is also easily to notice that the sharp diffraction peak at $2\theta = 40°$ which is characteristic to palladium and also the characteristic peaks of Fe_3O_4 is shown as a sharp diffraction peak at $2\theta = 35°$. The very small broad peak around $2\theta = 26°$ in Pd- Fe_3O_4 /G sample could suggest the presence of a minor component of multilayer graphene.

148

The diffraction peaks (2θ) of Pd- Fe_3O_4 /G at 40, 46.8, and 68.2 are ascribed to the (111), (200), and (220) planed of Pd NPs which are similar to pure palladium and also to the peaks of Pd- Fe_3O_4 as shown.

Figure 7-4 displays representative TEM images of the Pd-Fe_3O_4/G catalyst before and after reaction. The TEM images show the presence of uniform well-dispersed Pd-Fe_3O_4 nanoparticles on Graphene. From these TEM images; it is obvious that the catalyst has excellent dispersion of Pd – Fe_3O_4 on the graphene surface and also it has smaller particle size which is a very important and decisive factor in catalysis. This is very consistent with the catalytic activity data obtained from experimental testing of this catalyst under batch reaction conditions as mentioned in the previous chapter. It is very interesting to note the role of Pd^{+2} in assisting the formation of magnetite nanoparticles onto the surface of the nanosheets of graphene. Generally, it is clear that palladium presence is a decisive factor in avoiding the agglomeration of products after microwave-assisted reduction of graphene oxide with Fe^{+2} alone using hydrazine hydrate. From these TEM images; it was found that the particle size of Pd was Pd was (4-6 nm) and Fe_3O_4 was (16-18 nm) as shown in the previously mentioned figure.
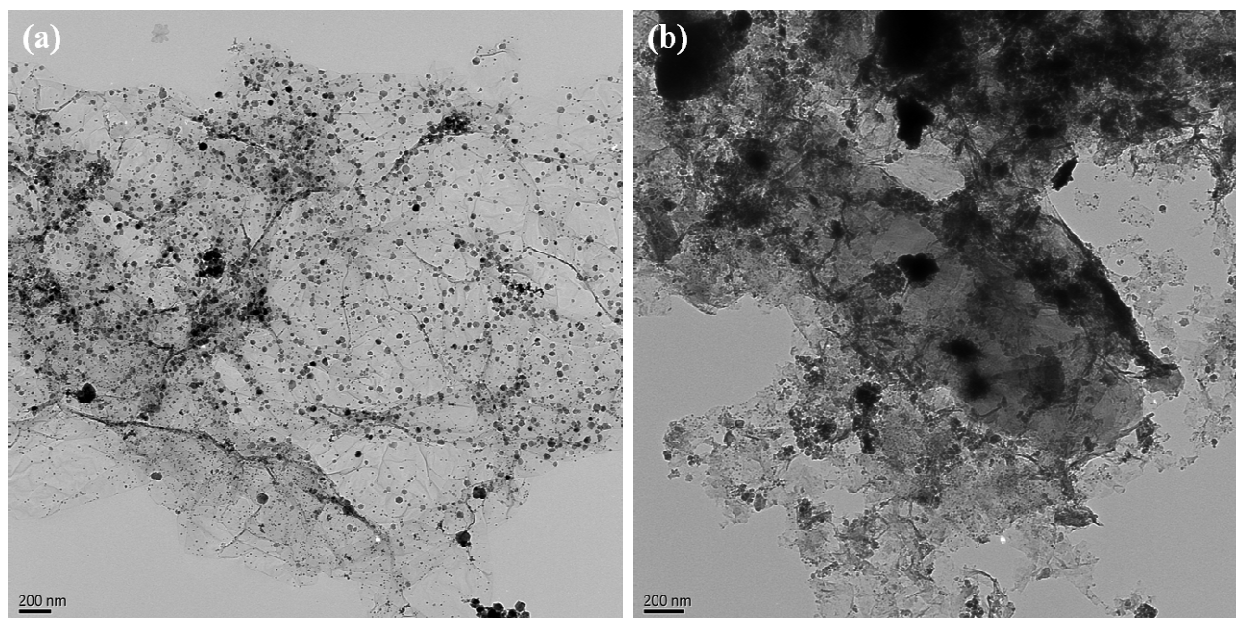
Figure 7-4 TEM images of Pd-Fe$_3$O$_4$ supported on Graphene (a) before the reaction, (b) after the reaction.
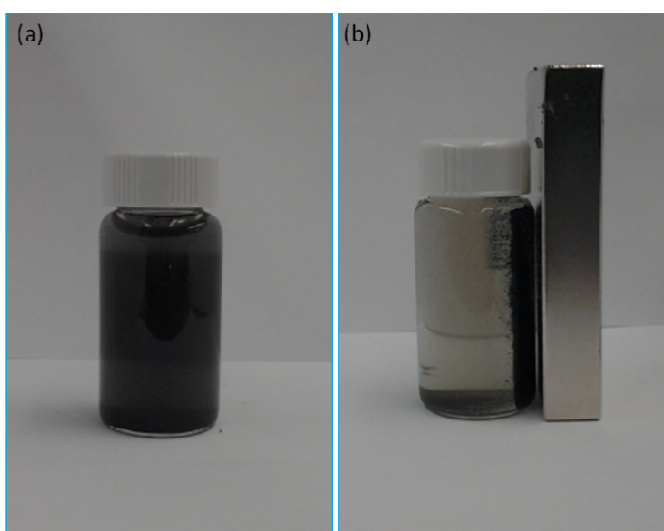
Figure 7-5 (a) Catalyst after preparation. (b) Separating the catalyst using a strong magnet.

Figure 7-5 shows the unique magnetic properties of the Pd-Fe$_3$O$_4$ supported on Graphene

catalyst when using an external magnetic field.

150
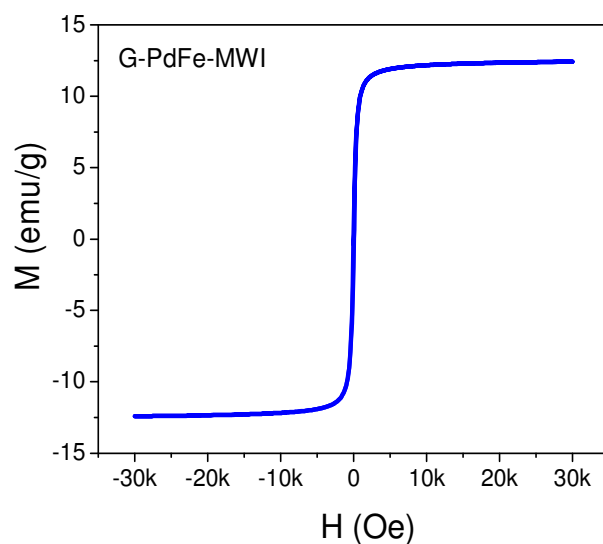
Figure 7-6 Magnetic hysteresis loops of Pd - Fe₃O₄ supported on Graphene.

The magnetic properties of catalyst were carried out by using Vibrating Sample Magnetometer (VSM) analysis. **Figure 7-6** presents the magnetic hysteresis loop of Pd - Fe₃O₄ supported on Graphene.

This figure simply shows the hysteresis curves obtained for Pd - Fe₃O₄ supported on Graphene with an applied field sweeping from -30 to 30 kOe. The hysteresis loops of prepared sample reveal superparamagnetic behavior at room temperature with nearly zero coercivity and extremely low remnant magnetization values.

The lack of remaining magnetization when the external magnetic field is removed is in agreement with a superparamagnetic behavior observed in graphene nanosheets decorated with Pd-Fe₃O₄ nanoparticles.

The XPS technique is more sensitive for the analysis of surface oxides than XRD. The Pd-Fe₃O₄/G had a C1s binding energy around 284.5 eV derived from the carbon contamination in the analysis.

151
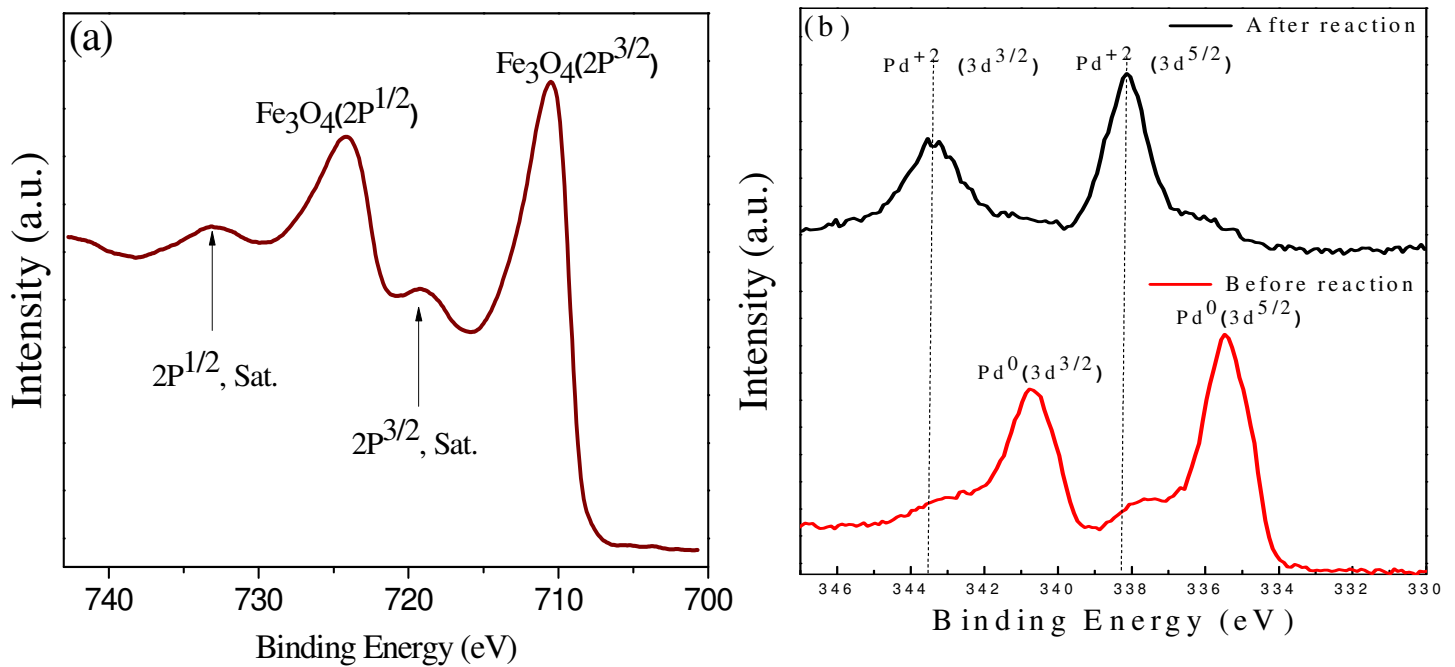
Figure 7-7 (a) XPS-Fe2p, (b) XPS-Pd3d before and after reaction for Pd - Fe₃O₄ supported on Graphene.

Samples showed that the binding energy (the energy difference between the initial and final states of the photoemission process) of Fe 2P 3/2 was 710.5 eV, indicating that the Fe was present as $Fe_3 O_4$ and also the binding energy of Fe 2P 1/2 was 723.7 eV indicating that Fe was present in the oxidation state of $Fe_3 O_4$ as shown in **Figure 7-7a. Figure 7-7b** shows that most of Pd is in the form of Pd^0 which besides excellent dispersion of palladium on graphene surface as shown previously in TEM images is consistent with experimental data that reveals the excellent catalytic activity of this catalyst among all catalysts that were investigated for Suzuki cross coupling reactions as previously mentioned in chapter 7. The binding energies of Pd 3d5/2 was 334.8, 335.14 eV, and Pd 3d3/2 was 340.1, 340.57 eV corresponding to Pd^0.

Similarly, the binding energies of Pd 3d3/2 was 341.38, 343.2 eV, and Pd 3d5/2 was 336.23, 337.85 eV corresponding to Pd (II) which as indication that Pd^0 was converted to Pd (II) after reaction was done as shown in **Figure 7-7b**.

152

Actually this is also consistent with the results that confirmed that the catalyst was catalytically deactivated which has been also explained due to the agglomeration that was noticed on graphene surface after reaction was done as previously shown in TEM images as in **Figures 7-4a,b**.

These TEM images clearly demonstrate the agglomeration and accumulation of the Pd-Fe$_3$O$_4$ nanoparticles on the surface of graphene. This result indicates that the mechanism of deactivation of the catalyst is likely to involve the formation of aggregated Pd nanoparticles which leads to the decrease in the surface area and saturation of the coordination sites. After completion of the experiments, the Pd-Fe$_3$O$_4$/G was separated from the cartridge for characterization.

The reaction solution was analyzed by ICP-MS, and the palladium content in the solution was determined to be 700 ppb. Such a small amount of leached palladium may argue against complete heterogeneity of the catalytic system in this reaction. However, further evidence on the nature of the catalytic mechanism is the failure to observe reactivity after the removal of the supported nanoparticles from the reaction medium.[284]

1 1'-biphenyl -4- carboxaldehyde
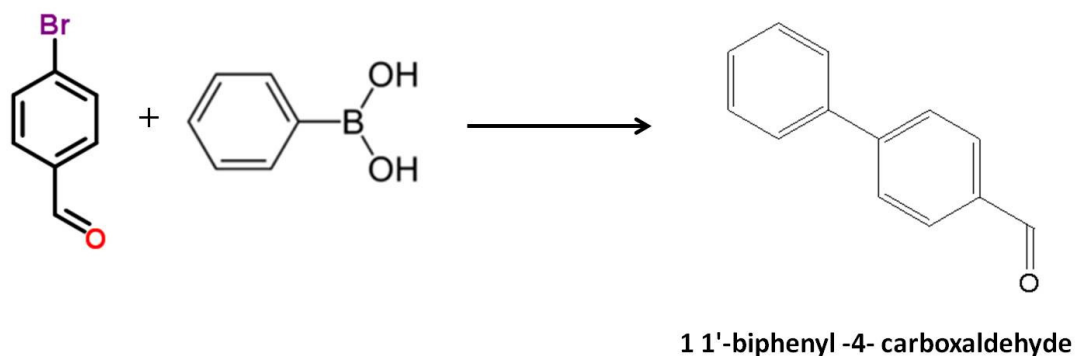
Scheme 7-1 Suzuki cross-coupling reaction with Pd-Fe$_3$O$_4$/G

153

In **Scheme 7-1**, 4-bromobenzaldehyde was selected instead of bromobenzene that was selected before in **Scheme 6-1** for two reasons, the first reason is to avoid homo coupling reaction that may occur under these reaction conditions and the second reason is to avoid formation of any solid products that may produced from this reaction under the reaction conditions which may lead to clogging of tubes of instruments in which the reactants flow over the catalyst. In addition to these precautions that were taken into consideration; different ratios of solvent systems were investigated to find the optimum conditions under which we could run the experiment with highest possible conversion.

Table 7-1 Conversion percentage using different ratios of solvent systems for Pd-Fe$_3$O$_4$/G catalyst[*]

Run	Temp. (℃)	Mw. Time (min.)	Solvent (ml.)	Conversion (%)
1	80	10	4	100

[*] 0.5 mol. % (Pd-Fe$_3$O$_4$/ G) Catalyst – Solvent (C$_2$H$_5$OH : H$_2$O = 1: 1)
  0.5 mol. % (Pd-Fe$_3$O$_4$/ G) Catalyst – (C$_2$H$_5$OH : H$_2$O : THF = 1 : 1 : 1)
  0.5 mol. % (Pd-Fe$_3$O$_4$/ G) Catalyst – (C$_2$H$_5$OH : H$_2$O : THF = 1.8 : 1.8 : 0.4) i.e (C$_2$H$_5$OH : H$_2$O : THF = 4.5 : 4.5 : 1).

So, as in **Table 8-1**, it was possible to obtain 100% conversion by changing the ratios of water, ethanol, and THF to obtain the highest possible conversion with using the minimum amount of THF to make sure that all products will be in liquid form to avoid any undesired solid products that may cause clogging.

It is obvious from **Table 7-2** below, that the screening experiments that were performed in **Table 7-1** were critical experiments as conversion is changing dramatically according to several factors like reaction temperature, catalyst loading, and the most important factor which is the solvent system ratios.

Table 7-2 Conversion percentage using different reaction temperatures for Pd-Fe$_3$O$_4$/G catalyst*

Run	Temperature (℃)	Flow Rate (ml. /min.)	Amount (ml.)	Conversion (%)
1	80	1	10	**53**
2	80	1	10	17
3	80	1	10	14
4	80	1	10	13
5	100	0.7	10	**31**
6	100	0.7	10	15
7	100	0.7	10	14
8	100	0.7	10	13
9	100	0.7	10	9
10	120	0.6	10	**18**
11	120	0.6	10	15
12	120	0.6	10	12

* 50 mg of (Pd-Fe$_3$O$_4$/ G) Catalyst – (C$_2$H$_5$OH : H$_2$O : THF = 1 : 1 : 1)

According to the data collected from previously mentioned experiments, beside solvent system ratios; the catalyst loading amount should be varied to optimize the reaction conditions as shown in **Table 7-3**.

It was found that increasing catalyst loading from 50 mg to 100 mg, increasing temperature and decreasing the flow rate of reaction mixture over the catalyst in the CatCart cartridge enabled us from increasing the conversion percentage. It could be possible to collect about 30 mL of the product with conversion about 100%.

Table 7-3 Conversion percentage using 80°C reaction temperatures for Pd-Fe$_3$O$_4$/G catalyst*

Run	Temperature (℃)	Flow Rate (ml. /min.)	Amount (ml.)	Retention Time (min.)	Conversion (%)
1	80	0.8	10	12.5	100
2	80	0.8	10	12.5	95
3	80	0.8	10	12.5	87
4	80	0.8	10	12.5	76
5	80	0.8	10	12.5	64
6	80	0.8	10	12.5	59

* 100 mg of (Pd-Fe$_3$O$_4$/ G) Catalyst – (C$_2$H$_5$OH : H$_2$O : THF = 4.5 : 4.5 : 1)

In **Table 7-4**, it was found that increasing the reaction temperature from 80℃ to 100℃ and decreasing the flow rate from 0.8 mL/min. to 0.7 mL/min. didn't make any enhancement in conversion percentage as it was still possible to collect about 28 mL of the product with conversion about 100%.

Table 7-4 Conversion percentage using 100°C reaction temperatures for Pd-Fe$_3$O$_4$/G catalyst*

Run	Temperature (℃)	Flow Rate (ml. /min.)	Amount (ml.)	Retention Time (min.)	Conversion (%)
1	100	0.7	10	14	90
2	100	0.7	10	14	86
3	100	0.7	10	14	75
4	100	0.7	10	14	63
5	100	0.7	10	14	55
6	100	0.7	10	14	48
7	100	0.7	10	14	26

* 100 mg of (Pd-Fe$_3$O$_4$/ G) Catalyst – (C$_2$H$_5$OH : H$_2$O : THF = 4.5 : 4.5 : 1)

156

Table 7-5 Conversion percentage using 100° C reaction temperatures for Pd-Fe$_3$O$_4$/G catalyst[*]

Run	Temperature (℃)	Flow Rate (ml. /min.)	Amount (ml.)	Retention Time (min.)	Conversion (%)
1	100	0.6	20	33.3	98
2	100	0.6	20	33.3	97
3	100	0.6	20	33.3	90
4	100	0.6	40	66.6	76
5	100	0.6	20	33.3	62
6	100	0.6	20	33.3	44
7	100	0.6	20	33.3	24

[*] 100 mg of (Pd-Fe$_3$O$_4$ / G) Catalyst – (C$_2$H$_5$OH : H$_2$O : THF = 4.5 : 4.5 : 1)

In **Table 7-5**, it was found that maintaining the reaction temperature at 100℃ and decreasing the flow rate from 0.7 mL/min. to 0.6 mL/min. make a great enhancement in conversion percentage as it became possible to collect about 60 mL of the product with conversion about 100%.

Table 7-6 Conversion percentage using 100° C reaction temperatures for Pd-Fe$_3$O$_4$/G catalyst[*]

Run	Temperature (°C)	Flow Rate (ml. /min.)	Amount (ml.)	Retention Time (min.)	Conversion (%)
1	100	0.5	20	40	100
2	100	0.5	20	40	96
3	100	0.5	20	40	46
4	100	0.5	20	40	20
5	100	0.5	20	40	20
6	100	0.5	20	40	20
7	120	0.5	20	40	27

[*] 100 mg of (Pd-Fe$_3$O$_4$ / G) Catalyst – (C$_2$H$_5$OH : H$_2$O : THF = 4.5 : 4.5 : 1)

157

In **Table 7-6**, it was found that maintaining the reaction temperature at 100℃ and decreasing the flow rate from 0.6 mL/min. to 0.5 mL/min. decreased the enhancement that was achieved in conversion percentage as it became possible to collect just 40 mL of the product with conversion about 100%. So, from the previous study it was finally deduced that the optimum conditions to evaluate the catalytic activity of Pd-Fe3O4 supported on Graphene under continuous flow reaction conditions using Thales Nano X-Cube flow reactor is using 100 mg of catalyst in CatCart cartridge with a flow rate 0.6 mL/min. for the reactants over the catalyst under 100℃ as a reaction temperature.
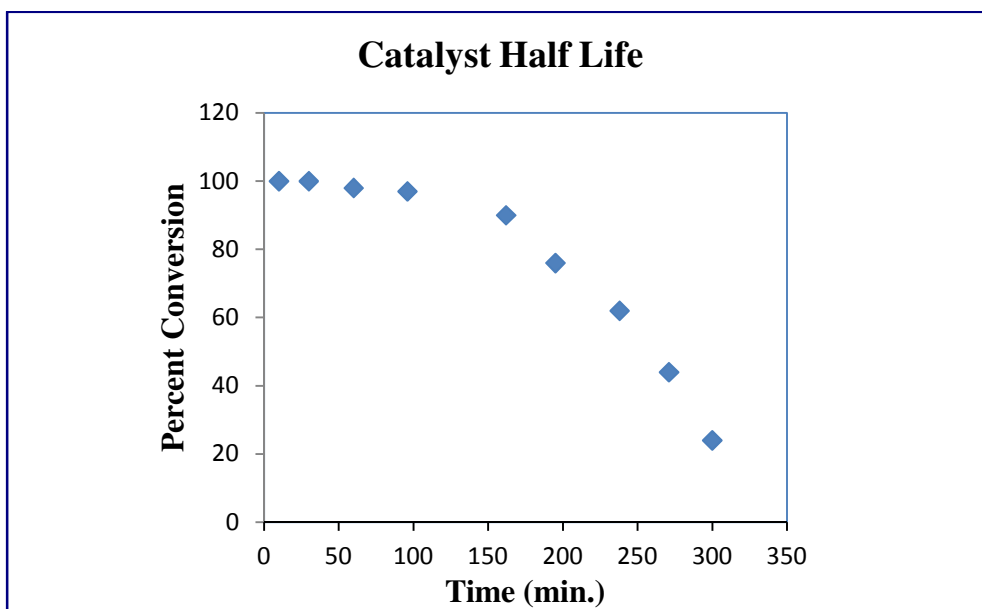
Figure 7-8 Catalyst half life under optimum reaction conditions.

Figure 7-8 gives an overview about the catalyst half life under the optimum reaction conditions that were previously investigated in **Table 7-5**. In this figure, it is obvious that the catalytic activity of the catalyst was very high (about 100% conversion) during the first 90 minutes from starting the reaction and then started to decrease gradually.

Table 7-7 Catalyst Loading Dependency for Pd-Fe₃O₄/G catalyst[*]

Catalyst Loading (mg)	100	50	25	10
Conversion (%) at Flow Rate (0.5 ml/min.)	100	73	64	43
Conversion (%) at Flow Rate (0.6 ml/min.)	98	68	56	28
Conversion (%) at Flow Rate (0.7 ml/min.)	90	58	48	17

Table 7-7 summarizes some of the critical data that was collected in the experimental work done. It gives an overview of the relation between the catalyst loading in (mg) of catalyst and its effect on the conversion percentage under different selected flow rates.
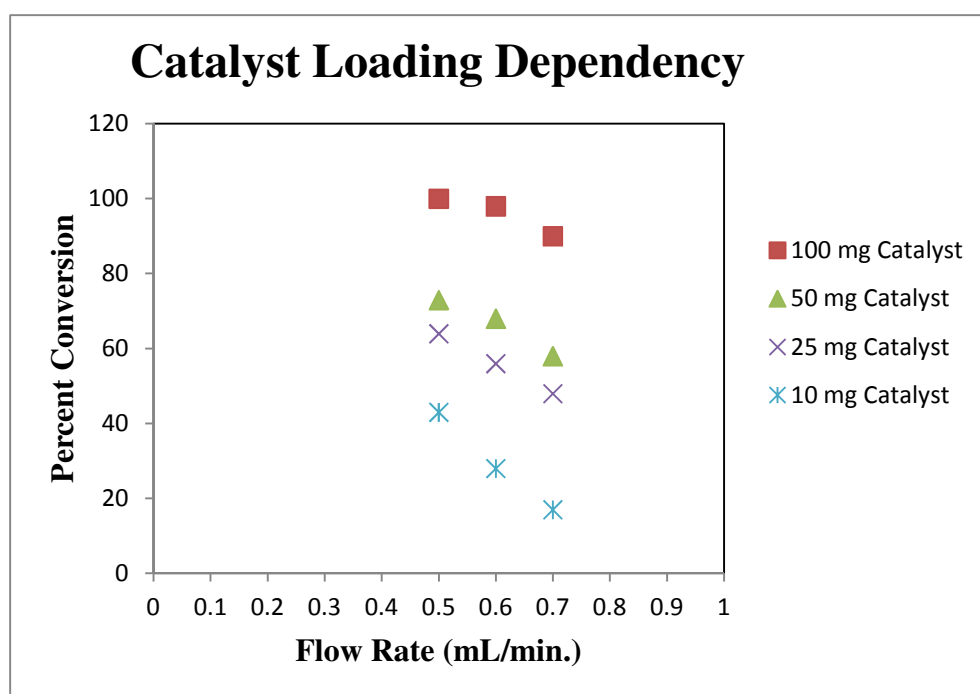
Figure 7-9 Catalyst loading dependency under different reaction conditions.

Figure 7-9 gives an overview about the catalyst loading dependency under different reaction conditions. From this figure, it is obvious that decreasing the flow rate for the same catalyst loading lead to an increase in the conversion percentage while increasing the catalyst loading for the same flow rate lead to an increase in the conversion percentage as well.

159

7.5 Conclusions

We also developed an efficient magnetic catalyst which has been successfully synthesized using a reliable, reproducible fast and simple method using microwave irradiation (MWI) approach. We report here a facile approach used for the synthesis of a well dispersed magnetically separable palladium-magnetite supported on graphene, which can act as a unique catalyst against carbon-carbon cross-coupling due to the well dispersion of palladium nano particles throughout the magnetite-graphene surface. The prepared catalysts are magnetic which offers an advantage in the separation process of catalyst from the reaction medium. Our catalyst showed high catalytic activity towards Suzuki cross – coupling reaction with 100% conversion for the catalyst first run and could be recycled up to eight times with high catalytic activity near 100%. The separation process is achieved via applying of strong external magnetic field which makes separation process easy, reliable and environmentally friendly. In summary, the flow chemistry provided higher selectivity and conversion rate than conventional batch methods within a shorter time.

In conclusion, we have shown that flow chemistry using X-Cube gave remarkable results for evaluating the catalytic activity of our catalyst that was prepared under batch reaction conditions towards Suzuki cross coupling reactions of 4-bromobenzaldehyde with phenyl boronic acid. Reaction parameters (solvent, catalyst, temperature) were rapidly optimized in the reactions. The short time of optimization allowed to a large number of optimizing reactions and facilitated generalization of the experiences.

CHAPTER 8   Laser Vaporization and Controlled Condensation (LVCC) of Pd/GO and Pd-Fe$_3$O$_4$/GO for Suzuki Cross-Coupling Reaction

8.1   Overview

In this chapter, graphene supported nanoparticles were synthesized using Laser Vaporization and Controlled Condensation (LVCC) for catalytic applications in the Suzuki cross-coupling reaction. This method is generally one of the earliest methods for producing nanoparticles by preparing it directly from a supersaturated vapor.[9-13] There are some advantages of using this technique like high purity of produced nano particles, producing films and coatings, production of high density vapor of any metal within a short time (1014 atoms / 10 ns), directional high speed vapor, simultaneous or Sequential evaporation of several metal targets or alloys, formation of selected oxides, sub-oxides and non-stiochometric oxides by controlling the partial pressure of oxygen, formation of nanoparticles of metals, oxides, alloys, filaments, carbides, sulfides, etc.[8, 16, 289-291] There is also some disadvantages like the high cost per gram of material, difficulty to produce large quantities of materials. The LVCC method is based mainly on nanoparticles formation through condensation from the vapor phase.[14] In LVCC method, the process consists of pulsed laser vaporization of a metal target into a selected gas mixture in a cloud chamber. The laser vaporization produces a high-density vapor a very short time - "10^{-8} s", in a directional jet that allows the directed deposition process.[17]
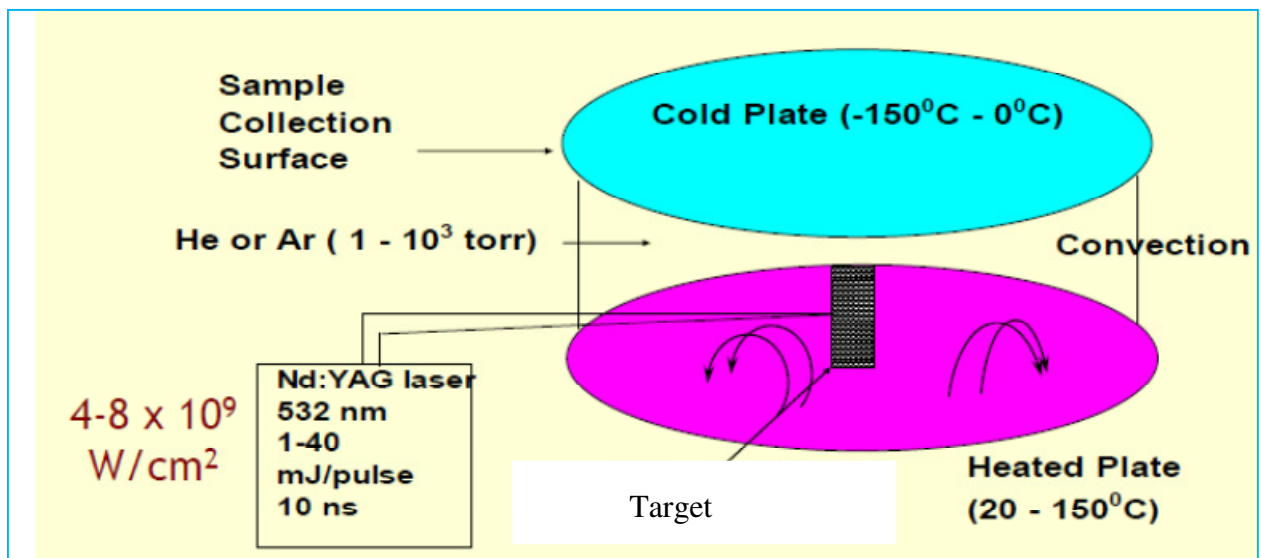
Figure 8-1 Experimental set-up for the synthesis of nano particles using LVCC [9-10]

The previous sketch for the cloud chamber used in LVCC method shows that it consists of two horizontal, circular stainless steel plates, separated by a glass ring. The metal target of interest "Pd for example" is fixed on the lower plate, and the chamber is filled with a pure carrier gas such as He or Ar (99.99 %) which are used because they are not reactive gases in case we don't need oxide formation which is happened in case of using a mixture containing a known composition of a reactant gas (e.g O_2 in case of oxides). It is important to maintain the metal target and the lower plate at a temperature higher than that of the upper one. The top plate can be cooled to less than 150 K by circulating liquid nitrogen (-150 – 0 K), and the lower plate (20-150 K). This large temperature gradient between the bottom and top plates results in a convection current which can be enhanced by using a heavy carrier gas like Ar under high pressure conditions of nearly 10^3 torr. Convection is important because it decreases the residence time by making circulation. So, Ar is better than He as a carrier gas because it is heavier than He, hence it convects more. The metal vapor is generated by pulsed laser vaporization using visible IR (532 nm) of YAG Laser (15-30 mJ/pulse, 10^{-8} s pulse).

162

The laser beam is moved on the metal surface in order to expose new surface to the beam. The role of convection in the experiments is to remove the small particles away from the nucleation zone (once condensed out of the vapor phase) before they can grow into larger particles. The rate of convection increases with the temperature gradient in the chamber. Therefore, by controlling the temperature gradient, the total pressure and the laser power. Generally this reaction utilizes pure Pd as the catalyst, which poses problems in recyclability and recovery. The substitution with a heterogeneous Pd catalyst could improve these difficulties but catalytic activity would be sacrificed. In an attempt to optimize recyclability, recovery and catalytic activity, the effects of varying compositions of Pd and Fe with graphene support were investigated with catalysis and characterized using UV-Visible Spectroscopy, Fourier Transform-Infrared (FT-IR) Spectroscopy, X-ray Photoelectron Spectroscopy (XPS) as well as tested for magnetic properties.

8.2   Introduction

Until recently, two-dimensional materials were considered thermodynamically unstable and therefore could not exist. Then in 2004 the discovery of graphene quickly elevated it to a status of potential wonder material for a wide range of technological applications.[292] Graphene is a two-dimensional carbon allotrope containing a single atomic layer of sp^2 hybridized aromatic carbons appearing as a honeycomb type structure.[293] The potential of graphene in the scientific community lies in its novel characteristics of being extremely thin, mechanically strong, transparent, as well as possessing high electrical and thermal conductivities.[264] These characteristics differ from other carbon allotropes because of graphene's two-dimensional structure where electron movement is limited to a narrower space opposed to a three-dimensional structure. [294]

163

There are a variety of methods for the preparation of graphene, among them is the reductions of graphene oxide (GO) using LVCC. This method provides a less toxic and shorter time of reaction than most conventional methods for the creation of graphene.[295-296]   The potential of graphene as a support for Pd-catalysts in the Suzuki cross-coupling reaction can have many advantages. The Suzuki cross-coupling is a catalyzed reaction between aryl boronic acid and an aryl halide producing a biaryl compound. [297] The benefits of graphene support are the provided thermal and chemical stability and reusability with limited loss in activity. The catalytic activity is greatly influenced by the size distribution of the Pd/G, the smaller the size of each particle the larger the total surface area available becomes, increasing activity. After the exfoliation and reduction of GO, graphene is left with several defects scattered across its lattice which promote Pd-G interactions improving catalytic activity.[22] These defects along with carbon bonding provide an electron rich support which stabilizes the metal nanoparticles preventing them from migrating and forming clusters that would decrease catalytic activity.[151, 297]

LVCC has the potential to create a smaller size distribution of the synthesized nanoparticles on graphene support, which ultimately would increase the effectiveness of this method for catalysis in the Suzuki cross coupling reaction. LVCC utilizes a high powered pulsed laser to ablate a bulk sample as well as control over the temperature gradient—providing convection, pressure, laser power and the atmosphere. The laser irradiates the target creating high density vapor while the inert atmosphere and convection current prevent the vaporized particles from growing into larger particles as they condense and deposit on the upper plate of the chamber.[298]

8.3 Experimental

8.3.1 Chemicals and reagents

Metal powders had been mixed according to calculations creating pellets with varying compositions of Fe/GO, Pd/GO and Pd-Fe/GO consisting of Fe/GO (20 wt% Fe - 80 wt% GO), Pd/GO (20 wt% Pd - 80 wt% GO), Pd-Fe/GO (15 wt% Pd - 5 wt% Fe - 80 wt% GO), Pd-Fe/GO (10 wt% Pd - 10 wt% Fe - 80 wt% GO), and Pd-Fe/GO (7 wt% Pd - 13 wt% Fe - 80 wt% GO). The GO flakes received were cut into a fine powder using razors as to create a pellet with evenly mixed particles. The aforementioned powders were then pressed into pellets using a manual press.

The nanoparticles were synthesized using LVCC with a pulsed Nd: YAG laser (532 nm). The target was placed in a metal holder adjusted to the focal point of the laser. The top plate was screwed on top the quartz ring and a vacuum created inside the chamber reduced the pressure to below 9 torr. This setup can be seen in **Figure 8-2**.
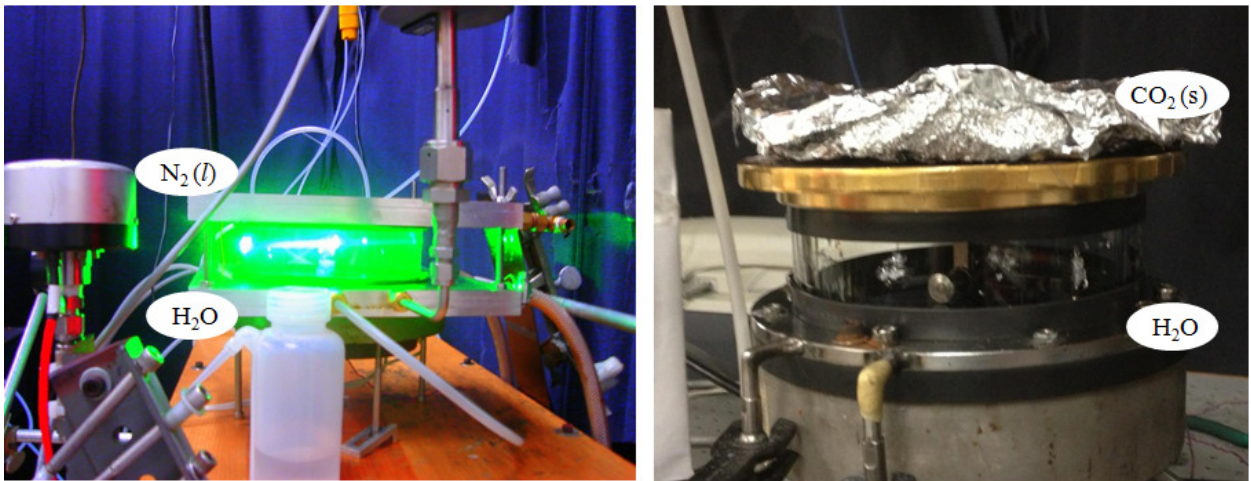
Figure 8-2 Setup of LVCC with N_2 (*l*) and CO_2 (s) [17]

Once the pressure was stable, He gas was added to increase the pressure to 300 torr.

165

Purging five times with He followed by a vacuum ensured there were no leaks or contaminant gases left inside the chamber. After the final purge, the pressure was increase to 800 torr. Hot water was circulated around the bottom plate and N_2 (*l*) was circulated over the top plate providing convection as the metal vaporized. The bottom plate was warmed to above 50 $^{\circ}$C and the top plate was cooled to below -30 $^{\circ}$C. The average temperature gradient created was between 60 - 90 $^{\circ}$C. Before LVCC, the laser was switched from low power to its high energy q-switch mode and operated at 2 watts. As the target was ablated, the laser beam was adjusted around the surface of the target and the pressure was maintained above 800 torr. After ablating as much of the target as possible, paper towels were wrapped around the top plate and kimwipes were placed around the quartz ring to absorb any further condensation.

8.4   Results and Discussion

The structures of graphene and graphene oxide can be visualized in **Figure 8-1** where graphene is shown to be a single layer of aromatic carbons and graphene oxide is composed of aromatic carbon atoms as well as reactive oxygen based functional groups. The samples were characterized using Fourier Transform-Infrared (FT-IR) and Ultraviolet-Visible Spectroscopy (UV-Vis). **Figure 8-3** shows the FT-IR spectra of graphene oxide prior to LVCC and the samples after LVCC reduction. The spectrum for GO shows characteristic peaks at 3400 cm^{-1} corresponding to the O-H stretching vibrations, 1720 cm^{-1} corresponding to C=O stretching vibrations, 1600 cm^{-1} corresponding to C=C stretching vibrations and 1075 cm^{-1} corresponding to C-O stretching. In comparison, the spectra for the samples after LVCC show the complete disappearance of stretching for related oxygen groups indicating the full reduction of graphene oxide.

166
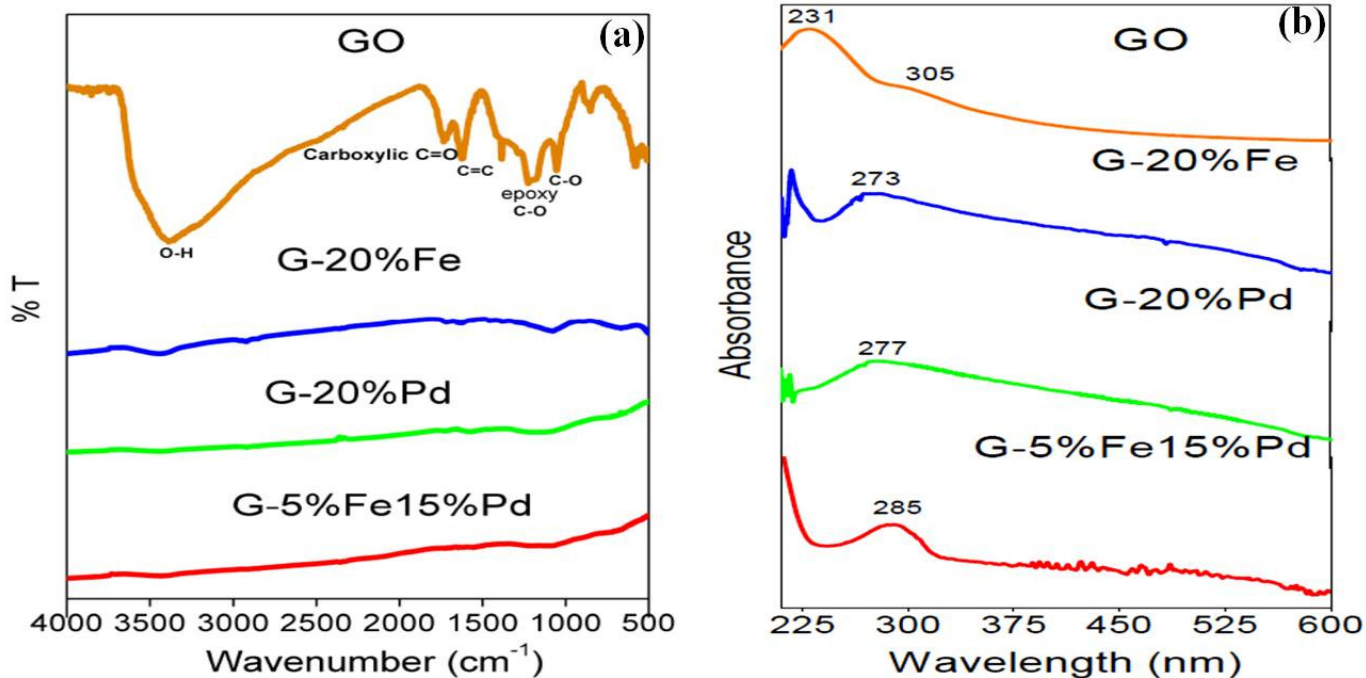
Figure 8-3 (a) FT-IR spectra of GO and samples after LVCC reduction in He environment, (b) UV-Vis Spectroscopy data of graphene oxide and samples after undergoing LVCC.

The GO spectrum contains a maximum at 231 nm corresponding to π→π* transitions of aromatic C–C bonds, and a shoulder at 305 nm, which is attributed to n→π* transitions of C-O bonds. After LVCC reduction, the UV-Vis spectra shows the maximum peak absorbance is shifted from 231 nm to 273 nm for 20% Fe/ 80% G, 277 nm for 20% Pd/ 80% G and 285 nm for 5% Fe- 15% Pd/ 80% G. The shift to the higher wavelength indicating a lower energy absorbance is due to the removal of the oxygen groups from graphene oxide during LVCC.
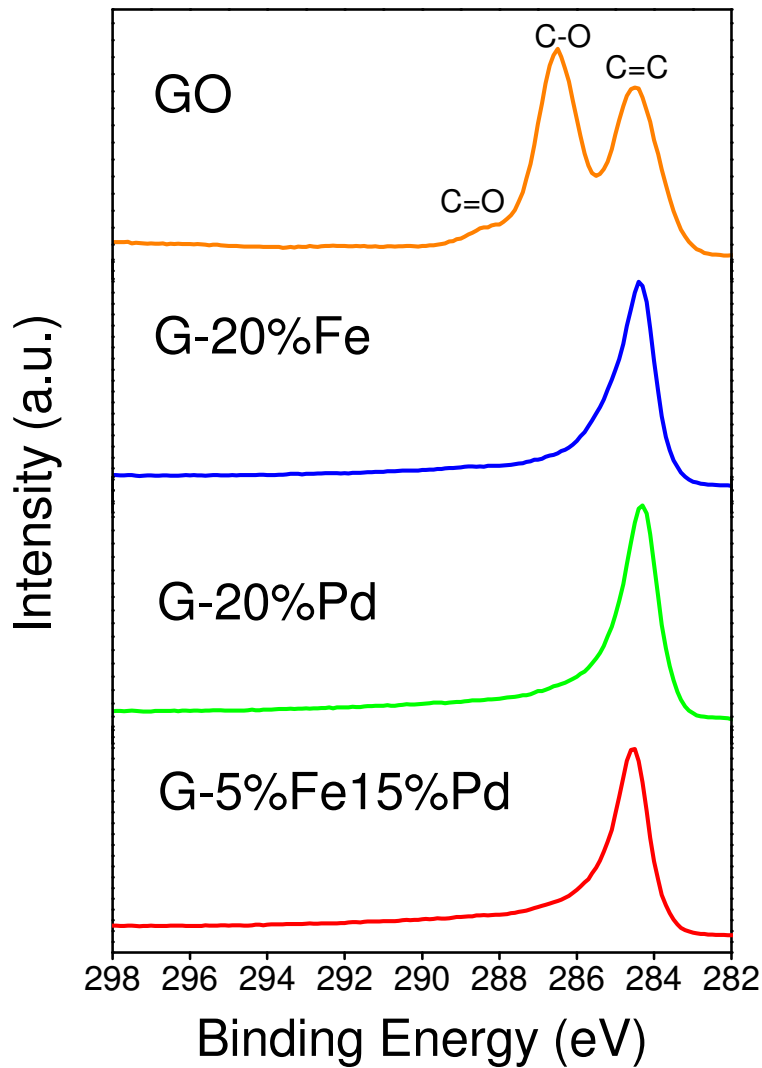
Figure 8-4 XPS spectra of C1 binding energies for GO and sample after LVCC reduction

X-ray Photoelectron Spectroscopy (XPS) spectra in **Figure 8-4** compares the C 1s binding energies for GO and LVCC reduced samples. The GO spectrum shows peaks at 285 eV, 286.7 eV and 287.7 eV corresponding to the C=C, C-O and C=O groups, respectively. After laser irradiation, C-O and C=O peaks are removed signifying the reduction of GO.

Figure 8-5 contains XPS spectra of the Pd3d binding energies for 20% Pd - 80% G and 15% Pd- 5% Fe/ 80% G. The spectra indicates the presence of Pd^0 after reduction due to the binding energies observed at 341 eV (Pd^0 $3d^{3/2}$) and 336 eV (Pd^0 $3d^{5/2}$) which is consistent with those found in literature.
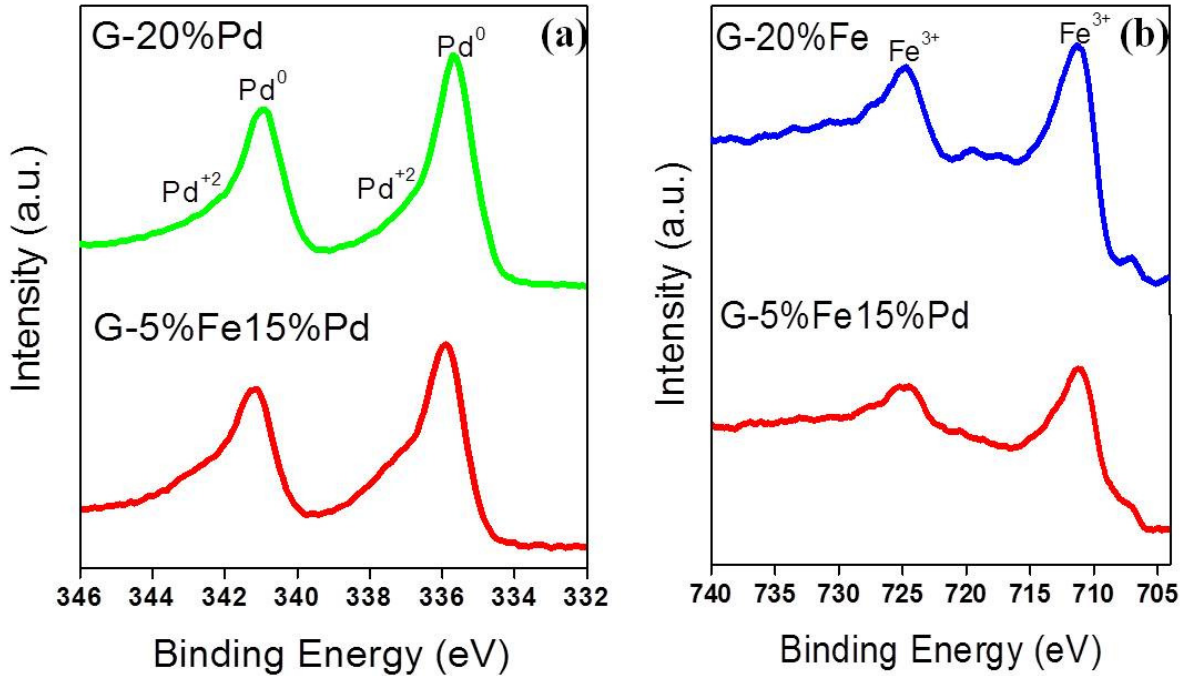
Figure 8-5 (a) XPS spectra of Pd3d, (b) XPS spectra of Fe2p Binding Energies

Figures 8-5 a, b summarizes the XPS data of Fe2p for 20% Fe - 80% G and 15% Pd- 5% Fe - 80% G. The spectra confirms the presence of Fe^{+3} due to the binding energies at 724 eV (Fe^{+3} $2p^{1/2}$) and 711.5 eV (Fe^{+3} $2p^{3/2}$) which is consistent with those found in literature.

169

The presence and strength of magnetic properties in Fe-G and Pd-Fe/G can be visualized in **Figure 8-6**. Once a magnetic field is applied to the samples, a magnetic moment can be observed due to the presence of Fe.
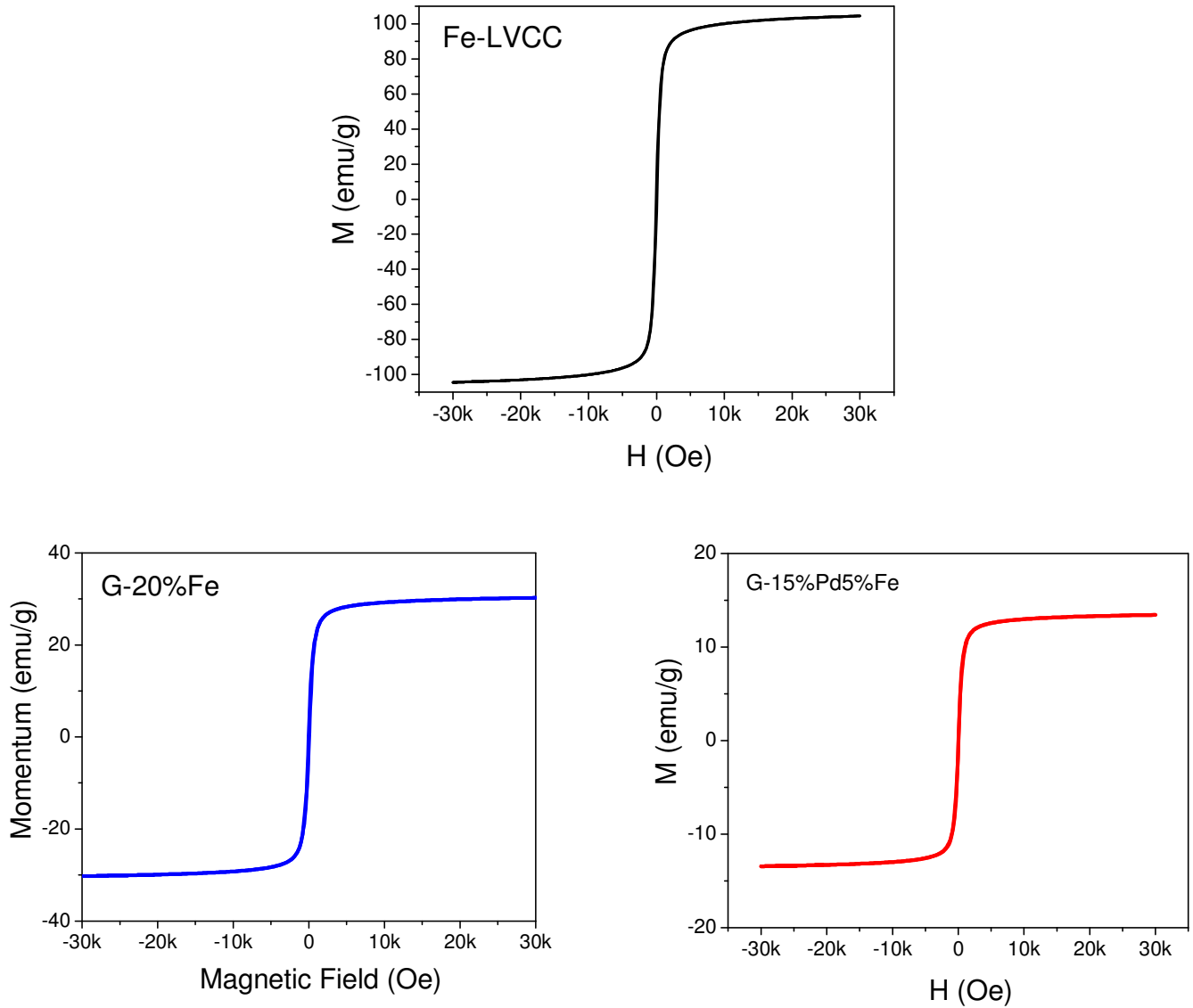
Figure 8-6 Magnetic data for Fe (top), Fe/G (bottom left) and Pd-Fe/G (bottom right)

Table 8-1 depicts the percent conversion obtained after each catalyst was tested in the Suzuki cross-coupling reaction for two runs. The catalyst was subjected to reaction conditions at 80 °C using MWI for five minutes.
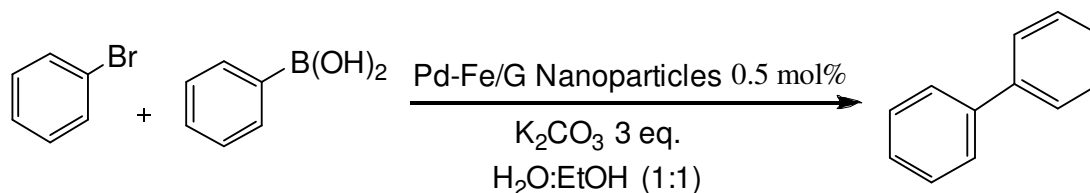
Table 8-1 Data collected for recycling of LVCC prepared catalysts. The catalysis was run for 5 minutes at 80 °C using MWI

Catalyst	Run 1 (% Conversion)	Run 2 (% Conversion)
20%Fe – 80%GO	No Reaction	No Reaction
20%Pd – 80%GO	100	-
7%Pd – 13%Fe - 80%GO	93	37
10%Pd – 10%Fe - 80%GO	100	68
15%Pd – 5%Fe - 80%GO	100	86

Without the active component, Pd, no reaction occurred while using the Fe/G catalyst. After increasing the Pd composition, recyclability and activity improved. When more Fe was present, conversion decreased as shown by the 7% Pd - 13% Fe - 80% G where conversion rate for the first run was only 93%. The conversion percent improved with equal compositions of Pd and Fe for both runs. The 15% Pd - 5% Fe - 80% G catalyst proved to be the best catalyst for the cross-coupling reaction which achieved 100% conversion for the first run and 86% conversion for the second run—the highest out of all catalysts for both runs. This is actually consistent with TEM images in **Figure 8-8** as that catalyst showed the best dispersion among other catalysts.
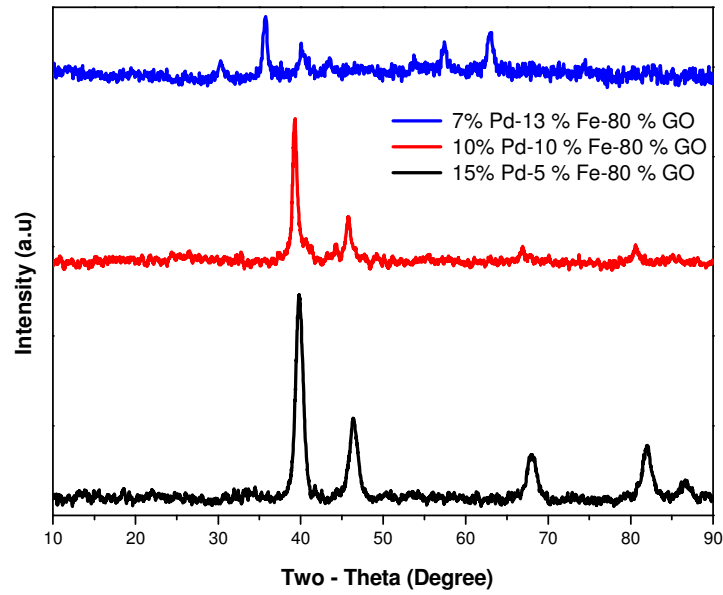
Figure 8-8-7 XRD Pattern of selected catalysts prepared by LVCC.
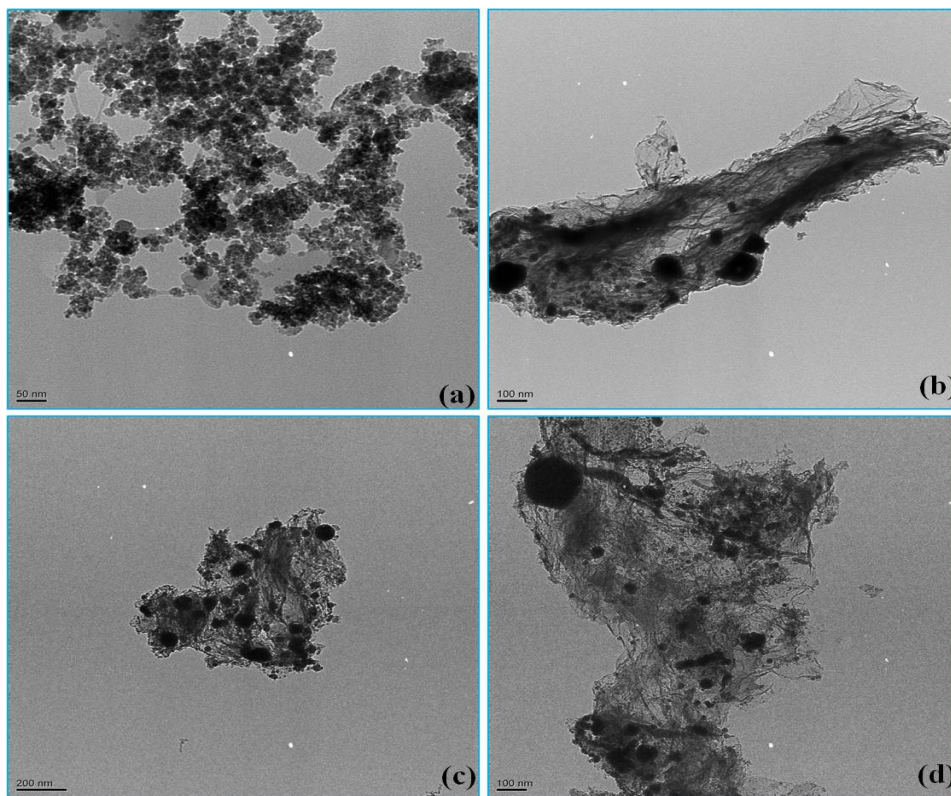
Figure 8-8 TEM images of (a) 20%Pd – 80%GO, (b) 7%Pd – 13%Fe - 80%GO, (c) 10%Pd – 10%Fe - 80%GO, (d) 15%Pd – 5%Fe - 80%GO.

172

Generally, the XRD pattern shown in **Figure 8-7** clearly indicates that the product is enriched with Fe_3O_4 and metal Pd (0). The palladium shows the typical sharp diffraction peak at $2\theta = 40°$. The XRD patterns indicate that the products were all (Fe_3O_4) magnetite with reference code (ICCD-00-003-0863). It is also easily to notice that the sharp diffraction peak at $2\theta = 40°$ which is characteristic to palladium and also the characteristic peaks of Fe_3O_4 is shown as a sharp diffraction peak at $2\theta = 35°$. The very small broad peak around $2\theta = 26°$ in Pd- Fe_3O_4 /G sample could suggest the presence of a minor component of multilayer graphene. The diffraction peaks (2θ) of Pd- Fe_3O_4 /G at 40, 46.8, and 68.2 are ascribed to the (111), (200), and (220) planed of Pd NPs which are similar to pure palladium and also to the peaks of Pd- Fe_3O_4 as shown.

8.5 Conclusions

The results indicate that LVCC is superior to other methods that often utilize toxic chemicals for the full reduction of GO. FT-IR data shows the disappearance of GO distinguishing O-H, C=O, C-O, C=C stretching indicating the formation of graphene. UV-Vis data shows peaks red shifted from 230 nm to 280 nm, characteristic of GO reduction and exfoliation. XPS data confirms Pd^o and Fe^{+3} present at the surface of the catalyst after reduction. The most effective magnetic catalyst synthesized was the 15% Pd- 5% Fe - 80% G. This result can be attributed to the Pd composition being greater than that of the Fe enabling favorable interactions between the Pd and G support increasing catalytic activity and reusability. The least effective catalyst was the 20% Fe - 80% G due to the lack of active component. The effects of manipulating the Pd-Fe/G composition and using different environments in the LVCC process can be investigated further to improve catalysis in cross-coupling reactions.

173

List of References

List of References

1.	El-Shall, M. S.; Hassan, H. A.; Abdelsayed, V.; AbouZeid, K. M., Microwave synthesis of graphene sheets and graphene-polymer nanocomposites. *Abstracts of Papers of the American Chemical Society* **2009,** 238.

2.	El-Shall, M. S.; Abdelsayed, V.; Khder, A.; Hassan, H. M. A.; El-Kaderi, H. M.; Reich, T. E., Metallic and bimetallic nanocatalysts incorporated into highly porous coordination polymer MIL-101. *Journal of Materials Chemistry* **2009,** 19, (41), 7625-7631.

3.	El-Shall, M. S., Metal nanocrystals supported on graphene sheets and highly porous coordination polymers. *Abstracts of Papers of the American Chemical Society* **2009,** 238.

4.	Xiao, C. W.; Ding, H.; Shen, C. M.; Yang, T. Z.; Hui, C.; Gao, H. J., Shape-Controlled Synthesis of Palladium Nanorods and Their Magnetic Properties. *Journal of Physical Chemistry C* **2009,** 113, (31), 13466-13469.

5.	Wang, H. Z.; Kou, X. L.; Zhang, L.; Li, J. G., Size-controlled synthesis, microstructure and magnetic properties of Ni nanoparticles. *Materials Research Bulletin* **2008,** 43, (12), 3529-3536.

6.	Epifani, M.; Pellicer, E.; Arbiol, J.; Morante, J. R., Metal Oxide Nanocrystals from the Injection of Metal Oxide Sols in a Coordinating Environment: Principles, Applicability, and Investigation of the Synthesis Variables in the Case Study of CeO(2) and SnO(2). *Chemistry of Materials* **2009,** 21, (5), 862-870.

7.	Malewicz, M.; Byrczek, M.; Teterycz, H.; Ieee, *Synthesis Of Zinc Oxide Nanotiles By Wet Chemical Route Assisted By Microwave Heating*. 2009; p 47-50.

8.	El-Shall, M. S.; Abdelsayed, V. M., Nanoparticles, filaments, fibers, and tree-like assemblies prepared by laser vaporization controlled condensation. *Abstracts of Papers of the American Chemical Society* **2003,** 225, U438-U438.

9.	ElShall, M. S.; Li, S. T.; Graiver, D.; Pernisz, U., Synthesis of nanostructured materials using a laser vaporization-condensation technique. In *Nanotechnology: Molecularly Designed Materials*, Chow, G. M. G. K. E., Ed. 1996; Vol. 622, pp 79-99.

10.	ElShall, M. S., Laser vaporization for the synthesis of nanoparticles and polymers containing metal particulates. *Applied Surface Science* **1996,** 106, 347-355.

11.	ElShall, M. S.; Graiver, D.; Pernisz, U.; Baraton, M. I., Synthesis and characterization of nanoscale zinc oxide particles .1. Laser vaporization condensation technique. *Nanostructured Materials* **1995,** 6, (1-4), 297-300.

175

12.   Elshall, M. S.; Slack, W.; Vann, W.; Kane, D.; Hanley, D., SYNTHESIS OF NANOSCALE METAL-OXIDE PARTICLES USING LASER VAPORIZATION CONDENSATION IN A DIFFUSION CLOUD CHAMBER. *Journal of Physical Chemistry* **1994,** 98, (12), 3067-3070.

13.   Pithawalla, Y. B.; Deevi, S. C.; El-Shall, M. S., Preparation of ultrafine and nanocrystalline FeAl powders. *Materials Science and Engineering a-Structural Materials Properties Microstructure and Processing* **2002,** 329, 92-98.

14.   Abdelsayed, V.; El-Shall, M. S.; Seto, T., Differential mobility analysis of nanoparticles generated by laser vaporization and controlled condensation (LVCC). *Journal of Nanoparticle Research* **2006,** 8, (3-4), 361-369.

15.   Abdelsayed, V.; Glaspell, G.; Nguyen, M.; Howe, J. M.; El-Shall, M. S., Laser synthesis of bimetallic nanoalloys in the vapor and liquid phases and the magnetic properties of PdM and PtM nanoparticles (M = Fe, Co and Ni). *Faraday Discussions* **2008,** 138, 163-180.

16.   Li, S. T.; Germanenko, I. N.; El-Shall, M. S., Nanoparticles from the vapor phase: Synthesis and characterization of Si, Ge, MoO3, and WO3 nanocrystals. *Journal of Cluster Science* **1999,** 10, (4), 533-547.

17.   Glaspell, G. P., Synthesis of cobalt nitrate hydrate nanoparticles using laser vaporization controlled condensation. *Abstracts of Papers of the American Chemical Society* **2003,** 225, U510-U510.

18.   Zedan, A. F.; Moussa, S.; Terner, J.; Atkinson, G.; El-Shall, M. S., Ultrasmall Gold Nanoparticles Anchored to Graphene and Enhanced Photothermal Effects by Laser Irradiation of Gold Nanostructures in Graphene Oxide Solutions. *Acs Nano* **2013,** 7, (1), 627-636.

19.   Zedan, A. F.; Abdelsayed, V.; Mohamed, M. B.; El-Shall, M. S., Rapid synthesis of magnetic/luminescent (Fe3O4/CdSe) nanocomposites by microwave irradiation. *Journal of Nanoparticle Research* **2013,** 15, (1).

20.   Herring, N.; Panda, A.; AbouZeid, K.; Almahoudi, S.; Olson, C.; Patel, A.; El-Shall, M. S., Microwave Synthesis of Metal Oxide Nanoparticles. In *Metal Oxide Nanomaterials for Chemical Sensors*, Carpenter, M. A.; Mathur, S.; Kolmakov, A., Eds. Springer New York: 2013; pp 245-284.

21.   Ye, D. X.; Moussa, S.; Ferguson, J. D.; Baski, A. A.; El-Shall, M. S., Highly Efficient Electron Field Emission from Graphene Oxide Sheets Supported by Nickel Nanotip Arrays. *Nano Letters* **2012,** 12, (3), 1265-1268.

22.   Moussa, S.; Siamaki, A. R.; Gupton, B. F.; El-Shall, M. S., Pd-Partially Reduced Graphene Oxide Catalysts (Pd/PRGO): Laser Synthesis of Pd Nanoparticles Supported on PRGO Nanosheets for Carbon-Carbon Cross Coupling Reactions. *Acs Catalysis* **2012,** 2, (1), 145-154.

176

23.   Herring, N. P.; Almahoudi, S. H.; Olson, C. R.; El-Shall, M. S., Enhanced photocatalytic activity of ZnO-graphene nanocomposites prepared by microwave synthesis. *Journal of Nanoparticle Research* **2012,** 14, (12).

24.   Abdelsayed, V.; Moussa, S.; Hassan, H. M.; Aluri, H. S.; Collinson, M. M.; El-Shall, M. S., Photothermal Deoxygenation of Graphite Oxide with Laser Excitation in Solution and Graphene-Aided Increase in Water Temperature. *Journal of Physical Chemistry Letters* **2010,** 1, (19), 2804-2809.

25.   Yamada, Y.; Ueda, A.; Zhao, Z.; Maekawa, T.; Suzuki, K.; Takada, T.; Kobayashi, T., Rapid evaluation of oxidation catalysis by gas sensor system: total oxidation, oxidative dehydrogenation, and selective oxidation over metal oxide catalysts. *Catalysis Today* **2001,** 67, (4), 379-387.

26.   Kudo, S.; Maki, T.; Yamada, M.; Mae, K., A new preparation method of Au/ferric oxide catalyst for low temperature CO oxidation. *Chemical Engineering Science* **2010,** 65, (1), 214-219.

27.   Zou, Z. Q.; Meng, M.; Zha, Y. Q., The effect of dopant Cu, Fe, Ni or La on the structures and properties of mesoporous Co-Ce-O compound catalysts. *Journal of Alloys and Compounds* **2009,** 470, (1-2), 96-106.

28.   Kandalam, A. K.; Chatterjee, B.; Khanna, S. N.; Rao, B. K.; Jena, P.; Reddy, B. V., Oxidation of CO on Fe(2)O(3) model surfaces. *Surface Science* **2007,** 601, (21), 4873-4880.

29.   Dong, J.; Xu, Z. H.; Kuznicki, S. M., Magnetic Multi-Functional Nano Composites for Environmental Applications. *Advanced Functional Materials* **2009,** 19, (8), 1268-1275.

30.   Tsoncheva, T.; Manova, E.; Velinov, N.; Paneva, D.; Popova, M.; Kunev, B.; Tenchev, K.; Mitov, I., Thermally synthesized nanosized copper ferrites as catalysts for environment protection. *Catalysis Communications* 12, (2), 105-109.

31.   Shen, H. Y.; Pan, S. D.; Fang, F.; Shi, J., Synthesis and Catalytic Study of Magnetic Separable Catalyst: M(Salen)-Functionalized Fe(3)O(4) Polymer Composite Materials (M = Ru(III), Cu(II), Fe(III)). In *New and Advanced Materials, Pts 1 and 2*, Zhou, H. Y.; Gu, T. L.; Yang, D. G.; Jiang, Z. Y.; Zeng, J. M., Eds. Vol. 197-198, pp 495-498.

32.   Baruwati, B.; Polshettiwar, V.; Varma, R. S., Magnetically recoverable supported ruthenium catalyst for hydrogenation of alkynes and transfer hydrogenation of carbonyl compounds. *Tetrahedron Letters* **2009,** 50, (11), 1215-1218.

33.   Sreedhar, B.; Kumar, A. S.; Yada, D., Magnetically Recoverable Pd/Fe(3)O(4)-Catalyzed Hiyama Cross-Coupling of Aryl Bromides with Aryl Siloxanes. *Synlett*, (8), 1081-1084.

34.   Ananikov, V. P.; Orlov, N. V.; Beletskaya, I. P.; Khrustalev, V. N.; Antipin, M. Y.; Timofeeva, T. V., New approach for size- and shape-controlled preparation of pd nanoparticles with organic ligands. Synthesis and application in catalysis. *Journal of the American Chemical Society* **2007,** 129, (23), 7252-+.

177

35.   Moreno-Manas, M.; Pleixats, R., Formation of carbon-carbon bonds under catalysis by transition-metal nanoparticles. *Accounts of Chemical Research* **2003,** 36, (8), 638-643.

36.   Tanikawa, K.; Egawa, C., Effect of barium addition on CO oxidation activity of palladium catalysts. *Applied Catalysis a-General* **2011,** 403, (1-2), 12-17.

37.   Slavinskaya, E. M.; Gulyaev, R. V.; Stonkus, O. A.; Zadesenets, A. V.; Plyusnin, P. E.; Shubin, Y. V.; Korenev, S. V.; Ivanova, A. S.; Zaikovskii, V. I.; Danilova, I. G.; Boronin, A. I., Low-temperature oxidation of carbon monoxide on Pd(Pt)/CeO2 catalysts prepared from complex salts. *Kinetics and Catalysis* **2011,** 52, (2), 282-295.

38.   Cargnello, M.; Wieder, N. L.; Montini, T.; Gorte, R. J.; Fornasiero, P., Synthesis of Dispersible Pd@CeO2 Core-Shell Nanostructures by Self-Assembly. *Journal of the American Chemical Society* **2010,** 132, (4), 1402-1409.

39.   Abdelsayed, V.; Aljarash, A.; El-Shall, M. S.; Al Othman, Z. A.; Alghamdi, A. H., Microwave Synthesis of Bimetallic Nanoalloys and CO Oxidation on Ceria-Supported Nanoalloys. *Chemistry of Materials* **2009,** 21, (13), 2825-2834.

40.   Yang, D. P.; Gao, F.; Cui, D. X.; Yang, M., Microwave Rapid Synthesis of Nanoporous Fe(3)O(4) Magnetic Microspheres. *Current Nanoscience* **2009,** 5, (4), 485-488.

41.   Yamauchi, T.; Tsukahara, Y.; Yamada, K.; Sakata, T.; Wada, Y., Nucleation and Growth of Magnetic Ni-Co (Core-Shell) Nanoparticles in a One-Pot Reaction under Microwave Irradiation. *Chemistry of Materials* 23, (1), 75-84.

42.   Wu, K. L.; Wei, X. W.; Zhou, X. M.; Wu, D. H.; Liu, X. W.; Ye, Y.; Wang, Q., NiCo(2) Alloys: Controllable Synthesis, Magnetic Properties, and Catalytic Applications in Reduction of 4-Nitrophenol. *Journal of Physical Chemistry C* 115, (33), 16268-16274.

43.   Xie, X. W.; Shen, W. J., Morphology control of cobalt oxide nanocrystals for promoting their catalytic performance. *Nanoscale* **2009,** 1, (1), 50-60.

44.   Salavati-Niasari, M.; Khansari, A.; Davar, F., Synthesis and characterization of cobalt oxide nanoparticles by thermal treatment process. *Inorganica Chimica Acta* **2009,** 362, (14), 4937-4942.

45.   Liu, W.; Li, B. J.; Gao, C. L.; Xu, Z., A Magnetically Separable Heterogeneous Catalyst Co@CoO Hollow Spheres: Synthesis and Catalytic Performance for the Selective Oxidation of Alcohol. *Chemistry Letters* **2009,** 38, (11), 1110-1111.

46.   Qiu, G. H.; Huang, H.; Genuino, H.; Opembe, N.; Stafford, L.; Dharmarathna, S.; Suib, S. L., Microwave-Assisted Hydrothermal Synthesis of Nanosized alpha-Fe(2)O(3) for Catalysts and Adsorbents. *Journal of Physical Chemistry C* 115, (40), 19626-19631.

47.   Liu, X. S.; Hu, F.; Zhu, D. R.; Jia, D. N.; Wang, P. P.; Ruan, Z.; Cheng, C. H., One-step synthesis of carbon nanotubes with Ni nanoparticles as a catalyst by the microwave-assisted polyol method. *Journal of Alloys and Compounds* 509, (6), 2829-2832.

178

48.   Hirvi, J. T.; Kinnunen, T. J. J.; Suvanto, M.; Pakkanen, T. A.; Norskov, J. K., CO oxidation on PdO surfaces. *Journal of Chemical Physics* **2010,** 133, (8).

49.   Nicolaou, K. C.; Bulger, P. G.; Sarlah, D., Palladium-catalyzed cross-coupling reactions in total synthesis. *Angewandte Chemie-International Edition* **2005,** 44, (29), 4442-4489.

50.   Tietze, L. F.; Dufert, A., Multiple Pd-catalyzed reactions in the synthesis of natural products, drugs, and materials. *Pure and Applied Chemistry* **2010,** 82, (7), 1375-1392.

51.   Ozawa, F.; Yamagami, I.; Nakano, M.; Fujisawa, F.; Yamamoto, A., PALLADIUM-CATALYZED CARBONYLATION OF AROMATIC-ALDEHYDES AND HYDROCARBONS - A NOVEL SYNTHETIC ROUTE TO ALPHA-KETO AMIDES VIA C-H ACTIVATION. *Chemistry Letters* **1989**, (1), 125-128.

52.   Wu, X. F.; Anbarasan, P.; Neumann, H.; Beller, M., Palladium-Catalyzed Carbonylative C-H Activation of Heteroarenes. *Angewandte Chemie-International Edition* **2010,** 49, (40), 7316-7319.

53.   Houlden, C. E.; Hutchby, M.; Bailey, C. D.; Ford, J. G.; Tyler, S. N. G.; Gagne, M. R.; Lloyd-Jones, G. C.; Booker-Milburn, K. I., Room-Temperature Palladium-Catalyzed C-H Activation: ortho-Carbonylation of Aniline Derivatives. *Angewandte Chemie-International Edition* **2009,** 48, (10), 1830-1833.

54.   Yin, G. C.; Jia, C. G.; Kitamura, T.; Yamaji, T.; Fujiwara, Y., A new efficient Pd-catalyzed synthesis of diphenyl carbonate with heteropolyacid as a cocatalyst. *Journal of Organometallic Chemistry* **2001,** 630, (1), 11-16.

55.   Polshettiwar, V.; Varma, R. S., Green chemistry by nano-catalysis. *Green Chemistry* 12, (5), 743-754.

56.   Yu, X. H.; Hu, Y. C.; Zhou, L.; Cao, F. J.; Yang, Y. X.; Liang, T.; He, J. H., Research Progress of Nanostructured Materials for Heterogeneous Catalysis. *Current Nanoscience* 7, (4), 576-586.

57.   Xu, Z. W.; Li, H. J.; Cao, G. X.; Cao, Z. Y.; Zhang, Q. L.; Li, K. Z.; Hou, X. H.; Li, W.; Cao, W. F., Synthesis of hybrid graphene carbon-coated nanocatalysts. *Journal of Materials Chemistry* 20, (38), 8230-8232.

58.   Xia, H. Q.; Cui, B.; Zhou, J. H.; Zhang, L. L.; Zhang, J.; Guo, X. H.; Guo, H. L., Synthesis and characterization of Fe(3)O(4)@C@Ag nanocomposites and their antibacterial performance. *Applied Surface Science* 257, (22), 9397-9402.

59.   Su, Q. M.; Li, J.; Zhong, G.; Du, G. H.; Xu, B. S., In Situ Synthesis of Iron/Nickel Sulfide Nanostructures-Filled Carbon Nanotubes and Their Electromagnetic and Microwave-Absorbing Properties. *Journal of Physical Chemistry C* 115, (5), 1838-1842.

60.   Rao, P. M.; Zheng, X. L., Unique Magnetic Properties of Single Crystal gamma-Fe(2)O(3) Nanowires Synthesized by Flame Vapor Deposition. *Nano Letters* 11, (6), 2390-2395.

61.   Coker, V. S.; Bennett, J. A.; Telling, N. D.; Henkel, T.; Charnock, J. M.; van der Laan, G.; Pattrick, R. A. D.; Pearce, C. I.; Cutting, R. S.; Shannon, I. J.; Wood, J.; Arenholz, E.; Lyon, I. C.; Lloyd, J. R., Microbial Engineering of Nanoheterostructures: Biological Synthesis of a Magnetically Recoverable Palladium Nanocatalyst. *Acs Nano* 4, (5), 2577-2584.

62.   Alonso-Nunez, G.; de la Garza, L. M.; Rogel-Hernandez, E.; Reynoso, E.; Licea-Claverie, A.; Felix-Navarro, R. M.; Berhault, G.; Paraguay-Delgado, F., New organometallic salts as precursors for the functionalization of carbon nanotubes with metallic nanoparticles. *Journal of Nanoparticle Research* 13, (9), 3643-3656.

63.   Xu, M. H.; Qi, X. S.; Zhong, W.; Ye, X. J.; Deng, Y.; Au, C. T.; Jin, C. Q.; Yang, Z. X.; Du, Y. W., Synthesis and Properties of Magnetic Composites of Carbon Nanotubes/Fe Nanoparticle. *Chinese Physics Letters* **2009,** 26, (11).

64.   Vaidya, S.; Ramanujachary, K. V.; Lofland, S. E.; Ganguli, A. K., Synthesis of Homogeneous NiO@SiO(2) Core-shell Nanostructures and the Effect of Shell Thickness on the Magnetic Properties. *Crystal Growth & Design* **2009,** 9, (4), 1666-1670.

65.   Senapati, K. K.; Borgohain, C.; Phukan, P., Synthesis of highly stable CoFe(2)O(4) nanoparticles and their use as magnetically separable catalyst for Knoevenagel reaction in aqueous medium. *Journal of Molecular Catalysis a-Chemical* 339, (1-2), 24-31.

66.   Zhu, Y. H.; Stubbs, L. P.; Ho, F.; Liu, R. Z.; Ship, C. P.; Maguire, J. A.; Hosmane, N. S., Magnetic Nanocomposites: A New Perspective in Catalysis. *Chemcatchem* 2, (4), 365-374.

67.   Zhang, R. Z.; Liu, J. M.; Wang, S. F.; Niu, J. Z.; Xia, C. G.; Sun, W., Magnetic CuFe(2)O(4) Nanoparticles as an Efficient Catalyst for C-O Cross-Coupling of Phenols with Aryl Halides. *Chemcatchem* 3, (1), 146-149.

68.   Vargas, C.; Balu, A. M.; Campelo, J. M.; Gonzalez-Arellano, C.; Luque, R.; Romero, A. A., Towards Greener and More Efficient C-C and C-Heteroatom Couplings: Present and Future. *Current Organic Synthesis* 7, (6), 568-586.

69.   Rosario-Amorin, D.; Gaboyard, M.; Clerac, R.; Nlate, S.; Heuze, K., Enhanced catalyst recovery in an aqueous copper-free Sonogashira cross-coupling reaction. *Dalton Transactions* 40, (1), 44-46.

70.   Andrade, A. L.; Souza, D. M.; Pereira, M. C.; Fabris, J. D.; Domingues, R. Z., Catalytic Effect of Magnetic Nanoparticles Over the H(2)O(2) Decomposition Reaction. *Journal of Nanoscience and Nanotechnology* **2009,** 9, (6), 3695-3699.

71.   Yan, J. M.; Zhang, X. B.; Han, S.; Shioyama, H.; Xu, Q., Magnetically recyclable Fe-Ni alloy catalyzed dehydrogenation of ammonia borane in aqueous solution under ambient atmosphere. *Journal of Power Sources* **2009,** 194, (1), 478-481.

72.   Mori, K.; Yamashita, H., Progress in design and architecture of metal nanoparticles for catalytic applications. *Physical Chemistry Chemical Physics* 12, (43), 14420-14432.

180

73. Rodriguez-Reinoso, F., The role of carbon materials in heterogeneous catalysis. *Carbon* **1998,** 36, (3), 159-175.

74. Berry, F. J.; Smith, M. R., THE PERFORMANCE OF IRON-CONTAINING CATALYSTS PREPARED AT LOW-TEMPERATURE FOR CARBON-MONOXIDE HYDROGENATION. *Hyperfine Interactions* **1991,** 67, (1-4), 549-557.

75. Scheuermann, G. M.; Rumi, L.; Steurer, P.; Bannwarth, W.; Mulhaupt, R., Palladium Nanoparticles on Graphite Oxide and Its Functionalized Graphene Derivatives as Highly Active Catalysts for the Suzuki-Miyaura Coupling Reaction. *Journal of the American Chemical Society* **2009,** 131, (23), 8262-8270.

76. Guillen, E.; Rico, R.; Lopez-Romero, J. M.; Bedia, J.; Rosas, J. M.; Rodriguez-Mirasol, J.; Cordero, T., Pd-activated carbon catalysts for hydrogenation and Suzuki reactions. *Applied Catalysis a-General* **2009,** 368, (1-2), 113-120.

77. Karousis, N.; Tsotsou, G. E.; Evangelista, F.; Rudolf, P.; Ragoussis, N.; Tagmatarchis, N., Carbon nanotubes decorated with palladium nanoparticles: Synthesis, characterization, and catalytic activity. *Journal of Physical Chemistry C* **2008,** 112, (35), 13463-13469.

78. Li, Z. C.; Zhou, Q. F., Preparation of nanopalladium from waste Pd-C catalyst. *Rare Metal Materials and Engineering* **2007,** 36, (9), 1685-1688.

79. Zhang, Y.; Chu, W.; Xie, L. J.; Sun, W. J., Preparation and Catalytic Performance of Carbon Nanotube Supported Palladium Catalyst. *Chinese Journal of Chemistry* 28, (6), 879-883.

80. Cao, G. X.; Fu, Y. W.; Sun, H. H.; Xu, Z. W.; Li, H. J.; Tian, S., Synthesis of Carbon Coated Nano Fe-Ni Magnetic Particles. *Chinese Journal of Inorganic Chemistry* 27, (7), 1431-1435.

81. Zhang, Y. X.; Yu, X. Y.; Jia, Y.; Jin, Z.; Liu, J. H.; Huang, X. J., A Facile Approach for the Synthesis of Ag-Coated Fe3O4@TiO2 Core/Shell Microspheres as Highly Efficient and Recyclable Photocatalysts. *European Journal of Inorganic Chemistry*, (33), 5096-5104.

82. Zhang, Y. Q.; Wei, X. W.; Yao, Z. J., Synthesis of Fe(3)O(4) Microspheres-Supported Catalysts for Suzuki Coupling Reaction. *Chinese Journal of Chemistry* 28, (11), 2274-2280.

83. Qi, G.; Liu, W.; Bei, Z. N., Fe(3)O(4)/ZnS Hollow Nanospheres: A Highly Efficient Magnetic Heterogeneous Catalyst for Synthesis of 5-Substituted 1H-Tetrazoles from Nitriles and Sodium Azide. *Chinese Journal of Chemistry* 29, (1), 131-134.

84. Nasr-Esfahani, M.; Hoseini, S. J.; Mohammadi, F., Fe(3)O(4) Nanoparticles as an Efficient and Magnetically Recoverable Catalyst for the Synthesis of 3,4-Dihydropyrimidin-2(1H)-ones under Solvent-Free Conditions. *Chinese Journal of Catalysis* 32, (9), 1484-1489.

85. Nakhjavan, B.; Tahir, M. N.; Panthofer, M.; Gao, H. T.; Schladt, T. D.; Gasi, T.; Ksenofontov, V.; Branscheid, R.; Weber, S.; Kolb, U.; Schreiber, L. M.; Tremel, W., Synthesis,

181

characterization and functionalization of nearly mono-disperse copper ferrite Cu(x)Fe(3-x)O(4) nanoparticles. *Journal of Materials Chemistry* 21, (19), 6909-6915.

86.   Lu, H. Y.; Yang, S. H.; Deng, J.; Zhang, Z. H., Magnetic Fe(3)O(4) Nanoparticles as New, Efficient, and Reusable Catalysts for the Synthesis of Quinoxalines in Water. *Australian Journal of Chemistry* 63, (8), 1290-1296.

87.   Liu, B.; Zhang, W.; Yang, F. K.; Feng, H. L.; Yang, X. L., Facile Method for Synthesis of Fe(3)O(4)@Polymer Microspheres and Their Application As Magnetic Support for Loading Metal Nanoparticles. *Journal of Physical Chemistry C* 115, (32), 15875-15884.

88.   He, L. H.; Yao, L.; Liu, F. J.; Qin, B.; Song, R.; Huang, W., Magnetic Fe(3)O(4)@Chitosan Nanoparticle: Synthesis, Characterization and Application as Catalyst Carrier. *Journal of Nanoscience and Nanotechnology* 10, (10), 6348-6355.

89.   He, H. K.; Gao, C., Synthesis of Fe(3)O(4)/Pt Nanoparticles Decorated Carbon Nanotubes and Their Use as Magnetically Recyclable Catalysts. *Journal of Nanomaterials*.

90.   Han, Y.; Wang, Y. J.; Li, L.; Wang, Y. P.; Jiao, L. F.; Yuan, H. T.; Liu, S. X., Preparation and electrochemical performance of flower-like hematite for lithium-ion batteries. *Electrochimica Acta* 56, (9), 3175-3181.

91.   Frost, C. G.; Mutton, L., Heterogeneous catalytic synthesis using microreactor technology. *Green Chemistry* 12, (10), 1687-1703.

92.   Firouzabadi, H.; Iranpoor, N.; Gholinejad, M.; Hoseini, J., Magnetite (Fe(3)O(4)) Nanoparticles-Catalyzed Sonogashira-Hagihara Reactions in Ethylene Glycol under Ligand-Free Conditions. *Advanced Synthesis & Catalysis* 353, (1), 125-132.

93.   Fihri, A.; Bouhrara, M.; Nekoueishahraki, B.; Basset, J. M.; Polshettiwar, V., Nanocatalysts for Suzuki cross-coupling reactions. *Chemical Society Reviews* 40, (10), 5181-5203.

94.   Falcon, H.; Tartaj, P.; Rebolledo, A. F.; Campos-Martin, J. M.; Fierro, J. L. G.; Al-Zahrani, S. M., Large-scale synthesis of porous magnetic composites for catalytic applications. In *Scientific Bases for the Preparation of Heterogeneous Catalysts: Proceedings of the 10th International Symposium*, Gaigneaux, E. M.; Devillers, M.; Hermans, S.; Jacobs, P. A.; Martens, J. A.; Ruiz, P., Eds. Vol. 175, pp 347-350.

95.   Chen, H. M.; Chu, P. K.; He, J. H.; Hu, T.; Yang, M. Q., Porous magnetic manganese oxide nanostructures: Synthesis and their application in water treatment. *Journal of Colloid and Interface Science* 359, (1), 68-74.

96.   Arundhathi, R.; Damodara, D.; Likhar, P. R.; Kantam, M. L.; Saravanan, P.; Magdaleno, T.; Kwon, S. H., Fe(3)O(4)@mesoporouspolyaniline: A Highly Efficient and Magnetically Separable Catalyst for Cross-Coupling of Aryl Chlorides and Phenols. *Advanced Synthesis & Catalysis* 353, (9), 1591-1600.

182

97. Li, H. F.; Huang, Y. H.; Zhang, Q.; Qiao, Y.; Gu, Y. S.; Liu, J.; Zhang, Y., Facile synthesis of highly uniform Mn/Co-codoped ZnO nanowires: Optical, electrical, and magnetic properties. *Nanoscale* 3, (2), 654-660.

98. Feng, C.; Zhang, Y. C.; Zhang, Y. N.; Wen, Y. L.; Zhao, J. Q., Study on Alumina-Supported Cobalt-Nickel Oxide Catalyst for Synthesis of Acetonitrile from Ethanol. *Catalysis Letters* 141, (1), 168-177.

99. Horikoshi, S.; Osawa, A.; Abe, M.; Serpone, N., On the Generation of Hot-Spots by Microwave Electric and Magnetic Fields and Their Impact on a Microwave-Assisted Heterogeneous Reaction in the Presence of Metallic Pd Nanoparticles on an Activated Carbon Support. *Journal of Physical Chemistry C* 115, (46), 23030-23035.

100. Yin, Y. Y.; Zhou, S. X.; Min, C.; Wu, L. M., Preparation of rattle-type magnetic mesoporous carbon spheres and their highly efficient adsorption and separation. *Journal of Colloid and Interface Science* 361, (2), 527-533.

101. Wu, H. Y.; Jiao, Q. Z.; Zhao, Y.; Liu, H. B.; Li, X. F.; Cao, Y.; Tang, X. L., Synthesis and Characterization of Zn/Ni/Fe Magnetic Composite Oxide Nanotubles Assembled in Porous Anodic Alumina. *Synthesis and Reactivity in Inorganic Metal-Organic and Nano-Metal Chemistry* 40, (9), 695-699.

102. Tasca, J. E.; Quincoces, C. E.; Lavat, A.; Alvarez, A. M.; Gonzalez, M. G., Preparation and characterization of CuFe(2)O(4) bulk catalysts. *Ceramics International* 37, (3), 803-812.

103. Pan, D. K.; Zhang, H., Synthesis and Characterization of Magnetic Mg-Al Mixed Oxides Submicro Particles with Core-Shell Structure. *Chinese Journal of Inorganic Chemistry* 27, (7), 1341-1347.

104. Uhm, Y. R.; Lee, H. M.; Olga, F.; Irina, O.; Marina, V.; Gennady, R.; Valery, C.; Rhee, C. K., Synthesis of carbon encapsulated metal (Ni and Cu) nano particles and applications for chiral catalysts. *Research on Chemical Intermediates* 36, (6-7), 867-873.

105. Konig, M.; Reith, L. M.; Monkowius, U.; Knor, G.; Bretterbauer, K.; Schoefberger, W., Suzuki-Miyaura cross-coupling reaction on copper-trans-A(2)B corroles with excellent functional group tolerance. *Tetrahedron* 67, (23), 4243-4252.

106. Ulusoy, M.; Sahin, O.; Kilic, A.; Buyukgungor, O., Multinuclear Cu(II) Schiff Base Complex as Efficient Catalyst for the Chemical Coupling of CO(2) and Epoxides: Synthesis, X-ray Structural Characterization and Catalytic Activity. *Catalysis Letters* 141, (5), 717-725.

107. Shylesh, S.; Wang, L.; Demeshko, S.; Thiel, W. R., Facile Synthesis of Mesoporous Magnetic Nanocomposites and their Catalytic Application in Carbon-Carbon Coupling Reactions. *Chemcatchem* 2, (12), 1543-1547.

108. Schatz, A.; Long, T. R.; Grass, R. N.; Stark, W. J.; Hanson, P. R.; Reiser, O., Immobilization on a Nanomagnetic Co/C Surface Using ROM Polymerization: Generation of a

183

Hybrid Material as Support for a Recyclable Palladium Catalyst. *Advanced Functional Materials* 20, (24), 4323-4328.

109.   Borhade, S. R.; Waghmode, S. B., Studies on Pd/NiFe(2)O(4) catalyzed ligand-free Suzuki reaction in aqueous phase: synthesis of biaryls, terphenyls and polyaryls. *Beilstein Journal of Organic Chemistry* 7.

110.   Tsvelikhovsky, D.; Popov, I.; Gutkin, V.; Rozin, A.; Shvartsman, A.; Blum, J., On the Involvement of Palladium Nanoparticles in the Heck and Suzuki Reactions. *European Journal of Organic Chemistry* **2009**, (1), 98-102.

111.   Gaikwad, A. V.; Holuigue, A.; Thathagar, M. B.; ten Elshof, J. E.; Rothenberg, G., Ion- and atom-leaching mechanisms from palladium nanoparticles in cross-coupling reactions. *Chemistry-a European Journal* **2007,** 13, (24), 6908-6913.

112.   Novoselov, K. S.; Geim, A. K.; Morozov, S. V.; Jiang, D.; Zhang, Y.; Dubonos, S. V.; Grigorieva, I. V.; Firsov, A. A., Electric Field Effect in Atomically Thin Carbon Films. *Science* **2004,** 306, (5696), 666-669.

113.   Li, D.; Muller, M. B.; Gilje, S.; Kaner, R. B.; Wallace, G. G., Processable aqueous dispersions of graphene nanosheets. *Nat Nano* **2008,** 3, (2), 101-105.

114.   Zhou, Z. X.; Tian, S. Q.; Zeng, D. W.; Tang, G.; Xie, C. S., MOX (M = Zn, Co, Fe)/AP shell-core nanocomposites for self-catalytical decomposition of ammonium perchlorate. *Journal of Alloys and Compounds* **2012,** 513, 213-219.

115.   Herzing, A. A.; Kiely, C. J.; Carley, A. F.; Landon, P.; Hutchings, G. J., Identification of active gold nanoclusters on iron oxide supports for CO oxidation. *Science* **2008,** 321, (5894), 1331-1335.

116.   Zhong, Z. Y.; Lin, J. Y.; Teh, S. P.; Teo, J.; Dautzenberg, F. M., A rapid and efficient method to deposit gold particles on catalyst supports and its application for CO oxidation at low temperatures. *Advanced Functional Materials* **2007,** 17, (8), 1402-1408.

117.   Kustov, A. L.; Frey, A. M.; Larsen, K. E.; Johannessen, T.; Norskov, J. K.; Christensen, C. H., CO methanation over supported bimetallic Ni-Fe catalysts: From computational studies towards catalyst optimization. *Applied Catalysis a-General* **2007,** 320, 98-104.

118.   Al-Sayari, S.; Carley, A. F.; Taylor, S. H.; Hutchings, G. J., Au/ZnO and Au/Fe2O3 catalysts for CO oxidation at ambient temperature: comments on the effect of synthesis conditions on the preparation of high activity catalysts prepared by coprecipitation. *Topics in Catalysis* **2007,** 44, (1-2), 123-128.

119.   Moreau, F.; Bond, G. C., CO oxidation activity of gold catalysts supported on various oxides and their improvement by inclusion of an iron component. *Catalysis Today* **2006,** 114, (4), 362-368.

184

120.   Daniells, S. T.; Overweg, A. R.; Makkee, M.; Moulijn, J. A., The mechanism of low-temperature CO oxidation with Au/Fe2O3 catalysts: a combined Mossbauer, FT-IR, and TAP reactor study. *Journal of Catalysis* **2005,** 230, (1), 52-65.

121.   Boyd, D.; Golunski, S.; Hearne, G. R.; Magadzu, T.; Mallick, K.; Raphulu, M. C.; Venugopal, A.; Scurrell, M. S., Reductive routes to stabilized nanogold and relation to catalysis by supported gold. *Applied Catalysis a-General* **2005,** 292, 76-81.

122.   Shen, Y. X.; Lu, G. Z.; Guo, Y.; Wang, Y. Q.; Guo, Y. L.; Wang, L.; Zhen, X., An excellent support of Pd-Fe-O-x catalyst for low temperature CO oxidation: CeO2 with rich (200) facets. *Catalysis Communications* **2012,** 18, 26-31.

123.   Skala, T.; Tsud, N.; Prince, K. C.; Matolin, V., Bimetallic bonding and mixed oxide formation in the Ga-Pd-CeO2 system. *Journal of Applied Physics* **2011,** 110, (4).

124.   Nabae, Y.; Yamanaka, I., Alloying effects of Pd and Ni on the catalysis of the oxidation of dry CH4 in solid oxide fuel cells. *Applied Catalysis a-General* **2009,** 369, (1-2), 119-124.

125.   Heide, P., *X-ray Photoelectron Spectroscopy: An Introduction to Principles and Practices*. John Wiley & Sons: 2011.

126.   Chernavskii, P. A.; Dalmon, J. A.; Perov, N. S.; Khodakov, A. Y., Magnetic Characterization of Fischer-Tropsch Catalysts. *Oil & Gas Science and Technology-Revue De L Institut Francais Du Petrole* **2009,** 64, (1), 25-48.

127.   Zhang, D. E.; Yang, W.; Wang, M. Y.; Zhang, X. B.; Li, S. Z.; Han, G. Q.; Ying, A. L.; Tong, Z. W., Facile synthesis of flower-like nickel nanocrystals and properties. *Journal of Physics and Chemistry of Solids* 72, (12), 1397-1399.

128.   Yang, Y. Z.; Liu, X. G.; Han, Y. X.; Ren, W. F.; Xu, B. S., Ferromagnetic Property and Synthesis of Onion-Like Fullerenes by Chemical Vapor Deposition Using Fe and Co Catalysts Supported on NaCl. *Journal of Nanomaterials*.

129.   Surowiec, Z.; Gac, W.; Wiertel, M., The Synthesis and Properties of High Surface Area Fe(2)O(3) Materials. *Acta Physica Polonica A* 119, (1), 18-20.

130.   Senthilkumar, B.; Selvan, R. K.; Vinothbabu, P.; Perelshtein, I.; Gedanken, A., Structural, magnetic, electrical and electrochemical properties of NiFe(2)O(4) synthesized by the molten salt technique. *Materials Chemistry and Physics* 130, (1-2), 285-292.

131.   Prakash, I.; Nallamuthu, N.; Muralidharan, P.; Venkateswarlu, M.; Misra, M.; Mohanty, A.; Satyanarayana, N., Preparation and characterization of nanocrystalline CoFe(2)O(4) deposited on SiO(2): in situ sol-gel process. *Journal of Sol-Gel Science and Technology* 58, (1), 24-32.

132.   Guo, Y.; Azmat, M. U.; Liu, X. H.; Ren, J. W.; Wang, Y. Q.; Lu, G. Z., Controllable synthesis of hexagonal close-packed nickel nanoparticles under high nickel concentration and its catalytic properties. *Journal of Materials Science* 46, (13), 4606-4613.

185

133.   Chen, L.; Zhu, Q. S.; Hao, Z. G.; Zhang, T.; Xie, Z. H., Development of a Co-Ni bimetallic aerogel catalyst for hydrogen production via methane oxidative CO_2 reforming in a magnetic assisted fluidized bed. *International Journal of Hydrogen Energy* 35, (16), 8494-8502.

134.   Wu, L.; He, Y. M.; Fan, Q. H., Controlled Reversible Anchoring of?6-Arene/TsDPEN-Ruthenium(II) Complex onto Magnetic Nanoparticles: A New Strategy for Catalyst Separation and Recycling. *Advanced Synthesis & Catalysis* 353, (16), 2915-2919.

135.   Taufany, F.; Pan, C. J.; Chou, H. L.; Rick, J.; Chen, Y. S.; Liu, D. G.; Lee, J. F.; Tang, M. T.; Hwang, B. J., Relating Structural Aspects of Bimetallic Pt(3)Cr(1)/C Nanoparticles to Their Electrocatalytic Activity, Stability, and Selectivity in the Oxygen Reduction Reaction. *Chemistry-a European Journal* 17, (38), 10723-10734.

136.   Sharma, S.; Gajbhiye, N. S.; Ningthoujam, R. S., Synthesis and self-assembly of monodisperse Co(x)Ni(100-x) (x=50, 80) colloidal nanoparticles by homogenous nucleation. *Journal of Colloid and Interface Science* 351, (2), 323-329.

137.   Lin, K. S.; Adhikari, A. K.; Tsai, Z. Y.; Chen, Y. P.; Chien, T. T.; Tsai, H. B., Synthesis and characterization of nickel ferrite nanocatalysts for CO_2 decomposition. *Catalysis Today* 174, (1), 88-96.

138.   Khadzhiev, S. N.; Krylova, A. Y., Fischer-tropsch synthesis in a three-phase system over nanocatalysts (review). *Petroleum Chemistry* 51, (2), 74-85.

139.   Hong, J. P.; Chu, W.; Ying, Y. X.; Chernavskii, P. A.; Khodakov, A., Plasma-assisted design of supported cobalt catalysts for Fischer-Tropsch synthesis. In *Scientific Bases for the Preparation of Heterogeneous Catalysts: Proceedings of the 10th International Symposium*, Gaigneaux, E. M.; Devillers, M.; Hermans, S.; Jacobs, P. A.; Martens, J. A.; Ruiz, P., Eds. Vol. 175, pp 253-257.

140.   Gao, Y.; Zhao, J. Z.; Zhou, B.; Zhu, Y. C.; Wang, Z. C., Aqueous synthesis of flower-like nickel nanostructures under the induction of magnetic field. *Colloids and Surfaces a-Physicochemical and Engineering Aspects* 368, (1-3), 137-141.

141.   Moussa, S. O.; El-Shall, M. S., Fabrication of nanostructured nickel and titanium aluminides starting from elemental nanopowders. *Materials Chemistry and Physics* **2008,** 112, (3), 1015-1020.

142.   Norton, D. M.; Mitchell, E. A.; Botros, N. R.; Jessop, P. G.; Baird, M. C., A Superior Precursor for Palladium(0)-Based Cross-Coupling and Other Catalytic Reactions. *Journal of Organic Chemistry* **2009,** 74, (17), 6674-6680.

143.   Fouad, O. A.; El-Shall, M. S., MICROWAVE IRRADIATION ASSISTED GROWTH OF Cu, Ni, Co METALS AND/OR OXIDES NANOCLUSTERS AND THEIR CATALYTIC PERFORMANCE. *Nano* **2012,** 7, (5).

144.   Siamaki, A. R.; Khder, A. E. S.; Abdelsayed, V.; El-Shall, M. S.; Gupton, B. F., Microwave-assisted synthesis of palladium nanoparticles supported on graphene: A highly active

186

and recyclable catalyst for carbon-carbon cross-coupling reactions. *Journal of Catalysis* **2011,** 279, (1), 1-11.

145.   Hassan, H. M. A.; Abdelsayed, V.; Khder, A.; AbouZeid, K. M.; Terner, J.; El-Shall, M. S.; Al-Resayes, S. I.; El-Azhary, A. A., Microwave synthesis of graphene sheets supporting metal nanocrystals in aqueous and organic media. *Journal of Materials Chemistry* **2009,** 19, (23), 3832-3837.

146.   Abdelsayed, V.; Aljarash, A.; El-Shall, M. S., INOR 58-Microwave synthesis of passivated nanoalloys with controlled size and shape. *Abstracts of Papers of the American Chemical Society* **2008,** 236.

147.   Shviro, M.; Zitoun, D., Nickel nanocrystals: fast synthesis of cubes, pyramids and tetrapods. *Rsc Advances* **2013,** 3, (5), 1380-1387.

148.   Pourmortazavi, S. M.; Rahimi-Nasrabadi, M.; Khalilian-Shalamzari, M.; Zahedi, M. M.; Hajimirsadeghi, S. S.; Omrani, I., Synthesis, structure characterization and catalytic activity of nickel tungstate nanoparticles. *Applied Surface Science* **2012,** 263, 745-752.

149.   Zedan, A. F.; Sappal, S.; Moussa, S.; El-Shall, M. S., Ligand-Controlled Microwave Synthesis of Cubic and Hexagonal CdSe Nanocrystals Supported on Graphene. Photoluminescence Quenching by Graphene. *Journal of Physical Chemistry C* **2010,** 114, (47), 19920-19927.

150.   Mohamed, M. B.; AbouZeid, K. M.; Abdelsayed, V.; Aljarash, A. A.; El-Shall, M. S., Growth Mechanism of Anisotropic Gold Nanocrystals via Microwave Synthesis: Formation of Dioleamide by Gold Nanocatalysis. *Acs Nano* **2010,** 4, (5), 2766-2772.

151.   Moussa, S.; Abdelsayed, V.; El-Shall, M. S., Laser synthesis of Pt, Pd, CoO and Pd-CoO nanoparticle catalysts supported on graphene. *Chemical Physics Letters* **2011,** 510, (4-6), 179-184.

152.   Fukui, K.; Igawa, Y.; Arimitsu, N.; Suzuki, M.; Segawa, T.; Fujii, K.; Yamamoto, T.; Yoshida, H., Mechanism of synthesis of metallic oxide powder from aqueous metallic nitrate solution by microwave denitration method. *Chemical Engineering Journal* **2012,** 211, 1-8.

153.   Herring, N. P.; AbouZeid, K.; Mohamed, M. B.; Pinsk, J.; El-Shall, M. S., Formation Mechanisms of Gold-Zinc Oxide Hexagonal Nanopyramids by Heterogeneous Nucleation using Microwave Synthesis. *Langmuir* **2011,** 27, (24), 15146-15154.

154.   Glaspell, G. P.; Anderson, J.; Wilkins, J. R.; El-Shall, M. S., Vapor phase synthesis of upconverting nanocrystals to generate red, green, blue and white light. *Abstracts of Papers of the American Chemical Society* **2009,** 237.

155.   AbouZeid, K. M.; Mohamed, M. B.; Abdelsayed, V.; Aljarash, A.; El-Shall, M. S., Shape controlled anisotropic gold nanocrystals via microwave synthesis. *Abstracts of Papers of the American Chemical Society* **2009,** 238.

187

156.   Fouad, O. A.; Glaspell, G.; El-Shall, M. S., Growth and characterization of ZnO, SnO2 and ZnO/SnO2 nanostructures from the vapor phase. *Topics in Catalysis* **2008,** 47, (1-2), 84-96.

157.   LaMer, V. K.; Dinegar, R. H., Theory, Production and Mechanism of Formation of Monodispersed Hydrosols. *Journal of the American Chemical Society* **1950,** 72, (11), 4847-4854.

158.   Wang, D. S.; Li, X. Y.; Li, H.; Li, L. S.; Hong, X.; Peng, Q.; Li, Y. D., Semiconductor-noble metal hybrid nanomaterials with controlled structures. *Journal of Materials Chemistry A* **2013,** 1, (5), 1587-1590.

159.   Li, P.; Wang, D. S.; Wei, Z.; Peng, Q.; Li, Y. D., Systematic Synthesis of ZnO Nanostructures. *Chemistry-a European Journal* **2013,** 19, (11), 3735-3740.

160.   Xie, T.; Li, S. A.; Wang, W. B.; Peng, Q.; Li, Y. D., Nucleation and Growth of BarF(x)Cl(2-x) Nanorods. *Chemistry-a European Journal* **2008,** 14, (31), 9730-9735.

161.   Peng, X. G.; Wickham, J.; Alivisatos, A. P., Kinetics of II-VI and III-V colloidal semiconductor nanocrystal growth: "Focusing" of size distributions. *Journal of the American Chemical Society* **1998,** 120, (21), 5343-5344.

162.   Ning, H. Q.; Peng, F. F.; Zhu, S. F.; Hu, Q. H.; Li, Z. R.; Zhao, J.; Zhao, Q.; Huang, S. D.; Jin, X., Coarsening kinetics of multiaxial forging (MAF) formed AZ91D magnesium alloy in semisolid state. *Materials Research Innovations* **2013,** 17, S16-S20.

163.   Peng, Z. A.; Peng, X. G., Mechanisms of the shape evolution of CdSe nanocrystals. *Journal of the American Chemical Society* **2001,** 123, (7), 1389-1395.

164.   Hummers, W. S.; Offeman, R. E., Preparation of Graphitic Oxide. *Journal of the American Chemical Society* **1958,** 80, (6), 1339-1339.

165.   Geim, A. K., Graphene: Status and Prospects. *Science* **2009,** 324, (5934), 1530-1534.

166.   Blake, P.; Brimicombe, P. D.; Nair, R. R.; Booth, T. J.; Jiang, D.; Schedin, F.; Ponomarenko, L. A.; Morozov, S. V.; Gleeson, H. F.; Hill, E. W.; Geim, A. K.; Novoselov, K. S., Graphene-Based Liquid Crystal Device. *Nano Letters* **2008,** 8, (6), 1704-1708.

167.   Geim, A. K.; Novoselov, K. S., The rise of graphene. *Nat Mater* **2007,** 6, (3), 183-191.

168.   Bai, H.; Li, C.; Shi, G., Functional Composite Materials Based on Chemically Converted Graphene. *Advanced Materials* **2011,** 23, (9), 1089-1115.

169.   Izadi-Najafabadi, A.; Yamada, T.; Futaba, D. N.; Yudasaka, M.; Takagi, H.; Hatori, H.; Iijima, S.; Hata, K., High-Power Supercapacitor Electrodes from Single-Walled Carbon Nanohorn/Nanotube Composite. *ACS Nano* **2011,** 5, (2), 811-819.

170.   Lin, Y.; Baggett, D. W.; Kim, J.-W.; Siochi, E. J.; Connell, J. W., Instantaneous Formation of Metal and Metal Oxide Nanoparticles on Carbon Nanotubes and Graphene via Solvent-Free Microwave Heating. *ACS Applied Materials & Interfaces* 3, (5), 1652-1664.

171. Cong, H.-P.; He, J.-J.; Lu, Y.; Yu, S.-H., Water-Soluble Magnetic-Functionalized Reduced Graphene Oxide Sheets: In situ Synthesis and Magnetic Resonance Imaging Applications. *Small* 6, (2), 169-173.

172. Chandra, V.; Park, J.; Chun, Y.; Lee, J. W.; Hwang, I.-C.; Kim, K. S., Water-Dispersible Magnetite-Reduced Graphene Oxide Composites for Arsenic Removal. *ACS Nano* 4, (7), 3979-3986.

173. Lee, J.-K.; Gwinner, M. C.; Berger, R.; Newby, C.; Zentel, R.; Friend, R. H.; Sirringhaus, H.; Ober, C. K., High-Performance Electron-Transporting Polymers Derived from a Heteroaryl Bis(trifluoroborate). *Journal of the American Chemical Society* **2011,** 133, (26), 9949-9951.

174. Yang, X.; Zhang, X.; Ma, Y.; Huang, Y.; Wang, Y.; Chen, Y., Superparamagnetic graphene oxide-Fe3O4 nanoparticles hybrid for controlled targeted drug carriers. *Journal of Materials Chemistry* **2009,** 19, (18), 2710-2714.

175. Liang, J.; Xu, Y.; Sui, D.; Zhang, L.; Huang, Y.; Ma, Y.; Li, F.; Chen, Y., Flexible, Magnetic, and Electrically Conductive Graphene/Fe3O4 Paper and Its Application for Magnetic-Controlled Switches. *The Journal of Physical Chemistry C* 114, (41), 17465-17471.

176. Yang, J.; Fang, H.-H.; Ding, R.; Lu, S.-Y.; Zhang, Y.-L.; Chen, Q.-D.; Sun, H.-B., High-Quality Large-Size Organic Crystals Prepared by Improved Physical Vapor Growth Technique and Their Optical Gain Properties. *The Journal of Physical Chemistry C* **2011,** 115, (18), 9171-9175.

177. Zhou, G.-W.; Wang, J.; Gao, P.; Yang, X.; He, Y.-S.; Liao, X.-Z.; Yang, J.; Ma, Z.-F., Facile Spray Drying Route for the Three-Dimensional Graphene-Encapsulated Fe2O3 Nanoparticles for Lithium Ion Battery Anodes. *Industrial & Engineering Chemistry Research* **2012,** 52, (3), 1197-1204.

178. Su, J.; Cao, M.; Ren, L.; Hu, C., Fe3O4â€"Graphene Nanocomposites with Improved Lithium Storage and Magnetism Properties. *The Journal of Physical Chemistry C* **2011,** 115, (30), 14469-14477.

179. Sun, S.; Zeng, H.; Robinson, D. B.; Raoux, S.; Rice, P. M.; Wang, S. X.; Li, G., Monodisperse MFe2O4 (M = Fe, Co, Mn) Nanoparticles. *Journal of the American Chemical Society* **2003,** 126, (1), 273-279.

180. Shavel, A.; Rodríguez-González, B.; Pacifico, J.; Spasova, M.; Farle, M.; Liz-Marzán, L. M., Shape Control in Iron Oxide Nanocrystal Synthesis, Induced by Trioctylammonium Ions. *Chemistry of Materials* **2009,** 21, (7), 1326-1332.

181. Wang, X.; Zhao, Z.; Qu, J.; Wang, Z.; Qiu, J., Shape-Control and Characterization of Magnetite Prepared via a One-Step Solvothermal Route. *Crystal Growth & Design* **2010,** 10, (7), 2863-2869.

189

182. Li, X.; Si, Z.; Lei, Y.; Tang, J.; Wang, S.; Su, S.; Song, S.; Zhao, L.; Zhang, H., Direct hydrothermal synthesis of single-crystalline triangular Fe3O4 nanoprisms. *CrystEngComm* **2010,** 12, (7), 2060-2063.

183. Ye, Q.-L.; Kozuka, Y.; Yoshikawa, H.; Awaga, K.; Bandow, S.; Iijima, S., Effects of the unique shape of submicron magnetite hollow spheres on magnetic properties and domain states. *Physical Review B* **2007,** 75, (22), 224404.

184. Chalasani, R.; Vasudevan, S., Form, Content, and Magnetism in Iron Oxide Nanocrystals. *The Journal of Physical Chemistry C* **2011,** 115, (37), 18088-18093.

185. Ho, C.-H.; Tsai, C.-P.; Chung, C.-C.; Tsai, C.-Y.; Chen, F.-R.; Lin, H.-J.; Lai, C.-H., Shape-Controlled Growth and Shape-Dependent Cation Site Occupancy of Monodisperse Fe3O4 Nanoparticles. *Chemistry of Materials* **2011,** 23, (7), 1753-1760.

186. Zhu, M.; Diao, G., Synthesis of Porous Fe3O4 Nanospheres and Its Application for the Catalytic Degradation of Xylenol Orange. *The Journal of Physical Chemistry C* **2011,** 115, (39), 18923-18934.

187. Lu, W.; Shen, Y.; Xie, A.; Zhang, X.; Chang, W., Novel Bifuncitonal One-Dimensional Fe3O4/Se Nanocomposites via Facile Green Synthesis. *The Journal of Physical Chemistry C* **2010,** 114, (11), 4846-4851.

188. Hwang, S. O.; Kim, C. H.; Myung, Y.; Park, S.-H.; Park, J.; Kim, J.; Han, C.-S.; Kim, J.-Y., Synthesis of Vertically Aligned Manganese-Doped Fe3O4 Nanowire Arrays and Their Excellent Room-Temperature Gas Sensing Ability. *The Journal of Physical Chemistry C* **2008,** 112, (36), 13911-13916.

189. Gao, G.; Liu, X.; Shi, R.; Zhou, K.; Shi, Y.; Ma, R.; Takayama-Muromachi, E.; Qiu, G., Shape-Controlled Synthesis and Magnetic Properties of Monodisperse Fe3O4 Nanocubes. *Crystal Growth & Design* **2010,** 10, (7), 2888-2894.

190. Li, L.; Yang, Y.; Ding, J.; Xue, J., Synthesis of Magnetite Nanooctahedra and Their Magnetic Field-Induced Two-/Three-Dimensional Superstructure. *Chemistry of Materials* **2010,** 22, (10), 3183-3191.

191. Chen, Y.-J.; Zhang, F.; Zhao, G.-g.; Fang, X.-y.; Jin, H.-B.; Gao, P.; Zhu, C.-L.; Cao, M.-S.; Xiao, G., Synthesis, Multi-Nonlinear Dielectric Resonance, and Excellent Electromagnetic Absorption Characteristics of Fe3O4/ZnO Core/Shell Nanorods. *The Journal of Physical Chemistry C* **2010,** 114, (20), 9239-9244.

192. Shen, J.; Hu, Y.; Shi, M.; Li, N.; Ma, H.; Ye, M., One Step Synthesis of Graphene Oxideâˆ'Magnetic Nanoparticle Composite. *The Journal of Physical Chemistry C* 114, (3), 1498-1503.

193. Wang, Y.; Zhang, H.; Yao, D.; Pu, J.; Zhang, Y.; Gao, X.; Sun, Y., Direct electrochemistry of hemoglobin on graphene/Fe3O4 nanocomposite-modified glass carbon

electrode and its sensitive detection for hydrogen peroxide. *J. Solid State Electrochem.* **2013,** 17, (Copyright (C) 2013 American Chemical Society (ACS). All Rights Reserved.), 881-887.

194. Xu, Y.; Lv, Z.; Xia, Y.; Han, Y.; Lou, B.; Wang, E., Highly porous magnetite/graphene nanocomposites for a solid-state electrochemiluminescence sensor on paper-based chips. *Anal. Bioanal. Chem.* **2013,** 405, (Copyright (C) 2013 American Chemical Society (ACS). All Rights Reserved.), 3549-3558.

195. Hu, A.; Chen, X.; Tang, Y.; Yang, L.; Xiao, H.; Fan, B., A facile method to synthesize Fe3O4/graphene composites in normal pressure with high rate capacity and cycling stability. *Mater. Lett.* **2013,** 91, (Copyright (C) 2013 American Chemical Society (ACS). All Rights Reserved.), 315-318.

196. Zhang, Y.; Cheng, Y.; Zhou, Y.; Li, B.; Gu, W.; Shi, X.; Xian, Y., Electrochemical sensor for bisphenol A based on magnetic nanoparticles decorated reduced graphene oxide. *Talanta* **2013,** 107, (Copyright (C) 2013 American Chemical Society (ACS). All Rights Reserved.), 211-218.

197. Wang, T.; Liu, Z.; Lu, M.; Wen, B.; Ouyang, Q.; Chen, Y.; Zhu, C.; Gao, P.; Li, C.; Cao, M.; Qi, L., Graphene-Fe3O4 nanohybrids: Synthesis and excellent electromagnetic absorption properties. *J. Appl. Phys. (Melville, NY, U. S.)* **2013,** 113, (Copyright (C) 2013 American Chemical Society (ACS). All Rights Reserved.), 024314/1-024314/8.

198. Abdelsayed, V.; El-Shall, M. S., Vapor phase nucleation on neutral and charged nanoparticles: Condensation of supersaturated trifluoroethanol on Mg nanoparticles. *The Journal of Chemical Physics* **2007,** 126, (2), 024706-6.

199. Chen, S. T.; Si, R.; Taylor, E.; Janzen, J.; Chen, J. Y., Synthesis of Pd/Fe3O4 Hybrid Nanocatalysts with Controllable Interface and Enhanced Catalytic Activities for CO Oxidation. *Journal of Physical Chemistry C* **2012,** 116, (23), 12969-12976.

200. Ivanova, A. S.; Slavinskaya, E. M.; Gulyaev, R. V.; Zaikovskii, V. I.; Stonkus, O. A.; Danilova, I. G.; Plyasova, L. M.; Polukhina, I. A.; Boronin, A. I., Metal-support interactions in Pt/Al2O3 and Pd/Al2O3 catalysts for CO oxidation. *Applied Catalysis B-Environmental* **2010,** 97, (1-2), 57-71.

201. Manna, L.; Scher, E. C.; Alivisatos, A. P., Synthesis of Soluble and Processable Rod-, Arrow-, Teardrop-, and Tetrapod-Shaped CdSe Nanocrystals. *Journal of the American Chemical Society* **2000,** 122, (51), 12700-12706.

202. Chang, C. H.; Paul, B. K.; Remcho, V. T.; Atre, S.; Hutchison, J. E., Synthesis and post-processing of nanomaterials using microreaction technology. *Journal of Nanoparticle Research* **2008,** 10, (6), 965-980.

203. Zhao, C. X.; He, L. Z.; Qiao, S. Z.; Middelberg, A. P. J., Nanoparticle synthesis in microreactors. *Chemical Engineering Science* 66, (7), 1463-1479.

204. Cao, S. W.; Zhu, Y. J.; Chang, J., Fe3O4 polyhedral nanoparticles with a high magnetization synthesized in mixed solvent ethylene glycol-water system. *New Journal of Chemistry* **2008,** 32, (9), 1526-1530.

205. Satsuma, A.; Sato, R.; Osaki, K.; Shimizu, K., Unique effect of surface area of support on propene combustion over Pd/ceria. *Catalysis Today* **2012,** 185, (1), 61-65.

206. Qu, F. L.; Sun, H. Y.; Zhang, S. F.; You, J. M.; Yang, M. H., Electrochemical sensing platform based on palladium modified ceria nanoparticles. *Electrochimica Acta* **2012,** 61, 173-178.

207. Mira, C.; Calvino, J. J.; Perez-Omil, J. A.; Rodriguez-Izquierdo, J. M.; Bernal, S., A novel procedure for accurate estimations of the lattice parameter of supported nanoparticles from the analysis of plan view HREM images: Application to the structural investigation of Pd/CeO2 catalysts. *Catalysis Today* **2012,** 180, (1), 174-183.

208. Mayernick, A. D.; Janik, M. J., Methane oxidation on Pd-Ceria: A DFT study of the mechanism over PdxCe1-xO2, Pd, and PdO (vol 2781, pg 16, 2011). *Journal of Catalysis* **2012,** 286, 299-299.

209. Zhao, M.; Li, X.; Zhang, L. H.; Zhang, C.; Gong, M. C.; Chen, Y. Q., Catalytic decomposition of methanol to carbon monoxide and hydrogen over palladium supported on Ce0.65Zr0.30La0.05O2 and La-Al2O3. *Catalysis Today* **2011,** 175, (1), 430-434.

210. Wieder, N. L.; Cargnello, M.; Bakhmutsky, K.; Montini, T.; Fornasiero, P.; Gorte, R. J., Study of the Water-Gas-Shift Reaction on Pd@CeO2/Al2O3 Core-Shell Catalysts. *Journal of Physical Chemistry C* **2011,** 115, (4), 915-919.

211. Wattanathana, W.; Lakkham, A.; Kaewvilai, A.; Koonsaeng, N.; Laobuthee, A.; Veranitisagul, C., Preliminary Study of Pd/CeO2 Derived from Cerium Complexes as Solid Support Catalysts for Hydrogenation Reaction in a Micro-reactor. In *9th Eco-Energy and Materials Science and Engineering Symposium*, Yupapin, P. P.; PivsaArt, S.; Ohgaki, H., Eds. 2011; Vol. 9.

212. Wang, Q. Y.; Li, G. F.; Zhao, B.; Zhou, R. X., Investigation on properties of a novel ceria-zirconia-praseodymia solid solution and its application in Pd-only three-way catalyst for gasoline engine emission control. *Fuel* **2011,** 90, (10), 3047-3055.

213. Wang, J. Q.; Zhang, B. Y.; Shen, M. Q.; Wang, J.; Wang, W. L.; Ma, J.; Liu, S. X.; Jia, L. W., Effects of Fe-doping of ceria-based materials on their microstructural and dynamic oxygen storage and release properties. *Journal of Sol-Gel Science and Technology* **2011,** 58, (1), 259-268.

214. Wang, J. Q.; Shen, M. Q.; Wang, J.; Wang, W. L., Steam effects over Pd/Ce0.67Zr0.33O2 three-way catalyst. *Journal of Rare Earths* **2011,** 29, (3), 217-224.

215.   Wang, B.; Weng, D. A.; Wu, X. D.; Ran, R., Modification of Pd-CeO2 catalyst by different treatments: Effect on the structure and CO oxidation activity. *Applied Surface Science* **2011,** 257, (9), 3878-3883.

216.   Sanjaykumar, S. R.; Mukri, B. D.; Patil, S.; Madras, G.; Hegde, M. S., Ce0.98Pd0.02O2-delta: Recyclable, ligand free palladium(II) catalyst for Heck reaction. *Journal of Chemical Sciences* **2011,** 123, (1), 47-54.

217.   Kwon, K.; Lee, K. H.; Jin, S. A.; You, D. J.; Pak, C., Ceria-promoted oxygen reduction reaction in Pd-based electrocatalysts. *Electrochemistry Communications* **2011,** 13, (10), 1067-1069.

218.   Li, X.; Wang, X. W.; Zhao, M.; Liu, J. Y.; Gong, M. C.; Chen, Y. Q., Ca-Modified Pd/CeO2-ZrO2-Al2O3 Catalysts for Methanol Decomposition. *Chinese Journal of Catalysis* **2011,** 32, (11), 1739-1746.

219.   Esteves, P.; Wu, Y.; Dujardin, C.; Dongare, M. K.; Granger, P., Ceria-zirconia mixed oxides as thermal resistant catalysts for the decomposition of nitrous oxide at high temperature. *Catalysis Today* **2011,** 176, (1), 453-457.

220.   Bali, S.; Huggins, F. E.; Ernst, R. D.; Pugmire, R. J.; Huffman, G. P.; Eyring, E. M., Iron-Ceria Aerogels Doped with Palladium as Water-Gas Shift Catalysts for the Production of Hydrogen. *Industrial & Engineering Chemistry Research* **2010,** 49, (4), 1652-1657.

221.   Chen, M.; Ma, Y.; Song, C.; Zhang, T.; Zheng, X. M., Preparation and Performance of Ce-Pt-Pd/Stainless Steel Wire Meshes Catalyst. *Chinese Journal of Catalysis* **2009,** 30, (7), 649-653.

222.   Nolan, M.; Verdugo, V. S.; Metiu, H., Vacancy formation and CO adsorption on gold-doped ceria surfaces. *Surface Science* **2008,** 602, (16), 2734-2742.

223.   Minato, T.; Susaki, T.; Shiraki, S.; Kato, H. S.; Kawai, M.; Aika, K.-i., Investigation of the electronic interaction between TiO2(1 1 0) surfaces and Au clusters by PES and STM. *Surface Science* **2004,** 566-568, (Part 2), 1012-1017.

224.   Xu, Y.; Mavrikakis, M., Adsorption and Dissociation of O2 on Gold Surfaces:â€‰ Effect of Steps and Strain. *The Journal of Physical Chemistry B* **2003,** 107, (35), 9298-9307.

225.   Zou, H.; Lin, Y. S.; Rane, N.; He, T., Synthesis and Characterization of Nanosized Ceria Powders and High-Concentration Ceria Sols. *Industrial & Engineering Chemistry Research* **2004,** 43, (12), 3019-3025.

226.   Liu, D.; Yates, M. Z., Fabrication of Size-Tunable TiO2 Tubes Using Rod-Shaped Calcite Templates. *Langmuir* **2007,** 23, (20), 10333-10341.

227.   Nian, J.-N.; Teng, H., Hydrothermal Synthesis of Single-Crystalline Anatase TiO2 Nanorods with Nanotubes as the Precursor. *The Journal of Physical Chemistry B* **2006,** 110, (9), 4193-4198.

228.	Khan, M. A.; Yang, O. B., Optimization of Silica Content in Initial Solâˆ'Gel Grain Particles for the Low Temperature Hydrothermal Synthesis of Titania Nanotubes. *Crystal Growth & Design* **2009,** 9, (4), 1767-1774.

229.	Kim, H. Y.; Lee, H. M.; Henkelman, G., CO Oxidation Mechanism on CeO2-Supported Au Nanoparticles. *Journal of the American Chemical Society* **2012**

134, (3), 1560-1570.

230.	Weng, M. H.; Ju, S. P., CO Oxidation Mechanism on Tungsten Nanoparticle. *The Journal of Physical Chemistry C* **2012,** 116, (35), 18803-18815.

231.	Wannakao, S.; Nongnual, T.; Khongpracha, P.; Maihom, T.; Limtrakul, J., Reaction Mechanisms for CO Catalytic Oxidation by N2O on Fe-Embedded Graphene. *The Journal of Physical Chemistry C* **2012,** 116, (32), 16992-16998.

232.	Nie, X.; Qian, H.; Ge, Q.; Xu, H.; Jin, R., CO Oxidation Catalyzed by Oxide-Supported Au25(SR)18 Nanoclusters and Identification of Perimeter Sites as Active Centers. *ACS Nano* **2012,** 6, (7), 6014-6022.

233.	Kim, H. Y.; Henkelman, G., CO Oxidation at the Interface between Doped CeO2 and Supported Au Nanoclusters. *The Journal of Physical Chemistry Letters* **2012,** 3, (16), 2194-2199.

234.	Zhu, G.-m.; Qu, Z.-b.; Zhuang, G.-l.; Xie, Q.; Meng, Q.-q.; Wang, J.-g., CO Oxidation by Lattice Oxygen on V2O5 Nanotubes. *The Journal of Physical Chemistry C* **2011,** 115, (30), 14806-14811.

235.	Sanchez-Dominguez, M.; Liotta, L. F.; Di Carlo, G.; Pantaleo, G.; Venezia, A. M.; Solans, C.; Boutonnet, M., Synthesis of CeO2, ZrO2, Ce0.5Zr0.5O2, and TiO2 nanoparticles by a novel oil-in-water microemulsion reaction method and their use as catalyst support for CO oxidation. *Catalysis Today* **2010,** 158, (1-2), 35-43.

236.	Li, Y.; Zhou, Z.; Yu, G.; Chen, W.; Chen, Z., CO Catalytic Oxidation on Iron-Embedded Graphene: Computational Quest for Low-Cost Nanocatalysts. *The Journal of Physical Chemistry C* **2010,** 114, (14), 6250-6254.

237.	Li, Q.; Zhang, Y.; Chen, G.; Fan, J.; Lan, H.; Yang, Y., Ultra-low-gold loading Au/CeO2 catalysts for ambient temperature CO oxidation: Effect of preparation conditions on surface composition and activity. *Journal of Catalysis* **2010,** 273, (2), 167-176.

238.	Christmann, K.; Schwede, S.; Schubert, S.; Kudernatsch, W., Model Studies on CO Oxidation Catalyst Systems: Titania and Gold Nanoparticles. *ChemPhysChem* **2010,** 11, (7), 1344-1363.

239.	Cargnello, M.; Wieder, N. L.; Montini, T.; Gorte, R. J.; Fornasiero, P., Synthesis of Dispersible Pd@CeO2 Coreâˆ'Shell Nanostructures by Self-Assembly. *Journal of the American Chemical Society* **2009,** 132, (4), 1402-1409.

240.   Camellone, M. F.; Fabris, S., Reaction Mechanisms for the CO Oxidation on Au/CeO2 Catalysts: Activity of Substitutional Au3+/Au+ Cations and Deactivation of Supported Au+ Adatoms. *Journal of the American Chemical Society* **2009,** 131, (30), 10473-10483.

241.   Deng, W.; Flytzani-Stephanopoulos, M., On the Issue of the Deactivation of Au–Ceria and Pt–Ceria Water–Gas Shift Catalysts in Practical Fuel-Cell Applications. *Angewandte Chemie* **2006,** 118, (14), 2343-2347.

242.   Deng, W.; Flytzani-Stephanopoulos, M., On the Issue of the Deactivation of Au–Ceria and Pt–Ceria Water–Gas Shift Catalysts in Practical Fuel-Cell Applications. *Angewandte Chemie International Edition* **2006,** 45, (14), 2285-2289.

243.   Shelef, M.; McCabe, R. W., Twenty-five years after introduction of automotive catalysts: what next? *Catalysis Today* **2000,** 62, (1), 35-50.

244.   Ligthart, D. A. J. M.; van Santen, R. A.; Hensen, E. J. M., Supported Rhodium Oxide Nanoparticles as Highly Active CO Oxidation Catalysts. *Angewandte Chemie International Edition* **2011,** 50, (23), 5306-5310.

245.   Glaspell, G.; Hassan; Elzatahry, A.; Fuoco, L.; Radwan, N. R. E.; El-Shall, M. S., Nanocatalysis on Tailored Shape Supports:â€‰ Au and Pd Nanoparticles Supported on MgO Nanocubes and ZnO Nanobelts. *The Journal of Physical Chemistry B* **2006,** 110, (43), 21387-21393.

246.   Glaspell, G.; Fuoco, L.; El-Shall, M. S., Microwave Synthesis of Supported Au and Pd Nanoparticle Catalysts for CO Oxidation. *The Journal of Physical Chemistry B* **2005,** 109, (37), 17350-17355.

247.   Hashmi, A. S. K.; Hutchings, G. J., Gold Catalysis. *Angewandte Chemie International Edition* **2006,** 45, (47), 7896-7936.

248.   Hickey, N.; Arneodo Larochette, P.; Gentilini, C.; Sordelli, L.; Olivi, L.; Polizzi, S.; Montini, T.; Fornasiero, P.; Pasquato, L.; Graziani, M., Monolayer Protected Gold Nanoparticles on Ceria for an Efficient CO Oxidation Catalyst. *Chemistry of Materials* **2007,** 19, (4), 650-651.

249.   Pavlova, S. N.; Sadykov, V. A.; Bulgakov, N. N.; Bredikhin, M. N., The Influence of Support on the Low-Temperature Activity of Pd in the Reaction of CO Oxidation: 3. Kinetics and Mechanism of the Reaction. *Journal of Catalysis* **1996,** 161, (2), 517-523.

250.   Haruta, M., Novel catalysis of gold deposited on metal oxides. *Catalysis Surveys from Japan* **1997,** 1, (1), 61-73-73.

251.   Haruta, M., Catalysis of Gold Nanoparticles Deposited on Metal Oxides. *CATTECH* **2002,** 6, (3), 102-115.

252.   Zou, X.; Xu, J.; Qi, S.; Suo, Z.; An, L.; Li, F., Effects of preparation conditions of Au/FeOx/Al2O3 catalysts prepared by a modified two-step method on the stability for CO oxidation. *Journal of Natural Gas Chemistry* 20, (1), 41-47.

195

253.	Kung, M. C.; Davis, R. J.; Kung, H. H., Understanding Au-Catalyzed Low-Temperature CO Oxidation. *The Journal of Physical Chemistry C* **2007,** 111, (32), 11767-11775.

254.	Chen, Y.-J.; Yeh, C.-t., Deposition of Highly Dispersed Gold on Alumina Support. *Journal of Catalysis* **2001,** 200, (1), 59-68.

255.	Lin, C.-H.; Lin, S. D.; Lee, J.-F., Chlorine Residue in the Au/γ-Al_2O_3 Prepared by $AuCl_3$ Impregnation—an EXAFS Analysis. *Catalysis Letters* **2003,** 89, (3), 235-242.

256.	Oh, H. S.; Yang, J. H.; Costello, C. K.; Wang, Y. M.; Bare, S. R.; Kung, H. H.; Kung, M. C., Selective Catalytic Oxidation of CO: Effect of Chloride on Supported Au Catalysts. *Journal of Catalysis* **2002,** 210, (2), 375-386.

257.	Senra, J. D.; Malta, L. F. B.; da Costa, M.; Michel, R. C.; Aguiar, L. C. S.; Simas, A. B. C.; Antunes, O. A. C., Hydroxypropyl-alpha-Cyclodextrin-Capped Palladium Nanoparticles: Active Scaffolds for Efficient Carbon-Carbon Bond Forming Cross-Couplings in Water. *Advanced Synthesis & Catalysis* **2009,** 351, (14-15), 2411-2422.

258.	Ding, L.; Guo, H.; Zhang, J. Q.; Zhang, Y. K.; He, T. C.; Mo, Y. J., Preparation of palladium nanoparticles by laser ablation and its spectral properties study. *Spectroscopy and Spectral Analysis* **2008,** 28, (9), 2053-2057.

259.	Calo, V.; Nacci, A.; Monopoli, A.; Detomaso, A.; Iliade, P., Pd nanoparticle catalyzed Heck arylation of 1,1-disubstituted alkenes in ionic liquids. Study on factors affecting the regioselectivity of the coupling process. *Organometallics* **2003,** 22, (21), 4193-4197.

260.	Kim, J. Y.; Park, K.; Bae, S. Y.; Kim, G. C.; Lee, S.; Choi, H. C., Preparation, characterization and catalytic properties of Pd-decorated carbon nanotubes possessing different linkers. *Journal of Materials Chemistry* 21, (16), 5999-6005.

261.	Hu, C. G.; Bai, Z. Y.; Yang, L.; Lv, J.; Wang, K.; Guo, Y. M.; Cao, Y. X.; Zhou, J. G., Preparation of high performance Pd catalysts supported on untreated multi-walled carbon nanotubes for formic acid oxidation. *Electrochimica Acta* 55, (20), 6036-6041.

262.	Evangelisti, C.; Panziera, N.; D'Alessio, A.; Bertinetti, L.; Botavina, M.; Vitulli, G., New monodispersed palladium nanoparticles stabilized by poly-(N-vinyl-2-pyrrolidone): Preparation, structural study and catalytic properties. *Journal of Catalysis* 272, (2), 246-252.

263.	Borkowski, T.; Trzeciak, A. M.; Bukowski, W.; Bukowska, A.; Tylus, W.; Kepinski, L., Palladium(0) nanoparticles formed in situ in the Suzuki-Miyaura reaction: The effect of a palladium(II) precursor. *Applied Catalysis a-General* 378, (1), 83-89.

264.	Wu, S. X.; He, Q. Y.; Zhou, C. M.; Qi, X. Y.; Huang, X.; Yin, Z. Y.; Yang, Y. H.; Zhang, H., Synthesis of Fe3O4 and Pt nanoparticles on reduced graphene oxide and their use as a recyclable catalyst. *Nanoscale* **2012,** 4, (7), 2478-2483.

265.   Zhang, R. Z.; Liu, J. M.; Li, F. W.; Wang, S. F.; Xia, C. G.; Sun, W., Magnetically Separable and Versatile Pd/Fe3O4 Catalyst for Efficient Suzuki Cross-Coupling Reaction and Selective Hydrogenation of Nitroarenes. *Chinese Journal of Chemistry* 29, (3), 525-530.

266.   Golubina, E. V.; Lateva, E. S.; Lunin, V. V.; Telegina, N. S.; Stakheev, A. Y.; Tundo, P., The role of Fe addition on the activity of Pd-containing catalysts in multiphase hydrodechlorination. *Applied Catalysis a-General* **2006,** 302, (1), 32-41.

267.   Rumi, L.; Scheuermann, G. M.; Mulhaupt, R.; Bannwarth, W., Palladium Nanoparticles on Graphite Oxide as Catalyst for Suzuki-Miyaura, Mizoroki-Heck, and Sonogashira Reactions. *Helvetica Chimica Acta* 94, (6), 966-976.

268.   Ramulifho, T.; Ozoemena, K. I.; Modibedi, R. M.; Jafta, C. J.; Mathe, M. K., Fast microwave-assisted solvothermal synthesis of metal nanoparticles (Pd, Ni, Sn) supported on sulfonated MWCNTs: Pd-based bimetallic catalysts for ethanol oxidation in alkaline medium. *Electrochimica Acta* **2012,** 59, 310-320.

269.   Hungria, A. B.; Calvino, J. J.; Anderson, J. A.; Martinez-Arias, A., Model bimetallic Pd-Ni automotive exhaust catalysts: Influence of thermal aging and hydrocarbon self-poisoning. *Applied Catalysis B-Environmental* **2006,** 62, (3-4), 359-368.

270.   Hungria, A. B.; Fernandez-Garcia, M.; Anderson, J. A.; Martinez-Arias, A., The effect of Ni in Pd-Ni/(Ce,Zr)O-x/Al2O3 catalysts used for stoichiometric CO and NO elimination. Part 2: Catalytic activity and in situ spectroscopic studies. *Journal of Catalysis* **2005,** 235, (2), 262-271.

271.   Luo, J. Y.; Meng, M.; Li, X.; Li, X. G.; Zha, Y. Q.; Hu, T. D.; Xie, Y. N.; Zhang, J., Mesoporous Co(3)O(4)-CeO(2) and Pd/Co(3)O(4)-CeO(2) catalysts: Synthesis, characterization and mechanistic study of their catalytic properties for low-temperature CO oxidation. *Journal of Catalysis* **2008,** 254, (2), 310-324.

272.   Igarashi, H.; Uchida, H.; Watanabe, M., Mordenite-supported noble metal catalysts for selective oxidation of carbon monoxide in a reformed gas. *Chemistry Letters* **2000**, (11), 1262-1263.

273.   Pavlova, S. N.; Sadykov, V. A.; Bulgakov, N. N.; Bredikhin, M. N., The influence of support on the low-temperature activity of Pd in the reaction of CO oxidation .3. Kinetics and mechanism of the reaction. *Journal of Catalysis* **1996,** 161, (2), 517-523.

274.   Liu, W. H.; Fleming, S.; Lairson, B. M., Reduced intergranular magnetic coupling in Pd/Co multilayers. *Journal of Applied Physics* **1996,** 79, (7), 3651-3655.

275.   Li, X. Y.; Wang, X.; Song, S. Y.; Liu, D. P.; Zhang, H. J., Selectively Deposited Noble Metal Nanoparticles on Fe3O4/Graphene Composites: Stable, Recyclable, and Magnetically Separable Catalysts. *Chemistry-a European Journal* **2012,** 18, (24), 7601-7607.

276.   Chandra, S.; Bag, S.; Das, P.; Bhattacharya, D.; Pramanik, P., Fabrication of magnetically separable palladium-graphene nanocomposite with unique catalytic property of hydrogenation. *Chemical Physics Letters* 519-20, 59-63.

197

277. Hu, J. F.; Wang, Y. P.; Han, M.; Zhou, Y. M.; Jiang, X. Q.; Sun, P. P., A facile preparation of palladium nanoparticles supported on magnetite/s-graphene and their catalytic application in Suzuki-Miyaura reaction. *Catalysis Science & Technology* 2, (11), 2332-2340.

278. Young, J. N.; Chang, T. C.; Tsai, S. C.; Yang, L.; Yu, S. J., Preparation of a nonleaching, recoverable and recyclable palladium-complex catalyst for Heck coupling reactions by immobilization on Au nanoparticles. *Journal of Catalysis* 272, (2), 253-261.

279. Soomro, S. S.; Ansari, F. L.; Chatziapostolou, K.; Kohler, K., Palladium leaching dependent on reaction parameters in Suzuki-Miyaura coupling reactions catalyzed by palladium supported on alumina under mild reaction conditions. *Journal of Catalysis* 273, (2), 138-146.

280. Li, Y.; Fan, X. B.; Qi, J. J.; Ji, J. Y.; Wang, S. L.; Zhang, G. L.; Zhang, F. B., Palladium nanoparticle-graphene hybrids as active catalysts for the Suzuki reaction. *Nano Research* 3, (6), 429-437.

281. Agostini, G.; Groppo, E.; Piovano, A.; Pellegrini, R.; Leofanti, G.; Lamberti, C., Preparation of Supported Pd Catalysts: From the Pd Precursor Solution to the Deposited Pd(2+) Phase. *Langmuir* 26, (13), 11204-11211.

282. Bai, Z. Y.; Yang, L.; Guo, Y. M.; Zheng, Z.; Hu, C. G.; Xu, P. L., High-efficiency palladium catalysts supported on ppy-modified C(60) for formic acid oxidation. *Chemical Communications* 47, (6), 1752-1754.

283. Glaspell, G.; Hassan, H. M. A.; Elzatahry, A.; Abdalsayed, V.; El-Shall, M. S., Nanocatalysis on supported oxides for CO oxidation. *Topics in Catalysis* **2008,** 47, (1-2), 22-31.

284. Siamaki, A. R.; Khder, A. E. S.; Abdelsayed, V.; El-Shall, M. S.; Gupton, B. F., Microwave-assisted synthesis of palladium nanoparticles supported on graphene: A highly active and recyclable catalyst for carbon-carbon cross-coupling reactions. *Journal of Catalysis* 279, (1), 1-11.

285. Razzaq, T.; Glasnov, T. N.; Kappe, C. O., Accessing Novel Process Windows in a High-Temperature/Pressure Capillary Flow Reactor. *Chemical Engineering & Technology* **2009,** 32, (11), 1702-1716.

286. Falus, P.; Boros, Z.; Hornyanszky, G.; Nagy, J.; Darvas, F.; Urge, L.; Poppe, L., Reductive amination of ketones: novel one-step transfer hydrogenations in batch and continuous-flow mode. *Tetrahedron Letters* **2011,** 52, (12), 1310-1312.

287. Janos, B.; Arpad, K.; Laszlo, U.; Ferenc, D.; Jozsef, B.; Rita, S. F., Double carbonylation of iodobenzene in a microfluidics-based high throughput flow reactor. *Journal of Molecular Catalysis a-Chemical* **2009,** 302, (1-2), 76-79.

288. Csajagi, C.; Borcsek, B.; Niesz, K.; Kovacs, I.; Szekelyhidi, Z.; Bajko, Z.; Urge, L.; Darvas, F., High-efficiency aminocarbonylation by introducing CO to a pressurized continuous flow reactor. *Organic Letters* **2008,** 10, (8), 1589-1592.

198

289.   Germanenko, I. N.; Dongol, M.; Pithawalla, Y. B.; El-Shall, M. S.; Carlisle, J. A., Effect of atmospheric oxidation on the electronic and photoluminescence properties of silicon nanocrystals. *Pure and Applied Chemistry* **2000,** 72, (1-2), 245-255.

290.   Li, S. T.; El-Shall, M. S., Synthesis of nanoparticles by reactive laser vaporization: silicon nanocrystals in polymers and properties of gallium and tungsten oxides. *Applied Surface Science* **1998,** 127, 330-338.

291.   Li, S. T.; Silvers, S. J.; ElShall, M. S., Surface oxidation and luminescence properties of weblike agglomeration of silicon nanocrystals produced by a laser vaporization-controlled condensation technique. *Journal of Physical Chemistry B* **1997,** 101, (10), 1794-1802.

292.   Xi, P. X.; Chen, F. J.; Xie, G. Q.; Ma, C.; Liu, H. Y.; Shao, C. W.; Wang, J.; Xu, Z. H.; Xu, X. M.; Zeng, Z. Z., Surfactant free RGO/Pd nanocomposites as highly active heterogeneous catalysts for the hydrolytic dehydrogenation of ammonia borane for chemical hydrogen storage. *Nanoscale* **2012,** 4, (18), 5597-5601.

293.   Huang, L.; Liu, Y.; Ji, L. C.; Xie, Y. Q.; Wang, T.; Shi, W. Z., Pulsed laser assisted reduction of graphene oxide. *Carbon* **2011,** 49, (7), 2431-2436.

294.   He, G.; Liu, W.; Sun, X.; Chen, Q.; Wang, X.; Chen, H., Fe3O4@graphene oxide composite: A magnetically separable and efficient catalyst for the reduction of nitroarenes. *Materials Research Bulletin* 48, (5), 1885-1890.

295.   Compagnini, G.; Russo, P.; Tomarchio, F.; Puglisi, O.; D'Urso, L.; Scalese, S., Laser assisted green synthesis of free standing reduced graphene oxides at the water-air interface. *Nanotechnology* **2012,** 23, (50).

296.   Liu, Y.; Huang, L.; Guo, G. L.; Ji, L. C.; Wang, T.; Xie, Y. Q.; Liu, F.; Liu, A. Y., Pulsed Laser Assisted Reduction of Graphene Oxide as a Flexible Transparent Conducting Material. *Journal of Nanoscience and Nanotechnology* **2012,** 12, (8), 6480-6483.

297.   Li, Y. B.; Mi, X.; Huang, M. M.; Cai, R. R.; Wu, Y. J., The catalytic activity of a novel recyclable alkoxypalladium complex in Suzuki reaction. *Tetrahedron* **2012,** 68, (40), 8502-8508.

298.   Pithawalla, Y. B.; El-Shall, M. S.; Deevi, S., Laser based synthesis of intermetallic Cu-Zn nanoparticles and filaments. *Scripta Materialia* **2003,** 48, (6), 671-676.

199